Investigation of the Surface Reconstruction and Gas Phase Composition during Growth by MOVPE

Dissertation

zur
Erlangung des Doktorgrades
der Naturwissenschaften
(Dr. rer. nat.)

dem

Fachbereich Physik
der Philipps-Universität Marburg

vorgelegt von

Oliver Peter Maßmeyer, M.Sc.

aus

Schwalmstadt

Marburg (Lahn), 2020

Vom Fachbereich Physik der Philipps-Universität Marburg
als Dissertation angenommen am: 02.02.2021
Erstgutachter: Prof. Dr. Kerstin Volz
Zweitgutachter: Prof. Dr. Carsten von Hänisch
Drittgutachter: Prof. Dr. Ferdinand Scholz
Tag der mündlichen Prüfung: 16.02.2021
Hochschulkennziffer: 1180

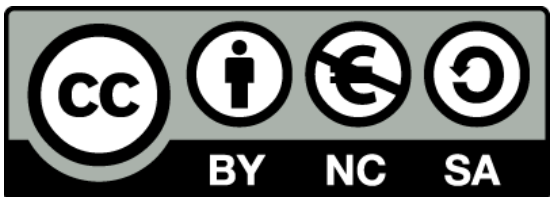

Zusammenfassung (Summary in German)

Die metallorganische Gasphasenepitaxie (metal organic vapor phase epitaxy, MOVPE) hat eine wichtige Rolle als Herstellungsmethode der III-V-Halbleitermaterialien für optoelektronische Anwendungen inne. Dies beinhaltet unter anderem die Herstellung von Telekommunikationslasern, Leuchtdioden, hocheffizienten Solarzellen und Hochfrequenzbauteilen im industriellen Maßstab. Obwohl sich die MOVPE als Abscheidungsmethode für Halbleitermaterialien seit ihrer Entdeckung und Entwicklung in den 1960er Jahren weitreichend etabliert hat, sind immer noch viele fundamentale Fragen über die grundlegenden physikalischen Effekte des Wachstumsprozesses ungeklärt. Dies liegt in der Komplexität der korrekten Beschreibung der auftretenden thermodynamischen, kinetischen und hydrodynamischen Effekte begründet und resultiert in einer eher phänomenologischen Beschreibung des epitaktischen Wachstumsprozesses. Dennoch dient die MOVPE zur Herstellung von neuen metastabilen Materialien, die eine Grundlage für die Erfindung und Optimierung von neuartigen Bauelementen bilden.

Eine Herangehensweise ist der Einsatz von verdünnt stickstoff- und verdünnt bismuthaltigen Materialien, die auf den III-V-Halbleitern Galliumarsenid (GaAs) und Galliumphosphid (GaP) basieren. Diese Materialien sind vielversprechend, um einen kleinen Beitrag zu aktuellen Themen wie der Verlangsamung der globalen Erwärmung beizutragen, indem zum Beispiel die Energieeffizienz der heutzutage genutzten Telekommunikationslaser verbessert wird. Die verdünnt bismuthaltigen Materialien zeigen das Potential, den Energieverbrauch der Laserdioden, die für den Datentransfer im Internet mit Emissionswellenlängen von 1.3 µm and 1.55 µm genutzt werden, drastisch zu reduzieren. Die weit höhere theoretische Effizienz der verdünnt bismuthaltigen Materialien im Vergleich zu den zur Zeit genutzten (Ga,In)(As,P)-Laserdioden liegt in der Unterdrückung von internen Verlustprozessen begründet, welche die Effizienz der (Ga,In)(As,P)-Laserdioden drastisch senkt. Des Weiteren werden die verdünnt stickstoffhaltigen Materialien als potentielle Lösung für effizientere Telekommunikationslaser diskutiert. Hier könnte das (Ga,In)(N,As)-Materialsystem große Vorteile im Hinblick auf die thermische Stabilität der Laserstrukturen liefern. Zusätzlich können die Laserstrukturen auf Basis des gut erforschten GaAs-Materialsystems hergestellt werden und somit im Gegensatz zur Herstellung der (Ga,In)(As,P)-Laserdioden auf InP-Basis von einer fortschrittlicheren technologischen Umsetzung profitieren. Neben der Anwendung als Lasermaterial werden die verdünnt stickstoffhaltigen Materialien zur Realisierung von hocheffizienten Solarzellen im Kontext der erneuerbaren Energien diskutiert. In diesem Zusammenhang könnten Materialkombinationen wie (Ga,In)(N,As), Ga(N,As,Sb) oder Ga(N,As,Bi) Anwendung in sogenannten Mehrfachsolarzellen finden. Die genannten Materialien könnten in diesem Konzept die Solarzellenschicht für die effiziente Absorption des Sonnenlichts im Wellenlängenbereich zwischen 1.1 µm and 1.4 µm verbessern, wodurch theoretische Umwandlungswirkungsgrade von über 50 % erreicht werden könnten. Dieser Wirkungsgrad sollte ausreichen, um im Preis-Leistungs-Vergleich in Konkurrenz zu der Silizium basierten Solarzellentechnologie zu treten. Die Herstellung der

genannten neuartigen Materialien konnte allerdings noch nicht mit der notwendigen Materialzusammensetzung sowie ausreichender struktureller Qualität und Reinheit realisiert werden und ist daher ein Thema der aktuellen Forschung.

Diese Arbeit soll mit einem kleinen Anteil zu der Realisierung der Anwendung dieser neuartigen Materialen beitragen und das grundlegende Verständnis zum epitaktischen Wachstum mittels MOVPE verbessern. Im ersten Teil dieser Untersuchungen wurde dazu die Oberflächenstruktur von verschiedenen verdünnt stickstoffhaltigen und verdünnt bismuthaltigen Schichten mit der Reflektionsanisotropiespektroskopie (reflection anisotropy spectroscopy, RAS) analysiert. Die RAS diente dabei zur *in-situ* Analyse der beim epitaktischen Wachstum von Ga(As,Bi)- und Ga(N,As)-Halbleiterschichten auftretenden Oberflächenrekonstruktionen, welche Rückschlüsse auf die Anordnung der Atome auf der Halbleiteroberfläche ermöglicht. Für die Untersuchung von Ga(N,As) wurde dazu der Einfluss des bereits etablierten 1,1-di-methyl-hydrazin (UDMHy) Präkursors und des neuartigen di-*tert*-butyl-amino-arsan (DTBAA) Präkursors auf die Oberflächenstruktur des Halbleiters GaAs untersucht. Die Zugabe von UDMHy auf die GaAs (001) Oberfläche resultierte in einer signifikanten Änderung der Oberflächenrekonstruktion von der arsenreichen c(4×4)β Oberfläche hin zu einer gallium- oder stickstoffreichen (2×6)/(6×6) Oberfläche. Im Vergleich dazu zeigte der analoge Prozess mit DTBAA eine Stabilisierung der arsenreichen c(4×4)β Oberflächenrekonstruktion aufgrund der intrinsischen Bereitstellung von Arsen des Präkursors. Während des Wachstums von Ga(N,As) durch die Zugabe von *tert*-butyl-arsan (TBAs) und tri-ethyl-gallium (TEGa) zeigte sich unabhängig vom verwendeten Stickstoffpräkursor und unabhängig von der Ausgangskonfiguration der unterliegenden GaAs Oberfläche ein Übergang zu der gleichen gallium- oder stickstoffreichen (2×6)/(6×6) Oberflächenrekonstruktion. Die Unabhängigkeit von der Ausgangsoberfläche wurde durch das Wachstum einer Ga(N,As) Schicht auf einer speziell präparierten (2×4) GaAs Oberfläche untersucht. Auf der Grundlage dieser Ergebnisse wurden atomar abrupte Ga(N,As) Zwischenschichten auf GaAs mittels verschiedener Wachstumssequenzen mit einem vermutlichen Stickstoffeinbau von bis zu 16 % realisiert. Die Wachstumssequenzen basierten dabei auf den Erkenntnissen zu den Ga(N,As) Oberflächenrekonstruktionen, und der Epitaxie-Prozess konnte mittels RAS *in-situ* überwacht werden.

Die Experimente zu den Ga(As,Bi) Halbleiterschichten wurden analog dazu mit der Untersuchung des Einflusses des tri-methyl-bismut (TMBi) Präkursors auf die GaAs (001) Oberfläche begonnen. Wie von dem bereits bekannten Verhalten des Aufschwimmens von Bi auf der Wachstumsoberfläche zu erwarten war, zeigte sich ein starker Einfluss von Bi auf die Oberflächenstruktur. Die Zugabe von TMBi bewirkte eine Änderung von der arsenreichen c(4×4)β Oberfläche zu einer vermutlich bismuthaltigen (4×3) Oberfläche. Dieser Wechsel zwischen den Oberflächenrekonstruktionen konnte in direkten Zusammenhang mit der notwendigen Oberflächenbelegung mit Bi während des Wachstumsprozesses zur Realisierung von Ga(As,Bi) Schichten mit hoher kristalliner Qualität gebracht werden. Diese Bi-benetzte Oberfläche wurde weiter in Hinblick auf ihre thermische Stabilität, die Widerstandsfähigkeit gegen Änderungen der umgebenden Bedingungen und ihre Aufbauzeit analysiert. Die Hinzugabe von TBAs und TEGa, was das Wachstum von Ga(As,Bi) hervorruft, resultierte in einer weiteren Modulation der Oberflächenrekonstruktion zu einer Bi-benetzten c(4×4)β Oberfläche. Weiter zeigte die Ausbildung der Oberflächenrekonstruktion der Wachstumsoberfläche von Ga(As,Bi) ein sehr sensitives Verhalten auf Änderungen im Gasphasenverhältnis von TBAs/TEGa, was den sehr kleinen möglichen Wachstumsbereich von Ga(As,Bi) unterstreicht. Zusätzliche Experimente wurden auf vorher präparierten (2×4) GaAs Oberflächen durchgeführt. Diese zeigen, dass sich die Oberflächenrekonstruktion von Ga(As,Bi) der unterliegenden

Oberflächenstruktur anpasst. Zur Untersuchung der ‘verdünnt stickstoff- und verdünnt bismuthaltigen Strukturen wurde außerdem die Oberflächenmorphologie mittels Rasterkraftmikroskopie (atomic force microscopy, AFM) und die Materialzusammensetzung mittels hochauflösender Röntgenbeugung (high resolution X-ray diffraction, HR-XRD) analysiert. Die Analyse der Materialzusammensetzung zeigte, dass der Stickstoffeinbau in GaAs auf galliumreicheren Oberflächen wie der (2×4) Oberfläche bevorzugt ist, sowie, dass ein erhöhter Bismuteinbau in GaAs auf der arsenreicheren c(4×4)β Oberfläche gegeben ist.

Im zweiten Teil der vorliegenden Doktorarbeit wurde ein neues Massenspektrometer zur Echtzeitanalyse der Gasphasenzusammensetzung während des Abscheidungsprozesses von III-V-Halbleitermaterialen eingesetzt. In diesem wurde die thermische Zerlegung der neuartigen Stickstoffpräkursoren DTBAA, di-*tert*-butyl-amino-phosphan (DTBAP) und di-*tert*-butyl-arsenyl-di-methyl-hydrazin (DTBADMHy) untersucht. Zur Analyse der Zerlegungstemperaturen und der Zerlegungsreaktionen dieser Präkursoren wurden diese Reaktionen zunächst unabhängig voneinander (unimolekular) in dem verwendeten AIXTRON AIX 200 MOVPE Reaktor untersucht. Diese Untersuchungen beinhalten neben den neuartigen Stickstoffpräkursoren DTBAA, DTBAP und DTBADMHy die Analyse der unimolekularen Zerlegung der Gruppe-III-Präkursoren tri-methyl-gallium (TMGa), TEGa, tri-*tert*-butyl-gallium (TTBGa) und der Gruppe-V-Präkursoren TMBi, TBAs, *tert*-butyl-phosphane (TBP) und UDMHy. Die Zerlegungsreaktionen zeigen eine gute Übereinstimmung zu früheren Zerlegungsstudien und bestätigen dadurch die Praktikabilität und Verlässlichkeit des neuartigen Massenspektrometerkonzepts. Ein großer Vorteil dieser Studie ist die Untersuchung all dieser unimolekularen Reaktionen unter vergleichbaren Bedingungen im selben Reaktorsystem, wodurch eine gute Grundlage für weitere Zerlegungsstudien geschaffen wurde. Die neuen Zerlegungsstudien der genannten neuartigen Stickstoffpräkursoren ist von grundlegender Bedeutung, um das vorteilhafte Einbauverhalten dieser Präkursoren bei Wachstumstemperaturen unterhalb von 500 °C zu verstehen. Die Präkursoren DTBAA, DTBAP und DTBADMHy weisen alle eine direkte N-As beziehungsweise eine direkte N-P Bindung auf. Die Zerlegungsanalyse zeigte, dass diese Bindung sich als erster Schritt im Mechanismus der Homolyse oder Heterolyse unter Freisetzung von Aminylradikalen (NH_2•) spaltet. Diese NH_2• Radikale werden für den effizienten N-Einbau bei niedrigen Temperaturen sowie für die Limitierung des N-Einbaus bei hohen Temperaturen durch Bildung von NH_3 verantwortlich gemacht. Der As- beziehungsweise P-Einbau hängt mit der Zerlegung der im ersten Reaktionsschritt gebildeten größeren Radikale di-*tert*-butyl-arsan (DTBAs•) und di-*tert*-butyl-phosphan (DTBP•) zusammen. Aufbauend auf der Untersuchung der unimolekularen Zerlegungsreaktionen wurde die Gasphasenzusammensetzung während des Wachstums von GaAs-, GaP- und GaN-Halbleitermaterialien analysiert. Die aufgetretenen bimolekularen Reaktionen wurden am ausführlichsten für die Präkursorkombinationen von TBAs mit TMGa, TEGa und TTBGa untersucht. Die entsprechenden Ergebnisse zeigen einen starken Einfluss der Ga-Präkusoren auf die Zerlegung des TBAs. Unter anderem wurde die Zerlegungstemperatur von TBAs bis auf die Zerlegungstemperatur der Ga Präkursoren herabgesetzt, was sich mit einem katalytischen Effekt der zerlegten Ga Präkursoren erklären lässt. Diese Katalyse reduziert die Zerlegungstemperatur des TBAs von 350 °C auf bis zu 160 °C bei Kombination mit TTBGa. Dieser Katalyseprozess ist besonders für das Wachstum von GaAs bei tiefen Temperaturen interessant. Weitere Zerlegungsexperimente wurden für verschiedene Gasphasenverhältnisse von TBAs/TEGa zwischen 0.5 und 10 durchgeführt. Hierbei wurden hochsensitive Messungen der Zerlegungsprodukte mittels selektivem Ionenauswurfs (stored wave inverse Fourier transformation, SWIFT) aus der Ionenfalle realisiert. Die Ergebnisse zeigten, dass ein

Alkylaustausch als wichtiger Schritt in der katalytischen Zerlegung von TBAs und den Ga Präkursoren stattfindet. Passend dazu wurde der Einfluss der Ga Präkursoren während des Wachstums von GaP auf die Zerlegung von TBP untersucht. Analog zur TBAs Studie zeigte sich eine Reduktion der Zerlegungstemperatur des TBP durch die Katalyse mittels der bereits zerlegten Ga Präkursoren. Allerdings liegt die dabei bestimmte Zerlegungstemperatur durchschnittlich 50 °C höher als beim TBAs. Dies lässt sich erklären, wenn sowohl die vergleichsweise stärkere C-P Bindung des TBP als auch die Alkylgruppen der Ga Präkursoren in die Zerlegungsreaktion involviert sind, was die Idee des Alkylaustausches untermauert. Die abschließenden Experimente wurden in Hinblick auf die Analyse von Adduktreaktionen im Wachstumsprozess durchgeführt. Die Adduktbildung ist beispielsweise für die Präkursorkombinationen von UDMHy mit TMGa und TEGa vorhergesagt, konnte aber bisher nur indirekt überprüft werden. Die Analyse der entsprechenden bimolekularen Reaktionen in der Ionenfalle zeigte die Bildung von größeren Addukten wie $(CH_3)_2NN[(CH_3)_2Ga]_2NN(CH_3)_2$ bei Raumtemperatur zwischen UDMHy und TMGa. Analog zeigte sich die Bildung von $(CH_3)_2NN[(C_2H_5)_2Ga]_2NN(CH_3)_2$ mit UDMHy und TEGa.

Abschließend lässt sich sagen, dass die Analyse der Oberflächenstrukturen und der Gasphase während des Wachstumsprozesses mit MOVPE neue Einblicke in den Abscheidungsprozess von III-V-Halbleitern hervorgebracht hat, besonders im Hinblick auf die verdünnt stickstoff- und verdünnt bismuthaltigen Materialsysteme. Beide Analysemethoden, sowohl die Oberflächenanalyse mittels RAS als auch die Gasphasenanalyse mittels Massenspektrometrie, ermöglichten zusätzliche Einblicke in die auftretenden chemischen Reaktionen und eine direkte Kontrolle des Wachstumsprozesses. Zukünftig sollten die Anwendung und das Verständnis dieser Methoden auf neuartige Materialen angewendet werden. Besonders die Analyse von ternären, quaternären oder neuartigen 2D-Materialsystemen ist interessant, da diese vorrausichtlich die Grundlage für neuartige Anwendungen im Themengebiet der Halbleiter bilden.

Danksagung (Acknowledgment)

Im Vorfeld meiner Arbeit möchte ich mich bei allen Personen bedanken, die mich in den letzten 3 Jahren bei meiner Forschung durch aufschlussreiche wissenschaftliche Diskussionen sowie durch sehr willkommene Abwechslung und Ratschläge im privaten Bereich unterstützt haben. Mein Dank gilt dabei besonders:

- Prof. Dr. Kerstin Volz für die Betreuung meiner Dissertation, die damit verbundenen zahlreichen und hilfreichen wissenschaftlichen Diskussionen und Ratschläge sowie für die Möglichkeit die vorliegende Arbeit in ihrer Arbeitsgruppe zu schreiben.

- Prof. Dr. Carsten von Hänisch für die Übernahme des Zweitgutachtens meiner Arbeit, die hilfreichen Diskussionen vor allem mit Bezug auf aufgetretene chemische Fragestellungen und seiner Arbeitsgruppe, ins besondere Christian Ritter und Marcel Köster für die Herstellung der untersuchten, neuartigen metallorganischen Präkursoren.

- Prof. Dr. Ferdinand Scholz für die Übernahme des Drittgutachtens meiner Arbeit und die damit verbundenen zusätzlichen inhaltlichen Anregungen. Sowie für die Teilnahme an meiner Disputation.

- Prof. Dr. Florian Gebhard für die Teilnahme als dritter Prüfer in meiner Prüfungskommission.

- Prof. Dr. Wolfgang Stolz für die Unterstützung und hilfreichen Diskussionen, besonders mit Bezug auf das epitaktische Wachstum und die Interpretation von Massenspektren.

- Der DFG für die Finanzierung meiner Projekte im Rahmen des GRK 1782 “Functionalization of Semiconductors” & SFB 1083 “Structure & Dynamics of Internal Interfaces”.

- Dem iTrap Team von Carl Zeiss SMT GmbH, insbesondere Hin Yiu Chung, Rüdiger Reuter, Valerie Derpmann und Yessica Brachthaeuser für die Ratschläge und Diskussionen zur Funktionsweise der neuartigen Ionenfalle.

- Meiner Arbeitsgruppe für die schöne Arbeitsatmosphäre und das hilfreiche Feedback bei all meinen Seminarvorträgen und fachspezifischen Fragen. Ganz besonders sind hier Thomas Ochs, Stefan Reinhard, Celina Becker, Elke Vaupel, Marina Koch, Isabelle Kimmel und Marieke Sycha für die technische und administrative Unterstützung hervorzuheben.

- Thilo, Johannes und Damien für die schöne Atmosphäre im Büro, die zahlreichen, aufschlussreichen und thematisch relevanten Diskussionen sowie die nette Abwechslung zwischendurch.

- Johannes Haust, Ebunoluwa Odofin, Robin Günkel und Sebastian Inacker für die schöne Zeit und die erfolgreichen Ergebnisse in wissenschaftlicher Zusammenarbeit.

- Magda, all meinen Freunden und meiner Familie für die schöne Zeit, die Unterstützung in allen Lebenslagen und Aufmunterungen. Ohne Euch wäre meine Dissertation in dieser Weise nicht möglich gewesen.

Contents

Chapter 1

Introduction

Today's society benefits from a large number of technological, social and economic inventions and developments that have improved our lives in many aspects for thousands of years. However, there are still a lot of essential tasks to be solved on our planet and beyond to improve and adjust living conditions. This covers topics such as food security, employment security, gender equality, globalization, the fourth industrial revolution, space exploration, healthcare, including the present challenge of a global pandemic, climate change and many more.[1,2] To solve all these tasks new scientific discoveries will play a significant role.
The focus of this work is meant to make a small contribution to possible solutions in the field of climate change. In particular, the research has been done for the improvement in the fabrication of novel material systems, which are discussed for applications such as telecommunications lasers, light emitting diodes, highly efficient solar cells or high frequency devices. These device applications are mainly based on III-V compound semiconductors materials that are produced by metalorganic vapor phase epitaxy (MOVPE) on an industrial scale, with a global market value of over 90 billion dollars today.[3]

One research approach with respect to the climate change is connected with the poor energy efficiency of the currently used telecommunication lasers. These telecommunications lasers are used for the data transfer across the internet via glass fibers networks. Due to every days usage of social media, streaming platforms, smartphone communication and new concepts in the scope of the 'Internet of Things' the data communication largely increases by about 60 % each year.[4] Consequently, this results in an astonishingly high energy consumption by the internet of about 10 % of the global electricity demand today.[5] Besides the large energy consumption of the data storage centers, the telecommunication could be improved by the exchange of the currently used indium gallium arsenide phosphide (Ga,In)(As,P) laser diodes, which are deposited on InP substrates. These laser structures have a low efficiency of 20 % due to internal loss processes in the active region such as Auger recombination and inter-valence band absorption (IVBA), resulting in heat generation.[6–8] The generated heat leads to an increased temperature of the devices and consequently device cooling is required. These additional cooling efforts drop the effective efficiency of the (Ga,In)(As,P) laser diodes by a further magnitude.[6] Since the data communication is based on light emission at a wavelength of 1.3 µm or 1.55 µm, due to the absorption minima of the glass fibers at these wavelengths, new laser devices emitting at these wavelength are desired.

A possible optimization in this regard is the use of 'dilute bismide' containing gallium arsenide, Ga(As,Bi), as high efficient telecommunications lasers. Besides the fact that

Ga(As,Bi) can be deposited on high-quality GaAs substrates, a large benefit of Ga(As,Bi) compared with the currently used (Ga,In)(As,P) material system is the predicted suppression of internal loss processes such as Auger recombination and IVBA for bismut fractions above 10 %.[9,10] However, due to the high metastability of the Ga(As,Bi) material system the realization of high quality Ga(As,Bi) structures with more than 10 % Bi incorporation is an ongoing challenge. Nevertheless, this offers a large opportunity to improve the energy consumption of these devices and therefore to contribute to solutions regarding the climate change.

Another research approach is the investigation of materials based on 'dilute nitride' containing gallium arsenide, Ga(N,As). This material family is also discussed for applications as telecommunication laser emitting at 1.3 µm or 1.55 µm, by using indium gallium nitride arsenide (Ga,In)(N,As) as active medium. One benefit of the (Ga,In)(N,As) material system is a higher temperature stability due to a higher electron confinement in the conduction band of the material as well as the possibility to be deposited on GaAs substrates.[11,12] Furthermore, different material combinations such as (Ga,In)(N,As), Ga(N,As,Sb) or Ga(N,As,Bi) are discussed for the application in high efficient multi junction solar cells, which is a promising concept in terms of renewable energy. Compared to the widely spread usage of silicon solar cells with an energy conversion efficiency of up to 25 %,[13] the concept of multi junction solar cells can reach theoretical efficiencies over 50 % under concentrated sun light.[14,15] To achieve increasing efficiencies, new material systems need to be examined, especially ones which exhibit an efficient light absorption in the wavelength range between 1.1 µm and 1.4 µm. These more advanced solar cell concepts are currently used in space technology for electricity generation on satellites. Nevertheless, a further improvement of the energy conversion efficiency could make these solar cells competitive with the silicon based solar cells in terms of cost efficiency.[16] The 'dilute bismides' and 'dilute nitrides' will potentially lead to new inventions in the fields of space exploration and climate change.

The remaining challenge is the deposition of the 'dilute bismides' and 'dilute nitrides' material systems with the desired composition, crystalline quality and material purity. Due to the metastability of these materials, the fabrication is quite challenging and can only be realized with growth methods such as MOVPE operating far-off from thermodynamic equilibrium conditions.[17–22] However, the realization of the desired structural and optical properties in order to be competitive to the currently used device applications has not be reached so far. The 'dilute bismides', among other things, suffer from reaching a Bi incorporation of above 10 % and show the accumulation of Bi on the growth surface.[18] The 'dilute nitrides' on the other hand are for example limited in their optical performance, which is related to C incorporation from the used metal organic raw materials (precursors).[11] Therefore, the epitaxial growth process of both material families as well as of the primary GaAs system is analyzed in the framework of the presented thesis in terms of their surface structure on an atomic level and their gas phase reactions which are occurring during the MOVPE process.

This thesis is written in cumulative form and is structured as following: Chapter 2 covers an overview of the underlying physical theory of semiconductor materials with focus on 'dilute bismides' and 'dilute nitrides'. Furthermore, an introduction into the formation of surface structures on semiconductors and into the design of metal organic precursors as raw materials for MOVPE is given. Chapter 3 covers an overview of the applied experimental methods with focus on the MOVPE technique for the deposition of semiconductor materials, the reflection anisotropy spectroscopy (RAS) for analysis of the surface structure and mass spectrometry, which is used to break down the decomposition

reactions of the used precursors. Chapter 4 focuses on the *in-situ* investigations of the surface structure during MOVPE growth of ‘dilute bismides’ and ‘dilute nitrides’ by RAS. This chapter is aimed to improve the understanding of the Bi and N incorporation into GaAs to support the developments in this field. Chapter 5 presents the results of the decomposition analysis of different metal organic precursors by a highly sensitive mass spectrometer provided by Carl Zeiss SMT GmbH. This includes the study of already established precursors as well as of newly synthesized N precursors, which are potential candidates to solve the problematic C incorporation in the ‘dilute nitrides’. Furthermore, the mass spectrometer is used to study reactions involving two or more precursors to enhance the general understanding of the growth process by MOVPE. The scientific publications directly related to the topics of Chapter 4 and 5 are presented in Chapter 7 after a short summary of this thesis in Chapter 6.

Chapter 2

Material Systems and Precursors

2.1 Material Systems and Surface Structures

Chapter 2 covers the fundamental properties of the investigated material systems Ga(N,As) and Ga(As,Bi) combined with their relevance for possible device applications. Prior to this, the fundamental GaAs system is discussed, since in both cases the ternary compound contains only small amounts of N or Bi, respectively. In the last section the fundamentals of semiconductor surfaces with focus on the formation of surface reconstructions are presented.

2.1.1 GaAs (001)

The first GaAs crystal was created in the 1920s by V.M. Goldschmidt and was found to crystallize in the zincblende structure.[23] This structure is formed by a fcc lattice with a diatomic basis at the atomic positions $(0,0,0)$ and $(1/4, 1/4, 1/4)$. For GaAs this basis is occupied with one As and one Ga atom, as illustrated in Figure 1.

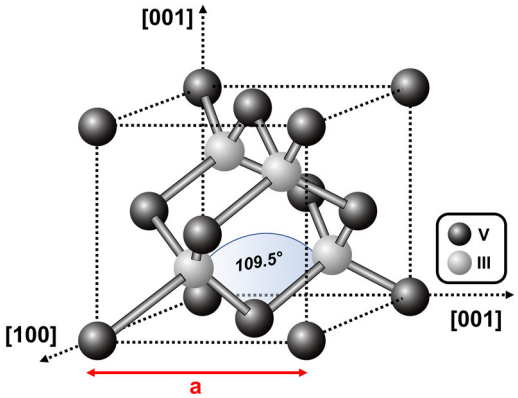

Figure 1: Schematic of the crystal structure of GaAs (zincblende structure).

The crystal structure results from the formation of tetrahedral bonds between the Ga and the As atoms under an angle of 109.5°. The bonds are caused by sp^3 hybridization of the atomic orbitals and are found to exhibit a mixture of covalent and ionic bond character, with an ionic fraction around 0.3.[24] This leads to a bond length and distance to the next neighboring atom of $r_0 = \sqrt{3}a/4 = 2.44793\,\text{Å}$, resulting in the cubic lattice constant of $a = 5.65325\,\text{Å}$.[25] Besides its structural, mechanical, elastic, vibrational and thermal properties covered in ref.[26], GaAs exhibits interesting optical and electrical properties that are used in high performance device applications such as high electron mobility transistors or solar cells.[15,27,28] The optical and electrical properties can be explained within the band structure model of semiconductors. In this model the movement of the carriers, e.g., an electron is treated as quasi free propagation of an electron wave and is only influenced by the charge of the atom cores in the crystal. Due to Bragg reflections in the crystal and the crystal symmetry, this leads to formation of standing

electron waves, which can be described in terms of overlapping atomic orbitals leading to continuous energy bands.[29,30] These standing waves can be separated in energy, leading to prohibited regions in the band structure model of a semiconductor. The band structure of GaAs is shown around the Γ - point in Figure 2.

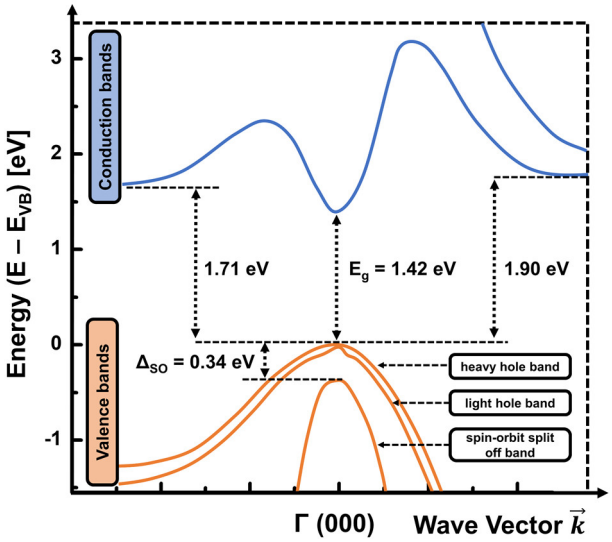

Figure 2: Band diagram of GaAs for the upper part of the valence band and the lower part of the conduction band around the Γ-point. The direct and indirect energy gaps are given for room temperature. The illustration is adapted from ref.[26]

The smallest energy gap between the highest occupied states in the valence band and the lowest unoccupied states in the conduction band is called **band gap** and is given for GaAs at the Γ-point. Since this energetic maximum and minimum are located at the same position in the k-space, GaAs is categorized as a direct semiconductor. This configuration in the band structure allows a direct transition without the addition of a lattice vibration (phonon) to fulfill the momentum conservation, resulting, e.g., in a high probability for radiative recombination or absorption, between the energy bands. The band gap for GaAs is given with an energy of 1.42 eV, which corresponds to light emission with a wavelength of 873 nm in a radiative recombination. This wavelength is suitable for photonic applications near the mid infrared region. The direct band gap further leads to very efficient absorption of photons with an energy higher than this band gap, which is utilized, e.g., in thin-film solar cell concepts.[28] The band diagram includes other local minima in the conduction band, leading to available indirect transitions, which need the absorption or emission of a phonon, at higher energies. The valence band structure consists of three different bands around the Γ-point, built up out of the energetically degenerated heavy and light hole bands as well as the energetically separated spin-orbit split-off band. These bands are formed due to the spin-orbit interaction between the (p- and s-) orbitals that build up the valence band. The shown curvatures in the dispersion relation are inversely related to different effective masses of the hole carriers in these bands. The effective mass determines the velocity for charge transfer in these bands and explains the nomenclature.[26,31,32] The more complex valence band structure results in the possibility of further transitions, e.g., an absorption event can occur between the light hole, the heavy hole or the spin-orbit split-off band, a so called inter valence band absorption.

A more expanded description of the properties of single crystalline GaAs can be found in ref.[26].

2.1.2 Ga(N,As) and Ga(As,Bi) (001)

This subsection covers the effect of the incorporation of dilute amounts of foreign atoms, such as nitrogen (N) or bismuth (Bi) on the band structure of GaAs. A change of the band structure is directly related to changes in the electronic and optical properties of the semiconductor, giving the possibility of new device applications and concepts using material systems such as Ga(N,As) or Ga(As,Bi).

A partial substitution of one of the host elements in GaAs, e.g., in the As sub-lattice by an atom with a smaller or larger covalent radius such as N or Bi causes a change of the bonds in the crystal, leading to a change of the interatomic distances in the crystal. This subsequently changes the band structure since it originates from the electronic states formed by the orbitals, which are influenced by the kind of atoms and bond lengths in the crystal.[31] This variation of the bond lengths leads to an effective change of the lattice constant of the ternary compound with respect to the GaAs lattice constant. If either of the mentioned materials are grown on GaAs, which is referred to as heteroepitaxy, a mechanical stress arises in the grown layer due to the difference in the lattice constants, which leads to a global distortion of the lattice, called strain ϵ. If the difference in lattice constants is not too large (approx. below 1 %) and if a critical thickness t_c is not surpassed, the stress only causes strain, without formation of crystal defects, which is referred to as pseudomorphic growth. For pseudomorphic conditions the evolving in-plane (biaxial) strain $\epsilon^{||}$ can be defined with respect to the lattice constant a_{sub} of the substrate and the lattice constant $a_{relaxed}^{layer}$ of the unstrained (relaxed) layer:[31]

$$\epsilon^{||} = \frac{a_{sub} - a_{relaxed}^{layer}}{a_{sub}} \qquad (2.1)$$

Under these pseudomorphic conditions the evolving strain is categorized into **tensile strain** ($a_{relaxed}^{layer} < a_{sub}$) and **compressive strain** ($a_{relaxed}^{layer} > a_{sub}$), depending on the size of the unstrained lattice constant $a_{relaxed}^{layer}$ of the grown layer with respect to the lattice constant of the substrate a_{sub}. The mentioned biaxial strain in the material has a direct influence on the band structure of the grown material, which is shown in Figure 3.

For common zinc blende materials, the band gap reduces for tensile strain and increases for compressive strain. In general, the largest effect is predicted to occur due to downward or upward movement of the conduction band. However, since an isolated measurement of the valence band and the conduction band is experimentally difficult, these assumptions are based on theoretical predictions.[31] In case of an applied strain the degeneracy in the valance band is lifted at the Γ-point, leading to two distinguishable bands at this point.

For most ternary compound semiconductors in the configuration $(A_x, B_{1-x})C$ or $A(B_x, C_{1-x})$ the change of the band gap energy E_g in dependence on the composition x on the substituted element A or B can be described empirically by introducing a quadratic dependence with a material specific bowing parameter b:[31]

$${E_g}^{ABC}(x) = x \cdot {E_g}^{AB} + (1-x) \cdot {E_g}^{AC} - b \cdot x \cdot (1-x) \qquad (2.2)$$

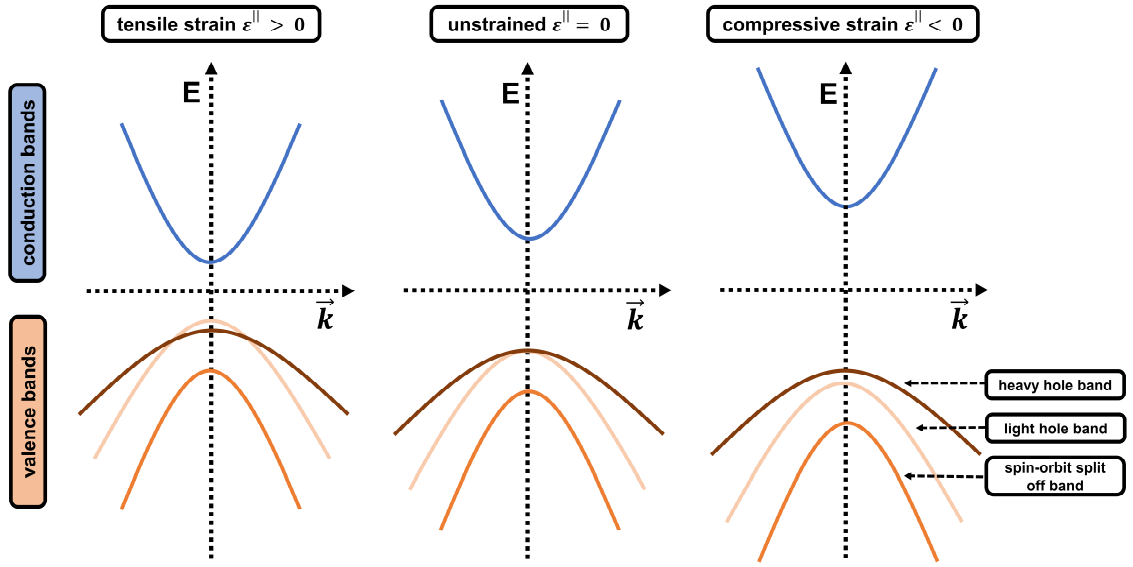

Figure 3: Illustration for the effect of biaxial strain $\epsilon^{||}$ on the size of the band gap and the relative positions of the heavy hole, light hole and spin-orbit split-off valence bands. Introduction of strain lifts the degeneracy of the light hole band and heavy hole band at the Γ-point. Tensile strain leads to a reduction and compressive strain to an increase of the band gap.

Equation 2.2 allows the calculation of the band gap energy, if the binary band gap energies ${E_g}^{AB}$ and ${E_g}^{AC}$ are given. This bowing behavior can still be compatible with the virtual crystal approximation (VCA) by choosing the right parameters without introducing a bowing parameter.[33] The VCA assumes a linear relation between the change of the lattice parameter and the concentration of the substituted element.[33]

However, Ga(N,As) as well as Ga(As,Bi) both show a very large reduction of the band gap energy with about 150 meV for the first % of N and about 80 to 90 meV per % of Bi.[34–40] In both cases, this results in enormously large bowing parameters for the reduction of the band gap. However, the underlying physics are not sufficiently explained in terms of bowing and the VCA model. In the current point of view, this strong band gap reduction is best explained in terms of a band anti-crossing model, which is illustrated in Figure 4 for Ga(N,As) and Ga(As,Bi).[41–47]

In this model, the incorporation of small amounts of N or Bi is treated as isoelectric impurity. The small number of foreign atoms leads to the formation of localized states. Due to the much smaller (larger) covalent radius and larger (lower) electronegativity of nitrogen (bismuth) compared to the exchanged As atoms the formed states are located deep in the conduction and valence band, respectively. This localization of the states in the respective bands leads to an interaction of the localized states with the conduction or valence bands originating from the GaAs host lattice, resulting in the formation of new energetically higher E_+ and lower E_- bands with respect to the GaAs bulk bands. In case of N the band anti-crossing occurs in the conduction band and in case of Bi the interaction occurs in the valence band due to the location of the respective states.

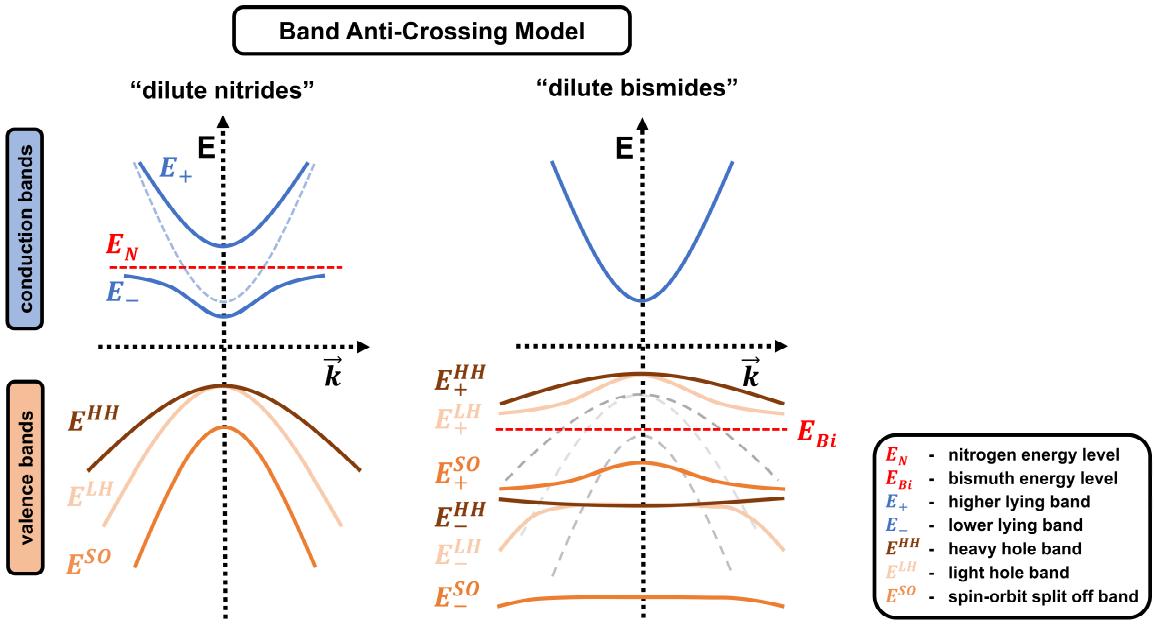

Figure 4: Illustration of the band gap reduction in Ga(N,As) and Ga(As,Bi) in terms of the band anti-crossing model. Incorporation of dilute amounts of N or Bi causes the formation of localized states that are located deep within the conduction or valence band, respectively. The interaction of these localized states with the bands originating from the GaAs host lattice are predicted to lead to the formation of new E_+ and E_- bands.

The validity of the band anti-crossing model was first demonstrated for dilute N containing quaternary (Ga,In)(N,As).[41] The experiments show the existence of the predicted higher E_+ and lower E_- bands with respect to the conduction band energy E_{CB} of the host lattice. Since the N level is located at E_N about 0.25 eV higher than the conduction band, the strong interaction leads to a large band gap reduction in Ga(N,As).[41,48] The energetic positions of the new bands can be calculated by describing the coupling between the N states and the conduction band states by a coupling matrix element V_{CB-N}:

$$E_\pm = \frac{1}{2}\left(E_N + E_{CB} \pm \sqrt{(E_N - E_{CB})^2 + 4V_{CB-N}^2}\right) \qquad (2.3)$$

Due to the location of the N-level deep in the conduction band, the valence band is mainly unaffected. This leads to no significant change of the light and heavy hole and the spin-orbit split-off band.

Due to the resulting strong band gap reduction, III-V semiconductors containing small amounts of nitrogen, 'dilute nitrides', are discussed for various device applications. The large effect of the N on the conduction band structure can be used to create a high electron confinement, which can be beneficial to realize laser structures with high thermal stability. Combined with the large band gap reduction, this could, e.g., be used to realize laser structures operating with light emission at 1.3 µm or 1.55 µm, usable for telecommunication.[12] Another application is the use as active region in high performance multi-junction solar cells. In these materials such as (Ga,In)(N,As) or Ga(N,As,Sb) are discussed as a layer with a band gap of 1 eV to potentially reach conversion efficiencies of more than 50 % under concentrated sun light.[14,15]

On the other hand, in case of 'dilute bismides' only the existence of the E_+ bands has been experimentally proven.[49] Therefore Equation 2.3 can be written as:

$$E_+ = \frac{1}{2}\left(E_{Bi} + E_{VB} + \sqrt{(E_{Bi} - E_{VB})^2 + 4V_{VB-Bi}^2}\right) \quad (2.4)$$

where E_{Bi} is the energy of the Bi induced states in relation to the valence band edge E_{VB} of GaAs. The theory for Ga(As,Bi) has further been improved using a tight-binding model to lead to an agreement of the predicted band gap with experimental data across a large composition range.[47] Furthermore, a combination with the VCA model leads to a sufficient description of the conduction and spin-orbit split-off bands, as their position varies linearly with the Bi fraction. The spin-orbit splitting Δ_{SO}, which describes the energetic distance between the spin-orbit split-off band and the light and heavy hole bands, is shown to be largely dependent on the atomic number of the incorporated elements. Since Bi possesses a large atomic number, the spin-orbit splitting is largely enhanced by incorporation of Bi into GaAs.[35,47,49,50] The incorporation of more than 10 % of Bi is predicted to lead to a band alignment, in which Δ_{SO} becomes larger than the band gap E_g. This situation leads to the suppression of possible internal loss processes such as inter-valence band absorption and Auger recombination, involving the transitions from the conduction to the heavy hole and from the spin-orbit split-off to heavy hole band (CHSH).[9,10,49,50] The CHSH transitions are the main loss mechanisms in the currently used telecommunication laser diodes based on InP.[6,51,52] This combined with the strong band gap reduction makes Ga(As,Bi) a potential candidate for application as a high efficient laser emitting in the telecommunication window at 1.55 µm. The mentioned prevention of the CHSH transitions should lower the heat generation in the device and consequently lead to an increased efficiency of Ga(As,Bi). The lower heat generation is advantageous compared to InP, which presents much poorer efficiencies due to the need of additional external cooling, which is necessary to stabilize the laser emission at 1.55 µm.[9]

The realization of the growth of 'dilute nitrides' on GaAs or in general is quite challenging due to the metastability of the Ga(N,As) material system. One approach is the growth by metal organic vapor phase epitaxy (MOVPE), which will be described in Chapter 3.1. Besides a fine adjustment of the process parameters, the 'dilute nitrides' are especially suffering from unwanted carbon incorporation. This carbon contamination was shown to significantly increase the threshold current density of laser devices based on 'dilute nitrides'.[53,54] The carbon incorporation is believed to originate from the currently used and established metal organic nitrogen precursors, such as 1,1-di-methyl-hydrazine (UDMHy). This point is addressed by the investigation of newly designed N-precursors in terms of their reaction products occurring during the thermal decomposition. The decomposition reactions are investigated by mass spectrometry in this thesis. Furthermore, the use of UDMHy as precursors shows low N incorporation efficiencies.[55,56] Therefore, a large excess of the N precursor is supplied in the growth process, which might also effect the surface structure. The low efficiency might be related to formation of stable decomposition products, which will be treated in terms of mass spectrometry. The potential effect on the surface structure is investigated *in-situ* by analysis of the surface structure with reflection anisotropy spectroscopy (RAS).

Likewise, the realization of 'dilute bismides' on GaAs is quite challenging, since the fabrication of the desired material composition has not been reached, while maintaining high crystalline quality.[18] To provide the above mentioned emission at the telecommunication window of 1.55 µm, Bi concentrations in GaAs of more than 10 % have

to be realized.[9,18,38] Due to the metastability of the Ga(As,Bi) material system, Bi exhibits a low solubility in GaAs, prohibiting the growth under thermodynamic equilibrium conditions.[20] Like for 'dilute nitrides' the growth of Ga(As,Bi) far off from equilibrium can be realized with MOVPE. It has been shown that a precise control of the growth parameters is necessary to realize high quality Ga(As,Bi) layers. Otherwise, phase separation leads to droplet formation on the growth surface.[57–59] Furthermore, a coverage of the surface with bismuth prior to the growth seems to be necessary to realize a homogenous growth of the material. This led to the development of a more complicated growth model for growth of Ga(As,Bi) by MOVPE.[18,60–62] To understand this growth behavior and to enhance the Bi incorporation as well as the crystalline quality the Ga(As,Bi) growth surface is studied *in-situ* by RAS and is further correlated to mass spectrometry (MS) investigations in the framework of this thesis.

A more expanded description of the material properties and the growth of 'dilute bismides' and 'dilute nitrides' can be found in ref.[38,63] and ref.[64], respectively.

2.1.3 Surface Structure

This subsection covers a short introduction into surface reconstructions based on the example of GaAs. The focus will be laid on possible atomic rearrangements at the surface, its effect on the electronic surface structure and the relevance of the surface structure with respect to device applications.

Compared to the atomic arrangement in the bulk structure of a crystal, as covered in Chapter 2.1.1, the symmetry is broken at the surface. In the simplest case, the surface will adopt to the structure of the underlying crystal. However, this situation is often not energetically favorable. Therefore, a **relaxation** of the atoms in the top-most layers is expected including a vertical distortion of the atoms as shown in Figure 5 a).[31] Besides a vertical rearrangement also lateral distortions can occur. The GaAs (001) surface will be considered as an example in the following. As covered in Chapter 2.1.1, each atom forms four bonds to neighboring atoms in the zinc blende structure of GaAs. At the (001) surface two bonds will be unsaturated due to missing bonding partners, leading to the formation of so-called dangling bonds, illustrated in Figure 5 a).

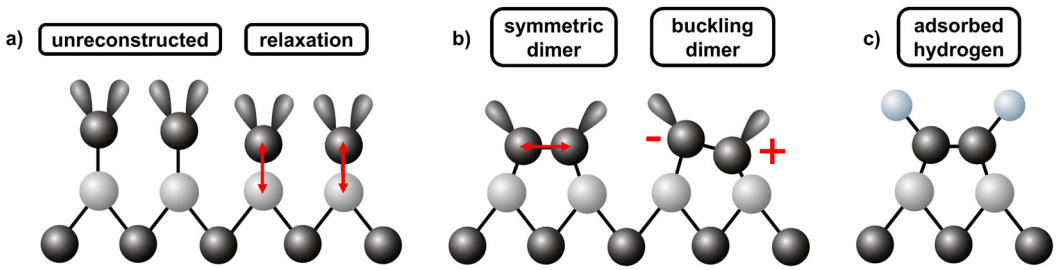

Figure 5: Illustration of the atomic rearrangement during the formation of a surface reconstruction on a (001) surface in the zinc blende structure. a) Unreconstructed surface showing the effect of surface relaxation. b) Dimerization processes leading to formation of symmetric or asymmetric dimers. c) Changed bonding configuration by adsorption of molecules such as hydrogen from the surrounding vapor phase.

In case of the GaAs (001) surface, these dangling bonds exhibit unsatisfied valences, which leads to an unfavorable energy state of the surface. The dangling bonds will be partly satisfied by formation of bonds with neighboring surface atoms to reduce the total number of dangling bonds at the surface. In this example two unsaturated bond orbitals, each occupied by one electron, are forming one filled bridge bond orbital parallel to the

surface. This formation of a dimer is shown in Figure 5 b). These dimers can further minimize their energy by charge redistribution between the remaining dangling bonds, leading to a vertical and lateral distortion of the atoms to each other (buckling dimer).[31,65]

In the bulk crystal, the bonds are formed by sp^3 hybridization of the atomic s- and p-orbitals, as mentioned in Chapter 2.1.1. The energy level of the resulting hybrid orbital ϵ_{hyb} is given by a linear combination of the involved orbitals resulting in an energy level $\epsilon_{hyb} = (\epsilon_s + 3\epsilon_p)/4$ for each atom.[66] Each bond in the bulk crystal is then formed by a linear combination of two hybrid orbitals leading to bonding $\epsilon_{bonding}$ and antibonding $\epsilon_{antibonding}$ energy levels. The linear combinations of the bonding orbitals result in the formation of the occupied valence band states and the conduction band states are formed by linear combinations of the antibonding states. At the surface further energy levels are given due to dangling bonds or dimer formation. A model for the energetic description of the formation and occupation of the bond orbitals at the surface with respect to the bulk states is given in Figure 6. The formed dangling bonds as well as dimers result in new energy states that lie in the conduction band, the valence band or within the band gap of the host material. The energy level of a dangling bond $\epsilon_{dangling}$ is given by the energy of its hybrid orbital, while a dimer forms a new bonding ϵ^{+}_{dimer} and antibonding ϵ^{-}_{dimer} level.[31,66]

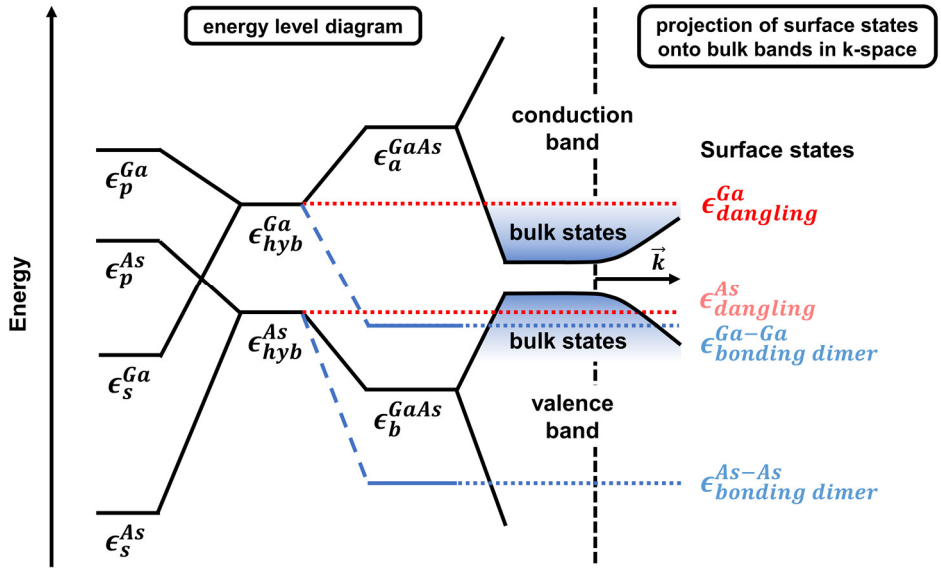

Figure 6: Illustration of the energy levels ϵ of the bond orbitals given for GaAs. The energy levels of the dangling bonds $\epsilon_{dangling}$ or of the formed dimers ϵ_{dimer} can lead to the formation of new surface states lying in the conduction, valence band or the band gap of the host material.

Beyond the formation of dimers, the rearrangements to minimize the surface energy generally leads to the formation of a larger surface unit cell named **surface reconstruction**. Such surface reconstructions include the distortion of the top most layers of the bulk structure. The distortion can extend up to a few nanometers into the bulk crystal. For semiconductor surfaces the electron counting rule is often used to obtain models for the surface structure of real surfaces.[67] The resulting structures largely reduce the number of dangling bonds by putting all available electrons into a bonding configuration. The resulting reconstructions are classified by the symmetry with respect to the structure of the bulk crystal, which is the cubic lattice for the investigated materials. A nomenclature of the formed 2D lattices is given by Wood's notation.[68] For this the basis vectors b_i of the surface

reconstruction are given as integer multiples of the basis vectors of the bulk crystal a_i. These integers are supplemented by addition of prefixes (primitive – p, centered – c) and suffixes (rotation – R), denominating the rotation of the surface structure with respect to the bulk structure. As an example, a p(2×2) surface reconstruction exhibits a surface structure twice as large in x- and y-direction compared to the bulk crystal without rotation. A (√4×√4)R45° notation describes a rotation of 45° with respect to the bulk crystal. The same surface reconstruction is also expressed by c(4×4), naming a larger cell that exhibits the same feature in the center of the surface unit cell as at the edges. This notation is used to stick to the geometry of the underlying crystal to avoid rotations.[65]

Since the surface is the contact of the crystal to the surrounding ambient, the formed surface reconstruction and therefore the minimized energy largely depends on these ambient conditions as well as the temperature, which defines the equilibrium state of the surface. The ambient can change the surface reconstruction by adsorption of new atomic species from the vapor phase onto the surface, which is illustrated in Figure 5 c). With reference to MOVPE a large variety of surface reconstructions of GaAs can be present during the growth of a semiconductor device.[69] The available surface reconstructions are exemplarily shown in a surface diagram obtained for GaAs in Figure 7.

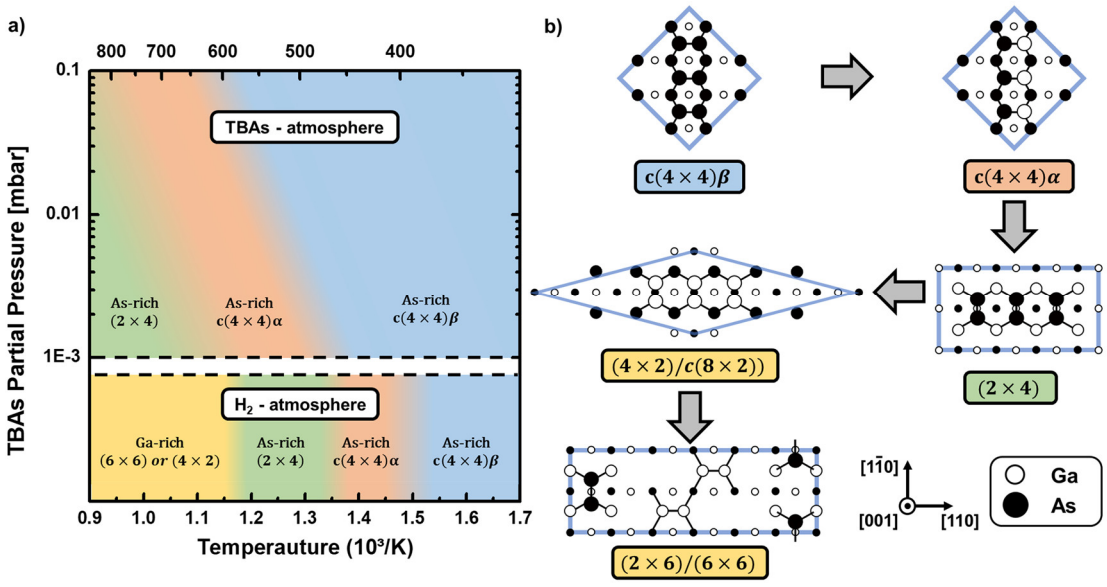

Figure 7: a) Surface phase diagram of GaAs (001) under MOVPE conditions. The formed surface reconstructions change depending on the As partial pressure and the temperature. The phase diagram is acquired for the used AIXTRON AIX 200 system from experimental data obtained by H. Döscher and myself. b) Illustration of the most common GaAs surface reconstructions. The transition from the As-rich to the Ga-rich surfaces is indicated by the grey arrows.

Due to the higher vapor pressure of As compared to Ga, the As will desorb faster from the surface. This incongruent evaporation of As leads to lack of As at higher temperatures. Consequently, the surface becomes less As-rich with increasing temperature. This is seen in a change from the very As-rich c(4×4) surface reconstructions via the less As-rich (2×4) surfaces to the Ga-rich (4×2)/c(8×2) and (2×6)/(6×6) surface reconstructions. The incongruent evaporation of As from the growth surface further leads to the need to grow GaAs in an As-rich (group-V-rich) environment to ensure a sufficient As supply. Therefore, also a dependence of the formed surface reconstruction on the As partial pressure is seen. With increasing As supply the surface reconstruction at a given temperature becomes more As-rich. This can be used to stabilize the more As-rich surfaces, which are unavailable at the same temperature in a different atmosphere, e.g., under H_2 or N_2. The

mentioned and generally observed “standard” reconstructions of GaAs have been extensively studied in the past under various MOVPE as well as molecular beam epitaxy (MBE) conditions.[70,71] Besides the differences of the deposition techniques, the obtained surface reconstructions are shown to be identically, allowing a direct comparison between the two methods.

In conclusion the surface structure of a semiconductor is important for the growth and the properties of a device structure. From an epitaxial point of view, the surface structure can influence the type of the growth mode that is occurring on the surface, as it is, e.g., determining the diffusivity on the surface.[72,73] This can be seen in a stepwise growth or as island growth. Further, the surface reconstruction can have a significant impact on the *heterogeneous* decomposition of the precursors occurring on the sample surface.[69] The surface reconstruction can also significantly affect the doping, which can be necessary to enhance the conductivity of the desired device. It was, e.g., seen that Si incorporates into Ga(As,Bi) as n-type on surface reconstructions exhibiting stable As dimers and as p-type on surface reconstructions with a lack of As dimers.[74] Furthermore, the importance of well-defined surface structures becomes more and more relevant, when a larger stack of different layers is needed to realize the desired heterostructure. At each interface in such a device structure, any defect in the surface structure, e.g., a misplaced or missing atom, can lead to the formation of a larger crystal defect evolving through the structures grown on top. This can result in broken or poor devices. On the other hand, the surface becomes more important as the device structures are forced to become smaller in the upscaling and miniaturization competition of the semiconductor industry. This is, e.g., seen in the aim for large-scale production of 5 nm transistors.[75] The surface of a solid can further act as an own device. As described above, the rearrangement of the atoms in the surface reconstruction can create new electronic states existing on the surface. These states, e.g., are used in topological insulators that are discussed as possible materials for quantum computation.[76]

All these points make a study of the surface structure a precious topic. For a more extensive description of the surface properties and structure the reader is referred to different books from the literature.[31,65]

2.2 Synthesis and Decomposition of the Precursors

In this subsection the fundamental requirements of precursors used in MOVPE and an introduction to basic reaction kinetics is given. Afterwards, the general synthesis procedure and the most relevant decomposition reactions of the used metal organic precursors are described. All shown reactions represent findings from formerly published studies.

2.2.1 Requirements for Precursors

The requirements for the used metal organic precursors appear to be very stringent:[69,77–80]

- The storage of the precursors has to be secured by means of a long-term stability of the metal organic source molecules.
- Ideally, there should be no inherent limitation of the purity of the precursor. This includes on the one hand potential parasitic reactions such as polymerization of the precursor. On the other hand, no unwanted impurities resulting from the synthesis of the precursors should occur.
- Showing minimal toxic characteristics and easy handling.

- Ideally being a liquid source at room temperature, which results in comfortable and safe handling.
- A high vapor pressure at temperatures between 0 °C and 20 °C is desired. Ideally, the vapor pressure is in a range around 5 × 10³ Pa (50 mbar) to achieve a sufficient flux rate.
- The precursors need to exhibit a pyrolysis temperature below the desired growth temperature of the material system, which in general lies between 400 °C and 1000 °C. Especially the decomposition temperature has to be suitable for the combination of the used precursors.
- The precursors should form stable decomposition products in the abstraction reactions of the alkyl groups to reduce the connected carbon incorporation.

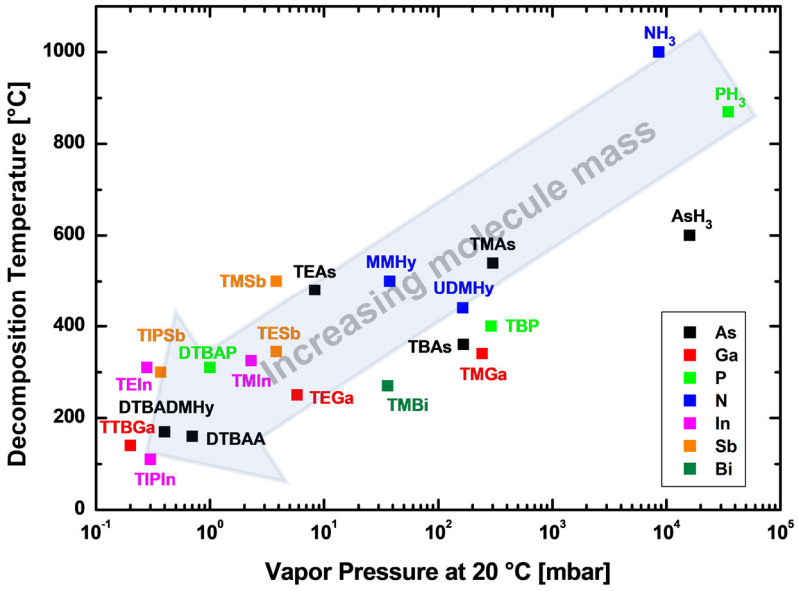

Figure 8: General tendency of the decomposition temperature of some commonly used precursors and the precursors investigated in this work with respect to the molecule mass and vapor pressure. The data of the decomposition temperatures and vapor pressures are partly taken from ref.[69,77,82]

In Figure 8 the decomposition temperature and vapor pressure of some commonly used precursors are compared to the precursors used in this study. The decomposition temperature as well as the vapor pressure of metal organic precursors are generally decreasing with increasing atomic number of the metal, metalloid or nonmetal atom, which is connected to the alkyl groups of the precursor. The term metalloid describes chemical elements such as As or Sb, which are by definition neither a metal nor a nonmetal. The mentioned behavior for the decomposition temperature and vapor pressure is true for metal, metalloid or nonmetal atoms in the same column of the periodic table. The reduced decomposition temperature coincides with an increasing difference in the energy levels of the atomic orbitals, which are involved in the bond formation. A larger energy difference between the orbitals generally leads to a reduced metal carbon bond strength in the molecule. This bond strength is further reduced by an increasing number or size of the connected alkyl group. This is on the one hand caused by steric reasons, which enhances the *homolytic* fission of the bond and a higher stability of formed radicals due to better delocalization of the free electron, known as hyperconjugation.[81] On the other hand, with increasing alkyl size and quantity, the number of H atoms in a β-position increases, which leads to the possibility of *β-H elimination* reactions that occur at low temperatures. This is, e.g., seen in the lower decomposition temperature of *tert*-butyl-arsane (TBAs - 134 u) compared to tri-ethyl-arsane (TEAs - 162 u).[77] The reduction of the vapor pressure is

related to a generally stronger intermolecular interaction between larger molecules, which here implies longer C-chains and an increased number of H atoms. However, e.g., the Van der Waals interaction is weakened for molecules with more branched alkyl groups, leading, e.g., to a lower vapor pressure for tri-ethyl-indium (TEIn - 202 u) compared to tri-isopropyl-indium (TIPIn - 244 u).[69]

2.2.2 Synthesis

As mentioned in Chapter 2.2.1 very stringent restrictions are given for the metal organic precursors. Especially the demand of high purity metal organic precursors implies the need of very selective chemical reactions for the synthesis of the precursors. This avoids the formation of waste products in the synthesis and generally allows a high production yield, which becomes more important for large-scale production. Furthermore, the products need to be viable for post synthesis purification and the educts used for the fabrication 'logically' have to be available in high purity and high amounts. Finally, an appropriate reaction concerning easy handling and safety is chosen.[69,73,80]

Different synthesis mechanisms, such as metalation, metal-halogen exchange, carbene insertion etc. have been studied for the fabrication of metal organic precursors. Here the focus will be laid on the synthesis via **Grignard reactions**, since all of the used alkyl substituted metal organic group-III and -V precursors can generally be synthesized with this procedure. However, for high purity synthesis of the group-III precursors, different approaches are advantageous, which will be discussed at the end of this chapter. The formation of the used Grignard reagent in these reactions was first described in 1900 by V. Grignard.[83] A Grignard reagent is formed by reaction of an alkyl or aryl halide with metallic Mg in the presence of a coordinating solvent. As coordinating solvent some kind of ether such as di-ethyl-ether ($(C_2H_5)_2O$) is chosen since the Grignard reagent is volatile against protic solvents such as water (H_2O) and the coordinating effect of the ether prevents the precipitation of MgX_2 in the reaction. In this mechanism the bond between the halogen atom X (e.g., Br, Cl, I) and the alkyl or aryl substituent R (e.g., CH_3, C_2H_5, C_4H_9) is broken by an electron transfer from the metallic Mg atom to the halogen atom X, followed by the bond dissociation. Afterwards the Grignard reagent R-Mg-X is formed by creation of new bonds. This reaction is schematically shown in Reaction 1.[83,84]

Reaction 1: Formation of the Grignard reagent. Here X can be substituted by a halogen atom and R represents the desired alkyl or aryl group.

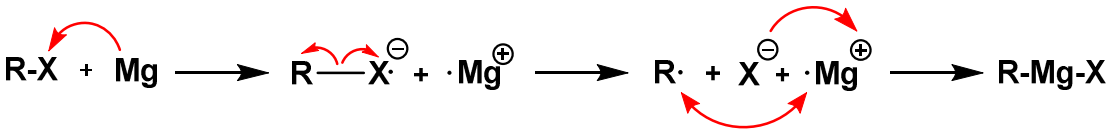

For the precursor synthesis the formed Grignard reagent R-Mg-X is selected according to the desired alkyl group that should be combined to the group-III or -V element in the next reaction step. The synthesis procedure will be shown exemplarily for the synthesis of group-V precursors containing As or P and one or two *tert*-butyl groups (C_4H_9). For this, *tert*-butyl-magnesium-chloride (C_4H_9MgCl) can be chosen as the Grignard reagent. The C_4H_9MgCl reacts in a nucleophile substitution with the As or P containing educts. These educts generally contain the group-V atom bonded to one or more halogen atoms. For the shown example, this is given as arsenic ($AsCl_3$) or phosphorous-tri-chloride (PCl_3). The corresponding Grignard reaction is shown in Reaction 2.

Reaction 2: Grignard reaction for the formation of a new C-X bond. Here M can be substituted by the desired group-III or -V atom such as Ga, P or As.

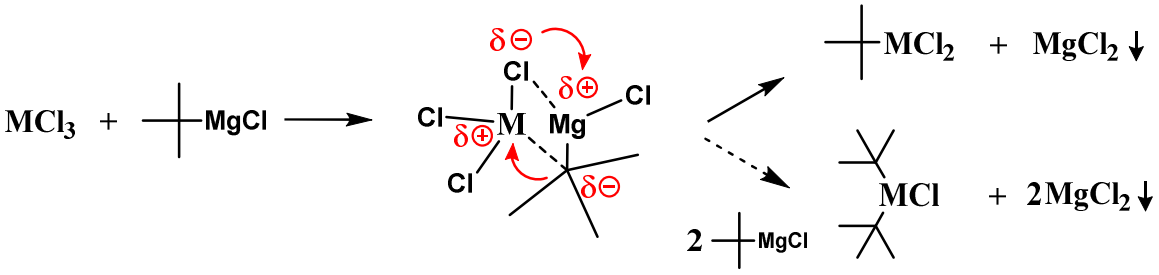

In this step, the alkyl group of the Grignard reagent is exchanged with the halogen atoms bonded to M = As, P. This leads to the formation of a *tert*-butyl-M-di-chloride ($C_4H_9MCl_2$) and magnesium-di-chloride ($MgCl_2$), which precipitates as salt and can simply be filtered off. The reaction is again done in di-ethyl-ether due to the volatile reactants. The di-ethyl-ether is removed under reduced pressure and the products are purified by fractional distillation. The number of added alkyl groups is selectively controlled by the stoichiometry of the used educts.[85]

In the second step, the remaining halogen atoms can be exchanged with the desired atoms or functional groups. This is done by choice of a fitting reactant. Possible reactants are, e.g., lithium-aluminum-hydride ($LiAlH_4$) for substitution of Cl with H atoms or ammonia (NH_3) for substitution of Cl^- with NH_2^-. This substitution reaction is exemplarily shown in Reaction 3 for the synthesis of *tert*-butyl-arsane (TBAs),[85] *tert*-butyl-phosphane (TBP),[86] di-*tert*-butyl-amino-arsane (DTBAA)[87,88] and di-*tert*-butyl-amino-phosphane (DTBAP),[89,90] the most extensively studied group-V precursors in the framework of this thesis.

Reaction 3: Exemplary substitution reactions for the last step in the synthesis of tert-butyl-arsane (TBAs), tert-butyl-phosphane (TBP), di-tert-butyl-amino-arsane (DTBAA) and di-tert-butyl-amino-phosphane (DTBAP).

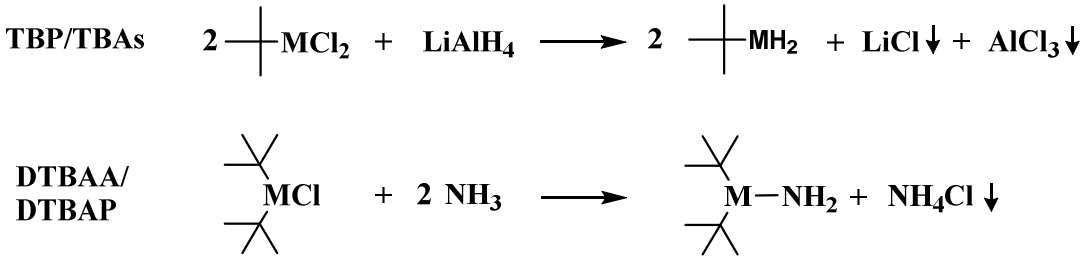

The substitution reactions are again done in di-ethyl-ether ($(C_2H_5)_2O$) as a solvent and at reduced temperatures around 0 °C. The formed side products, such as lithium-chloride (LiCl), aluminum-chloride ($AlCl_3$) and ammonium-chloride (NH_4Cl), precipitate and are filtered off. The solvent is again removed under reduced pressure and the final products are further purified by fractional distillation.

For the synthesis of the used group-III precursors tri-methyl-gallium (TMGa), tri-ethyl-gallium (TEGa) and tri-*tert*-butyl-gallium (TTBGa), also the Grignard reaction can be used.[91] However, due to the Lewis acid property of the group-III elements, the resulting GaR_3 is dissolved in the coordinating solvent. Therefore, the used di-ethyl-ether cannot be easily removed, which is conflicting with the aim of high purity precursors.[92,93] Different synthesis routes using removable, non-coordinating solvents are discussed in the literature.[93] Similar to the Grignard reagent organolithium reagents (RLi) can be used for synthesis of the Ga precursors.[91,94] Starting from gallium-tri-chloride ($GaCl_3$) the

organolithium reagent is added dropwise, which is, e.g., realized in the case of TTBGa with benzene (C_6H_6) as non-coordinating solvent, which can be removed in a second step. The reaction is shown in Reaction 4.

Reaction 4: Exemplary synthesis route for group-III precursors such as tri-methyl-gallium (TMGa), tri-ethyl-gallium (TEGa) or tri-tert-butyl-gallium (TTBGa).

$$GaCl_3 + n\,RLi \longrightarrow n\,LiCl + R_nGaCl_{3-n}$$

As before the lithium-cloride (LiCl) is removed by filtration and the solvent can be removed at reduced pressure. The final precursor can be further purified by fractional distillation.[91]

A more expanded description of different synthesis routes for the mentioned and other precursors can be found in the literature.[73,93,95,96]

2.2.3 Reaction Kinetics

This subsection will briefly discuss the fundamental theory of chemical reaction kinetics. The reaction kinetics are particularly useful to describe the later discussed growth process by metal organic vapor phase epitaxy (MOVPE). Even though the process can be described by fundamental thermodynamic considerations, the reaction kinetics give information about the underlying reaction steps, the rate of the involved growth steps and the required time to attain equilibrium.[69]

The decomposition reactions occurring during MOVPE can be classified in different categories. A reaction that is occurring in the same phase (gaseous, liquid or solid) is called **homogenous** reactions. Reactions that are proceeding in two or more phases, e.g., catalytic surface reactions are labeled as **heterogeneous** reactions. In addition, the *homogenous* or *heterogeneous* reactions that are involving only one molecule, of the type $AB \rightarrow A + B$, are classified as **unimolecular** and reactions of the form $A + B \rightarrow C + D$ are referred to as **bimolecular** reactions. For *bimolecular* reactions or reactions that involve even a higher number of reactants the reaction rate depends on the collision probability of the involved molecules.[69]

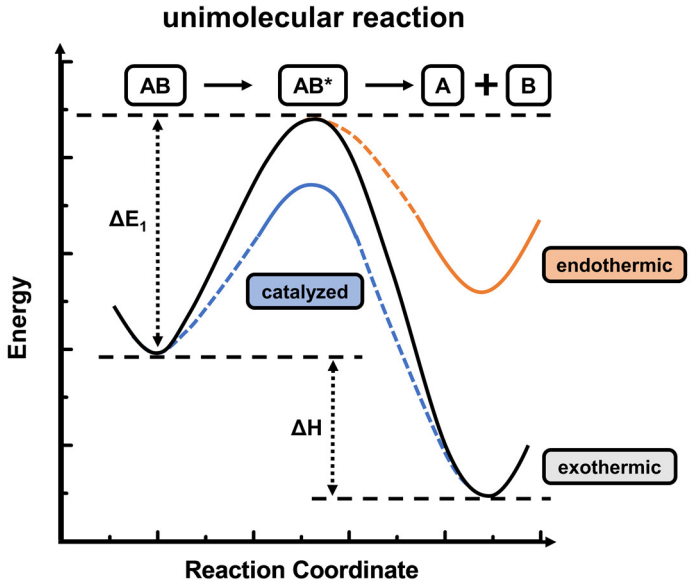

Figure 9: Energy landscape of a unimolecular decomposition reaction of molecule AB in case of an exothermic, exothermic catalyzed and endothermic reaction. The energy is plotted versus the reaction coordinate.

The energy landscape of an *unimolecular* decomposition reaction is shown in Figure 9. A given molecule AB receiving thermal energy larger than the energetic barrier ΔE_1 will be first transferred into an activated state AB^* in a *unimolecular* reaction. The activated state AB^* is decomposed in the next step by formation of the reaction products A and B under the release of the reaction enthalpy ΔH.[69,82,97] The release of energy is common for decomposition reactions, since these are generally exothermic. For a *unimolecular* decomposition reaction of a precursor the reaction rate k_1 for a given temperature T can be expressed by an Arrhenius equation:

$$k_1 = A_1 \exp\left(\frac{-\Delta E_1}{RT}\right) \tag{2.5}$$

Here R is the universal gas constant, which is equivalent to the Boltzmann constant k_B. The pre-exponential factor A_1 describes the attempt frequency of the reaction and is directly connected to the Entropy ΔS and the used temperature of the reaction. A_1 can be expressed by:

$$A_1 = \frac{k_B T}{h} \cdot \exp\left(\frac{\Delta S}{R}\right) \tag{2.6}$$

If the entropy change ΔS of a reaction approaches zero, the attempt frequency A_1 is in the range of 10^{13} Hz for the temperature range between 300 °C and 1000 °C given in MOVPE conditions. Any deviation from this value indicates a change of the entropy S.[69,98]

Analogue to the *unimolecular* reactions, the reaction kinetics of multi molecular reactions can be described in a more sophisticated way.[69]

2.2.4 Reaction Mechanisms

In this subsection a short overview about the most important decomposition mechanisms, as well as a few *bimolecular* reactions of metal organic precursors will be given. The focus will be laid on reaction mechanisms that are relevant for the investigated metal organic precursors in this thesis.

For the *unimolecular* reactions, the most frequently observed decomposition is simple **homolytic fission**.[69,99] Homolysis describes the bond dissociation between the alkyl group R and the group-III or group-V atom M. In this dissociation process, the two electrons involved in the original bond are distributed to both reaction products. This results in formation of two radical species.[100]

Reaction 5: Homolytic fission reaction (homolysis).

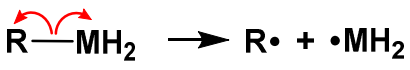

Similar to *homolysis* the bond can be broken including an unequal distribution of the involved electrons. This reaction mechanism is called **heterolytic fission** that leads to one positively charged M^+ and one negatively charged fragment R^-. Here the charge distribution depends on the electronegativity of the involved atomic species.[100]

Reaction 6: Heterolytic fission reaction (heterolysis).

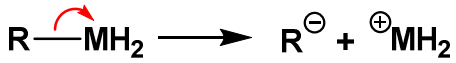

For metal organic precursors with larger alkyl groups such as *tert*-butyl-arsane (TBAs) **intramolecular coupling** can occur. In the *intramolecular coupling* reaction, a rearrangement of the molecule in the transition state of the decomposition reaction appears. In the transition state of the TBAs the one hydrogen atom H interacts with the central carbon atom of the *tert*-butyl group. This leads to the formation of a free electron pair at the M atom and isobutane.[69,82,100,101] In case of TBAs, this decomposition reaction could also be referred to as **reductive elimination**.

Reaction 7: Intramolecular coupling on the example of TBAs (M = As).

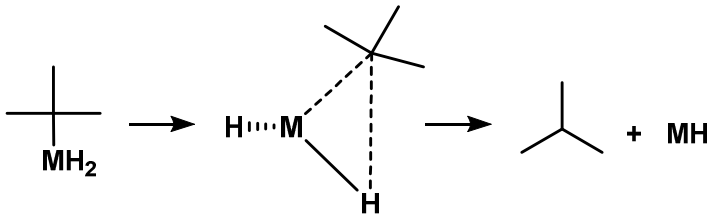

Another decomposition mechanism for alkyl groups $R \geq C_2H_5$ is the possibility of **β-H elimination** reactions. In the *β-H elimination* the filled or unfilled p-orbital interacts with a H atom in β position at the alkyl group.[69,102] This leads to a complex transition state with elongated bonds and a rearrangement of the involved electrons. Group-III precursors exhibit an empty p-orbital at the group-III atom. In the transition state, this leads to an attraction of a H atom in β position to the group-III atom and to an elongation of the involved C-H bond. The alkyl group is then abstracted from the group-III atom under formation of a C=C double bond. For group-V atoms such as P, As, Sb, Bi, first the bond between the C_α and the group-V atom breaks, including charge transfer towards the group-V atom. In the second step the group-V atom forms a bond to the H_{tr} atom and the H_{tr}-C_β bond breaks under formation of a C=C double bond.[102]

Reaction 8: β-H elimination reaction for the example of a group-V (a) and a group-III (b) precursor. Red arrows indicate the largest bond elongation and blue arrows represent charge transfer.

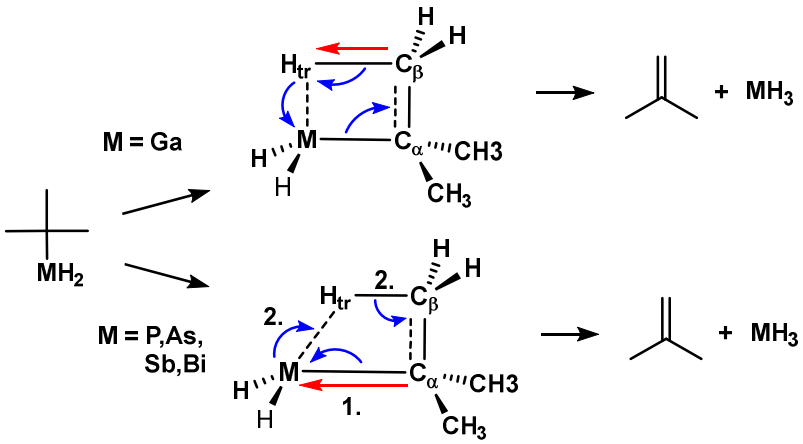

Further, a more specific case of *homolytic* fission, the abstraction of atomic or molecular hydrogen from precursors such as TBAs is predicted. In this **abstraction reaction** one or two hydrogen atoms dissociate from the precursor prior to the removal of an alkyl group.[103,104]

Reaction 9: Hydrogen abstraction as special case of bond homolysis

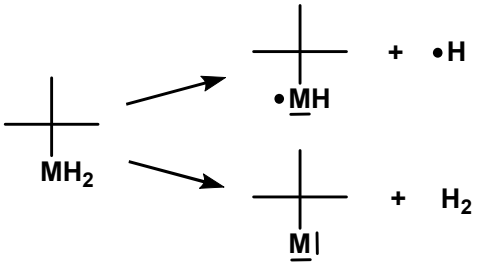

In the case of *bimolecular* reactions, the attack of radicals is discussed in the literature. These **radical reactions** can either occur due to available hydrogen radicals H• resulting from the precursor decomposition, by desorption from the surface or by formation in reactions of H_2 with other alkyl radicals. Since the rate of *bimolecular* reactions depends on the collision probability, these reactions are more likely at higher pressures and consequently higher input concentrations.[69] Furthermore, the radical reactions depend on the C-H bond strength, which varies for different precursors.[105]

Reaction 10: Radical reactions on the example of precursors with three methyl groups.

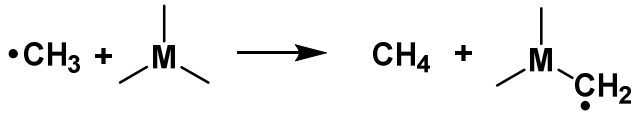

In addition, the possibility of **hydrogenolysis** might be given, since H_2 is used as a carrier gas in MOVPE. Hydrogenolysis describes the dissociation of a C-C or C-M bond involving the breaking of the H_2 molecule. In the given example this leads to formation of RH and HMR_{x-1}.[69]

Reaction 11: Hydrogenolysis on the example of precursors with three methyl groups.

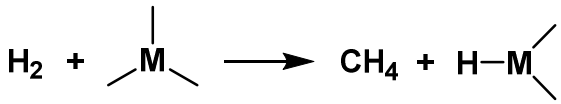

At last a direct interaction between two different precursors can occur in the MOVPE process. On the one hand, **alkyl exchange** reactions are discussed in this respect. In this reaction mechanism the alkyl group R_1 of precursor A exchanges with the alkyl group R_2 of precursor B. This was for example observed in the decomposition study of tri-ethyl-gallium (TEGa) and tri-methyl-indium (TMIn).[106]

Reaction 12: Alkyl exchange reaction on the example of methyl and ethyl groups.

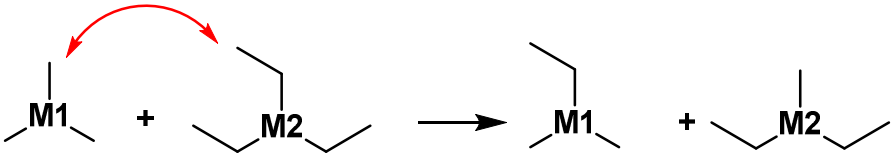

On the other hand, the possibility of **adduct formation** is given. Adduct formation describes the direct addition of two or more molecules including all atoms of the involved molecules. In case of group-III atoms, which exhibit an empty p-orbital and in case of group-V atoms, which exhibit a free electron pair (filled p-orbital) *adduct formation* is not unlikely. The direct observation of adducts in MOVPE studies has been difficult due to the used analysis techniques. However, there are some studies showing indirect proofs of

adduct formation. This is, e.g., seen in studies of the *bimolecular* decomposition of 1,1-di-methyl-hydrazine (UDMHy) with tri-methyl- or tri-ethyl-gallium.[107,108]

Reaction 13: Adduct formation between a group-V precursor with the metal or metalloid atom M1 and a group-III precursor with the metal or metalloid atom M2.

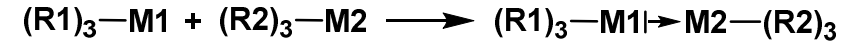

The above-described reactions mechanisms sum up the most frequently observed and predicted reaction pathways for the decomposition of metalorganic compounds under MOVPE conditions. However, many further reaction mechanisms can be included in the real growth process. Especially, more complex surface reactions (*heterogeneous*) are expected to occur, which are the topic of ongoing research and cannot entirely be covered here.

For a more detailed description of the work done in the decomposition analysis of metal organic precursors, the reader is referred to the literature.[69]

Chapter 3

Experimental Methods

In this section an overview of the used experimental methods will be given. The focus will be laid on the fundamental parts of the respective techniques that are of particular interest with respect to the evaluation of the achieved experimental data. For further insight in the different techniques, a reading recommendation will be given at the end of each subchapter.

3.1 Metal Organic Vapor Phase Epitaxy (MOVPE)

The development of metal organic vapor phase epitaxy (MOVPE) as a production technique for semiconductor devices on an industrial scale started in the late 1960s. At that time Manasevit and Simpson were searching for a method to deposit optoelectronic semiconductors such as GaAs on various available substrates that were not latticed matched such as spinel or sapphire.[73] Since then the method has developed over the past 50 years by introduction of commercially available reactor systems in the late 1980s and commercial supply of GaAs and Si substrates into a multibillion dollar market. Especially, the success of high efficient and robust white light emitting diodes (LEDs) based on (Ga,In)N revolutionized the lighting market. The fundamental research on the underlying blue LED consequently received the noble prize in 2014.[109–111] Many other semiconductor devices have been developed over the years such as mass production of vertical cavity surface emitting lasers, whose production process control can be directly done on the substrate compared to edge emitting lasers; multijunction solar cells, which are shown to reach conversion efficiencies over 44 % and high electron mobility transistors operating at several hundreds of GHz, which are, e.g., based on GaAs as host material.[112–114]

Despite the larger variety and success of the MOVPE technique there are still many remaining questions to understand the underlying physics of this deposition technique. The growth process is generally driven by thermodynamics, the kinetic constraints and the hydrodynamics, the latter is very specifically dependent on the reactor geometry. Due to this complexity of the MOVPE technique, a more phenomenological understanding has been established over the years.[31,69,78] The schematic reaction steps for the deposition of single crystalline materials by MOVPE is exemplarily shown for the growth of GaAs in Figure 10 a).

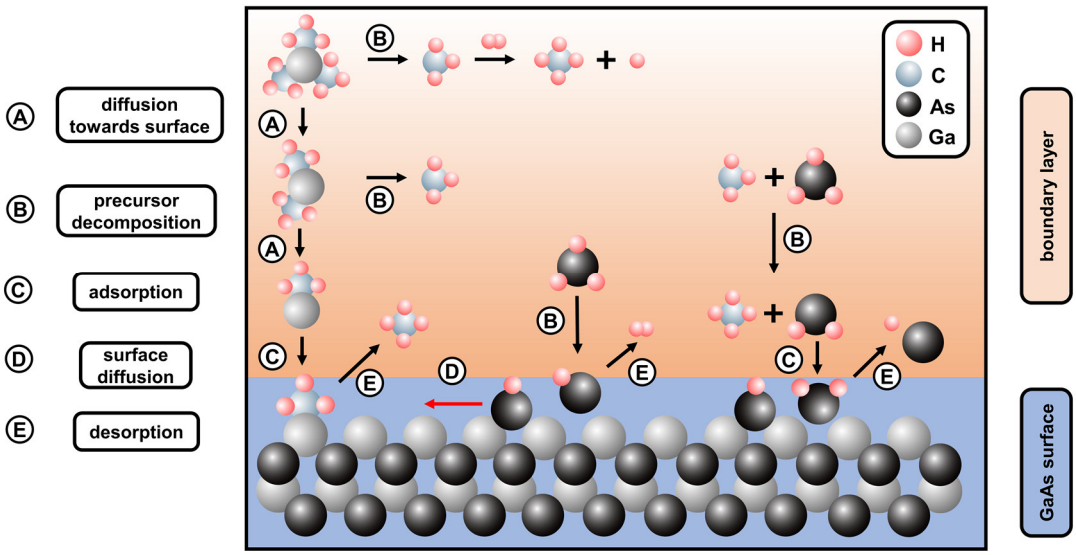

Figure 10: a) Schematic representation of the fundamental reaction steps in the deposition of GaAs by MOVPE. As an example, the main gas phase and surface reactions for the growth of GaAs with TMGa and AsH_3 are shown. The orange shaded area is referred to as boundary layer.

In the growth process the metal organic precursors (MOs) are supplied in a laminar gas flow above the heated substrate. The MOs will diffuse towards the substrate due the drop of the chemical potential between the gas phase and the solid, e.g., caused by a concentration gradient, and reach the "stagnant" boundary layer, which is defined as the region with a reduced gas velocity due to the interaction of the molecules with the substrate surface. Within the boundary layer the precursors can decompose, if enough thermal energy is transferred by collisions with the carrier gas and are further transported to the surface by diffusion. The decomposed or partly decomposed precursors will then adsorb on an available surface site and diffuse to a preferred surface step or kink. These surface sites are energetically beneficial due to the higher number of next neighbor atoms, which are available for bond formation. The remaining alkyl groups of the MOs ideally desorb in the next reaction step from the surface leading to the incorporation of the desired atomic species from the respective precursors. Even for the extensively studied growth of GaAs with tri-methyl-gallium (TMGa) and arsine (AsH_3), many reactions are discussed for this process. Some of the fundamental reactions are schematically shown in Figure 10.

All these different reactions result in a strong dependence of the growth rate on the substrate temperature during the deposition process as seen in Figure 11. The growth rate is limited by the slowest reaction step in the deposition process. At high temperature the growth rate is exponentially decreasing due to the increase in thermal energy, which allows the desorption rate of the elements due to their vapor pressure to be higher than the deposition rate (**desorption limited region**). In the **transport limited region**, the growth rate is determined by the diffusion of the precursors through the boundary layer towards the substrate surface. The growth rate slightly increases due to a higher diffusion rate with increasing temperature. At low temperatures the growth rate is determined by the decomposition rate of the used precursors (**kinetically limited**). The slope of the respective growth rate can be correlated to the activation energy of the rate limiting step in the precursor decomposition process.[73]

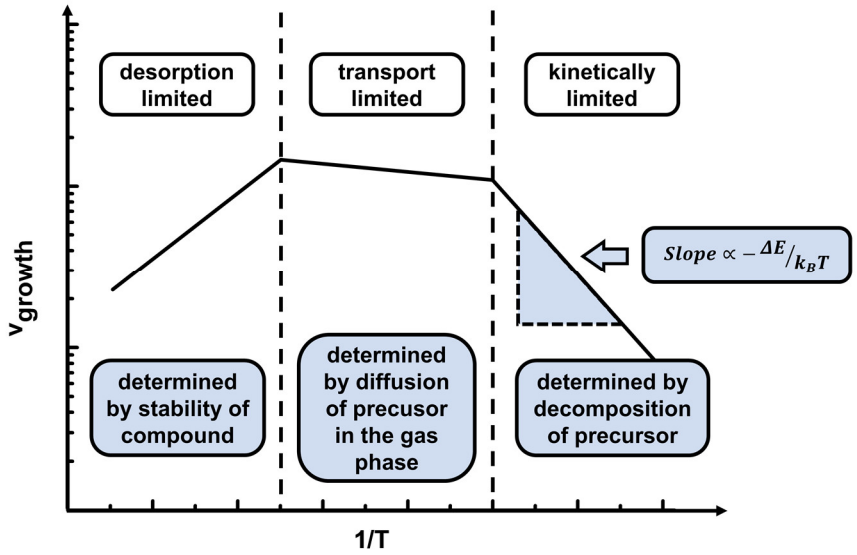

Figure 11: Schematic representation dependence of the growth rate on the temperature in MOVPE. The growth rate shows three different regimes. The kinetically limited region at low temperatures, the transport limited region in the intermediate temperature range and the desorption limited region at high temperatures.

In this work, a commercially available AIXTRON AIX 200 system is used as a research reactor. The setup of the machine is sketched in Figure 12.

As carrier gas in this system highly purified H_2 is used, which is switched to N_2 for maintenance of the system. The carrier gas flows through the MOs, which are stored in stainless steel containers called bubblers. The bubblers are located in water baths that are kept at a constant temperature, ideally below room temperature to prevent any pre-reactions and condensation of the MOs in any part of the pipe system. Furthermore, the bubblers prevent contamination of the MOs and protect the operator, since these precursors are in general toxic as well as pyrophoric, as mentioned in Chapter 2.2.1. To allow a precise control of the amount of MOs that is necessary for the deposition of the investigated materials, the pressure (P_C) of the bubbler, the flux (Q_S) into the bubbler and the vapor pressure (P_V) of the MOs are adjusted. Hereby the vapor pressure is controlled by the temperature of the bubbler. With respect to the used reactor pressure (P_R) and the total gas flux (Q_{tot}) through the reactor the partial pressure (P_P) of the MOs results as:

$$P_P = \frac{Q_S}{Q_{tot}} \cdot \frac{P_V}{P_C - P_V} P_R \qquad (3.1)$$

The MOs are then transported by separated pipes for the group-III and the group-V precursors into the reactor chamber, which is of importance to prevent any pre-reactions that might occur in the gas phase. The used system has a horizontal reactor design as sketched in Figure 12. The reactor consists of quartz crystal (SiO_2), which is suitable to withstand the used deposition temperatures that are typically in the range between 400 °C to 1000 °C depending on the material system. Additionally, an exchangeable SiO_2 liner is put into the reactor, which is meant to lead to a laminar flow profile and to allow cleaning of the system between the experiments. The thermal energy is supplied by infrared heating lamps below the graphite susceptor. The phase transition of an Al/Si eutectic at 577 °C is used for the calibration of the exact surface temperature. For the epitaxial process the substrate is placed in the middle of the susceptor on top of a rotating plate. The rotation is

used to realize better homogeneity across the whole substrate. The last part of the MOVPE system consists of an exhaust gas unit with a scrubber module. The scrubber is needed to bind the toxic reaction products before the cleaned gas is released into the air.

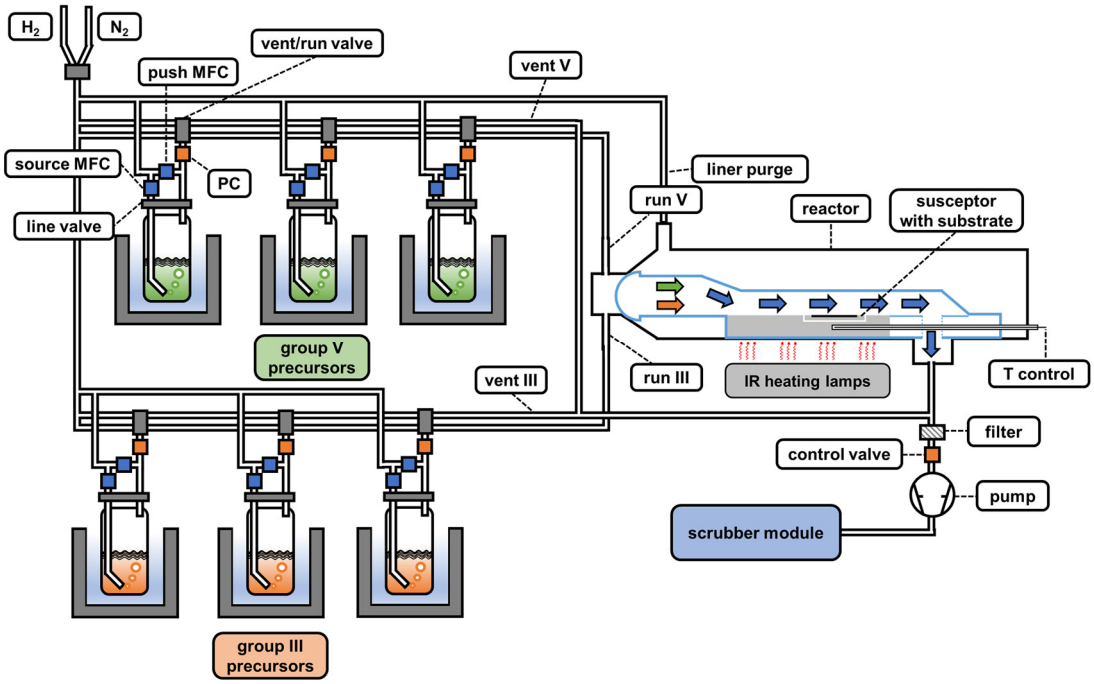

Figure 12: Sketch of the used AIXTRON AIX 200 MOVPE system. The MOVPE system is partitioned in the gas mixing cabinet, including the storage of the metal organic precursors in bubblers and the pipe system, the reactor chamber, in which the deposition process is realized and the exhaust system for filtering of the toxic waste products.

Since the reactor geometry and settings can have a strong impact on the gas phase and surface reactions that might occur upon the decomposition of the MOs, the reactor parameters were fixed for the experiments at P_R = 50 mbar and Q_S = 6800 sccm. The total surface area of the liner is estimated with 720 cm² including the susceptor surface of 100 cm². Since the epitaxial process does not selectively occur on the sample surface and the susceptor, but also deposition occurs on the walls of the liner this area is of interest when discussing surface dominated decomposition reactions.

For a more detailed view on the fundamentals and further applications of MOVPE the reader is referred to established textbooks.[31,69,78,115]

3.2 Reflection Anisotropy Spectroscopy (RAS)

Reflection anisotropy spectroscopy (RAS), also referred to as reflectance difference spectroscopy (RDS), is a surface sensitive and non-destructive optical probe, which can be used under various environmental conditions. In principle RAS measures the difference of reflectance (Δr) under normal incidence between two orthogonal polarizations of light.[70,116,117] With respect to the (001) surface of a cubic semiconductor with the surface plane (x, y) the equation writes as:

$$\frac{\Delta r}{r} = \frac{2(r_x - r_y)}{r_x + r_y} \tag{3.2}$$

where r is given by the complex Fresnel reflection amplitudes.[116,118] Since the interaction of light with matter is completely described by the dielectric tensor ϵ of the material, the RAS signal can be connected to the surface dielectric function (ϵ_s) by the use of a simple 3-layer model with abrupt transitions, which is shown in Figure 13 a).

In this model, the optical response of a surface layer with thickness d is described by ϵ_s, which is stacked in-between a semi-infinite bulk (ϵ_B) and vacuum layer (ϵ_V). The difference between the in-plane components ($\Delta\epsilon_s = (\epsilon_s^x - \epsilon_s^y)$) gives rise to the RAS signal, given that d is small compared to the wavelength of light λ. With the 3-layer model, Equation 3.2 can be rewritten with the imaginary unit i as:[118]

$$\frac{\Delta r}{r} = \frac{4\pi i d}{\lambda} \cdot \frac{\Delta\epsilon_s}{\epsilon_B - 1} \tag{3.3}$$

Both equations show that the RAS signal is closely related to the symmetry of the investigated surface and bulk structure. Therefore, an isotropic bulk structure is required to ensure a surface sensitive probe. Most III-V semiconductors crystallize in a cubic crystal structure, which fulfils this condition in $[001]$ direction and therefore makes a surface analyzation possible. Since the RAS signal is connected to the dielectric functions ϵ_s and ϵ_B, it is specified by optical transitions related to the atomic structure of the surface layers.[116] Furthermore, since the beam size of RAS spectrometers usually is of millimeter dimension, the technique averages over a large area with respect to the size of the surface unit cell. Therefore, the microscopic surface anisotropy of a surface reconstruction needs to expand over a macroscopic area to generate a significant contribution to the RAS signal. So far, Equation 3.3 fully describes the RAS signal in terms of material properties, however, it does not give any insight into the underlying physical process. Different approaches are used to enhance the understanding of RAS and establish a better basis for the interpretation of RAS spectra, which is still a challenge up to now. If on the one hand the anisotropic thin film has electronic states that participates in optical transitions only for a specific polarization, $\Delta\epsilon_s$ can be modelled surprisingly well by a single harmonic oscillator at this energy, which is, e.g., used for the Cu (110) surface.[120–122] These real surface state related features typically result in a modulation of the RAS signal for photon energies up to 2.6 eV. On the other hand, for surfaces that only show relaxation in the upper layers such as the GaAs (110), GaP (110) or Cu (110), surface bulk-bulk transitions have a large contribution to the optical anisotropy. Using an energy derivative model, these transitions were attributed to an anisotropic perturbation of the bulk states by the

surface.[123] This model has been successfully applied for the interpretation of RAS features of Cu (110) surfaces within the energy range from 3 to 5.5 eV.[124]

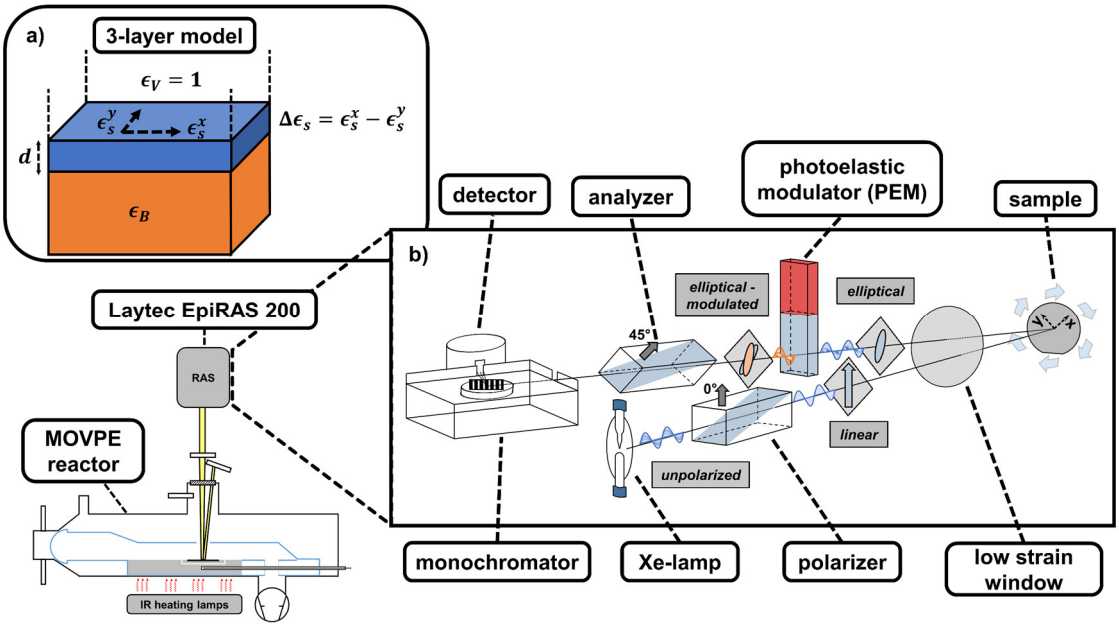

Figure 13: Schematic setup of the used Laytec EpiRAS 200 equipment. The illustration shows a sketch of the 3-layer model (a), which is used for correlation of the RAS signal to the surface dielectric function (ϵ_s), the connection of the RAS to the MOVPE reactor and the most important optical components in the RAS setup (b). The illustration of the RAS setup is adapted from ref.[119]

In the current state of the art, RAS spectra are simulated based on density functional theory (DFT), which is used to create the electronic structure of the inserted atomic surface structure.[125] In the first approaches, DFT was used together with the 'local density approximation' (LDA) to describe the exchange correlation potential. However, LDA only treats the ground state of the system and therefore does not result in the best agreement with experimental RAS spectra. This approach is expanded by adding the propagation of electrons in order to treat electronic excitations within the system. This results in Hedin's equations whose first order solution is called the 'GW' approximation (G: Green's function, W: Coulomb interaction). At first sight the 'GW' approximation did not lead to a significantly better agreement to the RAS data. However, using a second iteration of Hedin's equation (Bethe-Salpeter equation) further effects such as local field and excitonic effects are added and lead under the right circumstances to a quantitative agreement of the calculated RAS spectra with the experiment.[116] Since it is necessary to use the exact atomic surface structure to generate this quantitative agreement, the surface structure can in theory be identified even more precisely by RAS than by other surface sensitive methods such as low energy electron diffraction (LEED), reflection high-energy electron diffraction (RHEED) or scanning tunneling microscopy (STM).[116] Furthermore, the responsible transitions for features in the RAS spectra can be evaluated within the calculation. This makes RAS a very powerful tool which should still gain a lot of attention in the next decades.

With the raising market in semiconductor fabrication starting in the 1960s, the need of *in-situ* probes to monitor the growth process emerged. The invention of RAS goes back to the 1980s and was aimed to study III-V semiconductor surface reconstructions during MOVPE growth where the pressure is too high for electron-based techniques such as LEED, RHEED or STM. Similar to the conceptually closely related spectroscopic ellipsometry or other polarimetry techniques, which measure the polarization state of light

upon reflection, a polarization modulation is used to enhance the signal to noise ratio. In the very first setup, this was achieved by rotating the sample with an angular frequency ω.[126] Another approach would be to rotate the polarizer instead of the sample. However, mechanically rotating components are always difficult to maintain and generally slow ($\leq 10^2$ Hz). Therefore, electro-optic modulation is used, which results in frequencies in the MHz region allowing time resolutions in the ms range. This even allows observation of monolayer growth oscillations.[127] The technical implementation is realized by the use of a photo elastic modulator (PEM) in RAS setups, which basically functions like a dynamic wave plate. The PEM only modulates the light component parallel to its modulation axis while the perpendicular polarization remains unaffected. This is achieved by applying an electric field to a piezoelectric crystal coupled to a transparent material such as fused silica (SiO_2). The resulting mechanical stress induces birefringence in the fused silica with a modulation frequency near to the resonance of the crystal to achieve a significant signal modulation. Over the years these and further improvements in the setup led to the development of commercially available RAS equipment for *in-situ* monitoring of semiconductor growth.[128,129]

The most commonly used setup, which is the one used in this thesis, is shown in Figure 13. A Xenon gas discharge lamp is used as a light source, which emits unpolarized light. The light is then linearly polarized in (x, y)-direction by a polarizer prism utilizing the birefringence of the material. The linearly polarized light is then passed through an unstrained window, which is used to enclose the MOVPE reactor. By addition of an additional H_2 purge beneath the window the coating of the window and the reactor chamber is prevented during the growth process. Furthermore, a specific liner with an additional hole right above the growth area is necessary to pass the light onto the sample. Otherwise, the coating of the liner during the process would prevent the light from reaching the sample surface. The incident, linearly polarized light then is reflected at the surface. Since the investigated material commonly has a higher refractive index than air, the phase of the linear polarized light is changed by π. This leads to linear polarized light after reflection from an isotropic surface.[130] If an anisotropy is present on the surface, the phase of the light changes directional leading to elliptical polarized light after reflection. This polarization state is then modulated by the PEM. The modulation leads to a change of the elliptical polarization with respect to the modulation frequency f = 50 kHz of the PEM. By a second polarizer prism (analyzer) rotated by 45° the polarization modulation is converted into an intensity modulation. After passing a monochromator, which selects the wavelength of the xenon lamp, the intensity modulation is detected by a photodiode. From this intensity modulation, the contribution of the two directions r_x and r_y to the total reflection signal r can be extracted, which forms the RAS signal (Equation 3.2). With this setup, the RAS signal can either be detected as spectrum in dependence on the complete spectral range of the xenon lamp from 1.5 to 5.2 eV or monitored time-dependent at a single wavelength/energy as a transient. The shape of the RAS spectrum represents the underlying surface reconstruction like a fingerprint and therefore can be used to identify known surface reconstructions of the investigated semiconductor surfaces. Under MOVPE conditions the sample is additionally rotated with a frequency of 0.1 to 5 Hz. The rotation additionally modulates the measured signal and needs to be fitted in order to obtain the RAS signal. Since for each rotation only one data point is obtained, this leads to a limitation of the time resolution to around 1 s.

Conclusively, the RAS measurement enables an *in-situ* feedback of the growth surface, which can be used to determine the exact temperature of the substrate by measuring the reflectance of the substrate, to measure the growth rate using Fabry-Pérot or monolayer

oscillations, to identify the surface reconstruction and even to control the growth of complex device structures. The latter is, e.g., shown for *in-situ* controlled growth of vertical cavity surface emitting lasers (VCSEL) structures based on (Ga,In)P as active region.[131] For a more in-depth theoretical description of RAS the reader is referred to ref.[116]

3.3 Mass Spectrometry

This section gives a brief introduction into the development and fundamentals of mass spectrometry, followed by a description of the mass spectrometer used in this thesis.

3.3.1 General Considerations

Today mass spectrometry is used as analytical technique in various areas of expertise such as chemistry, biochemistry, pharmacy, medicine, physics and many more related fields. On the one hand mass spectrometry is used in very practical ways, e.g., as quality assurance of pharmaceutical products or groceries. On the other hand, it is used for structural analysis of unknown substances, identification of isotopic abundance or is even employed in space missions. [132–137]

In mass spectrometry the analyte, in most cases any kind of molecule or element, is analyzed with respect to its mass over charge ratio (m/z). E. Goldstein and W. Wien did the fundamental experiments that discovered this possibility in 1898. They showed the detection of positively charged ion radiation, called canal rays. These rays emitted by different cathode materials were later characterized by J. J. Thomson with respect to their mass, velocity and orbit radius of the underlying molecules.[138–141] This led to the design of the first modern mass spectrometer in 1918 by A. J. Dempster.[142] Based on these fundamental studies several mass spectrometer concepts have been developed until today. The most commonly used concepts are based on mass separation by time of flight, magnetic sector fields, linear quadrupoles, quadrupole ion traps or orbitraps.[133,143] In all these concepts, the analyzed molecules have to be transferred into the gas phase in the first step. The gas molecules are then analyzed as charged ions with respect to their mass over charge ratio. The creation of the ions can be realized by different ionization techniques such as the classical electron impact ionization, thermal ionization, chemical ionization, electron spray ionization, field ionization or laser desorption ionization.[144–149]

The fundamentals of the ionization process will be explained for the electron impact ionization, since this technique is used in the presented studies. In the electron impact ionization process an electron beam with an energy of 70 eV is created. This is done by emitting electrons from the cathode material by thermionic emission, which are then accelerated by an applied voltage, defining the kinetic energy of the electrons. In the ionization process, the projectile electron interacts with the analyte to eject an electron from the molecule leading to a positively charged ion. The chosen energy of 70 eV is on the one hand needed to transfer enough energy in the collision with the analyte to overcome the ionization energy. The ionization energy generally varies between 7 eV and 15 eV, excluding the noble gases.[132,150] On the other hand, the ionization cross-section reaches a plateau around 70 eV, which results in reproducibly detected intensities, despite some divergence in the electron energy. This enables the quantitative comparison among mass spectra detected in different experimental setups. The ionization cross-section is shown for different molecules in Figure 14 a). Since only a portion of the kinetic energy of the projectile electron is transferred in the ionization process, the probability to ionize the target molecule increases with increasing energy of the electrons. The cross-section

describes the effective area, which the electron has to path through to get into interaction with the target molecule. The cross-section reduces, and therefore the ionization probability, when the electron energy is increased to energies above 80 eV. For higher energies, the velocity of the electron becomes so large, that the reduced interaction time reduces the effective cross-section of the target molecule. Therefore, the cross-section is generally larger for larger molecules with similar chemical characteristics and is enhanced for molecules exhibiting free electron pairs or π bonds instead of σ bonds.[132,151,152]

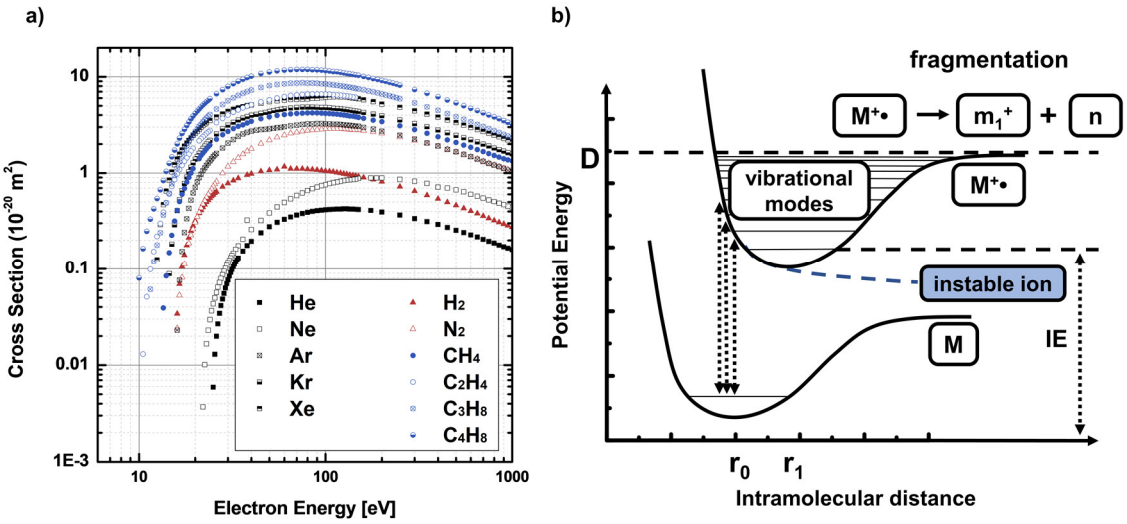

Figure 14: a) General dependence of the ionization cross-section of different elements and organic molecules on the electron energy used for the electron impact ionization. b) Illustration of the electron ionization process of a diatomic molecule M. In the electron impact ionization, the molecule M is receiving some energy E, which will lift the molecule into the excited state M⁺•. If the transferred energy is larger than the bond dissociation energy D, the molecule will dissociate into a charged (m_1^+) and a neutral particle (n). The ionization energy of the molecule M is included as IE. The cross-section data is taken from ref.[153–157] *and the illustration is adapted from ref.*[132,133,158,159].

Since the energy of the electrons in most cases is also higher than the bond strengths in the analyzed molecules, these are also fragmented in the ionization process. The ionization process is illustrated for a diatomic molecule M by treating the internal energy E of the molecule in dependence on its intermolecular distance r in Figure 14 b). Before the interaction of the electron with the analyzed molecule, the molecule is in its energetic ground state. Due to the high velocity of the electrons, the interaction time of the electrons with the molecule is in the range of 10^{-16} s, which is two magnitudes lower than the frequency of vibrations of molecular bonds. Therefore, the excitation of the molecule into an excited and charged state M⁺• is shown by vertical transitions in this picture, involving no change of the intramolecular distance. Depending on the transferred energy, different vibrational modes of the excited molecule M⁺• are stimulated. If the transferred energy is larger than the dissociation energy D, the molecule will receive enough energy to dissociate into a charged m_1^+ and a neutral fragment n. This behavior leads to the detection of molecule specific ionization patterns in the collected mass spectra, which have to be identified based on large data bases established for mass spectrometry.[132,133]

The next segment in a mass spectrometer is designed for the separation of the ions according to their mass over charge ratio to distinguish them in the detection process. The separation is generally done by the help of electric and magnetic fields or by separation according to the travel time of the accelerated ions. Especially for magnetic sector field setups the separation concept leads to the detection of one mass signal at a time, which results in long measurement times for a single mass spectrum.[132,160]

For the detection of the separated ions different detector systems can be applied. Mainly the separated ions can be detected by a kind of current measurement after amplification of a signal generated by the ions. This can be realized, e.g., by a Faraday-Cup, secondary electron multipliers, channel electron multipliers, microchannel plates or for simultaneous detection of a small mass range by conversion of the signal into photon generation, followed by detection by a photodiode array or a CCD camera.[132,133]

Since the mass separation and detection is generally different, these parts will be discussed in more detail in Section 3.3.2. For a more general description of the presented mass spectrometry concepts and the underlying fundamental concepts, the reader is referred to established textbooks in this field.[132,133]

3.3.2 Fourier Transformation based Quadrupole Ion Trap

The mass analysis of the process gas in the MOVPE system has been realized by the connection of a quadrupole ion trap mass spectrometer from Carl Zeiss SMT GmbH to the system. The implementation of the setup and the first proof of concept were carried out by L. Nattermann.[104,161] The functional principle of the ion trap is based on the Paul trap, which uses dynamical electric fields to store the charged ions.[162] The ion trap is connected inline to the MOVPE system, which is shown in Figure 15.

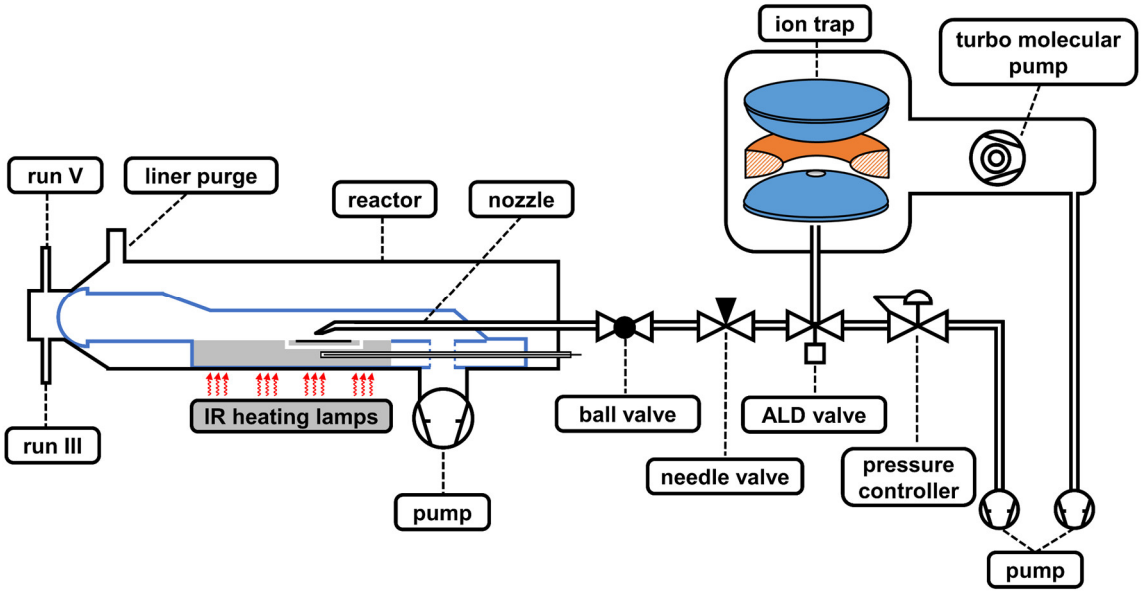

Figure 15: Illustration of the connection of the ion trap mass spectrometer to the MOVPE reactor system.

The setup is designed to realize real time investigations of the dissociation products, which are produced in the different reaction steps during the thermal decomposition of the precursors above and on the growth area, as described in Chapter 3.1. This is realized by the collection of the process gas above the middle of the susceptor with a quartz crystal nozzle. The analytes are then carried through a bypass system towards the mass spectrometer. To ensure a steady gas flow and similar pressure conditions compared to the settings in the reactor system, the bypass flow is adjusted by a needle valve and the pressure is controlled by a pressure controller and a vacuum pump. The bypass can further be completely disconnected by a ball valve next to the reactor chamber and is connected to the exhaust gas system of the MOVPE system. A small gas portion is pulsed into the ion trap with an atomic layer deposition (ALD) valve from the bypass. The ALD valve allows

short gas pulses in the millisecond range, which is sufficient to overcome the pressure difference between the rough vacuum in the reactor chamber and the bypass of 10 mbar to 50 mbar to the ultra-high vacuum of p < 10^{-8} mbar used in the ion trap.

The ion trap consists of a ring, a bottom, and a top electrode as shown in Figure 16 a). For the storage of the ions in the ion trap, an alternating current applied to the ring electrode creates an oscillating electric field of the shape $\mathrm{V} \cdot \cos(\Omega \mathrm{t})$. This electric field generates an electric potential ϕ_0 at the time t in the form:[132,163]

$$\phi_0 = \mathrm{U} + \mathrm{V}\cos(\Omega t) \tag{3.4}$$

The potential is given by the strength of the electric field V, which oscillates with a frequency Ω in the radio frequency range and a constant potential field U in z direction, if any voltage is applied between the top and bottom electrodes.

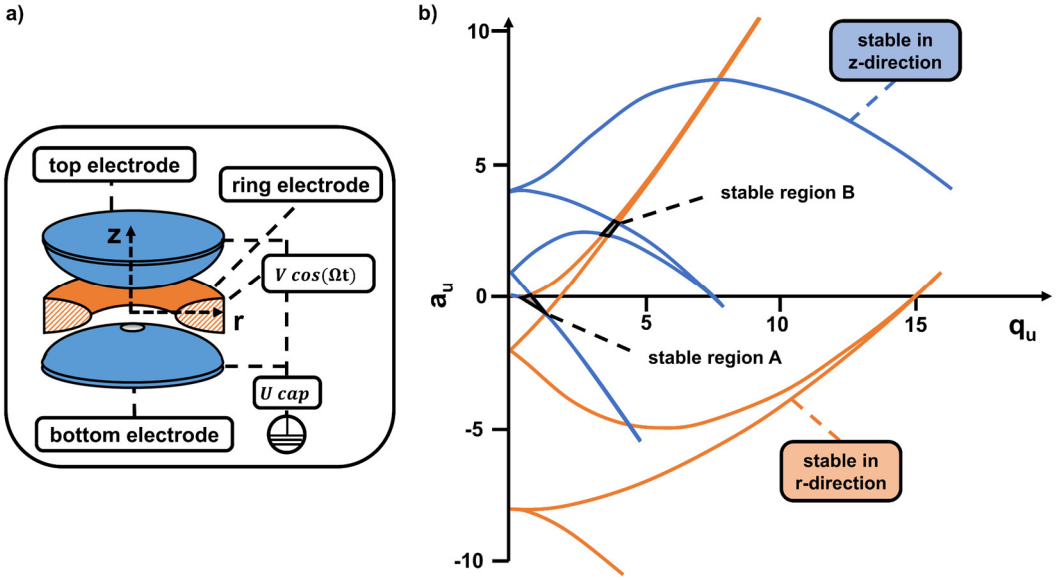

Figure 16: a) Sketch of an ion trap chamber, including the ring, top and bottom electrodes and the applied voltages. b) Mathieu stability diagram using the generalized coordinates (a_u, q_u). The stable regions in z - and r - direction are matched. The shaded areas A and B represent areas of stable ion motions in the ion trap. The illustration is adapted from ref.[163].

The equation of motions of the captured ions in the given potential are mathematically described by Mathieu equations. With the potential given in Equation 3.4 the equations of motions in z- and r-direction of an ion with mass m_i in cylindrical coordinates can be written as:[132,163]

$$\begin{aligned} \frac{\mathrm{d}^2\mathrm{z}}{\mathrm{dt}^2} - \frac{4\mathrm{e}}{\mathrm{m_i}(\mathrm{r_0^2} + 2\mathrm{z_0^2})}(\mathrm{U} - \mathrm{V}\cos(\Omega\mathrm{t}))\mathrm{z} = 0 \\ \frac{\mathrm{d}^2\mathrm{r}}{\mathrm{dt}^2} + \frac{2\mathrm{e}}{\mathrm{m_i}(\mathrm{r_0^2} + 2\mathrm{z_0^2})}(\mathrm{U} - \mathrm{V}\cos(\Omega\mathrm{t}))\mathrm{z} = 0 \end{aligned} \tag{3.5}$$

The space of the ion motion in z- and r-direction is limited by the geometry of ion trap, which is given by the maximum distance r_0 and z_0 from the center of the trap to the edges

of the electrodes. The solution of these equations can be parameterized by a_u (parameter of the time invariant field) and q_u (parameter of the time variant field) as:[132,163]

$$a_z = -2a_r = -\frac{16eU}{m_i(r_0^2 + 2z_0^2)\Omega^2}$$
$$q_z = -2q_r = \frac{8eV}{m_i(r_0^2 + 2z_0^2)\Omega^2} \qquad (3.6)$$

This form of the solution can be used to create a stability diagram of the captured ions within the ion trap, given in Figure 16 b). The figure shows that the largest area for a stable ion path in z- and r-direction is given in region A close to the center of the ion trap. This region is used for the storage of the captured ions. From the illustration and Equation 3.6 it is apparent, that a lower limit for the mass over charge ratio (m/z) of the captured ions is given by the geometry and the applied voltages at the trap. The motion of ions on stable ion trajectories is often visualized by the mechanical analogue of a particle sitting on a rotating saddle plane.[164]

The real-time investigations of the stored ions are made possible by a Fourier transformation-based detection concept of the generated ions in the ion trap, which is illustrated in Figure 17.

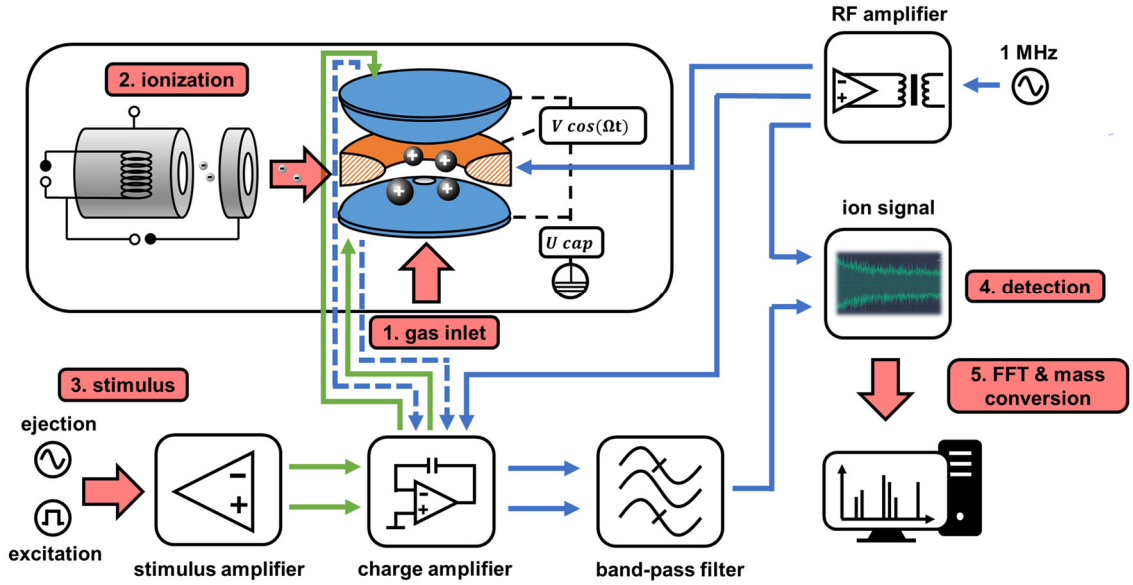

Figure 17: Schematic of the functional principle of the ion trap setup developed by Carl Zeiss SMT GmbH. The illustration shows the most important technical components and the different steps in the measurement procedure to obtain a mass spectrum as an output.

In the overall measurement procedure, a small gas volume of the analyte is pulsed by the ALD valve into the ion trap (1.). This gas inlet time is adjusted in the range between 10 ms to 200 ms. The adjustment of the gas inlet time regulates the total amount of the analyte gas that is added into the ion trap. After this, the time until the ionization is initiated can be adjusted. During this time, the number of molecules in the ion trap is reduced by the pumping of the turbo molecular pump attached to the ion trap. In the next step, the analyte is ionized by electron impact ionization (2.) as described in Section 3.3.1. Consequently, the molecules are now charged, which allows to capture the created ions by an oscillating electric field, which is applied to the ring electrode of the ion trap. After the ionization a further waiting time can be chosen before the captured ions are stimulated by a voltage

applied between the bottom and the top electrode of the ion trap (3.). The stimulus initiates a displacement of the ions from their trajectories in the ion trap. In this process, ions with the same m/z ratio are excited in phase and form 'ion clouds'. During the following relaxation of the 'ion clouds' onto their original path, an induced mirror image current between the bottom and the top electrode is measured with respect to the time (4.). This current transient includes the resulting oscillation frequencies of the ion motions in the trap. By using fast Fourier transformation of the current signal, an intensity versus frequency spectrum is generated. The frequencies are afterwards converted into the mass of the ions by a reciprocal dependence $\mathrm{m_i} \propto 1/f$ (5.).

In addition to the standard measurement procedure, the stored ions can be selectively removed from the ion trap by resonant excitation of the ions. This is done by using stored waveform inverse Fourier transformation (SWIFT).[132,165,166] SWIFT allows the ejection of captured ions, which may overlap small ion signals. By this the SWIFT technique is used to realize high sensitivity measurements with this setup.

To conclude the description of the novel ion trap setup, a short summary of the mass spectrometer specifications is given to benchmark this setup. The fast Fourier transformation-based concept results in a measurement time below 2 s for a single mass spectrum. This is making the setup suitable for real time analysis of the MOVPE process. Furthermore, this ion trap exhibits a good mass resolution of $m/\Delta m \gg 2000$, which allows the detection of heavy molecules up to 2000 u and shows very high sensitivity in the parts per trillion range. The high sensitivity was demonstrated by the detection of a part per trillion volume of diborane (B_2H_6) in H_2.[165,167] The development of this high sensitivity mass spectrometer originates from the development of a process control tools for detection of photo resist residuals in the high purity atmospheres during photolithography. Additionally, the setup is designed to be protected against corrosion, which is essential for the analysis of reactive species in the MOVPE process.

3.4 Characterization Techniques

In this section, a brief overview of the main ex-situ analysis techniques of the presented semiconductor heterostructures grown by MOVPE is given. First the setup of the used high-resolution X-ray diffraction system is discussed in Chapter 3.4.1, followed by a description of atomic force microscopy in Chapter 3.4.2.

3.4.1 High-Resolution X-Ray Diffraction (HR-XRD)

High-resolution X-ray diffraction (HR-XRD) is based on the interaction of an impinging X-ray beam with the electron shells of atoms in matter. The X-rays were first discovered and studied by W. Röntgen in 1895.[168] The description and application by utilization of X-rays for structural analysis of crystal structures, as given for semiconductor materials, was later implemented with the introduction of the theories by M. Laue in 1912 and W. Bragg in 1913.[169–171] Out of these discoveries, the X-ray diffraction has developed to a standardized analyzation technique of semiconductors and other solid or liquid materials.

In HR-XRD a X-ray impinging under an angle ω is diffracted at the atomic planes of the analyzed crystal. As discovered for the diffraction of visible light, the wavelength of the X-rays has to be in the same order of magnitude as the atomic distances (lattice constant) of the investigated crystal structures. These distances are typically given in units of angstrom (Å). A wavelength of 1 Å corresponds to a photon energy of $E = hc/\lambda = 12.40$ keV.[31] Highly monochromatic X-rays in this energy range are, e.g., created from the

$Cu_{K\alpha}$- line of the used X-ray gun connected to a four-times Germanium monochromator (4×Ge[220]). The scattering geometry of a HR-XRD setup is illustrated in Figure 18 a). The periodic arrangement of the atoms in the crystal lattice leads to an elastic scattering of the impinging X-ray waves with a well-defined phase relation. The diffracted waves will interfere constructively, if the phase difference between the diffracted rays X_1 and X_2 is given by an integer multiple n of the wavelength. The resulting direction of the scattered beam under this condition is given by Bragg's law, which is equivalent to Laue's condition:[31,169,170]

$$\boldsymbol{Bragg \Leftrightarrow Laue}$$

$$2d_{hkl} \sin\theta = n \cdot \lambda \Leftrightarrow \Delta\vec{k} = \vec{k} - \vec{k}_0 = \vec{G} \tag{3.7}$$

$$\boldsymbol{with}: d_{hkl} = \frac{2\pi}{|\vec{G}|} \xrightarrow{\text{cubic}} \frac{2\pi}{\frac{\lambda}{2a}\sqrt{h^2 + k^2 + l^2}} \tag{3.8}$$

In Bragg's equation the lattice plane distance d_{hkl} and the scattering angle θ is related to the wavelength λ of the impinging X-ray. For the Laue condition, the difference of the wave vectors of the impinging $\vec{k}_0$ and the scattered wave $\vec{k}$ have to be a reciprocal lattice vector $\vec{G}$. The lattice plane distance d_{hkl} can be expressed by the absolute value of the reciprocal lattice vector between the investigated set of planes, which are defined by the corresponding Miller indices (hkl).[29,172]

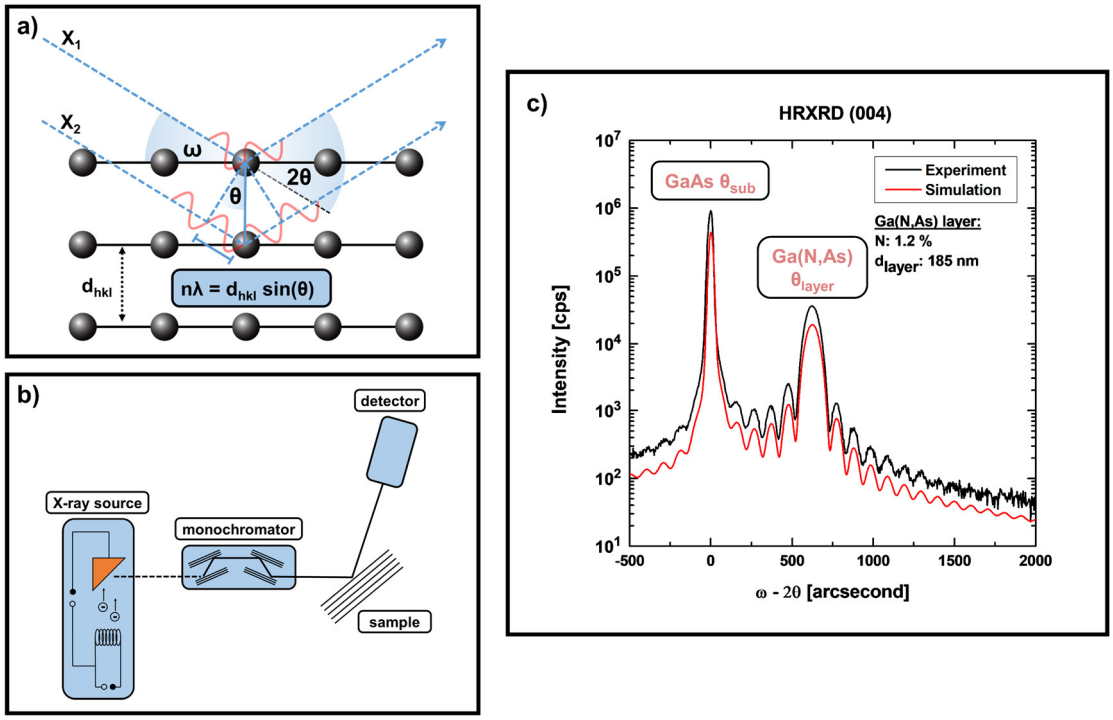

Figure 18: a) Illustration of the diffraction of an X-ray impinging under an angle ω on a crystal plane with a given in-plane lattice constant a and lattice plane distance d_{hkl}. Depending on the phase difference between the diffracted rays X_1 and X_2, constructive or destructive interference is detected under the angle 2θ. b) Simplified schematic of the ray path through the experimental setup of the used Panalytical X'Pert Pro system. c) Exemplary diffraction pattern (black line) of a Ga(N,As) bulk structure grown on GaAs with a dynamical simulation (red line) using the Panalytical X'Pert epitaxy software.

The intensity I of the detected wave is given by the sum of the contributions of all scattered waves originating from all atoms in the unit cell with respect to their phase. This is mathematically expressed by the structure factor F_{hkl}:[29,31]

$$I \sim |F_{hkl}|^2 \; with \; F_{hkl} = \sum_{\alpha} f_\alpha \, e^{-i \, \vec{G} \vec{r}_\alpha} \qquad (3.9)$$

where f_α describes the atomic form factor, which considers the scattering at specific kind of atoms, $\overrightarrow{r_\alpha}$ denotes the atomic position in the unit cell of the given crystal structure and $\vec{\mathrm{G}}$ is a reciprocal lattice vector.

For the structural analysis of the grown semiconductor structures a diffractogram is detected in an ω-2θ scan around the GaAs (0 0 4) reflection. In this scanning mode the impinging angle ω is varied by rotation of the sample and the detector is rotated accordingly by 2ω, which equals 2θ in this geometry. An exemplary diffractogram of a Ga(N,As) bulk structure grown on GaAs is given in Figure 18 c). This example illustrates the thickness and composition determination of a given semiconductor heterostructure. The incorporation of nitrogen into GaAs induces a tensile strain in the GaAs host matrix due to its smaller covalent radius compared to the substituted arsenic.[173] For pseudomorphic growth the grown layer will adopt to the in-plane lattice constant of the substrate, while the strain is seen by a tetragonal distortion of the crystal structure in growth direction.[174] For tensile strain this results in a reduction of the lattice distance in growth direction $\mathrm{a}_\perp$ of the grown layer compared to the substrate $\mathrm{a}_\perp < \mathrm{a}_{\mathrm{sub}}$. The change of the lattice plane distance leads according to Equation 3.7 to a larger scattering angle for constructive interference and is therefore detected at θ_{layer} compared to the substrate peak at θ_{sub}. The opposite case $a_\perp > a_{sub}$ is referred to as compressive strain. For pseudomorphic growth the in-plane strain $\epsilon^{||}$, as introduced in Equation 2.1, is equal to the in-plane lattice mismatch. Knowing the material specific elastic constants C_{11} and C_{12} of the grown material, the lattice mismatch $\Delta a/a_{sub}$ with respect to the substrate lattice constant a_{sub} with respect to the relaxed lattice constant $a_{relaxed}$ can be determined by:[31,175]

$$\frac{\Delta a}{a} = \frac{a_{relaxed} - a_{sub}}{a_{sub}} = \frac{C_{11}}{C_{11} + 2 \cdot C_{12}} \cdot \frac{a_\perp - a_{sub}}{a_{sub}} \qquad (3.10)$$

As result of Equation 3.10, the relaxed lattice constant of the grown layer can be calculated. With this the composition of a ternary layer, consisting of 3 different kinds of atoms $A(B,C)$, can be determined by simple linear correlation to the known lattice constants of the materials AB and AC. This relationship is named Vegard's law:[176]

$$a_{relaxed} = a_{A(B,C)} = x \cdot a_{AB} + (1 - x) \cdot a_{AC} \qquad (3.11)$$

The intensities in the diffractogram are related to the kind of scattering atoms as seen in Equation 3.9 and to the total number of scattering atoms, giving information about the thickness d_{layer} of the respective layers. In the case of structures consisting of multiple layers, e.g., given for multi-quantum well structures, the diffraction signal is further modulated by multiple interference originating from the interfaces in the structures. In this

case, the total strain can be evaluated by the position of the envelope in the diffractogram of the grown super-lattice structure.

For the fabrication of actual semiconductor devices, which are based on even more complex semiconductor heterostructures, a very precise composition and thickness determination is desired. Therefore, a dynamical X-ray simulation, implemented in the Panalytical X'Pert epitaxy software is used to model the experimental data sets.

For further insights into the theory of X-ray scattering the reader is referred to the literature.[177]

3.4.2 Atomic Force Microscopy (AFM)

Atomic force microscopy is based on the attractive and repulsive interaction of a sharp tip with a sample surface. G. Binning and coworkers developed the first experimental setup of an atomic force microscope in 1985.[178] An illustration of an AFM setup is shown in Figure 19, which is operated in trapping mode at a constant tip to sample distance.

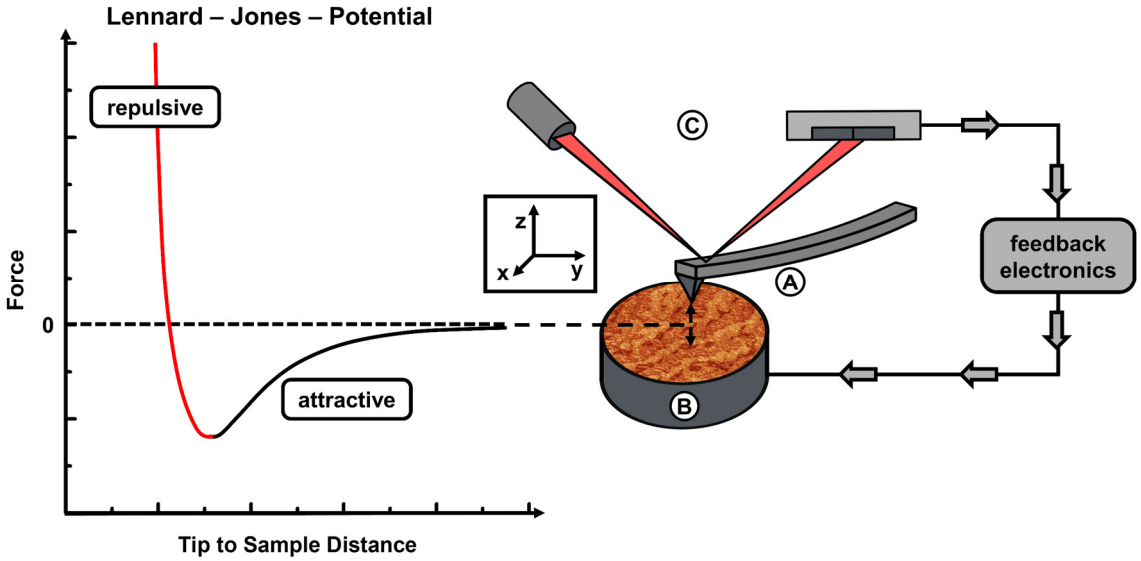

Figure 19: Schematic of the used atomic force microscope including the cantilever (A), the sample and sample stage (B), the laser and photodiode (C) and the feedback electronics. The attractive and repulsive forces between the tip and the sample for different tip-sample distances are given by the Lennard-Jones potential.

In this measurement mode, a sharp tip connected to a spring-like cantilever is excited to oscillate close to its natural frequency. The sample surface is scanned by moving the sample relatively to the position of the tip in the x-y plane by using a piezo crystal in the sample stage. If the tip is approached to the surface by a second piezo crystal, which controls the sample-to-tip distance in z-direction, the tip will start to interact with the atoms on the sample surface. This resulting force in dependence on the tip to sample distance of this interaction is described by the Lennard-Jones potential shown in Figure 19. In tapping mode, the interaction is dominated by attractive forces caused by Van-der-Waals interaction, since the tip is positioned in the downward slope of the attractive potential. If the topology of the sample changes during the scan, e.g., at a step edge, the oscillation frequency of the cantilever will be changed. Laser light reflected at the back of the cantilever and a split photodiode measures this change. The change of the oscillation is compensated by regulation of the tip to sample distance by the feedback system. The resulting movement of the tip with respect to the sample is converted into a height profile

of the sample. Afterwards, the profile is converted into an image of the surface and evaluated with the *Gwyddion* and *NanoScope* (Digital Instruments) software.

AFM measurements are often done in contact mode closer to the surface. In this mode strong repulsive forces, explained by Coulomb repulsion and the Pauli principle, change the deflection of the tip from the sample.[179,180] This change of the deflection is then converted into a height profile. Using AFM, height resolutions less than 1 nm are realized, which allow the observation of mono-atomic steps on the sample surface. The lateral resolution is limited to the radius of the tip, which is generally in the range of 5 to 20 nm. The lateral resolution can be enhanced by adsorption of a single molecule at the tip and reduction of thermal noise by operation at low temperatures. With these adjustments atomic resolution can be achieved.[181] Overall, this makes atomic force microscopy a powerful surface analysis technique, which can easily be applied under ambient conditions, with no severe restrictions to the sample characteristics. Furthermore, AFM allows measurements of the surface morphology in a few minutes, which is used as a direct feedback of the semiconductor structures grown in this thesis.

For a more detailed description of the tip to sample interaction, further measurement modes and setups, the reader is referred to ref.[181]

Chapter 4

Analysis of the Surface Structure

This chapter covers the *in-situ* analysis of the growth surface of 'dilute nitrides' and 'dilute bismides'. The growth surface was analyzed in terms of its anisotropy by reflection anisotropy spectroscopy (RAS - Chapter 3.2). The measured anisotropy is characteristic for the surface reconstruction present on the surface, which is identified by comparison of the experimental data to known RAS spectra. For 'dilute nitrides' the influence of the conventionally used UDMHy and the novel DTBAA precursor on the surface reconstruction of GaAs (001) is studied in the first part, including studies of the growth surface of Ga(N,As) layers. The gained knowledge is further applied to realization of Ga(N,As) interlayers in the GaAs host material. The *in-situ* analysis of 'dilute nitrides' is covered in Chapter 4.1. In the second part, the influence of TMBi on the surface reconstruction of GaAs (001) is discussed. The observed surface reconstructions are further studied in terms of their thermal stability and stability against changes of the ambient conditions. Furthermore, the surface reconstruction is analyzed during growth of Ga(As,Bi). The results are used to improve and confirm the growth model of Ga(As,Bi) on GaAs. The *in-situ* analysis of 'dilute bismides' is covered in Chapter 4.2.

4.1 Ga(N,As) (001)

The nitridation process of the GaAs (001) surface is analyzed in a first step to understand and improve the control of nitrogen incorporation into GaAs. A part of this work was investigated in the framework of my Master's thesis,[182] but will be shortly repeated and completed with further investigations done during my PhD work.

The nitridation process of the GaAs (001) surface is studied for the conventional UDMHy precursor as well as for a novel As and N source DTBAA. For these experiments the GaAs (001) was prepared by a standardized pretreatment including etching and different heating steps followed by an overgrowth of the GaAs substrate by GaAs under ideal growth conditions at 625 °C with a V/III ratio of 10 and a growth rate of about 0.5 nm/s. This surface develops an As-rich c(4×4)β surface reconstruction at a temperature of 550 °C under the supply of the As precursor TBAs with a constant partial pressure of 2×10^{-2} mbar. In case of UDMHy a strong influence on the anisotropy of the GaAs (001) surface is seen (Figure 1, Chapter 7.2.1). Supplying nitrogen in the

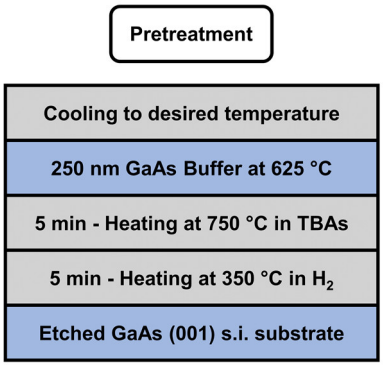

form of UDMHy leads to a conversion of the surface reconstruction to one describable by the Ga-rich (2×6)/(6×6) model.[71,183] The anisotropy signal of the (2×6)/(6×6) was obtained for high ratios of UDMHy/TBAs > 40. Smaller UDMHy/TBAs ratios showed a smooth transition between the c(4×4)β and the (2×6)/(6×6) surface reconstruction that could be expressed by a linear combination of the observed RAS spectra. Since the RAS averages over a large area, the surface reconstruction forms either an intermediate surface structure or different surface domains exhibiting the c(4×4)β or the (2×6)/(6×6) surface reconstructions. On the one hand, the change to the more Ga-rich surface reconstruction is believed to occur due to an enhanced desorption of As from the surface. This enhanced desorption might be ascribable to aminyl radicals (NH_2•), which are formed in the decomposition of the UDMHy precursor (compare Chapter 5.1). On the other hand, N atoms have to stick to the surface as well, leading to a further modulation of the surface reconstruction and consequently leading to incorporation of N into GaAs. This is supported by observation of the nitridation process in the common temperature range for growth of 'dilute nitrides' between 450 °C and 600 °C (Figure 4, Chapter 7.2.1). In this temperature range the c(4×4)β changes to the c(4×4)α surface reconstruction in case of pure GaAs for the chosen TBAs supply (Figure 7, Chapter 2.1.3). The nitride surface again shows a conversion towards the more Ga-rich (2×6)/(6×6) surface reconstruction. However, the observed anisotropy change cannot totally be explained by enhanced As desorption from the surface due to an increase of the temperature. This indicates that N has to build into the surface reconstruction. The observed conversion of the c(4×4)β towards the (2×6)/(6×6) surface reconstruction was shown to occur within a few seconds, by measuring the time of this conversion time-resolved at a fixed photon energy of 2.1 eV.

The same experiment was done for DTBAA and is reported for the use of *tert*-butyl-hydrazine (TBHy) in the literature.[184] The addition of DTBAA does not show a significantly different RAS signal compared to the one of the c(4×4)β surface reconstruction.[182] Even a small increase of the negative anisotropy signal at a photon energy of 2.6 eV is seen. Compared to UDMHy, the DTBAA not only supplies N to the surface, but additionally supplies As. The As originates from the intrinsic As-N bond of the DTBAA precursor, which dissociates in the first step of the precursor decomposition as covered in Chapter 5 and is furthermore shown to more efficiently incorporate As compared to N into GaAs.[55] Therefore, the DTBAA stabilizes the c(4×4)β surface reconstruction. Furthermore, in the literature the nitridation of the GaAs surface with TBHy is discussed and shows the formation of a (3×3) surface reconstruction.[184] This shows that the surface reconstruction is largely dependent on the used nitrogen source.

In the next step the Ga(N,As) (001) surface structure is studied during growth of the material with the precursors UDMHy, TBAs and TEGa (Figure 5, Chapter 7.2.1). For this the RAS spectra were taken during the growth of Ga(N,As) structures for a constant supply of TEGa with 8.2×10^{-3} mbar and different UDMHy/TBAs ratios between 2.5 and 10. For the lowest UDMHy/TBAs ratio of 2.5 the observed RAS signal is almost identical to the RAS signal for the nitrided surface discussed before with a ratio of UDMHy/TBAs = 5. This shows that the additional Ga supply changes the surface towards the more Ga-rich (2×6)/(6×6) surface reconstruction and supports the idea of an enhanced As desorption by supply of UDMHy. The same agreement between the RAS spectra of the nitrided surfaces and the growth surface is seen for higher UDMHy/TBAs ratios. The observed RAS spectra for the more Ga-rich surfaces were again describable by linear combinations of the c(4×4)β, the (2×4) and the (2×6)/(6×6) surface reconstructions. This represents again a conversion to the more Ga-rich surfaces. Compared to the nitridation experiment, the (2×6)/(6×6) surface reconstruction is already reached for a lower UDMHy/TBAs of 9.5 in contrast to the much higher value of 46 needed in the nitridation under TBAs and

UDMHy supply. This, as expected, indicates an enhanced change of the surface reconstruction by the additional Ga supply. The change in the RAS spectra was further shown to correlate to an increasing nitrogen incorporation in the respective layers.

Very similar, the RAS signal during growth of Ga(N,As) with DTBAA and TEGa indicates the same change of the surface reconstruction. This is illustrated in Figure 20 compared to selected data from Chapter 7.2.1.

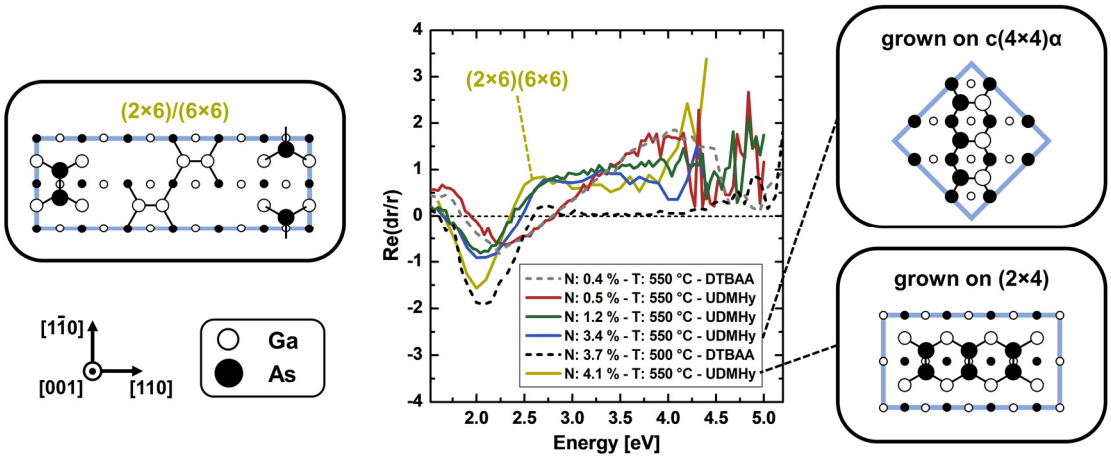

Figure 20: RAS spectra during the growth of Ga(N,As) layers with UDMHy and DTBAA for different nitrogen concentrations. The temperature was reduced from 550 °C to 500 °C to realize a comparable nitrogen content with DTBAA. For clarity, the relevant surface reconstructions models are added.

For low nitrogen concentrations, the RAS spectra during growth of Ga(N,As) with UDMHy and DTBAA are almost identical, showing the same change of the surface reconstruction. At higher nitrogen concentrations of about 4 % the shape of the RAS spectrum is still similar, but the growth surface with DTBAA shows deviations from the signal of the (2×6)/(6×6) surface reconstruction for higher energies. These changes might be caused by the lower temperatures, which were necessary to realize the higher nitrogen concentrations with DTBAA under the given experimental conditions. Nevertheless, here the change towards the more Ga-rich (2×6)/(6×6) surface reconstruction is also seen. Therefore, the more Ga-rich surface reconstruction seems to be necessary for the incorporation of N into GaAs. To underline the point an additional experiment was carried out on a beforehand prepared (2×4) surface reconstruction. The (2×4) surface reconstruction is reached by growth of GaAs at 550 °C with a comparably low gas phase ratio of V/III = 1.2 prior to the Ga(N,As) layer. The Ga(N,As) layer grown on this sample presented a higher nitrogen incorporation of 4.1 % compared to 3.4 % for the growth under the elsewise same growth conditions on the c(4×4)α surface reconstruction. Accordingly the RAS spectrum also changes more towards the (2×6)/(6×6) surface reconstruction for the higher nitrogen content. In conclusion, this indicates that a Ga-rich surface is beneficial to increase the N incorporation efficiency. However, no extensive study on the optical or electrical properties of the Ga(N,As) structure grown on the (2×4) was carried out. Nevertheless, the sample showed comparably good structural properties with respect to the surface structure and composition determined by AFM and HR-XRD, respectively.

Based on these findings the *in-situ* investigations were expanded to realize atomically sharp Ga(N,As) layers with relatively high N contents embedded into GaAs. This project is focused on the modulation of the band offsets for heterostructures based on GaAs. One idea is the implementation of these layers into W-type heterostructures. These W-type

heterostructures are named after the W-shaped conduction band structure in material combinations like Ga(In,As)/Ga(As,Sb)/Ga(In,As) or Ga(N,As)/Ga(As,Sb)/Ga(N,As) on GaAs. These structures utilize the possible type-II transitions between the electron quantum well (QW) of Ga(In,As) or Ga(N,As) and the hole QW of Ga(As,Sb) to achieve low emission wavelengths in the infrared region. Furthermore, the induced symmetry by the third QW leads to a higher overlap of the electron and the hole wavefunctions, which results in a higher recombination probability. Consequently, these W-type heterostructures are discussed as promising candidates for highly efficient telecommunication lasers.[185–187] One current problem in the growth of these structures is the realization of sharp interfaces due to segregation of antimony (Sb) on the growth surface. The introduction of a sharp Ga(N,As) layer may change the interface properties. On the other hand, the radiative recombination leading to the emission of photons in the telecommunication range occurs over the interface in these W-type structures. The introduction of a sharp interlayer of Ga(N,As) will increase or decrease the band offsets in the heterostructure in dependence of the N concentration. This change will have a direct impact on the recombination process via this interface, which is of fundamental interest. Furthermore, these layers might be useful to modulate the wave functions of the W-type structures. This could be beneficial to create a better wave function overlap and consequently enhance the probability of the used type-II transition in these structures. Therefore, different Ga(N,As) interlayers were grown on GaAs and structurally analyzed by AFM and HR-XRD. The structural analysis is more extensively covered in the framework of the Master´s thesis of E. Odofine.[188] Since the growth of the structures as well as the planning of the experiments was in part done by myself a short summary of the main results will be given here.

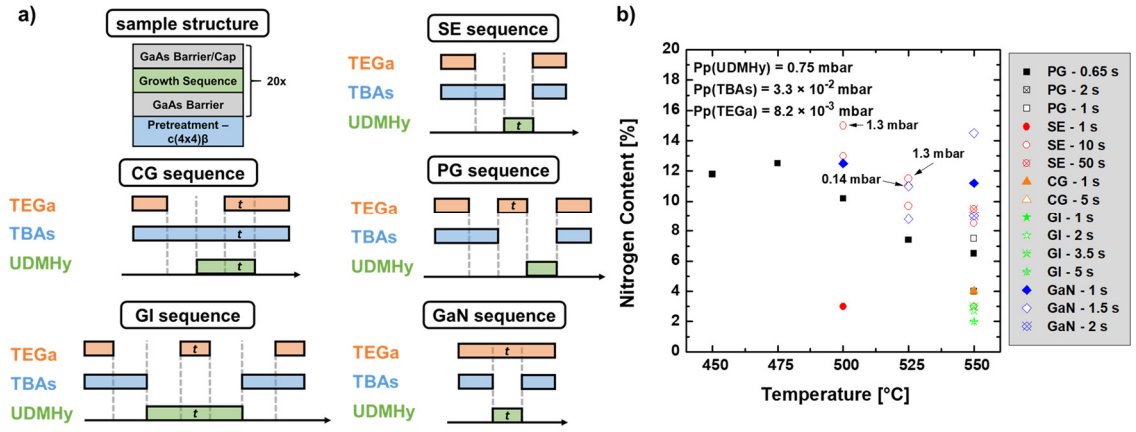

Figure 21: a) Illustration of the gas switching sequences used for the realization of the grown Ga(N,As) interlayers in GaAs. Namely continuous growth (CG), growth interruptions (GI), pulsed growth (PG), surface exchange (SE) and gallium nitride growth (GaN) were tested for the growth sequence. b) Determined nitrogen content in dependence on the growth temperature, supply time and UDMHy partial pressure (marked by arrows). The layer thickness was assumed to be one monolayer (1/2 of a unit cell) for the composition determination, unless the supply time in the respective growth sequence influences the layer thickness, e.g., in the case of CG with 5 s instead of 1 s.

For the realization of the Ga(N,As) interlayers, different gas switching sequences were carried out, which are illustrated together with the determined N content in Figure 21.The used switching sequences were partly adapted from former studies on a successful realization of GaP interlayers with thicknesses below 0.6 nm and P concentrations of 30 % to 40 % on GaAs.[189] To achieve a thin Ga(N,As) interlayer with a high amount of nitrogen a simple reduction of the growth time using continuous growth (CG) of Ga(N,As) with a growth interruption of 10 s under TBAs and for 10 s under TBAs and UDMHy did not show

an increase in the N incorporation. As shown this growth interruption with TBAs and UDMHy changes the surface of GaAs from the c(4×4)β to the (2×6)/(6×6) surface reconstruction, which was expected to be beneficial for the N incorporation. However, N incorporation is identical to the N incorporation of about 4 % in a 5x Ga(N,As)/GaAs multi quantum well structure grown with the same parameters, showing no significant increase in the average N incorporation. Nevertheless, there might be an increased N incorporation at the very interface between the Ga(N,As) layers and the GaAs layers, which is not visible in the HR-XRD diffractograms. In a second approach, growth interruptions (GI) with TBAs and UDMHy before and after a short gas pulse of TEGa and UDMHy were used.

This could ideally lead to a very thin layer of GaN. However, our first composition analysis suggests a nitrogen incorporation of 2 to 3 %. The first presumably higher N incorporation was achieved by suppling only UDMHy to the GaAs surface between 1 s and 50 s and directly switching to the growth of the GaAs barrier (surface exchange, SE). This leads to a very high effective N/As ratio within the reactor, which should result in a high N incorporation.[56] Furthermore, a pulsed growth (PG) of the interlayer with 1 s TBAs, 0.65 s to 2 s TEGa and 2 s UDMHy supply was investigated. The PG sequence also shows relatively high N incorporation. The PG could result in atomically thin layers, since a pulse duration of 0.65 s of TEGa is equivalent to roughly one monolayer of Ga on the surface for the given growth rate. For the last sequence, the TBAs supply was stopped and only TEGa and UDMHy were supplied during the growth of the Ga(N,As) interlayer (GaN sequence). For the GaN sequence, a HR-XRD of a sample grown at 525 °C is shown in Figure 22.

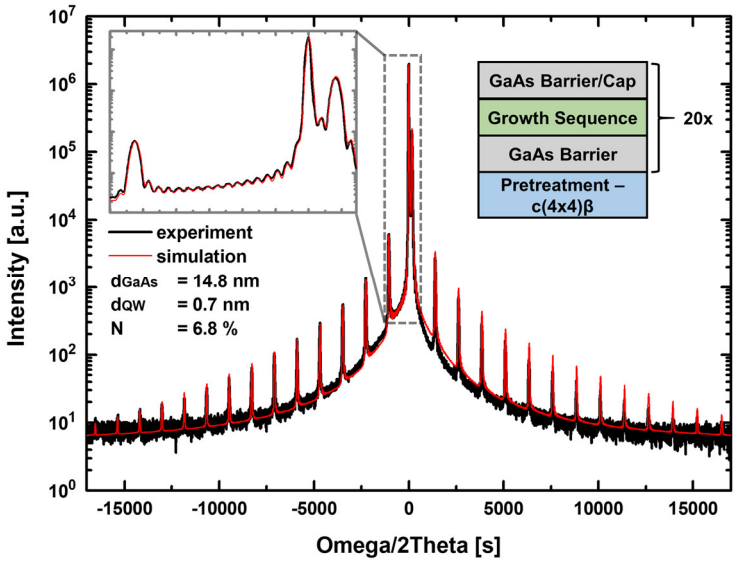

Figure 22: HR-XRD of an exemplary Ga(N,As) interlayer structure grown on GaAs (001) with the GaN sequence. The insets illustrate a magnification next to the substrate peak and the general layer structure.

The diffractogram clearly shows the interference arising from the repetition of the Ga(N,As) interlayers, which is shown in the inset and indicates a good structural quality of the GaAs/Ga(N,As) interfaces. The diffractogram fits well with the simulation with a N content of 6.8 % and a layer thickness of 0.7 nm, however both N content and layer thickness contribute quite similar to the total strain of the structure, which is accessible by HR-XRD (Chapter 3.4.1). By assuming a thickness down to one monolayer (1/2 of a unit cell) the PG, SE and GaN sequences presumably show nitrogen contents of up to 16 %. To gain a precise information of the layer thickness and N composition, the grown structures are

planned to be investigated in detail by transmission electron microscopy (TEM). The very first experiments carried out by A. Beyer have shown a layer thickness of about 1.2 nm for the grown interlayers. Using this thickness, the grown interlayers exhibit a N content of up to 4 %. However, the determination by HR-XRD only averages over the whole layer and a precise determination of the nitrogen content requires additional investigation with TEM. For this, one remaining challenge is to achieve a quantitative agreement for the simulated and the measured TEM images for low detector angles. These angles are of interest, since the Rutherford scattering of the electrons with the small N atoms results in small scattering angles. However, in this angular range further contributions such as plasmon scattering become increasingly important and have to be taken into account to achieve quantitative agreement of the experiment with the simulations, which is the topic of an additional project.[190,191] With this implementation, the exact compositional analysis of the nitrogen content in the grown layers by TEM could be realized in future work.

4.2 Ga(As,Bi) (001)

Motivated by the successful investigation of 'dilute nitrides' also the surface structure of 'dilute bismides' was investigated in the framework of this thesis. Similar to the case of the 'dilute nitrides' the very first experiments were done during the work for my Master`s thesis and were expanded with new findings during my PhD work. As guidance through the chapter, the observed RAS spectra for the investigation of the surface structure of 'dilute bismides' are summarized in Figure 23.

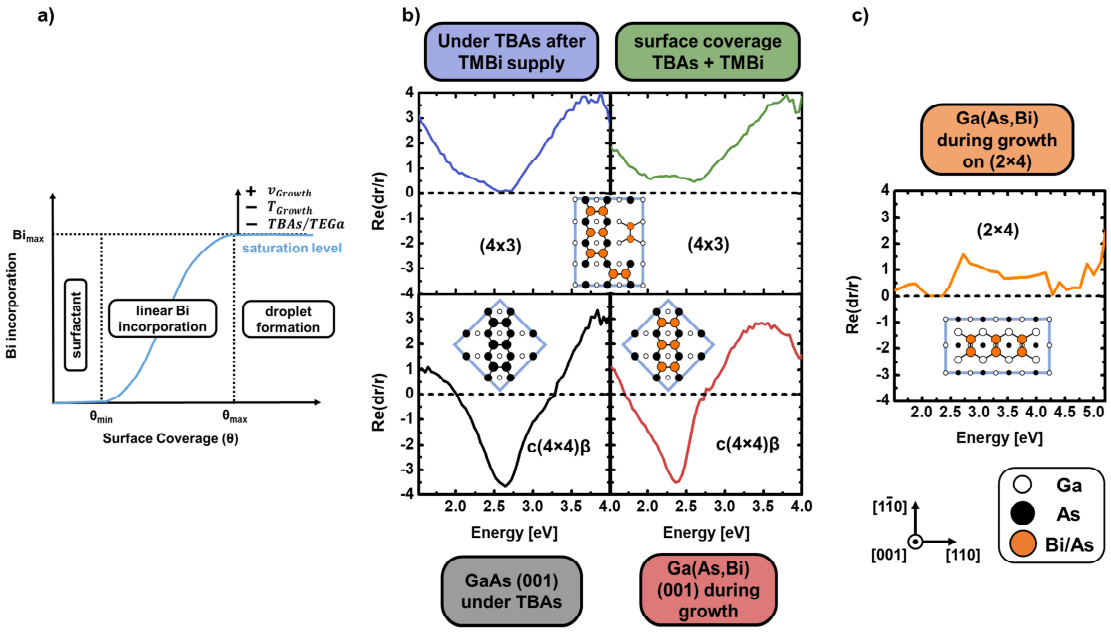

Figure 23: Overview of the RAS experiments carried out for the investigation of 'dilute bismides' on GaAs. a) Schematic illustration of the growth model for Ga(As,Bi) grown on GaAs by MOVPE after ref.[18] b) Selected RAS spectra from different surface configurations investigated for 'dilute bismides' on GaAs. c) RAS spectrum for the Ga(As,Bi) sample grown on an beforehand prepared GaAs (2×4) surface reconstruction.

The growth of Ga(As,Bi) on GaAs by MOVPE was found to be very limited in terms of the available growth window. Early investigations of this material system show that a sufficient Bi incorporation has only been realized in the temperature range between 375 °C and 450 °C. Due to the V-V competition between As and Bi during the growth, the growth window is limited to As/Ga ratios between 1 and 2.5 for a constant Bi supply.[18,60–62] Below

an As/Ga ratio of 1, formation of Ga droplets occurs. Above an As/Ga ratio of 2.5, accumulation of the non-incorporating Bi leads to droplets consisting of Ga and Bi on the growth surface.[20,57–59] These harsh limitations led to the development of a growth model for Ga(As,Bi), which is supported and expanded by the study of the surface reconstruction during the different steps in this work. The growth model suggests that for low Bi supply the Bi only acts as a surfactant on the growth surface with no notable Bi incorporation into GaAs. Exceeding a minimum coverage of Bi (Θ_{min}) on the surface, Bi incorporation sets in. For increasing surface coverage, the Bi incorporation then linearly increases until a saturation sets in above the maximal coverage with Bi (Θ_{max}). Above this point, the surplus Bi forms droplets on the growth surface. The maximum Bi incorporation is determined by this saturation level, which is dependent on the growth rate v_{growth}, the growth temperature T_{growth} and the As/Ga ratio.[18] This behavior led to the implementation of a Bi surface coverage prior to the growth of Ga(As,Bi) with TBAs and TMBi to prevent concentration gradients in the grown structures, which evolve due to a change in the Bi surface coverage throughout the growth of the respective layer. Furthermore, a desorption step has to be implemented to desorb any surplus Bi from the growth surface at higher temperatures, in order to avoid droplets on the growth surface, which are then incorporated into the next layer. This is crucial to make Ga(As,Bi) applicable in heterostructures.

In a first approach the effect of the evolving surface coverage on the GaAs (001) surface is analyzed by RAS *in-situ*. For this, the effect of TMBi on the GaAs (001) surface was studied at 400 °C. The temperature of 400 °C was chosen, since the most data on the growth of Ga(As,Bi) by MOVPE is given for this temperature.[18,60–62] At 400 °C the GaAs (001) surface forms a c(4×4)β surface reconstruction (black spectrum) after the pretreatment given in Chapter 4 followed by cooling to 400 °C under TBAs stabilization. The TBAs stabilization is kept throughout the experiment and the partial pressures are chosen with values similar to the ones used in ref.[18,61] to be comparable to the growth conditions of Ga(As,Bi). Subsequent supply of TMBi onto the TBAs stabilized surface showed a continuous modulation of the RAS signal of the c(4×4)β surface reconstruction towards the signal of the Bi terminated surface (Figure 1, Chapter 7.2.2). Additional Bi supply on the Bi terminated surface (blue spectrum) did not cause any further change of the RAS signal. The same experiment was carried out for a continuous TMBi and TBAs supply, which is used in the growth process to build up the surface coverage (green spectrum). The measured RAS spectrum of the surface coverage follows the RAS spectrum of the Bi terminated surface under TBAs supply for photon energies above 3 eV. In the energy range below 3 eV smaller deviations are seen. Mainly the anisotropy signal decreases from 3 down to 1.6 at a photon energy of 1.5 eV and a new positive feature evolves at 2.3 eV. These changes are attributed to a dynamic exchange of Bi and As on the sample surface, since turning off the TMBi supply caused the RAS signal to change back to the RAS spectrum of the Bi terminated surface. This indicates that the change of the surface reconstruction, which is correlated to the Bi surface coverage, can be reached by a continuous Bi supply as well as by pulsed supply of Bi onto the surface. The investigations further showed that Bi is accumulating on the growth surface, since the measured RAS spectra are stable and a conversion back to the As-rich c(4×4)β surface reconstruction is not possible at these temperatures. Since the RAS signal of the Bi terminated surface is unknown, no exact model of the surface structure can be given. Nevertheless, studies done in MBE show the formation of a (4×3) surface reconstruction via a disordered (1×3) surface reconstruction, when starting from a c(4×4) surface structure.[192] The (4×3) surface is a good guess for the underlying surface reconstruction, which could be a good starting point for theoretical calculations of the observed RAS spectra.

In the subsequent experiments, the buildup time of the surface coverage in dependence on the TBAs and TMBi partial pressure was evaluated by transient measurements at a fixed photon energy of 1.52 eV. In these transient measurements the conversion of the RAS signal of the As-rich c(4×4)β surface reconstruction to the Bi terminated surface is revealed. The results show that the buildup time of the surface coverage is independent of the TBAs supply and reduces linearly for increased TMBi supply (Figure 2, Chapter 7.2.2.). Analyzing the total amount of supplied TMBi to the reactor indicates an accumulation of Bi on the growth surface in addition to the change of the surface reconstruction. Since Bi, as covered above, seems not to change the RAS signal, further Bi is likely added as a homogenous layer on top of the surface reconstruction. Only for very large TMBi supply, the RAS signal is severely increased while the reflection signal drops, indicating the begin of droplet formation.

In the following the desorption of the accumulated Bi from the growth surface is studied. As done in ref.[18] the Bi terminated surface is heated under TBAs to 625 °C to desorb the Bi. Similar to the previous experiments, the desorption time in dependence on the amount of deposited Bi on the growth surface was studied using RAS transient measurements and shows as expected a proportional correlation of the desorption time and the amount of deposited Bi. The complete desorption of the Bi from the surface was proven by detection of the subsequent RAS signal at 400 °C under TBAs supply as well as by observation of AFM measurements of the surface after the experiments. The AFM images showed no evidence of droplet formation. This study further showed that the desorption rate of Bi from the surface is negligible below a temperature of 450 °C. Above 450 °C the desorption rate increases, however temperatures above 600 °C seem to be necessary in order to allow reasonable time for the desorption steps in the growth process of Ga(As,Bi). E.g., a prepared surface with 10 min supply of TBAs with 3.3×10^{-2} mbar and TMBi with 1.6×10^{-3} mbar at 400 °C led to a desorption time of 10 min at 625 °C. In order to stabilize the Bi terminated surface at higher temperature, a continuous supply of TBAs and TMBi is needed. This precise control of the Bi terminated surface might be used for *in-situ* control of Bi as a surfactant, which is applied in the growth of different material systems such as Ga(N,As)/GaAs and (Ga,In)As/InP.[193,194] To study this stabilization of the Bi surface coverage the pre-treated GaAs (001) surface was cooled down to 250 °C. At this temperature the TMBi as well as the TBAs are still stable in the gas phase, which is proven by mass spectrometry in a subsequent experimental run (Figure 5, Chapter 7.2.2). In this experiment, the temperature is stepwise increased under TBAs and TMBi supply. With increasing temperature the RAS signal evolves from the signal of the c(4×4)β surface reconstruction at 250 °C first to the signal of the Bi terminated surface around 350 °C. This clearly shows that only TMBi is decomposed at this surface temperature and that the TBAs precursor remains stable. The lower decomposition temperature of TMBi compared to TBAs agrees well to the studied TMBi decomposition in the gas phase by mass spectrometry. The mass spectrometry investigations show a decomposition temperature for TMBi of 290 ± 10 °C and for TBAs of 330 ± 10 °C (Figure 5, Chapter 7.2.2). These temperatures are determined from the calculated gas phase temperature. The temperature deviation of the decomposition temperature determined from the RAS results compared to the gas phase temperature is explained by the uncertainty in the gas phase temperature determination, which is simply calculated by a correlation of the measured TBAs decomposition curves from ref.[161] compared to published data from ref.[101]. Above 375 °C the RAS signal further changes towards the RAS signal observed during the surface coverage under TMBi and TBAs, underlining the decomposition of TBAs at the surface above this temperature. For higher temperature, the RAS signal remains quite

stable showing the possibility to stabilize the surface coverage at higher temperatures and therefore allows an *in-situ* control of Bi as a surfactant.

In the last experiment set, the surface reconstruction is monitored during the growth of Ga(As,Bi) on GaAs by RAS. In this experiment, RAS spectra were taken within the known growth window of Ga(As,Bi) on GaAs at a temperature of 400 °C. The structural analysis by means of AFM and HR-XRD agrees well to the formerly published data for growth of Ga(As,Bi) by MOVPE (Figure 6, Chapter 7.2.2).[18] The slight deviation in Bi incorporation, growth rate and possible As/Ga ratios are attributed to the adjustments in the experimental setup compared to the MOVPE setup used without RAS. Namely, the additional gas flux through the hole in the liner (compare Chapter 3.2) changes the flow conditions in the reactor, resulting by trend in a higher growth rate and slightly increased Bi incorporation. The measured RAS spectra show strong modulations for changes of the As/Ga ratio. Comparably the RAS spectra detected during growth of GaAs also show a very strong modulation using the same growth parameters, without TMBi supply. Conclusively the Ga(As,Bi) as well as the GaAs growth surface exhibits a more complex surface structure under these conditions. The analysis of the surface reconstruction is further complicated for Ga(As,Bi) due to the occurrence of Fabry-Perot oscillations in the RAS signal. These Fabry-Perot oscillations are seen due to the difference of the refractive index of Ga(As,Bi) compared to GaAs, leading to further modulation of the RAS signal in dependence on the layer thickness during growth of the Ga(As,Bi) layers. To keep some validity, the shown RAS spectra were taken at the same time step during the growth of the layer. Introducing the studied surface coverage prior to the growth resulted in a more distinct RAS spectrum during growth of a Ga(As,Bi) layer at a growth temperature of 400 °C (red spectrum). This layer showed a maximum Bi incorporation of 4.3 %. The RAS spectrum in this case was identified with the RAS spectrum of an energetically shifted c(4×4)β surface reconstruction. The energetic shift is in accordance to the expected band gap reduction of Ga(As,Bi) compared to GaAs, giving a very convincing proof for the formation of the c(4×4)β surface reconstruction on the Ga(As,Bi) growth surface. The observed c(4×4)β surface reconstruction gives a good basis for possible theoretical calculations of the observed RAS spectra to allow the development of the actual surface structure model. Additionally, these studies were continued at a higher temperature of 450 °C and a lower temperature of 375 °C. Beside small changes in the RAS signal, which were attributed to non-optimized growth conditions, the RAS spectrum also shows the formation of the c(4×4)β surface reconstruction during growth of Ga(As,Bi) at these temperatures. Additionally, the effect of the growth of Ga(As,Bi) on a different surface reconstruction was studied. Since comparable experiments under MBE conditions were done on the (2×4) surface reconstruction of GaAs, this surface reconstruction was chosen. The RAS signal of Ga(As,Bi) grown at 400 °C on a beforehand prepared (2×4) GaAs (001) surface showed the formation of the (2×4) surface reconstruction (orange spectrum). This shows that the Ga(As,Bi) surface adopts to the symmetry of the underlying surface reconstruction during growth. The preparation of the (2×4) surface reconstruction was done by growth of GaAs at 400 °C with a gas phase ratio of V/III = 2.5 prior to the Ga(As,Bi) growth. The AFM and HR-XRD measurements of the Ga(As,Bi) layer grown on the beforehand prepared (2×4) surface indicate a poorer surface quality and show a reduced Bi incorporation of 2.6 % compared to an incorporation of 3.1 % measured for the Ga(As,Bi) layer grown on the c(4×4)β surface reconstruction under the elsewise same growth conditions. These findings indicate that the c(4×4)β surface reconstruction seems to be the best choice for the growth of Ga(As,Bi) on GaAs. On the one hand, a higher incorporation is desired. On the other hand, the preparation of the less As-rich surface reconstruction such as the (2×4) or even Ga-rich surfaces such as the (2×6) or (4×2) surface reconstruction are not easily

accessible at the low growth temperatures needed for Bi incorporation. Therefore, using the c(4×4)β surface reconstruction avoids a more complex surface preparation.

The study of the Ga(As,Bi) and the Bi terminated GaAs surface reconstruction is finalized with a test concerning the stability of the surface reconstructions regarding cooling and changes of the environment to H_2, N_2 or air. The Bi terminated surface is shown to be stable while cooling to room temperature and against changes from the As-rich ambient under TBAs to H_2 or N_2, but did not show long term stability under air. The Ga(As,Bi) growth surfaces showed the same behavior and additionally the RAS signal was reproducible after storage under air for more than half a year. Despite the likely oxidation of the surface, the underlying surface reconstruction seems to be stable. These findings are quite promising to realize the transfer of grown Ga(As,Bi) samples into ultra-high vacuum for the analysis of the surface reconstructions by investigation with other surface sensitive methods such as STM or LEED. However, the first attempts of LEED investigations were not able to reveal the surface reconstruction and only showed evidence for cubic symmetry. An optimized transfer method to avoid contaminations should be applied in future studies to identify and support the present studies of the Ga(As,Bi) (001) surface reconstructions.

Chapter 5

Analysis of the Gas Phase Composition

The second part of the results of this thesis focuses on real time gas phase investigations of the decomposition reactions occurring for different metal organic precursors during the MOVPE process. At first the main results of the *unimolecular* decomposition reactions of three newly synthesized nitrogen precursors are given together with a short sum-up of reproductive studies on literature known precursors. Based on the gained knowledge from these studies the decomposition reactions for *bimolecular* reactions occurring during epitaxial growth are shown.

5.1 Unimolecular Decomposition Studies

In a first step the *unimolecular* decomposition of the selected metal organic precursors is studied in a novel setup for real time gas phase analysis, which is described in Chapter 3.3.2.

a)

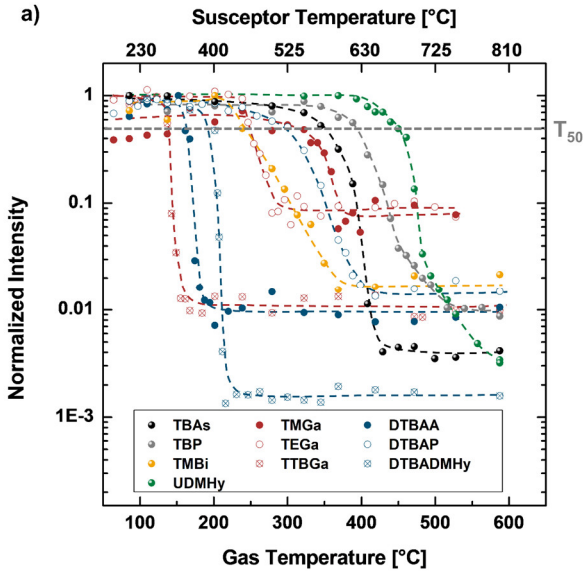

b)

Precursor	E_A in [eV]	E_A in [kcal/mol]	Log(A_0)	T_{decomp} in [°C]
TBAs	2.3 ± 0.4	55 ± 10	17 ± 4	360 ± 10
TBP	1.4 ± 0.1	32 ± 2	9 ± 1	400 ± 10
TMBi	0.6 ± 0.1	14 ± 2	11 ± 1	270 ± 10
UDMHy	1.4 ± 0.1	32 ± 2	24 ± 1	440 ± 10
TMGa	1.1 ± 0.2	25 ± 5	8 ± 2	340 ± 10
TEGa	1.3 ± 0.1	30 ± 2	11 ± 1	250 ± 10
TTBGa	3.1 ± 0.4	70 ± 10	35 ± 5	140 ± 10
DTBAA	2.8 ± 0.6	65 ± 15	70 ± 15	160 ± 10
DTBAP	1.2 ± 0.1	28 ± 2	20 ± 1	310 ± 10
DTBADMHy	2.1 ± 0.7	50 ± 15	50 ± 20	170 ± 10

Figure 24: a) Decomposition curves of TMGa, TEGa, TTBGa, TMBi, TBAs, TBP, UDMHy, DTBAA, DTBAP and DTBADMHy measured in the same reactor system. The decomposition temperature is defined with the temperature at which the intensity drops to half of its value (T_{50} line). b) Determined decomposition temperatures and activation energies.

The decomposition curves of the more established metal organic precursors TMGa, TEGa, TTBGa, TMBi, TBAs, TBP and UDMHy are given together with the newly synthesized single source precursors DTBAA, DTBAP and DTBADMHy in Figure 24. Due to the distance of the nozzle to the growth surface given by the setup the effective temperature of the collected gas is determined by correlation of the TBAs decomposition data from ref.[161] with data from ref.[101]. With this the measured susceptor temperature can be correlated to the gas phase temperature.

The decomposition investigations allow a well-founded comparison between the investigated precursors and make the investigation of *bimolecular* decomposition reactions possible. The evaluation of the decomposition reactions of the precursors TMGa, TEGa, TTBGa, TBAs and TBP are qualitatively in good agreement to data published before (Figure S1 to S5, Chapter 7.2.6).[101,159,195-206] All precursors show that dissociation can occur by bond *homolysis* (Reaction 5). *Homolysis* is shown to be the main decomposition reaction for precursors with methyl substituents such as the studied TMGa and TMBi. For these precursors, further *bimolecular* reactions such as *radical attack* on the parent molecule and *hydrogenolysis* are discussed (Reaction 10 and Reaction 11).[69] The present study shows no direct indication for the occurrence of *radical attacks* as decomposition pathway, which is attributed to the use of a lower reactor pressure and lower partial pressures of the precursors, compared to the studies done in the literature.[202] The *hydrogenolysis* reaction might occur, since H_2 as carrier gas is supplied as main species in the reactor. The expected larger reaction products in *hydrogenolysis* such as $(CH_3)_2GaH$ are likely to decompose at elevated temperatures before they can be detected in the mass spectrometer. The decomposition study showed formation of CH_4^+, which is expected in *hydrogenolysis*. However, CH_4^+ can also be formed from CH_3• radicals created by *homolysis* followed by a subsequent reaction with the carrier gas. For an observation of *hydrogenolysis*, either an alternative carrier gas such as deuterium (D_2) or deuterated precursors would be necessary, which is not covered in this study. For the precursors exhibiting larger alkyl groups, further decomposition pathways are discussed, which are supported by the presented studies. For ethyl or *tert*-butyl groups as substituent, the decomposition additionally occurs by *β-H* elimination (Reaction 8), which was, e.g., found to be the main decomposition pathway for TEGa and TBAs.[101,160,161] The dissociation by *β-H elimination* is proven by the detection of a reduced ion mass of the decomposition products. The proposed C=C double bond is formed under the abstraction of one H atom from the alkyl group. The resulting mass reduction by 1 u can clearly by resolved with the ion trap mass spectrometer. For TBAs and TBP the possibility of *intramolecular coupling* as well as *hydrogen abstraction* are discussed (Reaction 7 and Reaction 9). Detection of isobutane ($C_4H_{10}^+$) gives evidence for the *intramolecular coupling* reactions, however as discussed above for the methyl radicals, the detected $C_4H_{10}^+$ can be formed as well by reaction of *tert*-butyl radicals (C_4H_9•) with the H_2 carrier gas. The *hydrogen abstraction* as a first step in the decomposition reaction is predicted in ref.[103] and is supported by experiments done with our setup.[104] This gives a compound summary of the decomposition studies done on the established precursors investigated with the new mass spectrometer setup.

The main focus of this chapter is laid on the decomposition studies of the novel nitrogen-V precursors DTBAA, DTBAP and DTBADMHy in comparison to the conventionally used UDMHy. Based on the very promising N incorporation behaviors of the novel precursors,[55,90,207,208] the underlying gas phase reactions were studied to gain a thorough understanding of nitrogen incorporation as well as for the incorporation of As and P supplied by these precursors. The molecular structure of these precursors is designed to potentially reduce the carbon incorporation compared to structures grown with the

conventionally used nitrogen source UDMHy. UDMHy exhibits a direct N-N bond and N-C bonds in its molecular structure. The decomposition studies of this precursor, supported by the presented investigations, show formation of CH_4^+ formed by *homolytic fission* of the methyl groups from the precursor and the formation of larger stable fragments such as $(CH_3)_2NH^+$ by *homolytic fission* of the N-N bond and formation of $CH_3NCH_2^+$ by an *intramolecular coupling* reaction (Reaction 14 - Reaction 16).

Reaction 14: Homolytic fission of the N-N bond in UDMHy.

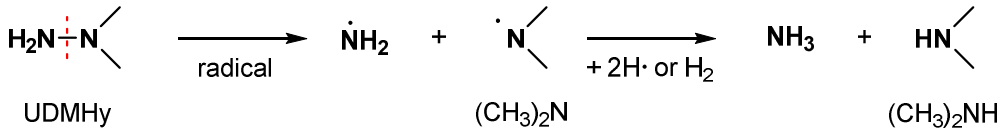

Reaction 15: Exemplary illustration for the homolytic fission of a methyl group from $(CH_3)_2N$•.

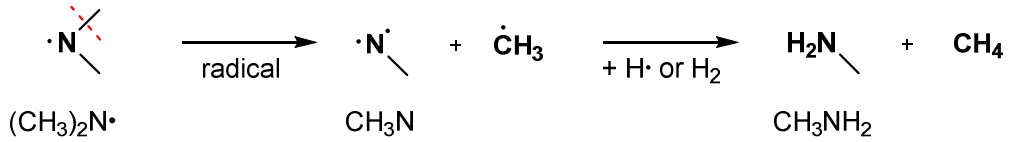

Reaction 16: Intramolecular coupling reaction leading to the formation of NH_3 and CH_3NCH_2.

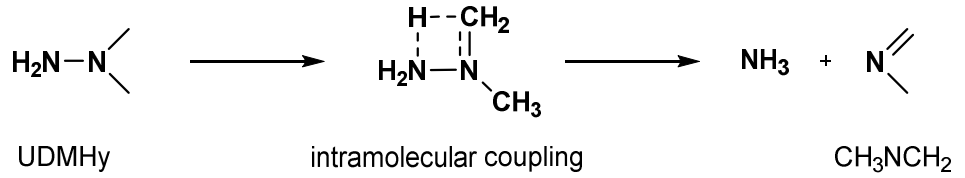

Reaction 17: Intramolecular coupling reaction leading to formation of CH_4 and N_2.

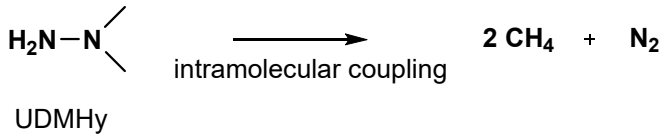

Both fragments are formed due to the C-N bond strength and are believed to lead together with formed methyl radicals (CH_3•) to carbon incorporation, which was reported to be the reason of increased threshold current densities in (Ga,In)(N,As) laser structures.[53,54] Furthermore, UDMHy shows the formation of N_2 in an *intramolecular coupling* reaction (Reaction 17). Since the formed N_2 exhibits high bond dissociation energies, it is stable in the used temperature range below 1000 °C.[209] The formation of N_2 explains the generally low nitrogen incorporation efficiency of UDMHy. E.g., as seen in Chapter 4, UDMHy needs to be offered with 10 times higher partial pressures compared to TBAs to realize a nitrogen incorporation of about 4 % into GaAs at a growth temperature of 550 °C. The decomposition reactions of UDMHy in our reactor system further showed that the larger fragment of $(CH_3)_2N$• further decomposes by abstraction of one methyl group to CH_3N and CH_3• at temperatures above 400 °C. The formation of CH_3N is supported by detection of $CH_3NH_2^+$. Detection of NH_3^+ supports the formation of NH_2• radicals from the fission of the N-N bond. The NH_2• radicals are believed to incorporate at low temperatures and desorb by formation of NH_3 at higher temperatures. As mentioned above, the formation of N_2 as decomposition product of UDMHy is expected from studies in the literature, which is additionally supported by quantum chemical gas phase calculations.[55,107] In contrast to the literature, the formation of N_2 is not supported by the presented measurements, showing that Reaction 17 might be prohibited. However, the presented study further showed that

N_2 is generally difficult to detect within the ion trap setup. This might be connected to the high electronegativity of N, which can prevent the electron ionization. These findings are also underlined by studies in low reactor pressure conditions (~ 80 mbar), which showed no strong increase of N_2.[108] One explanation could be that the formation of N_2 occurs in a *bimolecular* reaction after the decomposition of UDMHy. These *bimolecular* reactions are expected to be less probable under the low-pressure conditions of 50 mbar given in this study. Nevertheless, formation of N_2 cannot be completely excluded by the presented studies, but seems to be unlikely under the used experimental conditions.

In contrast to the molecular structure of UDMHy, the novel precursors DTBAA, DTBAP and DTBADMHy on the one hand exhibit larger alkyl groups in form of *tert*-butyl instead of methyl substituents. The larger alkyl groups are expected to reduce carbon incorporation, due to weaker bonding of the produced radical species upon decomposition as well as due to decomposition by *β-H elimination*, which leads to formation of stable molecules with a stronger C=C double bond.[69,210] On the other hand, the molecule structure exhibits no direct C-N bond, which is believed to cause the unwanted C incorporation as seen in the decomposition of UDMHy. Furthermore, DTBAA and DTBAP exhibit no N-N bond, which should effectively prevent the formation of N_2. The executed decomposition studies underline these considerations, which will be summarized here.

The decomposition temperatures of DTBAA, DTBAP and DTBADMHy are determined with T_{decomp}^{DTBAA} = 160 ± 10 °C, T_{decomp}^{DTBAP} = 310 ± 10 °C and $T_{decomp}^{DTBADMHy}$ = 170 ± 10 °C compared to UDMHy with T_{decomp}^{UDMHy} = 440 ± 10 °C (Chapter 7.2.3-7.2.5). These lower decomposition temperatures are shown to be very beneficial for the growth of 'dilute nitrides' on GaAs and GaP. For example the growth of Ga(N,P) on GaP/Si with DTBAP showed nitrogen contents above 10 % at 475 °C, which has not been realized with the use of UDMHy.[90] For DTBAA a 13 times higher N incorporation efficiency for the growth of Ga(N,As) on GaAs at 500 °C compared to identical structures grown with UDMHy is reported.[55] The growth studies using these novel precursors showed promising N incorporation behaviours for the growth of 'dilute nitrides' on GaAs or GaP/Si.[90,207,208]

All three novel precursors show the dissociation of the group-V-N bond by bond *homolysis* or *heterolysis* in the first decomposition step (Reaction 18).

Reaction 18: Initial bond homolysis or heterolysis step of the group-V-N bond. The reaction is investigated for M = As or P and R = H or $(CH_3)_2N$.

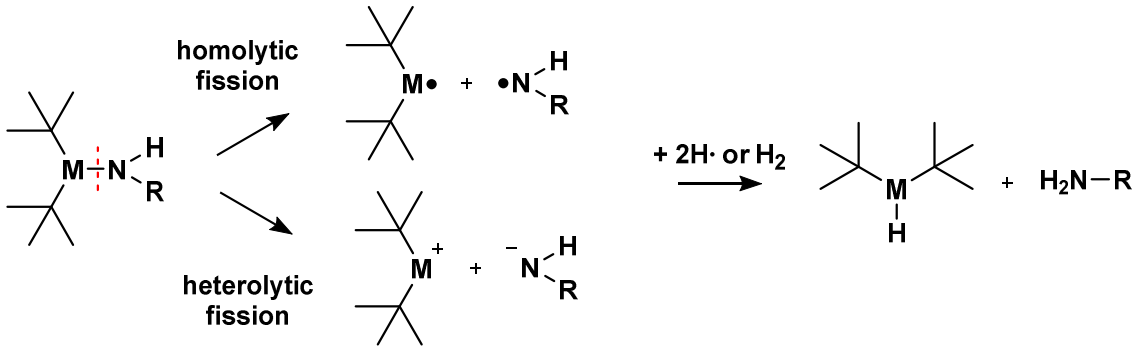

In case of DTBAA and DTBAP, Reaction 18 results in the formation of DTBAs• and DTBP•, respectively. The DTBAs• was found to decompose at 270 °C by *homolysis* and *intramolecular coupling* reactions of the *tert*-butyl groups seen by detection of isobutane$^+$ and *tert*-butyl$^+$ radicals and by *β-H elimination* leading to formation of isobutene$^+$ (Figure 3, Chapter 7.2.3). This is believed to be the main source of As originating from the

decomposition. No evidence for the formation of a larger fragment exhibiting an As-N bond was detected. This is also supported by the detection of NH_3^+ in the same magnitude of the parent molecule. The detected NH_3 indicates like discussed for UDMHy before the formation of aminyl radicals (NH_2•), supporting the N-As bond *homolysis* or *heterolysis* as main decomposition path. In the case of DTBAP the formation of DTBP• was not detectable in our setup, however it is believed to be formed in the decomposition reaction. Therefore, the absence of DTBP• is explained by a reduced stability leading to a direct dissociation or due to adsorption on available surfaces. As in the case for DTBAA, isobutane$^+$ and *tert*-butyl$^+$ radicals indicating the dissociation of the *tert*-butyl groups by *homolysis* and *intramolecular coupling* reactions are detected for the decomposition of DTBAP. The additionally detected isobutene$^+$ is attributed to dissociation by *β-H elimination* (Figure 8, Chapter 7.2.4). Again, NH_3^+ was detected in the same magnitude. For both precursors, the signal of the isobutane was seen to drop to about half of its value at higher temperatures. This reduction is interpreted as prohibition of the bond *homolysis* or *intramolecular coupling* of one *tert*-butyl group. According to Reaction 18, detection of NH_3^+ results from the formation of aminyl radicals (NH_2•), which react with the carrier gas H_2 or available H• radicals to form stable ammonia (NH_3). The NH_2• was found to be directly related to the N incorporation of the precursors. This statement is on the one hand proven, since no other N containing fragments were observable in the presented investigations. On the other hand, evaluation of the decomposition curves in an Arrhenius plot reveals the activation energy needed for the decomposition reaction. The activation energy for Reaction 18 is determined for DTBAA and DTBAP with E_A^{DTBAA} = 2.75 ± 0.6 eV and E_A^{DTBAP} = 1.4 ± 0.2 eV. In both cases a good agreement within the error of the experiments to the activation energy determined from the nitrogen incorporation for grown Ga(N,As) and Ga(N,P) structures is given.[55,90] This underlines the direct relation of the formed NH_2• to the nitrogen incorporation of these precursors. The formation of NH_2• explains that these novel precursors show high N incorporation at low temperatures, since NH_2• is very reactive.[211] However, the experiments also suggest a limitation for N incorporation at higher temperatures due to formation of the very stable NH_3.[212]

The third investigated precursor DTBADMHy is in a simple picture a combination of the DTBAA and the UDMHy precursor. The DTBADMHy decomposes by *homolytic* or *heterolytic* fission of the As-N bond in the first reaction step, leading to the formation of DTBAs• and $(CH_3)_2NNH$• (Reaction 18). This *homolysis* or *heterolysis* occurs at the same temperature of 170 ± 10 °C within the error of the measurement as seen for DTBAA (Figure 1, Chapter 7.2.5). The formed DTBAs• is shown to decompose accordingly to the observations for DTBAA at 290 ± 10 °C under the formation of isobutane$^+$, *tert*-butyl$^+$ radicals and isobutene$^+$. This supports the decomposition of the *tert*-butyl groups via *homolytic* fission, *intramolecular coupling* and *β-H elimination* reactions. Furthermore, the same drop in the intensity of isobutane$^+$ to half of its value is seen around 280 °C, showing a reduced probability of the *intramolecular coupling* reaction and bond *homolysis* at temperatures above 350 °C. These findings suggest an identical As incorporation behaviour for DTBADMHy compared to DTBAA. The N containing UMDHy part $(CH_3)_2NNH$• decomposes in a similar manner as seen for the UDMHy decomposition. Due to the formed $(CH_3)_2NNH$• radical, detected as UDMHy$^+$ and $(CH_3)_2NNH^{\bullet+}$, the decomposition temperature of this fragment is reduced to 270 ± 10 °C compared to 440 °C given for the *unimolecular* decomposition of UDMHy. The main detected decomposition products are $(CH_3)_2NH^+$ and $CH_3NCH_2^+$. In the following the mentioned decomposition pathways are referred to the reactions given in Chapter 7.2.5. The detected $(CH_3)_2NH^+$ is formed by *homolytic* fission of the N-N bond according to Reaction 2 followed by reaction

of $(CH_3)_2N•$ with H_2 or H•. The $CH_3NCH_2^+$ is either formed by *intramolecular coupling* seen in Reaction 3, which also produces $NH_2•$, or is formed by *H abstraction* from $(CH_3)_2N•$. Since NH_3^+ is detected right as the $CH_3NCH_2^+$ intensity rises, the *intramolecular coupling* reaction is believed to be the more dominant reaction pathway (Figure 2, Chapter 7.2.5). Contrary to the observation for UDMHy, not only the intensity of $(CH_3)_2NH^+$ drops at higher temperatures but also the intensity of $CH_3NCH_2^+$ decreases. This is correlated to the bond *homolysis* of $CH_3NCH•$ and $(CH_3)_2N•$ into smaller fragments such as NCH (27 u), CH_3N (29 u) and $CH_3•$, which were detected as NCH_3^+, $CH_3NH_2^+$ and CH_4^+, respectively. The detected CH_4^+ signal supports the bond homolysis reaction, since $CH_3•$ is expected to form in this decomposition reaction, according to Reaction 4. Similar to UDMHy, the C-N bond remains intact upon decomposition resulting in formation of stable N containing fragments. However, the N-N bond *homolysis* occurs at much lower temperatures compared to UDMHy in the gas phase, resulting in formation of $NH_2•$, which should lead to N incorporation. This correlates well to growth studies of Ga(N,As) on GaAs grown with DTBADMHy and TEGa. Here a N incorporation of up to 6 % at 425 °C was achieved (Figure 5, Chapter 7.2.5). This is explained by the formation of the less stable $(CH_3)_2NNH•$ compared to UDMHy, resulting in a higher N incorporation at lower temperatures.

In summary, an overview on the work done on *unimolecular* decomposition reactions in our reactor is given. The investigation of the novel N precursors DTBAA, DTBAP and DTBADMHy showed group-V-N bond *homolysis* or *heterolysis* in the first reaction step, explaining the lower decomposition temperature compared to UDMHy. This lower decomposition temperature was shown to be beneficial for nitrogen incorporation. The N incorporation is believed to be related to $NH_2•$ radicals formed upon decomposition. These explain the more efficient incorporation at lower temperatures as well as the limitation at higher temperatures.

5.2 Bimolecular Decomposition Studies

In the last section, the decomposition studies during the growth of GaAs and GaP will be summarized with respect to possible *bimolecular* decomposition reactions. The results will be compared to additional studies done for different V/III ratios during the growth of GaP. In the last step, the latest results for the *bimolecular* decomposition of UDMHy with TMGa and TEGa will be shown.

The *bimolecular* decomposition of TBAs or TBP with the Ga precursors TMGa, TEGa and TTBGa showed a strong effect of the Ga precursors on the decomposition of TBAs and TBP. As shown in Chapter 5.1 in Figure 24, the *unimolecular* decomposition temperature of the precursors are given with T_{decomp}^{TMGa} = 340 ± 10 °C, T_{decomp}^{TEGa} = 250 ± 10 °C, T_{decomp}^{TTBGa} = 140 ± 10 °C, T_{decomp}^{TBP} = 400 ± 10 °C and T_{decomp}^{TBAs} = 360 ± 10 °C. Surprisingly, the decomposition temperature of TBAs is reduced to the decomposition temperature of the Ga sources during the growth of GaAs, indicating a catalytic effect of the partly decomposed Ga precursor on the decomposition reaction of TBAs. To observe this strong catalytic effect, a V/III = 1 ratio was used. The gas phase ratio of V/III = 1 was essential to simultaneously track the decomposition of the Ga precursors in the same experimental run. The related decomposition temperatures for TBAs are determined with $T_{decomp}^{TBAs+TMGa}$ = 310 ± 10 °C, $T_{decomp}^{TBAs+TEGa}$ = 260 ± 10 °C and $T_{decomp}^{TBAs+TTBGa}$ = 170 ± 10 °C, showing a reduction of up to 200 °C of the decomposition temperature in presence of the partly decomposed Ga precursors (Figure 2, Chapter 7.2.6). The Ga precursors were measured within the same experiment, showing no effect of TBAs on the decomposition temperature of the Ga precursors. The determined decomposition temperatures agree well

within the error of the measurement to the *unimolecular* decomposition temperatures of the respective precursor and are determined with $T_{decomp}^{TMGa+\,TBAs}$ = 310 ± 10 °C, $T_{decomp}^{TEGa+\,TBAs}$ = 230 ± 10 °C and $T_{decomp}^{TTBGa+\,TBAs}$ = 150 ± 10 °C. These *bimolecular* decomposition reactions were further investigated utilizing the highly sensitive SWIFT technique of the ion trap mass spectrometer. With these measurements a detailed investigation of the arising decomposition products and fragments is possible. The *bimolecular* decomposition of TBAs and TMGa shows a significant increase of the isobutane$^+$ signal and a reduction of the isobutene$^+$ signal in contrast to the *unimolecular* decomposition. This indicates that for TBAs bond *homolysis* becomes the dominant decomposition reaction and the possibility of *β-H elimination* reaction is largely reduced. The increase of *homolytic* fission reactions near the surface is supported by the literature on surface catalytic reactions.[213] Besides the other described *unimolecular* decomposition products, the formation of methyl-arsane (MAs$^+$) and di-methyl-arsane (DMAs$^+$) as well as different fragments such as gallium (Ga$^+$), methyl-gallium (MGa$^+$), ethyl-gallium (EGa$^+$), isopropyl-gallium (IPGa$^+$), and *tert*-butyl-gallium (TBGa$^+$) is observed (Figure 3 and S7, Chapter 7.2.6). These fragments are explained by fragmentation of TBGa in the ionization process. The appearance of MAs$^+$, DMAs$^+$ and TBGa$^+$, which were not observed in the *unimolecular* decomposition, are best explained by formation in an *alkyl exchange* reaction (Reaction 12). The alternative explanation would be the formation of a larger adduct between TMGa and TBAs, which is then cracked in the ionization process resulting in the formation of the mentioned fragments. However, no evidence is seen for an *adduct formation*. Any formed adduct in the gas phase is expected to be detectable in our setup, as it is, e.g., seen for the *bimolecular* decomposition of UDMHy with TMGa or TEGa, which is discussed below.[107,108] Similarly, the formation of ethyl-arsane (EAs$^+$) and TBGa$^+$ is seen as side reaction in the decomposition of TEGa and TBAs again indicating an *alkyl exchange* as important reaction step (Figure 4 and S8, Chapter 7.2.6). For the *bimolecular* decomposition of TBAs and TTBGa, formation of TBAs$^+$ and TBGa$^+$ is seen (Figure 5 and S9, Chapter 7.2.6). Here both reactants are substituted with *tert*-butyl groups. In this case a simple *alkyl exchange* should not result in any energetic benefit for the involved molecules. Therefore, a simple *alkyl exchange* in the gas phase is most likely excluded. However, an energetic benefit in the *alkyl exchange* reaction might be given, if the Ga precursor is already partly decomposed or if the reaction is occurring *heterogeneously* on the formed GaAs surface. The possibility of *heterogenous* reactions was shown in various experiments in ref.[69,101] This behavior is exemplarily shown for the TBAs decomposition measured in the GaAs-coated liner. The *heterogenous* reaction of TBAs on GaAs results in a reduced decomposition temperature of $T_{decomp}^{TBAs-coated}$ = 250 ± 10 °C, showing a reduction of about 100 °C due to the surface catalysis.

This catalytic effect and the *alkyl exchange* are also used to explain the observations for the variation of the V/III ratio for the *bimolecular* decomposition of TEGa and TBAs. Here a strong reduction of the decomposition temperature of TBAs with decreasing V/III ratio is seen. The respective decomposition temperatures of TBAs are determined by $T_{decomp}^{V/III=10}$ = 310 ± 10 °C, $T_{decomp}^{V/III=4}$ = 310 ± 10 °C, $T_{decomp}^{V/III=2}$ = 290 ± 10 °C, $T_{decomp}^{V/III=1}$ = 250 ± 10 °C, $T_{decomp}^{V/III=0.75}$ = 235 ± 10 °C, $T_{decomp}^{V/III=0.5}$ = 220 ± 10 °C and deviate from the *unimolecular* decomposition temperature of T_{decomp}^{TBAs} = 360 ± 10 °C (Figure 6, Chapter 7.2.6). This effect is attributed to a site blocking of the formed DEAs in the *alkyl exchange* reaction on the growth surface. The possibility of the *alkyl exchange* should be enhanced for higher V/III ratios, which is supported by detection of a higher amount of the TBGa-related fragments for higher V/III ratios (Figure S10, Chapter 7.2.6). Consequently, the site blocking leads to a higher decomposition temperature for TBAs as

it prevents the surface catalytic reaction. For V/III ratios < 1, the number of catalytic reaction sites even increases due to the excess of partly decomposed TEGa. These findings were used to calculate an effective V/III ratio at the growth surface (Figure 6, Chapter 7.2.6). The effective V/III ratio deviates from the used gas phase ratio for temperatures below 350 °C and can therefore be very relevant for low temperature growth of GaAs. The decomposition products occurring from the *alkyl exchange* and the interpretation of site blocking, refers well to the observations of higher C incorporation at low temperatures attributed to adsorbed alkyl groups and may be related to formation of As antisites.[214]

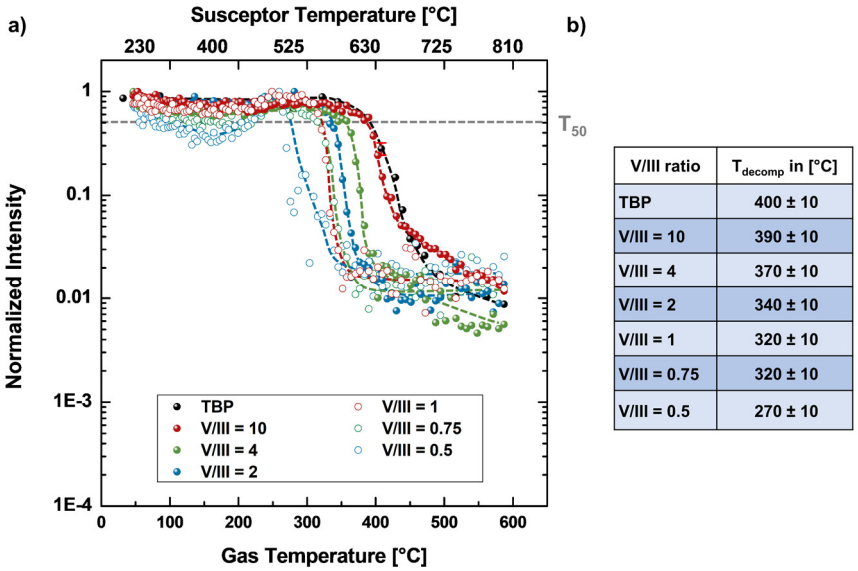

V/III ratio	T_{decomp} in [°C]
TBP	400 ± 10
V/III = 10	390 ± 10
V/III = 4	370 ± 10
V/III = 2	340 ± 10
V/III = 1	320 ± 10
V/III = 0.75	320 ± 10
V/III = 0.5	270 ± 10

Figure 25: a) Decomposition curves of TBP during growth of GaP for different V/III ratios. For this experiment the TEGa partial pressure was fixed at Pp(TEGa) = 8.2 × 10^{-3} mbar and the TBP partial pressure was varied systematically. For comparison, the decomposition curve of the unimolecular TBP decomposition is added. The decomposition temperature is defined with the temperature at which the intensity drops to half of its value (T_{50} line). b) Evaluated decomposition temperatures for TBP at different V/III ratios.

In analogy, the decomposition of TBP with the mentioned Ga precursors was investigated in the same manner. Here the decomposition temperatures were determined by $T_{decomp}^{TBP+TMGa}$ = 350 ± 10 °C, $T_{decomp}^{TBP+TEGa}$ = 315 ± 10 °C and $T_{decomp}^{TBP+TTBGa}$ = 250 ± 10 °C. Similar to the TBAs results an absolute temperature reduction, of up to 150 °C is seen. However, the decomposition temperature is not reduced down to the *unimolecular* decomposition temperature of the Ga source. This shows that the involved P-C bond exhibits a higher stability and that the underlying reaction cannot be described by a simple catalytic reaction. If only the supplied Ga is responsible for the catalytic effect, the TBP decomposition temperature should adopt to the decomposition temperature of the Ga precursor at higher temperatures, as seen in the studies on TBAs. In conclusion, the alkyl groups of the Ga precursor need to be involved in the reaction, supporting the suggested *alkyl exchange* reaction. The further study of TBP with TEGa for different V/III ratios shows a very similar reduction of the decomposition temperature of TBP with reduced V/III ratios. The decomposition temperatures are in this case determined by $T_{decomp}^{V/III=10}$ = 390 ± 10 °C, $T_{decomp}^{V/III=4}$ = 370 ± 10 °C, $T_{decomp}^{V/III=2}$ = 340 ± 10 °C, $T_{decomp}^{V/III=1}$ = 320 ± 10 °C, $T_{decomp}^{V/III=0.75}$ = 320 ± 10 °C, $T_{decomp}^{V/III=0.5}$ = 270 ± 10 °C and T_{decomp}^{TBP} = 400 ± 10 °C for the *unimolecular* decomposition of TBP. The corresponding decomposition curves are shown in Figure 25. As extensively discussed for TBAs, the results on the decomposition studies

of TBP also suggest a very similar decomposition behavior for the *bimolecular* reaction of TBP and the used Ga precursors. It is likely that a reaction product arising from an *alkyl exchange* reaction is responsible for the strong V/III dependence on the TBP decomposition. A more detailed analysis on the TBP decomposition with focus on the arising decomposition fragments is planned in the framework of the Master's thesis of J. Haust.

The very last experiments were done to show the possibility for detection of adducts in the gas phase or at the surface of the reactor system. Adducts formed on the surface are not expected to be detectable, due to their low vapor pressure, preventing desorption from the surface. The formation of gas phase adducts was reported in the literature for the *bimolecular* decomposition of TMGa and TEGa with UDMHy.[107,108] In both studies the formation of the observed adducts already occurred at room temperature and was only indirectly confirmed. As validation of these experiments, both precursor combinations were checked in the presented novel ion trap setup. The first results on the *bimolecular* decomposition of TMGa and UDMHy are shown in Figure 26 a).

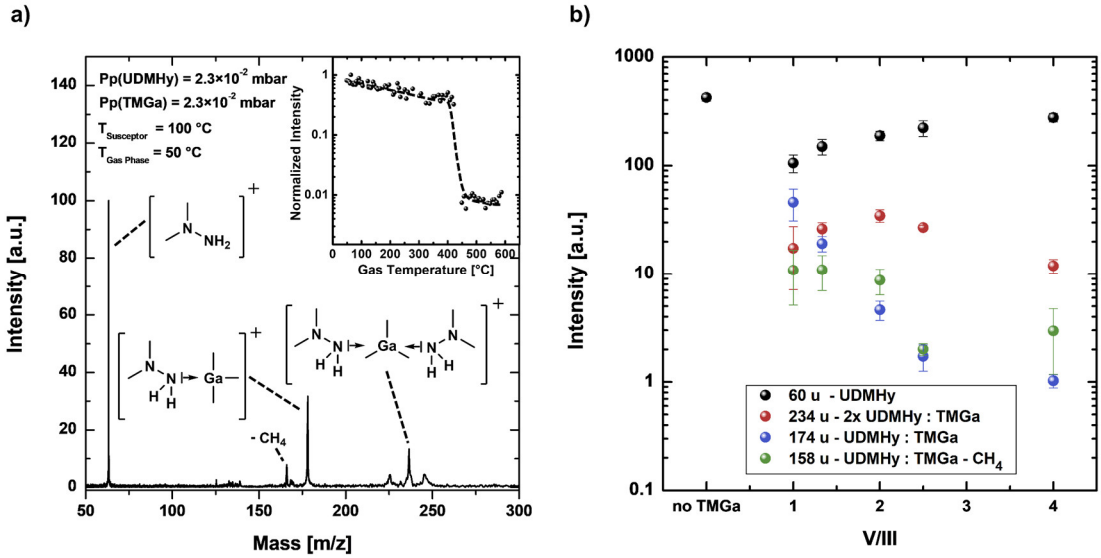

Figure 26: a) Mass spectrum at 100 °C during the bimolecular decomposition of UDMHy and TMGa with a used gas phase ration of V/III = 1. The insets show the proposed adduct formation as well as the measurement of the decomposition curve of UDMHy during the bimolecular decomposition. b) Intensity comparison at 100 °C for the proposed adducts for different V/III ratios. The intensity detected for UDMHy with the same partial pressure of 2.3 × 10⁻² mbar and without the addition of TMGa is included for comparison.

Compared to the *unimolecular* decomposition of UDMHy, a number of additional peaks with a higher mass than that of UDMHy and TMGa are already seen at a susceptor temperature of 100 °C. The additionally observed peaks are likely caused by formation of adducts in the gas phase. The smaller adduct is identified with UDMHy↦TMGa$^+$, which can lose one methyl group (CH_3) in the ionization process. This *adduct formation* was used to explain the results obtained in ref.[107]. In this study the *bimolecular* decomposition showed that the intensities for UDMHy as well as for TMGa vanishes at room temperature, which was interpreted to be caused by *adduct formation*. This kind of *adduct formation* has been investigated between electron acceptors such as TMGa or TMAl and electron donors such as NH_3, N_2H_4 or presumably UDMHy.[107,215–217] The detected higher mass is attributed to an adduct of two UDMHy molecules and one TMGa molecule (UDMHy↦TMGa↦UDMHy$^+$). As there are more peaks visible around this mass of 234 u, this adduct could also be a fragment of an even larger compound. This larger compound

could be the formation of $(CH_3)_2NN[(CH_3)_2Ga]_2NN(CH_3)_2$ by dimerization of two smaller UDMHy↦TMGa adducts under abstraction of two methyl groups ($2\times CH_3$). The idea of the formation of $(CH_3)_2NN[(CH_3)_2Ga]_2NN(CH_3)_2$ is founded in the observation of the analog dimer between the adducts of UDMHy and TEGa, which was studied in ref.[108] and will be discussed below for the investigations in the used ion trap setup. The *adduct formation* followed by the proposed dimerization is illustrated in Reaction 19.

Reaction 19: Schematic reaction for the adduct formation between UDMHy and TMGa followed by dimerization into $(CH_3)_2NN[(CH_3)_2Ga]_2NN(CH_3)_2$.

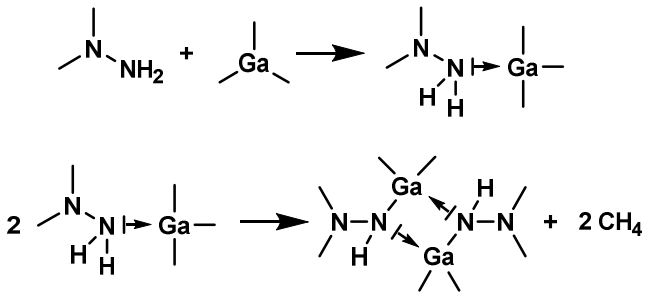

The *bimolecular* decomposition of UDMHy and TMGa further showed no influence of the TMGa on the UDMHy decomposition in terms of the decomposition temperature. The decomposition temperature of UDMHy was determined by 420 ± 10 °C in the *bimolecular* study, which is identical to the *unimolecular* decomposition study seen in Figure 24. The *adduct formation* is further investigated in dependence on the used V/III ratio by changing the TMGa supply, which is shown in Figure 26 b). Compared to the intensity detected for $UDMHy^+$ without TMGa, the addition of TMGa causes the $UDMHy^+$ intensity to drop by a factor of 4 for a gas phase ratio of V/III = 1, while the adduct peaks increase in intensity. This shows that the UDMHy is consumed in a large amount in the *adduct formation*. Increasing the V/III ratio by reducing the TMGa partial pressure leads to an increase of the $UDMHy^+$ signal, as it is supplied in excess compared to the TMGa. The V/III variation further shows an increase in the formation of larger adducts, including more than one UDMHy molecule (UDMHy↦TMGa↦$UDMHy^+$), while the adduct including an equal number of UDMHy and TMGa (UDMHy↦$TMGa^+$) reduces with increasing V/III ratio. For V/III larger than 2 the intensity of the larger adduct (UDMHy↦TMGa↦$UDMHy^+$) also decreases. This behavior is likely to be related to the overall reduced probability of *adduct formation* for a lower TMGa supply.

Reaction 20: Schematic reaction for the adduct formation between UDMHy and TEGa followed by dimerization into $(CH_3)_2NN[(C_2H_5)_2Ga]_2NN(CH_3)_2$.

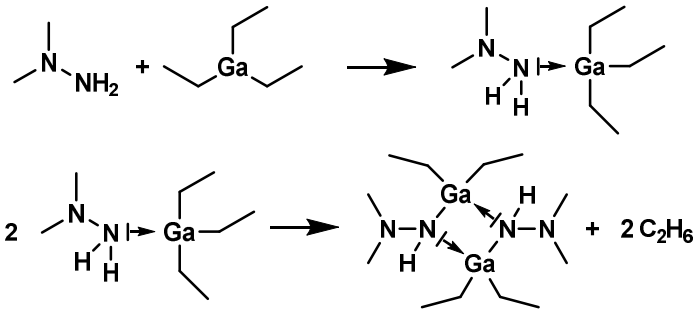

In analogy to the TMGa study the *adduct formation* between TEGa and UDMHy is studied in the ion trap setup. The first experiments suggest, similar to the TMGa experiments, the formation of adducts containing one or two UDMHy molecules. These are illustrated in the detected mass spectrum at 100 °C with a gas phase ratio of V/III = 1 in Figure 27.

The suggested *adduct formation* and the dimerization was first studied in ref.[108,218] and is illustrated in Reaction 20. These observations show the first direct proof of the *adduct formation* between TMGa, TEGa and UDMHy under MOVPE conditions and underline the possibility of the ion trap setup to detect the formation of adducts. Since the ion trap setup seems to be very suitable for the detection of larger adducts, a more extensive study of the *adduct formation* during the MOVPE process should be the content of prospective work in this field.

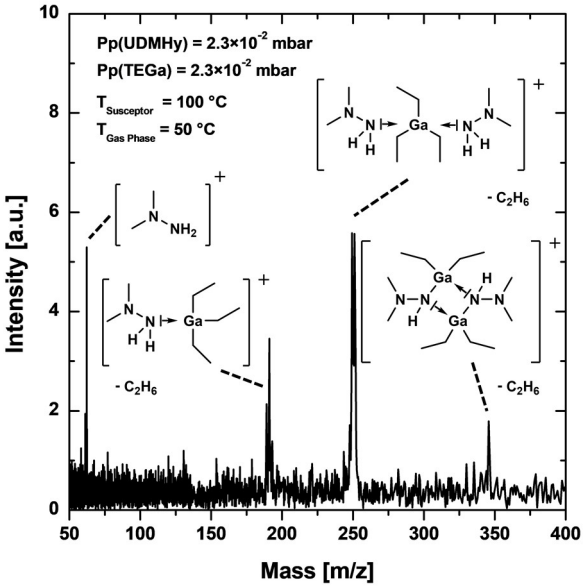

Figure 27: Mass spectrum at 100 °C during the bimolecular decomposition of UDMHy and TEGa with a gas phase ratio of V/III = 1. The insets show the proposed adduct formation.

Chapter 6

Summary and Outlook

Metal organic vapor phase epitaxy (MOVPE) plays an important role in the fabrication of optoelectronic devices based on III-V semiconductor materials such as telecommunications lasers, light emitting diodes, highly efficient solar cells or high frequency devices on an industrial scale. Even though the technique has been largely established since its invention in the 1960s, there are still many remaining questions to understand the physics of this deposition technique. This is caused by the complexity of the underlying thermodynamics, kinetics and hydrodynamics, resulting in a more phenomenological understanding of the epitaxial growth process. Nevertheless, the MOVPE technique is applicable for the realization of novel metastable materials paving the way for inventions in terms of new devices and device optimization.

One promising approach is the use of ‘dilute nitrides’ and ‘dilute bismides’ based on the gallium arsenide (GaAs) host material for an improvement of the practicability and the energy efficiency of the currently used devices to make a small contribution to solve environmental problems such as global warming. ‘Dilute bismides’ show the capability to decrease the energy consumption of laser diodes used for the telecommunication across the internet by light emission at 1.3 µm and 1.55 µm through glass fibers. The higher predicted efficiency of ‘dilute bismides’ is based on the prevention of internal loss mechanisms in the active region of the laser devices which are limiting the efficiency of the currently used (Ga,In)(As,P) laser diodes. Likewise, the ‘dilute nitride’ material family is discussed as potential candidate for highly efficient telecommunication lasers. Here material combinations such as (Ga,In)(N,As) are discussed, due to a potentially higher efficiency, a better thermal stability and the possibility to fabricate these laser structures on the well-established GaAs substrates. Besides this, the ‘dilute nitrides’ are discussed for application as highly efficient solar cells that are promising in terms of renewable energy. Here material combinations such as (Ga,In)(N,As), Ga(N,As,Sb) or Ga(N,As,Bi) are discussed as a layer in a multi-junction solar cell concept to improve the conversion efficiency of the junction responsible for absorption of sun light with a wavelength between 1.1 µm and 1.4 µm. An increase to conversion efficiencies over 50 % could make the multi-junction solar cells more competitive with respect to Si-based solar cells in terms of cost efficiency. However, the fabrication of these devices by MOVPE with respect to the desired material composition, structural quality and purity is a current challenge.

In this work a small contribution towards the possible realization of improved devices and towards a more detailed physical understanding of the related processes during growth is presented. This covers in the first part the investigation of surface structure of ‘dilute nitrides’ and ‘dilute bismides’ on an atomic scale by reflection anisotropy spectroscopy

(RAS). The RAS technique is used for *in-situ* analysis of the arising surface reconstructions of Ga(As,Bi) and Ga(N,As) layers during the growth by MOVPE. For the Ga(N,As) material system, this study includes the investigation of the already established nitrogen precursors 1,1-di-methyl-hydrazine (UDMHy) and the newly synthesized di-*tert*-butyl-amino-arsane (DTBAA) precursor. The initial point of these investigations is focused on the analysis of the GaAs host material. For a simple nitridation of the GaAs (001), surface both precursors show a different influence on the surface reconstruction. The supply of UDMHy to the GaAs (001) surface produced a strong change of the surface structure from the As-rich c(4×4)β surface reconstruction to the more Ga- or N-rich (2×6)/(6×6) surface reconstruction. Compared to this, the supply of DTBAA showed no strong modulation of the As-rich c(4×4)β surface. In contrast to UDMHy, the inbuilt additional As supply by DTBAA caused a stabilization of the given c(4×4)β surface. During the growth of Ga(N,As), by additional supply of *tert*-butyl-arsane (TBAs) and tri-ethyl-gallium (TEGa), the surface reconstruction changes to a more Ga- or N-rich (2×6)/(6×6) surface structure, independent from the choice of the N precursor and the underlying surface reconstruction. The latter was investigated by the growth of a Ga(N,As) layer on a prepared (2×4) reconstructed GaAs (001) surface. Based on the Ga(N,As) results, atomically abrupt Ga(N,As) layers with high N contents of presumably up to 16 % were realized by using different gas switching sequences in the growth process. These studies are of fundamental interest concerning the modification of the type-II transitions in W-type laser structures based on the Ga(N,As) and Ga(As,Sb) material systems.

In case of the Ga(As,Bi) material system, similar experiments were carried out starting with the influence of the tri-methyl-bismuth (TMBi) precursor on the GaAs (001) surface structure. As expected from the behavior of Bi to float on the growth surface without being incorporated, the supply of TMBi caused the As-rich c(4×4)β surface reconstruction to change presumably to a (4×3) surface reconstruction. This change of the surface reconstruction was directly related to the Bi surface coverage, which is an essential step for the realization of homogenous Ga(As,Bi) layers. The created Bi terminated surface was extensively studied in terms of the thermal stability, stability towards changes of the environmental conditions and its formation time. The addition of TBAs and TEGa for the growth of Ga(As,Bi) caused the surface reconstruction to further change to a Bi containing c(4×4)β surface reconstruction. Furthermore, the surface reconstruction was found to be very sensitive to variations of the TBAs/TEGa gas phase ratio, underlying former findings of a small growth window for the growth of Ga(As,Bi) on GaAs. Additional experiments on prepared (2×4) GaAs (001) surfaces showed that the Ga(As,Bi) surface structure is adopting to the underlying surface reconstruction during growth. For both material systems, further analysis of the surface morphology and material composition was done by post-growth investigation with atomic force microscopy (AFM) and high-resolution X-ray diffraction (HR-XRD). The compositional analysis gives evidence that the N incorporation is favored on more Ga-rich surfaces like the (2×4) surface reconstruction and that Bi incorporation is enhanced on the more As-rich c(4×4)β surface reconstruction compared to the (2×4) surface reconstruction.

The second part of this thesis covers the real-time analysis of the gas phase composition during the deposition of III-V semiconductor with focus on decomposition studies of the novel nitrogen precursors DTBAA, di-*tert*-butyl-amino-phosphane (DTBAP) and di-*tert*-butyl-arsenyl-di-methyl-hydrazine (DTBADMHy). As a general overview the decomposition temperature and decomposition reactions of the investigated precursors were studied independently to analyze the *unimolecular* decomposition reactions in the used horizontal AIXTRON AIX 200 MOVPE reactor. Besides the investigation of the novel N precursors, this includes the analysis of the *unimolecular* decomposition reactions of the

group-III precursors tri-methyl-gallium (TMGa), TEGa, tri-*tert*-butyl-gallium (TTBGa) and the group-V precursors TMBi, TBAs, *tert*-butyl-phosphane (TBP) and UDMHy. The decomposition reactions of these precursors show comprehensively a good agreement to formerly published decomposition data and proof the reliability of the measurements done with this ion trap setup. Very beneficial was the investigation of all these precursors under comparable experimental conditions in the same MOVPE reactor system, which resulted in a good data base for future investigations with this setup. The decomposition studies of the novel N precursors are of even more relevance, since growth studies with these precursors showed the simultaneous incorporation of N and As from the precursors and highlighted promising N incorporation characteristics for growth of 'dilute nitrides' at temperatures below 500 °C. The DTBAA, DTBAP and DTBADMHy precursor all exhibit a direct N-As or N-P bond, which was found to be dissociated in the first step of the decomposition reaction under formation of aminyl radicals (NH_2•). These radicals are believed to be responsible for N incorporation and lead to a limitation of the N incorporation at higher temperature due to the formation of the thermally very stable ammonia (NH_3). The As or P incorporation is connected to the decomposition of larger As or P compounds formed in the first bond *homolysis* or *heterolysis* step. These larger compounds were identified as di-*tert*-butyl-arsane (DTBAs•) or di-*tert*-butyl-phosphane (DTBP•). Based on the *unimolecular* decomposition experiments the investigation of the gas phase during the growth of GaAs, GaP and GaN was investigated. The occurring *bimolecular* reactions were most extensively studied for the precursor combination of TBAs and the Ga precursors TMGa, TEGa and TTBGa during the growth of GaAs. This study showed a strong influence of the decomposed Ga precursor on the TBAs decomposition. Here the decomposition temperature of TBAs was reduced down to the decomposition temperature of the respective Ga precursor. This is believed to occur due to a catalytic effect of the decomposed Ga precursor on the decomposition of the TBAs leading to a reduction of the decomposition temperature of TBAs from 350 °C down to 160 °C in combination with TTBGa. This catalyzed decomposition of TBAs is especially interesting for low temperature growth of GaAs-based materials. The further studies of the *bimolecular* decomposition of TBAs with TEGa were carried out for different gas phase ratios of TBAs/TEGa between 0.5 to 10 and by a more detailed analysis of the decomposition products, utilizing the selective removal of the trapped ions with stored wave inverse Fourier transformation (SWIFT) from the ion trap. These results show evidence for an *alkyl exchange* reaction to be included in the catalyzed *bimolecular* decomposition. The very same experiments were carried out for the *bimolecular* reactions between TBP and the Ga precursors during growth of GaP. Similarly, a strong reduction of the decomposition temperature of TBP by the addition of the Ga precursors was shown. However, the decomposition temperature is determined about 50 °C higher compared to the decomposition of the Ga sources. This shows that the C-P as well as the alkyl groups of the Ga precursor have to be involved in the decomposition reaction, supporting the proposed *alkyl exchange* reactions. The last experiments were carried out to show the investigation of *adduct formation* during epitaxial growth. For the precursor combinations of UDMHy with TMGa and TEGa, *adduct formation* is predicted, but only indirectly proven in literature. The analysis of these *bimolecular* reactions with the novel ion trap setup proves the formation of larger adducts such as $(CH_3)_2NN[(CH_3)_2Ga]_2NN(CH_3)_2$, which already form at room temperature for the combination of UDMHy and TMGa. Analogue formation of $(CH_3)_2NN[(C_2H_5)_2Ga]_2NN(CH_3)_2$ is supposed for UDMHy and TEGa.

Altogether, the analysis of the surface structure and the gas phase composition during growth by MOVPE has led to new insights in the deposition of III-V semiconductors with focus on novel material systems such as 'dilute bismides' and 'dilute nitrides'. Both

analysis techniques, the surface analysis by RAS and the gas phase analysis by mass spectrometry turned out to be very powerful for a direct feedback during the MOVPE process. The application and understanding of these techniques should be expanded to arising novel material systems. Especially, the analysis of ternary or quaternary compound semiconductors or of novel 2D materials would be desired, as these will presumably drive new applications in this field.

Chapter 7

Scientific Contribution

This chapter gives an overview on the scientific publications related to the presented PhD thesis. First a general overview of the work during this PhD study will be given. After this the publications directly related to the presented investigations of the surface structure and the gas phase, which are summarized in Chapter 4 and Chapter 5, will be presented with information about the personal contributions. In the last subsection further publications issued during the PhD work, conference talks and conference poster presentations will be listed, which fit into the topic of this thesis or include a significant contribution by myself.

7.1 Contribution Overview

The presented experimental results and interpretation of the shown measurement data are the result of plenty discussions and meetings in our research group and at different conferences. I especially benefited from the input by my supervisors Prof. Dr. Kerstin Volz and Prof. Dr. Carsten von Hänisch, as well as from the discussions with Prof. Dr. Wolfgang Stolz. The first experiments with regard to the *in-situ* analysis of semiconductor surface structures started with the connection of the RAS setup to the MOVPE system by H. Döscher. He started with investigations on the GaAs (001) surface reconstructions and introduced the measurement technique to me. Based on my assistance work on the GaAs surfaces, I started to investigate the surface structures of ‘dilute nitrides’ and ‘dilute bismides’ in the framework of my Master’s thesis and expanded the work with further in-depth experiments during my PhD work. The growth of the related ‘dilute nitrides’ and ‘dilute bismides’ structures were entirely done by myself. However, I am very thankful for the ideas and discussions with Eduard Sterzer, Lukas Nattermann, Peter Ludewig, Thilo Hepp and Johannes Glowatzki for the optimization of the MOVPE growth in this field. Especially the contribution of Thilo Hepp should be highlighted. He contributed by cooperation to the surface analysis of ‘dilute bismides’ by RAS, covered in Chapter 7.2.2. By the start of my PhD years I additionally adopted the topic of ‘real time gas phase investigations during MOVPE’ from Lukas Nattermann. Lukas Nattermann successfully implemented the novel ion trap setup of *Carl Zeiss SMT GmbH* to our MOVPE system. For the very first investigations on the decomposition of TBAs with this setup, I assisted Lukas Nattermann in part with the lab work and had the opportunity to get familiar with the operation of the ion trap setup. Starting from here, I analyzed the decomposition of various metal organic precursors with this setup. The data acquisition was partly done in collaboration with the research team of *Carl Zeiss*, who helped with discussions about the measurement data and in part with the data analysis. Furthermore, Sebastian Inacker, Johannes Haust, Ebunoluwa Odofin and Robin Günkel contributed in part to the presented

work on mass spectrometry and reflection anisotropy spectroscopy in the framework of practical courses or their Master's theses. With their assistance an already quite large data base on the decomposition reactions of the most frequently used precursors and of the newly synthesized nitrogen precursors could be established. The synthesis of these novel nitrogen precursors was done by Christian Ritter and Marcel Köster from the workgroup of Prof. Dr. Carsten von Hänisch and by Manuel Kapitein from *Dockweiler Chemicals*. Furthermore, the contributions of J. Glowatzki should be emphasized. He contributed equally to the publications 7.2.4 and 7.2.5, since he carried out the growth of the shown semiconductor structures for the analysis of the nitrogen incorporation behavior of the novel precursors. Overall, all presented decomposition and surface data in the publications 7.2.1 to 7.2.6, were mainly acquired and evaluated by myself.

7.2 Publications of this Work

7.2.1 Influence of UDMHy on GaAs (0 0 1) surface reconstruction before and during growth of Ga(N,As) by MOVPE

Authors: Oliver Maßmeyer, Eduard Sterzer, Lukas Nattermann, Wolfgang Stolz and Kerstin Volz

Publication: Applied Surface Science, Volume 458, 15 November 2018, Pages 512-516.

DOI: 10.1016/j.apsusc.2018.07.098

Abstract: III–V semiconductors containing small amounts of nitrogen ("dilute nitrides") are very promising material systems for optoelectronic applications. There are many studies about growth characterization of Ga(NAs) in metalorganic vapor phase epitaxy (MOVPE), but very little is known about the nitridation process on the GaAs (0 0 1) surface and the influence of the surface reconstruction on the nitrogen (N) incorporation. Therefore, we investigated GaAs (0 0 1) surfaces under different *tert*-butyl-arsine (TBAs) and 1,1-di-methyl-hydrazine (UDMHy) ambient conditions in MOVPE. For *in-situ* surface characterization, reflectance anisotropy spectroscopy (RAS) was used. Under sufficient TBAs stabilization, the surface forms an As-rich c(4×4)β surface reconstruction. This changes towards a more Ga-rich (2×6)/(6×6)-like reconstruction, if additional N is supplied. Therefore, UDMHy seems to enhance the As desorption from the surface or the surface reconstruction changes due to incorporated N. This conversion occurs rapidly within 5 s when UDMHy is supplied and was observed in a temperature range from 450 °C to 600 °C. The measured RAS spectra are then compared to the RAS spectra obtained during Ga(NAs) growth. These also exhibit a (2×6)/(6×6)-like surface reconstruction, which seems to be necessary to incorporate a sufficient amount of N into the GaAs crystal.

Authors' Contributions: My contribution to this work was the planning, the execution and interpretation of all shown experimental results. This includes the growth of the investigated semiconductor structures by MOVPE, the *in-situ* investigation of the surface structure by RAS, the compositional analysis by HR-XRD and the writing of the manuscript. E. Sterzer and L. Nattermann both supported the work by introducing the work flow in the MOVPE lab to myself as well as assisted with the planning of the experiments, the data interpretation and helped to improve the manuscript. W. Stolz and K. Volz supervised the work, helped with the data interpretation and the construction of the manuscript as well as secured the funding to support this study.

Applied Surface Science 458 (2018) 512–516

Contents lists available at ScienceDirect

Applied Surface Science

journal homepage: www.elsevier.com/locate/apsusc

Full Length Article

Influence of UDMHy on GaAs (0 0 1) surface reconstruction before and during growth of Ga(NAs) by MOVPE

O. Maßmeyer*, E. Sterzer, L. Nattermann, W. Stolz, K. Volz

Material Sciences Center and Faculty of Physics, Philipps-Universität Marburg, Germany

ARTICLE INFO

Keywords:
Characterization
Surface structure
Metalorganic vapor phase epitaxy
Nitrides
Semiconducting III–V materials
Reflectance anisotropy spectroscopy

ABSTRACT

III–V semiconductors containing small amounts of Nitrogen ("dilute nitrides") are very promising material systems for optoelectronic applications. There are many studies about growth characterization of Ga(NAs) in metalorganic vapor phase epitaxy (MOVPE), but very little is known about the nitridation process on the GaAs (0 0 1) surface and the influence of the surface reconstruction on the Nitrogen (N) incorporation. Therefore, we investigated GaAs (0 0 1) surfaces under different tertiarybutylarsine (TBAs) and 1,1-dimethylhydrazine (UDMHy) ambient conditions in MOVPE. For in situ surface characterization reflectance anisotropy spectroscopy (RAS) was used. Under sufficient TBAs stabilization the surface forms an As rich c(4 × 4)β surface reconstruction. This changes towards a more Ga rich (2 × 6)/(6 × 6)-like reconstruction if additional N is supplied. Therefore, UDMHy seems to enhance the As desorption from the surface or the surface reconstruction changes due to incorporated N. This conversion occurs rapidly within 5 s when UDMHy is supplied and was observed in a temperature range from 450 °C to 600 °C. The measured RAS spectra are then compared to the RAS spectra obtained during Ga(NAs) growth. These also exhibit a (2 × 6)/(6 × 6)-like surface reconstruction which seems to be necessary to incorporate a sufficient amount of N into the GaAs crystal.

1. Introduction

In investigations with reflectance anisotropy spectroscopy (RAS) - also known as reflectance difference spectroscopy (RDS) - many reconstructions of gallium arsenide (GaAs) (0 0 1) surfaces have been characterized and modeled. Especially in molecular beam epitaxy (MBE) this is possible by using electron based techniques like reflection high-energy electron diffraction (RHEED) and low-energy electron diffraction (LEED) or other ultra high vacuum (UHV) techniques like scanning tunneling microscopy (STM) to identify the surface reconstructions [1,2]. With the help of UHV transfer systems and by comparison to the MBE results these reconstructions were also observed in metalorganic vapor phase epitaxy (MOVPE), where the use of electrons is hindered by the rough vacuum in the reactor [3,4]. Furthermore there are also theoretical attempts in modeling the RAS spectra for known reconstructions [5–7]. With regard to nitrogen (N) containing GaAs, which is discussed for optoelectronic devices, the incorporation of N into the GaAs crystal is not fully understood. The incorporation efficiency depends on different factors like the choice of the precursor, gas phase ratios and temperature [8]. The incorporation might also be connected to surface interactions therefore it is of high interest to understand more about the nitridation processes on the GaAs (0 0 1) surface. For the use of tertiarybutylhydrazine (TBHy) as N precursor the GaAs surface seems to form a (3 × 3)-like reconstruction which was correlated to MBE results [9,10]. For growth of dilute nitrides however, 1,1-dimethylhydrazine (UDMHy) is mostly used as a nitrogen precursor in MOVPE [8]. Therefore we used the photon based RAS to investigate the influence of UDMHy on the GaAs (0 0 1) surface reconstruction under various partial pressures of UDMHy and different temperatures closely to typical growth conditions. In addition, the Ga (NAs) surface was analyzed during growth.

2. Experimental procedure

The investigated samples where grown in an Aixtron Aix 200 horizontal GFR reactor which is operated under a constant reactor pressure of 50 mbar (37.5 Torr) and a total flux of 6800 sccm palladium purified Hydrogen. The reactor is heated by 6 halogen lamps. To ensure identical GaAs (0 0 1) surface quality a 250 nm thick GaAs Buffer layer was grown at 625 °C under optimized growth conditions on each sample. For homogeneous growth the samples were additionally rotated with 50–70 rpm. In between the experiments and while changing the temperature in the reactor (450 °C to 600 °C) tertiarybutylarsine (TBAs) stabilization has been provided to prevent As desorption. For the

* Corresponding author.
E-mail address: Oliver.Massmeyer@physik.uni-marburg.de (O. Maßmeyer).

https://doi.org/10.1016/j.apsusc.2018.07.098
Received 16 April 2018; Received in revised form 1 June 2018; Accepted 12 July 2018

growth experiments triethylgallium (TEGa) has been used as group III precursor and TBAs as well as UDMHy as group V precursors. For the nitridation process TBAs ($2.04{\cdot}10^{-2}$ mbar) has been kept constant and the partial pressure of UDMHy has been varied between $4{\cdot}10^{-2}$ mbar and $9.3{\cdot}10^{-1}$ mbar. During Ga(NAs) growth $8.151{\cdot}10^{-3}$ mbar TEGa was supplied additionally.

The surface anisotropy has been monitored by a Laytec EpiRAS 200 setup which is attached above the reactor of the MOVPE system. RAS basically measures the difference in normal-incidence reflectance between two orthogonal polarizations of light. In [1,2] the experimental setup of RAS is described and the measured value $\Delta r/r$ is introduced. Due to our growth oriented setup we execute our measurements under wafer rotation. Therefore it cannot be distinguished between positive and negative RAS values, gaining the absolute RAS signal $|\Delta r/r|$. To regain information about the sign we carried out reference measurements without rotation and compared them to spectra from the literature. RAS allows investigations in two different modes. By measuring the whole energy range of the light source (Xe-lamp, 1.52–5 eV) a spectrum is detected. The RAS spectrum is a "fingerprint" for each surface reconstruction and therefore known surface reconstructions can be identified. At a fixed photon energy, a time transient can be measured to achieve a good time resolution ($\Delta t = 1$ s).

For composition analysis high resolution X-ray diffraction (HRXRD) using a Panalytical ẊPert Pro system with the Cu Kα1 wavelength (1.5405 Å) has been applied. The diffraction pattern around the GaAs (0 0 4) reflex was obtained and simulated with the ẊPert Epitaxy software.

3. Results and discussion

In this paper the influence of UDMHy on GaAs (0 0 1) surface reconstruction in MOVPE has been investigated by RAS. By using transients the time dependence of the nitridation process was observed. Additionally the reconstruction of Ga(NAs) (0 0 1) surface has been monitored during the growth process.

In Fig. 1a a GaAs (0 0 1) surface was investigated at 550 °C under various N/As ratios while keeping the TBAs partial pressure constant at $2.04{\cdot}10^{-2}$ mbar. Under pure TBAs ambient a c(4 × 4)β reconstruction is observed (black solid line) which is a common surface reconstruction of a GaAs [2]. By adding UDMHy into the reactor the spectra start to change. The peaks at 1.7 eV and 2.6 eV swap their signs and slightly shift their positions to higher energies (black to grey spectrum). Additionally the peak at around 4 eV decreases in intensity. For the highest V/V value (N/As = 46, grey solid line) a (2 × 6)/(6 × 6)-like reconstruction can be identified [2,3]. The (2 × 6)/(6 × 6) model consists of some As-As dimers (33% of a monolayer of As) on top of nearly one monolayer of Ga. In comparison the c(4 × 4)β model consists of 3 As-As dimers per unit cell on top of a monolayer of As. Therefore the (2 × 6)/(6 × 6) surface reconstruction is significantly more Ga-rich compared to the c(4 × 4)β model. Due to the fact that nitrogen was added to the surface one can assume enhanced As desorption from the surface (more Ga on top of the surface) or nitrogen building in the surface reconstruction (sitting on top of Ga places or indiffusion of N [9,11]) leading to a (2 × 6)/(6 × 6)-like spectrum.

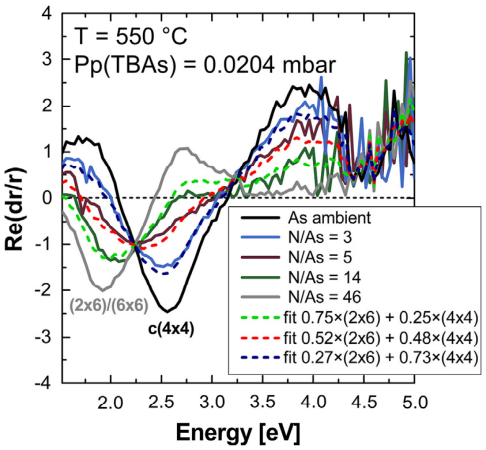

Fig. 2. RAS spectra of the GaAs (0 0 1) surface at 550 °C under a partial pressure of $2.04{\cdot}10^{-2}$ mbar of TBAs and at different partial pressures of UDMHy out of Fig. 1. The dashed lines indicate a linear combination between the c(4 × 4)β and the (2 × 6)/(6 × 6) surface reconstruction to fit N/As ratios of 3, 5 and 14 respectively.

The reconstruction of the changing surface is shown in Fig. 1b in form of a transient at 2.1 eV. Starting with a ratio of N/As = 14 the reconstruction changes from the more (2 × 6)/(6 × 6)-like surface reconstruction to the As rich c(4 × 4)β surface reconstruction in TBAs ambient (corresponding to the green solid line and black solid line respectively from Fig. 1a). At around 100 s the conversion to the more Ga rich surface under a ratio of N/As = 5 is depicted. The change of the reconstruction from N/As = 14 to pure As ambient occurs within roughly 5 s which is seen in the inlet of Fig. 1b. This rapid change could be a sign for rapid N-desorption from the surface and was observed for all individual N/As ratios out of Fig. 1a.

Another remarkable feature in Fig. 1a is the fix point at around 2.3 eV. This hints to some linear combination of the two reconstructions on the surface. Noting the grey spectrum as (2 × 6)/(6 × 6)

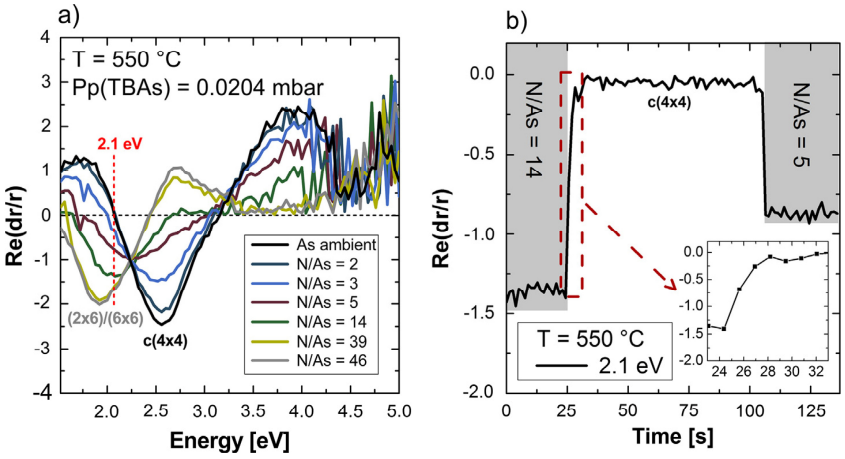

Fig. 1. (a) RAS spectra of the GaAs (0 0 1) surface at 550 °C at a partial pressure of $2.04{\cdot}10^{-2}$ mbar of TBAs and under different partial pressures of UDMHy. The surface reconstruction changes from a c(4 × 4)β (black spectrum) towards a (2 × 6)/(6 × 6) reconstruction (grey spectrum). RAS transient at 550 °C at an photon energy of 2.1 eV following the change between different N/As ratios out of a). The change of the surface reconstruction occurs within 5 s as indicated in the inlet.

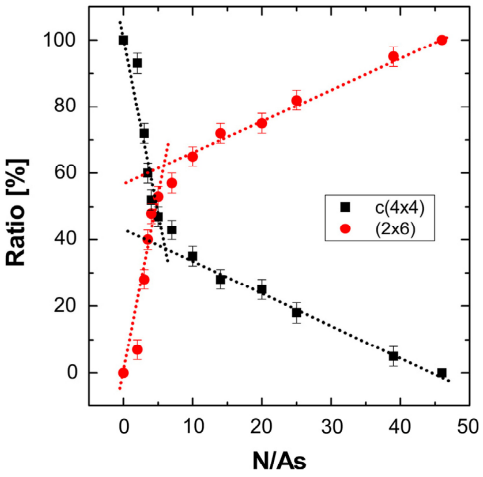

Fig. 3. Percentage of the c(4 × 4)β and the (2 × 6) reconstruction on the GaAs (0 0 1) surface during exposure to different N/As ratios that is determined by the fits out of Fig. 1. Two different linear behaviors indicated by dotted lines are observed. Up to a ratio of N/As = 5 it seems energetically easier to change the surface reconstruction towards the more Ga rich (2 × 6) reconstruction (high slopes of the linear fit). Afterwards larger amounts of N are needed to further change the surface reconstruction (small slopes).

reconstruction all intermediate spectra can be fitted as an linear combination of the c(4 × 4)β and (2 × 6)/(6 × 6) spectra. This is exemplary shown for 3 different N/As ratios (N/As = 3, 4, 14) in Fig. 2. The linear combinations are added as dotted spectra. Changes in RAS spectra or intermediate states are often described by a linear combination of two different reconstructions on the surface [2,3]. For each N/As ratio we obtain the percentage of each reconstruction on the surface. This is plotted in Fig. 3. As a first idea we estimate two linear dependences of the ratio between the two reconstructions on the ratio of N/As. Up to a fraction of 50% of the (2 × 6)/(6 × 6) surface reconstruction (which matches with low UDMHy pressures) it seems to be energetically easier for the system to change the reconstruction. Above a fraction of 50% the slope gets lower and it takes a lot more UDMHy to further change the reconstruction to a (2 × 6)/(6 × 6)-like one. Therefore the further change of the surface reconstruction seems to be less favored. When growing Ga(NAs) also large UDMHy partial pressures are needed to enable N incorporation at higher temperatures (550 °C) [8]. This could be a sign that the formation of the (2 × 6)/(6 × 6) surface reconstruction might be connected to the N incorporation.

This systematic change of the reconstruction can be seen in a wide temperature range which covers common growth temperatures of Ga (NAs) (450 °C to 600 °C). This temperature dependence is shown in Fig. 4 for different N/As ratios. As a comparison the temperature dependence for GaAs under TBAs stabilization is illustrated in Fig. 4a. The surface reconstruction typically changes from the c(4 × 4)β (As-As dimers on top) towards a c(4 × 4)α model (As-Ga dimers on top) when increasing the temperature while supplying a constant partial pressure of TBAs [2,12]. Due to incongruent evaporation at higher temperatures the As desorption is increased. Therefore a more Ga rich surface is observed by increasing the temperature. This is even enhanced by supplying UDMHy into the reactor, as seen in Fig. 4b to d. The change towards the (2 × 6)/(6 × 6)-like surface reconstruction for low UDMHy partial pressures is depicted in Fig. 4b. This cannot only be

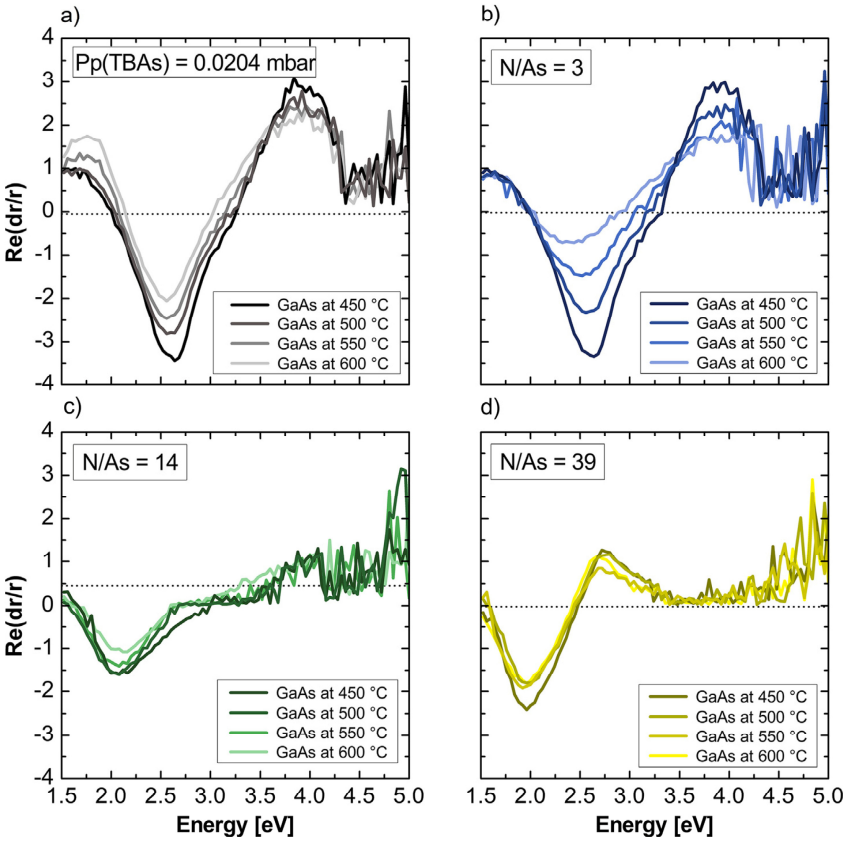

Fig. 4. RAS spectra of the GaAs (0 0 1) surface reconstruction for different N/As ratios (out of Fig. 1) during temperature variation (450–600 °C). (a) Change of the c(4 × 4)β reconstruction towards the c(4 × 4)α reconstruction while increasing the temperature under a constant partial pressure of 0.0204 mbar TBAs. (b)–(d) Temperature dependence of the RAS spectra at fixed N/As ratio of 3, 14 and 39 respectively.

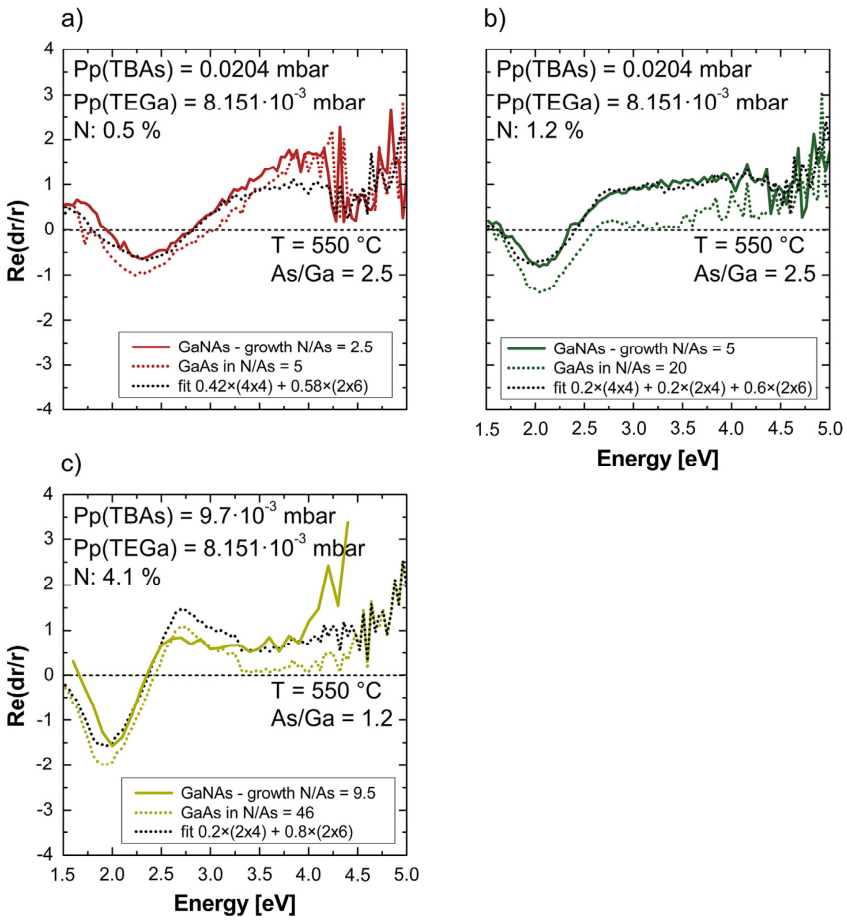

Fig. 5. RAS spectra during growth at 550 °C with a partial pressure of $2.04{\cdot}10^{-2}$ mbar TBAs, $8.151{\cdot}10^{-3}$ mbar TEGa and various UDMHy pressures (continues spectra) compared to results from Fig. 1 (dotted spectra). (a) For low N/As the spectra can be directly compared to the ambient conditions (red: growth N/As = 2.5 vs. ambient: N/As = 5). (b)–(c) Going to higher ratios (green and yellow respectively) the shape of the spectra remains similar to the ambient conditions and can be fitted with a linear combination of the c(4 × 4)β, (2 × 4) and (6 × 6) surface reconstructions (black dotted spectra).

attributed to the enhanced As desorption due to higher temperatures. In addition the additional N seems to alter the observed spectra. Notably the anisotropy at 1.5 eV stays constant and the anisotropy lowers significantly at 2.6 eV. This could be a hint that N is not only enhancing the As desorption but rather building into the surface. For higher partial pressures of UDMHy the surface forms already a more Ga or N rich surface. Therefore changing the temperature has not a huge impact on the surface reconstruction as seen in Fig. 4c and d.

During growth of Ga(NAs) the (2 × 6)/(6 × 6)-like reconstruction can be observed as shown in Fig. 5a to c. When growing the material the change of the spectrum arises at a low N/As = 2.5 ratio compared to a ratio of N/As = 5 for ambient conditions. This is most likely due to the additional TEGa in the reactor that leads to a more Ga rich surface by itself. In addition a linear combination of the c(4 × 4)β and the (2 × 6)/(6 × 6) surface reconstruction is fitted to the spectra (black dotted spectrum). During the growth of this layer 0.5% N was incorporated into the crystal. By using a higher ratio of N/As = 5 during Ga(NAs) growth the spectrum changes more towards the (2 × 6)/(6 × 6) reconstruction (green continues spectrum Fig. 5b). This can again be compared to the spectrum observed in ambient conditions of N/As = 20 (green dotted spectrum). A very good fit of the growth spectrum is reached when 20% of the (2 × 4) surface reconstruction is additionally added. The (2 × 4) surface reconstruction is less As rich than the c(4 × 4)β (50% of a monolayer of As on top of nearly one monolayer Ga). This indicates a more Ga rich (and/or N rich) surface during Ga(NAs) growth with higher N/As ratios. Under these conditions 1.2% Nitrogen has been incorporated into the crystal. The (2 × 6)/(6 × 6) reconstruction becomes even more pronounced when increasing the ratio to N/As = 9.5 while growing Ga(NAs) and in case of ambient conditions to N/As = 46 (yellow continuous and dotted spectrum respectively in Fig. 5c). For the growth with a high N/As ratio the As/Ga ratio was lowered from 2.5 to 1.2. The smaller As/Ga ratio needs to be considered when comparing the growth with low N/As ratios to the growth with a high N/As ratio (Fig. 5a and b compared to c). This changes the surface reconstruction even more towards a more Ga rich surface since a smaller amount of As is supplied into the reactor. Nevertheless the effect of the higher N/As should still be valid. The black dotted spectrum shows a good fit of the observed growth spectrum (yellow continuous spectrum). In this case the surface reconstruction can be described just by a linear combination of the (2 × 4) (20%) and the (2 × 6) (80%) model. For this high N/As ratio 4.1% N was incorporated into GaAs. Overall UDMHy and TEGa seem both to have a similar effect on the surface reconstruction that leads to a Ga and/or N rich surface.

V. Hoffmann et al. observed a (3 × 3) reconstruction during nitridation in MOVPE [9] which was additionally observed in MBE [10,11]. The (3 × 3) surface reconstruction occurred in tertiarybutylhydrazine (tBHy) ambient. This is in contrast to the (2 × 6)/

(6 × 6)-like surface reconstruction as seen with UDMHy. Both reconstruction models show As-As dimers on top of nearly one monolayer of Ga atoms. According to the models this corresponds to 22% to 44% of a monolayer of As for the 3 × 3 model and 33% of a monolayer of As in case of the (2 × 6) model after D. K. Biegelsen et al. [13]. This shows that both surface models have a similar amount of atomic species on top of the surface but a different atomic arrangement. Further investigations using the novel metal organic As-N precursor di-tertiary-buthyl-arsano-amine (DTBAA) show no strong change of the initial c(4 × 4)β surface reconstruction when DTBAA is supplied together with TBAs. This could be caused by the additional source of As from the precursor itself, that hinders N to incorporate into the surface reconstruction. Therefore, the nitridation process seems to be similar but also depending on the used precursor for MOVPE.

Like in the case of UDMHy, the conversion of the c(4 × 4)β to the (2 × 6)/(6 × 6)-like surface reconstruction during growth of Ga($N_{0.04}As_{0.96}$) has been observed with DTBAA as well. This leads to the conclusion, that this conversion of the surface reconstruction is necessary to incorporate a sufficient amount of N into the GaAs crystal. In contrast to UDMHy a significantly lower amount of DTBAA is needed to change the surface reconstruction to the (2 × 6)/(6 × 6)-like model. Therefore, the choice of the precursor seems crucial for the incorporation efficiency as reported by Sterzer et al. [14].

4. Summary and outlook

In this work firstly the influence of UDMHy (N) and TBAs (As) on the GaAs (0 0 1) surface reconstruction under MOVPE conditions has been investigated by reflectance anisotropy spectroscopy (RAS). By applying different gas phase ratios of N/As into the MOVPE reactor the reconstruction changed from a As rich c(4 × 4)β to a Ga rich (2 × 6)/(6 × 6)-like reconstruction while increasing the N/As ratio. Therefore, the additional N enhances the As desorption from the surface or incorporated N is leading to the change of the surface reconstruction. All observed reconstructions can be described by linear combinations of these two reconstruction models indicating a change towards a more Ga or N rich surface. This behavior has been investigated in a temperature range from 450 °C to 600 °C which seems to be enhanced for high N/As ratios and at low temperatures. By using a time transient measurement at 2.1 eV a rapid change within 5 s between the two surface reconstructions has been observed, which could be a sign for rapid N-desorption from the surface and shows the reversibility of the surface nitridation. In contrast to our findings the nitridation results in a (3 × 3) surface reconstruction at tertiarybutylhydrazine (tBHy) ambient [9]. Therefore, this process seems also to be dependent on the choice of the precursor. Secondly, the growth of Ga(NAs) layers where also studied under different N/As ratios leading to a similar change of the surface reconstruction which can be compared to the results of the surface at N/As ambient. The (2 × 6)/(6 × 6)-like reconstruction seems to be needed to incorporate a sufficient amount of roughly 4% of nitrogen into the GaAs crystal. During growth with di-tertiary-buthyl-arsano-amine (DTBAA) the same surface reconstruction has been observed for an incorporation of 4% N. In this case compared to UDMHy a lot less DTBAA is needed to form this surface reconstruction. This behavior shows, that the N incorporation efficiency depends on the surface reconstruction during growth and the efficiency to change the surface towards this surface reconstruction depends on the precusor. For the growth surfaces a good fit has been achieved by a linear combination of the (2 × 6)/(6 × 6), the (2 × 4) and the c(4 × 4)β surface reconstruction model of the GaAs (0 0 1) surface. This leads to the conclusion that both UDMHy (N) and TEGa (Ga) are changing the surface reconstruction towards the more Ga rich (2 × 6)/(6 × 6) model and shows that UDMHy either enhances the As desorption form the GaAs (0 0 1) surface and/or N is building into the surface reconstruction.

In future experiments the N incorporation will be investigated when growing Ga(NAs) layers on more Ga rich surfaces. These surfaces seem to be more energetically favorable during growth of the material system.

Acknowledgements

This work was supported by the German Research Foundation (GRK 1782: “Functionalization of Semiconductors”).

Declarations of interest

None.

References

[1] D.E. Aspnes, J.P. Harbison, A.A. Studna, L.T. Florez, Application of reflectance difference spectroscopy to molecular-beam epitaxy growth of GaAs and AlAs, J. Vac. Sci. Technol. A 6 (1327) (1988), https://doi.org/10.1116/1.575694.
[2] A. Ohtake, Surface reconstructions on GaAs(001), Surf. Sci. Rep. 63 (2008) 295–327, https://doi.org/10.1016/j.surfrep.2008.03.001.
[3] W. Richter, In-situ observation of MOVPE epitaxial growth, Appl. Phys. A 75 (2002) 129–140, https://doi.org/10.1007/s003390101061.
[4] P. Vogt, Th. Hannappel, S. Visbeck, K. Knorr, F. Willig, N. Esser, W. Richter, Atomic surface structure of the phosphorous-terminated InP(001) grown by MOVPE, Phys. Rev. B 60 (1999) R5117.
[5] W.G. Schmidt, F. Bechstedt, J. Bernholc, GaAs(0 0 1) surface reconstructions: geometries, chemical bonding and optical properties, Appl. Surf. Sci. 190 (2002) 264–268, https://doi.org/10.1016/S0169-4332(01)00862-5.
[6] W.G. Schmidt, F. Bechstedt, J. Bernholc, Understanding reflectance anisotropy: surface-state signatures and bulk-related features, J. Vac. Sci. Technol. B 18 (4) (2000), https://doi.org/10.1116/1.1305289.
[7] C. Hogan, R. Magri, R. Del Sole, Role of surface structural motifs on the stability and reflectance anisotropy spectra of Sb-rich GaSb(001) reconstructions, Phys. Rev. B 83 (2011) 155421, , https://doi.org/10.1103/PhysRevB.83.155421.
[8] Kerstin Volz, Jörg Koch, Falko Höhnsdorf, Bernardette Kunert, Wolfgang Stolz, MOVPE growth of dilute nitride III/V semiconductors using all liquid metalorganic precursors, J. Cryst. Growth 311 (2009) 2418–2426, https://doi.org/10.1016/j.jcrysgro.2008.09.210.
[9] V. Hoffmann, F. Poser, C. Kaspari, S. Weeke, M. Pristovsek, W. Richter, Nitrogen–arsenic exchange processes and investigation of the nitrided GaAs surfaces in MOVPE, J. Cryst. Growth 272 (2004) 30–36, https://doi.org/10.1016/j.jcrysgro.2004.10.029.
[10] H.D. Jung, N. Kumagai, T. Hanada, Z. Zhu, T. Yao, T. Yasuda, K. Kimura, In situ reflectance difference spectroscopy and reflection high-energy electron diffraction observation of nitridation processes on GaAs(001) surfaces, J. Appl. Phys. 82 (1997) 4684, https://doi.org/10.1063/1.366209.
[11] T. Imayoshi, H. Oigawa, H. Shigekawa, H. Tokumoto, Surface reconstruction of GaAs(001) nitrided under the controlled As partial pressure, Surf. Sci. 540 (2003) 577–582, https://doi.org/10.1016/S0039-6028(03)00821-5.
[12] D.E. Aspnes, New developments in spectroellipsometry: the challenge of surfaces, Thin Solid Films 233 (1993) 1–8, https://doi.org/10.1016/0040-6090(93)90050-Y.
[13] D.K. Biegelsen, R.D. Bringans, J.E. Northrup, L.-E. Swartz, Surface reconstructions of GaAs(100) observed by scanning tunneling microscopy, Phys. Rev. B 41 (5701) (1990), https://doi.org/10.1103/PhysRevB.41.5701.
[14] E. Sterzer, A. Beyer, L. Duschek, L. Nattermann, B. Ringler, B. Leube, A. Stegmüller, R. Tonner, C. von Hänisch, W. Stolz, K. Volz, Efficient nitrogen incorporation in GaAs using novel metal organic As–N precursor di-tertiary-butyl-arsano-amine (DTBAA), J. Cryst. Growth 439 (2016), https://doi.org/10.1016/j.jcrysgro.2015.12.032.

7.2.2 *In-situ* analysis of Bi terminated GaAs (001) and Ga(As,Bi) surfaces during growth by MOVPE

Authors: Oliver Maßmeyer, Thilo Hepp, Robin Günkel, Johannes Glowatzki, Wolfgang Stolz and Kerstin Volz

Publication: Applied Surface Science, Volume 533, 15 December 2020, 147401

DOI: 10.1016/j.apsusc.2020.147401

Abstract: The influence of tri-methyl-bismuth (TMBi) on the GaAs (0 0 1) surface reconstruction is studied *in-situ* by reflection anisotropy spectroscopy (RAS) in a metal organic vapor phase epitaxy (MOVPE) system. During supply of TMBi the RAS spectra indicate a change of the As-rich c(4×4)β surface reconstruction to a bismuth terminated surface reconstruction. This Bi terminated surface is correlated to the current understanding of growth mechanisms for III/V semiconductors containing small amounts of bismuth. The formation, thermal stability and influence of the ambient conditions on this surface is analyzed. The RAS results are correlated to mass spectrometric studies with a real time fast Fourier transform quadrupole ion trap mass spectrometer (iTrap), which is used inline in the same MOVPE system. Both results indicate an about 40 °C lower decomposition temperature of TMBi compared to TBAs. The decomposition temperatures are determined by mass spectrometry with 290 °C for TMBi and 330 °C for TBAs. Furthermore, the surface reconstruction is studied during growth of Ga(As,Bi) bulk layers grown on GaAs. Under ideal conditions, the RAS measurement of the Ga(As,Bi) growth surface shows the signal of a c(4×4)β surface reconstruction which is shifted to lower energies as compared to the GaAs surface reconstruction.

Authors' Contributions: My contribution to this work was the planning, the execution and interpretation of all shown experimental results. This includes the growth of the investigated semiconductor structures by MOVPE, the *in-situ* investigation of the surface structure by RAS, the compositional analysis by HR-XRD, the analysis of the surface morphology by AFM and the writing of the manuscript. T. Hepp and R. Günkel assisted with the *in-situ* investigations of the grown Ga(As,Bi) structures at higher growth temperatures of 450 °C and the growth on the alternative (2×4) surface reconstructions. All co-authors helped with the interpretation of the data and with the review of the manuscript. W. Stolz and K. Volz further supervised the work and secured the funding to support this study.

Applied Surface Science 533 (2020) 147401

Contents lists available at ScienceDirect

Applied Surface Science

journal homepage: www.elsevier.com/locate/apsusc

In situ analysis of Bi terminated GaAs (0 0 1) and Ga(As,Bi) surfaces during growth by MOVPE

O. Maßmeyer*, T. Hepp, R. Günkel, J. Glowatzki, W. Stolz, K. Volz

Material Sciences Center and Department of Physics, Philipps-Universität Marburg, Germany

ARTICLE INFO

Keywords:
Metal organic vapor phase epitaxy
Reflectance anisotropy spectroscopy
Dilute bismides
Surface reconstruction
Mass spectrometry
III/V semiconductors

ABSTRACT

The influence of trimethylbismuth (TMBi) on the GaAs (0 0 1) surface reconstruction is studied *in situ* by reflection anisotropy spectroscopy (RAS) in a metal organic vapor phase epitaxy (MOVPE) system. During supply of TMBi the RAS spectra indicate a change of the arsenic rich c(4 × 4)β surface reconstruction to a bismuth terminated surface reconstruction. This Bi terminated surface is correlated to the current understanding of growth mechanisms for III/V semiconductors containing small amounts of bismuth. The formation, thermal stability and influence of the ambient conditions on this surface is analyzed. The RAS results are correlated to mass spectrometric studies with a real time fast Fourier transform quadrupole ion trap mass spectrometer (iTrap), which is used inline in the same MOVPE system. Both results indicate an about 40 °C lower decomposition temperature of TMBi compared to TBAs. The decomposition temperatures are determined by mass spectrometry with 290 °C for TMBi and 330 °C for TBAs. Furthermore, the surface reconstruction is studied during growth of Ga(As,Bi) bulk layers grown on GaAs. Under ideal conditions, the RAS measurement of the Ga(As,Bi) growth surface shows the signal of a c(4 × 4)β surface reconstruction which is shifted to lower energies as compared to the GaAs surface reconstruction.

1. Introduction

Bismuth (Bi) containing GaAs ("dilute bismide") is receiving more and more interest over the last 20 years due to its promising electronic and optical properties [1–10]. By incorporation of Bi into GaAs the band gap is reduced by 80–90 meV per % of Bi [11–13], which is the largest reduction with respect to strain for all ternary GaAs based alloys and can be theoretically explained by a band anti crossing in the valence band [14]. Bi has a strong influence on the spin orbit splitting (Δ_{SO}), due to its large atomic number [15–18]. This separation of the spin orbit split off band and the heavy (HH) and light hole (LH) bands can become larger than the band gap in Ga(As,Bi) by incorporation of more than 10% of Bi [7,16,17,19]. Under these conditions internal loss processes like inter valence band absorption and Auger recombination, involving the transitions from the conduction to the heavy hole and from the spin orbit split off to heavy hole band (CHSH), are forbidden. This could lead to higher efficient devices operating at 1.55 µm compared to currently used telecommunication laser diodes based on InP, that suffer from CHSH Auger recombination as dominant loss process. The CHSH Auger recombination leads to production of heat in the device and therefore requires additional cooling, which results in worse device performance [20–22].

Due to the high metastability of the Ga(As,Bi) material system phase separation may occur leading to droplet formation on the growth surfaces, which can be problematic for realization of sharp hetero interfaces as needed in the devices [23–26]. Furthermore, low temperatures are required for incorporation of Bi into GaAs, which leads to formation of crystal defects such as As antisites known for GaAs [27]. Therefore, realization of high quality Ga(As,Bi) with Bi contents larger than 10% is still a challenge for structures grown by molecular beam epitaxy (MBE) [28–33] and especially by metal organic vapor phase epitaxy (MOVPE) [2,24,34–39].

Surface studies of MBE grown structures have shown that especially at low growth temperatures Bi is likely to stick to the surface and is changing the surface reconstruction of the GaAs (0 0 1) surface. Depending on the ambient conditions and elemental sources used in MBE, different surface reconstructions of Ga(As,Bi) are discussed in the literature [10,13]. At higher temperatures Bi can desorb from the growth surface [28,40–44] and is only acting as a surfactant leading to a (1 × 3) surface reconstruction on GaAs (0 0 1) [6,42,45,46]. At lower temperatures bismuth induced (2 × 1), (2 × 4), (4 × 3) and (4 × 4) reconstructions have been investigated [31,47–50]. Some of these surface reconstructions are also seen during GaAs growth, depending on the growth conditions used [31,49,51]. Furthermore, at very low

* Corresponding author.
E-mail address: Oliver.Massmeyer@physik.uni-marburg.de (O. Maßmeyer).

https://doi.org/10.1016/j.apsusc.2020.147401
Received 18 May 2020; Received in revised form 28 July 2020; Accepted 28 July 2020
Available online 05 August 2020

As_2:Ga flux the surface changes to a unusual (2 × 1) surface reconstruction. This (2 × 1) surface should be metallic and has been observed in various experiments, which show enhanced Bi incorporation for samples grown on this surface reconstruction [31,41–44,48,51–53].

Only very few studies on Ga(As,Bi) surface reconstructions have been done under MOVPE conditions by utilization of reflection anisotropy spectroscopy (RAS), showing a (3 × 8) like surface reconstruction, starting from a (2 × 4) surface reconstruction of GaAs (0 0 1) [40].

So far most surface studies for dilute bismides have been carried out under the ultrahigh vacuum conditions (UHV) used inline in MBE by electron based surface sensitive methods like scanning tunneling microscopy (STM), low energy electron diffraction (LEED), reflection high energy electron diffraction (RHEED), etc. In this work we used RAS, which is a photon based surface sensitive method, to analyze the surface reconstructions of dilute bismides occurring under MOVPE conditions. The MOVPE studies in the past have shown that the realization of high quality Ga(As,Bi) is limited to a very small growth window growth and that a surface coverage with Bi prior to the growth is necessary for realization of homogenous layers with high crystalline quality [33]. Both the small growth window and the surface coverage will be correlated to RAS measurements in this work to support and enhance the current understanding of the MOVPE growth mechanisms of this material system.

2. Experimental procedure

The investigated samples were grown or prepared in an AIXTRON AIX 200 MOVPE reactor with gas foil rotation (GFR). The MOVPE system consists of a horizontal reactor which is operated under a total flux of 6800 sccm H_2 carrier gas and a reactor pressure of 50 mbar. The samples are placed on a graphite susceptor, which can be heated up to 900 °C by halogen lamps below the susceptor. Exact and semi insulating GaAs (0 0 1) substrates were used in all experiments. The substrates are pretreated by an etching procedure with H_2O:H_2O_2:NH_3 solution and the samples were baked at 350 °C unstabilized for 5 min and at 750 °C under stabilization with tertiarybutylarsane (TBAs) for 5 min prior to the growth. A 250 nm thick GaAs buffer layer was grown at 625 °C under optimized growth conditions to ensure a reproducible surface quality. TBAs, triethylgallium (TEGa) and trimethylbismuth (TMBi) were used as precursors for Ga(As,Bi) growth and for the preparation of the Bi terminated surfaces. During all heating and cooling steps, the surface has been stabilized by TBAs to prevent incongruent evaporation of arsenic from the investigated surfaces. Varied temperatures in the reactor and different partial pressures of the precursors have been used throughout the experiments and will be stated for each experiment.

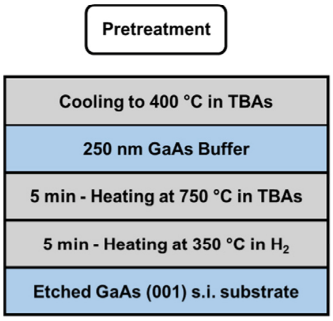

The surface anisotropy has been measured and monitored by an Laytec EpiRAS 200 setup which is located above the MOVPE reactor [54]. In RAS linear polarized light is impinging under normal incidence onto the sample and the induced change in polarization is analyzed. Since the cubic GaAs bulk is nearly optically isotropic, a surface sensitive signal is gained, by analyzing the difference in reflectance of two orthogonal polarizations. The gained signal $\Delta r/r$ can be related to the surface reconstruction by measuring the whole spectral range of the light source (Xe arc lamp, 1.52–5 eV). This spectrum is like a "fingerprint" of the surface reconstruction, which can be used to identify known surface reconstructions by comparison to available data from the literature. Additionally, transient measurements can be done at a fixed photon energy to gain comparably good time resolution ($\Delta t \approx 1$ s), which is sufficient to monitor e.g. the change between two surface reconstructions. Due to the GFR the sign of the RAS signal is lost and only the absolute value $|\Delta r/r|$ can be measured during growth of the layers. However, the sign can be determined by reference measurements without rotation. To allow an estimation of the experimental error for the given RA spectra, a selection of reproduced experiments is shown in the supporting information S0. Based on these, the shown and discussed changes of the spectra and transients are significant with regard to the experimental error.

The thermal decomposition of TBAs and TMBi has been measured within the same reactor system by a novel fast Fourier transform (FFT) quadrupole ion trap mass spectrometer (iTrap) from Carl Zeiss SMT GmbH [55]. The ion trap is attached to the MOVPE system by a bypass connection that is operated under stable flow and pressure conditions, similar to the pressure in the reactor. From the bypass a small volume of the analyte is pulsed by an atomic layer deposition valve into the ion trap. With this the large pressure difference between the reactor and the UHV of the ion trap is overcome. Due to the FFT technique a single mass spectrum is recorded within 2 s. The ions are generated by electron ionization in the ion trap. This setup has been shown to be very promising for decomposition studies and is described in more detail in [56,57].

To analyze the composition of the grown Ga(As,Bi) samples high resolution X-ray diffraction (HRXRD) was carried out. The used setup is a Panalytical X'Pert Pro system that uses the Cu $K_{\alpha 1}$ wavelength (1.5405 Å). The diffraction pattern around the GaAs (0 0 4) reflection was afterwards simulated by the X'Pert Epitaxy software.

The surface morphology of the grown layers was studied using a Nanoscope IIIa atomic force microscopy (AFM) in tapping mode.

3. Results and discussion

For a better understanding of the context of the presented experiments a short sum up of the growth of Ga(As,Bi) according to the literature is given [33,38,39,58]. The metastability of Ga(As,Bi) grown on GaAs leads to a small available growth window. In MOVPE for a significant Bi incorporation into GaAs the growth temperature has to be chosen between 375 °C and 450 °C. The best crystalline quality concerning optical properties are realized at 400 °C. Also at this temperature, the most experimental data has been acquired, which lead to the decision to study this temperature in more detail. Additionally to the harsh temperature restriction, also small As/Ga ratios between 1 and 2.5 have to be chosen, due to the V-V competition. Below As/Ga = 1 Ga droplets are formed, above As/Ga = 2.5 Bi incorporation is prevented, which leads to droplet formation on the growth surface. The growth studies led to the development of a growth model. This model suggests that for low Bi supply the Bi only floats on the surface. After a sufficient amount is reached, incorporation sets in. The Bi content than linearly increases until a saturation is reached. Above this level, the surplus Bi forms droplets. The linear increase of Bi incorporation leads to concentration gradients in grown structures, which were shown to be avoidable by introduction of a surface coverage with the used Bi and As precursors. Based on these studies, we decided to investigate the related growth surfaces and the impact of the surface coverage on the surface reconstruction.

In Section 3.1 the influence of the TMBi and TBAs precursor on the GaAs (0 0 1) surface reconstruction will be shown, which addresses the investigation of the needed surface coverage. Afterwards the thermal stability and the influence of altered ambient conditions on the

observed surface reconstruction will be discussed in Section 3.2. Finally, the change of the surface reconstruction during growth of Ga(As,Bi) layers is analyzed in the available growth window and compared to the proposed growth mechanisms for MOVPE grown Ga(As,Bi) in Section 3.3.

3.1. Bi induced surface reconstruction

Bi is known to have a large influence on the surface reconstruction of GaAs (001) surface by different experiments done in MBE. Accordingly, we supplied Bi in form of TMBi to the GaAs (001) surface under MOVPE conditions. We investigated the As rich c(4 × 4) surface reconstruction, which forms in the As rich ambient given in the MOVPE process. The As rich ambient is created due to the continuous supply of TBAs in our process. During growth of GaAs it is necessary to create an As rich ambient to prevent incongruent evaporation of As above 450 °C. Therefore, to stick to our growth conditions used in former studies and allow a valid comparison to these results the arising c(4 × 4)β surface reconstruction was chosen. Without TBAs supply in the H_2 atmosphere of the reactor the surface remains in the c(4 × 4)β surface reconstruction since no As is desorbing from the surface. To reach the (2 × 4) surface reconstruction used for the experiments done in [40] the surface has to be specifically prepared, which is usually not done in the growth process of Ga(As,Bi). However, a comparable experiment during growth of Ga(As,Bi) at 450 °C on a prepared (2 × 4) surface reconstruction will be discussed at the end of Section 3.1.3.

The RAS spectra of the GaAs (001) surface under TBAs stabilization with a partial pressure of 2.02 × 10^{-2} mbar at a temperature at 400 °C is shown as black spectrum in Fig. 1 a). Under these conditions the RAS signal corresponds to the arsenic rich c(4 × 4)β surface reconstruction [59,60]. The c(4 × 4)β surface is the starting reconstruction of the experiments and known to occur at low temperatures for GaAs as compared to the (2 × 4) surface reconstruction which was used in the MOVPE experiment mentioned above and during the MBE experiments [40,48,49]. The RAS signal changes by suppling TMBi with a partial pressure of 1.26 × 10^{-3} mbar. In the first approach, TMBi was subsequently supplied onto the GaAs surface. The first TMBi pulse of 10 s cases a reduction of the anisotropy at 2.65 eV as long as TMBi is opened. After TMBi is closed, the signal recovers again in about 30 s, but does not reach the starting intensity. After a stabilization of the RAS signal the full spectral range was covered in an RAS spectrum. The RAS spectrum shows an alteration over the whole energy range compare to the RAS signal of the c(4 × 4)β surface (red spectrum). The RAS signal remains stable throughout the measurement of the whole spectra, which was monitored by transient measurements at 2.65 eV during the TMBi supply and after the collected RAS spectrum (S1). In the same manner, further TMBi pulses onto the same surface with different supply times between 10 s and 30 s further change the RAS signal until a saturated signal is obtained (grey spectrum). Additional supply of TMBi does not change this surface, which indicates that a stable surface reconstruction seems to be formed. Only if TMBi is supplied for a much longer time ([1]approx. 30 min), the anisotropy rises strongly, which could be caused by droplet formation or roughening of the surface (S2). In comparison to the c(4 × 4)β spectrum, the negative anisotropy at 2.65 eV vanishes. This peak can be correlated to the As-As dimers in the c(4 × 4)β surface reconstruction and the corresponding transition fits to the energy of the E_1 critical point of GaAs [61]. On one hand, this feature in the RAS signal can be changed, if the TMBi influences the As-As dimers, maybe due to an exchange of Bi and As on the surface. Another idea would be possibly new dimers which could be Bi-Bi dimers that are formed perpendicular to the As-As dimers on the surface which would reduce or cancel the related feature in the RAS spectrum. This effect was e.g. seen for different dimer orientations on Silicon [62]. Compared to our findings, MBE studies show that the surface under As and Bi forms a (4 × 3) surface reconstruction via a disordered (1 × 3) surface, when starting from a c(4 × 4) surface reconstruction [31,49]. The (4 × 3) surface reconstruction could be an idea for the investigated surface, but this needs additional proof by other experimental methods or theoretical calculations of the observed spectra.

In the low energy range of the RAS spectrum the peak at 1.6 eV gets more intense and seems to shift to lower energies out of the detection range. In analogy the peak at 4 eV changes in the same manner and shifts to 3.75 eV. All findings indicate that TMBi alters the c(4 × 4)β reconstruction, most likely by termination with Bi. This would be in agreement with the experiments done in MBE.

The same surface can be reached by a continuous supply of TMBi and TBAs. This step is used for the mentioned surface coverage prior to the growth of Ga(As,Bi). The corresponding RAS spectra are shown in Fig. 1 b) and the change was monitored by a RAS transient at 1.52 eV in a second experimental run under the very same conditions, which is shown together with the reflection signal in Fig. 1 c). The transient is a cut through the spectra at 1.52 eV (blue dashed line). During simultaneous supply of TMBi and TBAs the Bi induced RAS signal changes slightly compared to the pulsed experiment (red spectrum). Especially at lower photon energies, the anisotropy changes, which could be caused by a dynamic exchange of Bi and As on the surface competing for group V sites on the surface. The signal changes back to the RAS spectrum of the first experiment, when the TMBi supply is stopped and remains in this configuration under TBAs supply. The RAS transient in Fig. 1 c) shows the evolution of the RAS signal during the used switching sequence. The gray shaded area indicates the time in which TMBi was opened. Starting from an Δr/r value of 1.3 for the c(4 × 4)β surface reconstruction the RAS signal increases to 2 for the dynamic surface reconstruction. About 70 s supply of TMBi is necessary to reach a stable RAS signal that corresponds to the red spectrum. This is also in good agreement to the subsequent TMBi pulses for a total time of 90 s to reach the Bi terminated surface in the first experiment. The signal further rises in roughly 30 s to about 2.9 when TMBi is closed, which corresponds to the grey spectrum. This indicates that the Bi induced surface reconstruction realized by TMBi pulses in Fig. 1 a) can also be reached by continuous supply of TMBi and TBAs. This conversion of the surface reconstruction occurs on a quite slow time scale of up to 100′s of a second. For comparison, the surface reconstruction of the GaAs (001) surface changes in less than 5 s by addition of 1,1-dimethylhydrazine [54]. A further indication for Bi sticking to the surface is the increase of the reflection signal seen in Fig. 1 c). Bi has a higher reflectivity for perpendicular reflection of light with a photon energy of 1.52 eV compared to GaAs [63,64]. Moreover, the formation of the Bi terminated surface can be monitored by the reflection signal, which makes *in situ* control of the Bi terminated surface in reactors not equipped with a RAS measurement system possible. This control is desirable for growth of Ga(As,Bi) as discussed in the next paragraph.

The formation of the discussed Bi induced surface reconstruction can be correlated to the growth mechanism proposed for Ga(As,Bi) growth by MOVPE. In our studies, we propose that Bi is floating on the growth surface until a critical Bi amount is reached upon which Bi incorporation starts into the growing layer. By further Bi supply the incorporation increases, leading to a concentration gradient in the structure, until a saturation level is reached. At this point formation of droplets might occur, depending on the growth conditions used [26,33,38,39,58]. The mentioned concentration gradient was reduced by introducing a surface coverage with As and Bi for 10 s prior to the growth [33,58]. This behavior can be explained by the RAS spectra discussed and by the transient measurements. When suppling TMBi together with TBAs firstly the RAS signal does not change for roughly 10–20 s, which could explain that nearly no Bi is incorporated into the material, if the As rich c(4 × 4)β is still intact. Afterwards it then takes 60 s more to reach a stable signal of the Bi induced surface. This

[1] Only an approximated value is given, since the TBAs and TMBi supply was changed during the experiment and the supply was stopped in between.

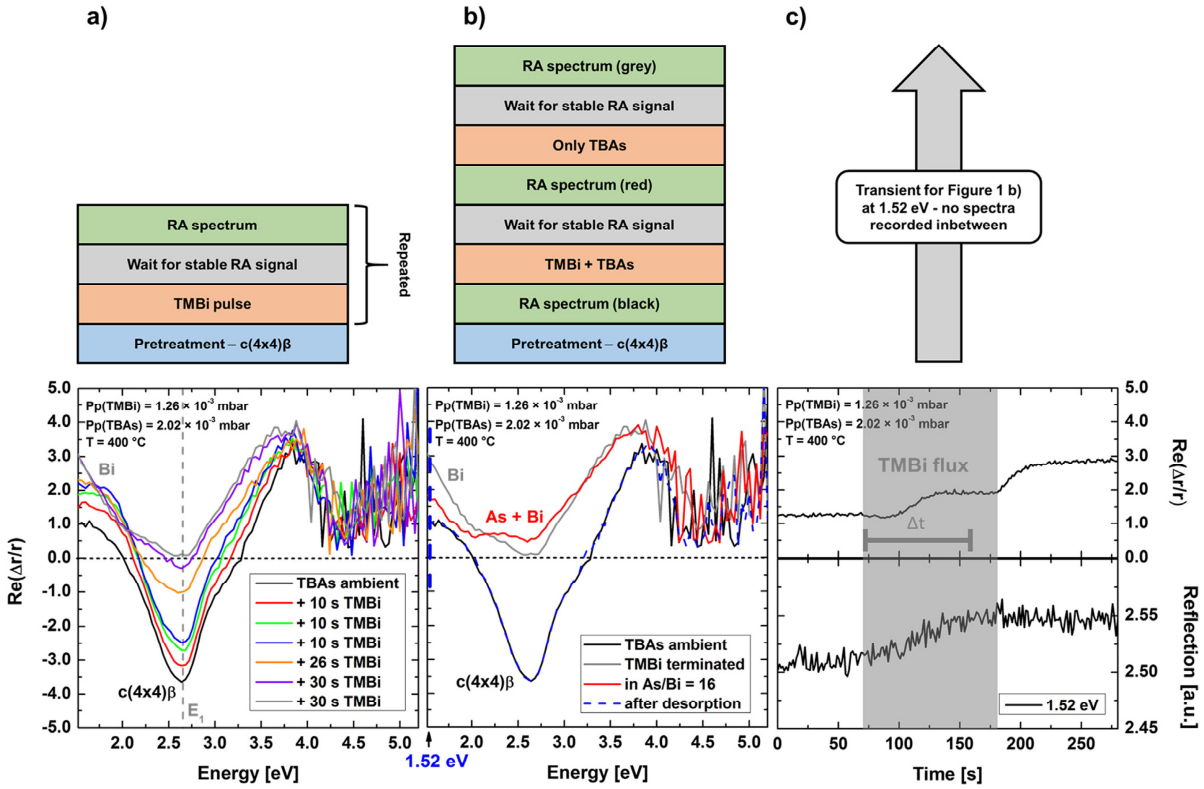

Fig. 1. a) RAS spectra of the GaAs (001) surface under a partial pressure of 2.02 × 10^{-2} mbar TBAs (black spectrum) and after different exposure times by TMBi with a partial pressure of 1.26 × 10^{-3} mbar. Different colors indicate intermediate spectra before the saturated surface is reached (grey spectrum). b) Variation of the experimental conditions to a continuous supply of TBAs and TMBi. Additionally, the RAS spectrum after desorption of the Bi terminated surface is included (blue spectrum). c) Top: RAS transient at 1.52 eV detected in an additional experimental run to monitor the change of the c(4 × 4)β reconstruction to the Bi terminated surface under simultaneous supply of TBAs and TMBi. Bottom: Change of the reflection signal during the transient measurement. (For interpretation of the references to colour in this figure legend, the reader is referred to the web version of this article.)

continuous change of the surface reconstruction could explain the formation of the concentration gradient, since a change of the surface reconstruction can have a strong impact on the incorporation behavior due to available adsorption sites, as it has been shown for Ga(As,Bi) growth [33,58]. This means that the necessary surface coverage is directly related to a change of the surface reconstruction prior to the growth of Ga(As,Bi).

In Fig. 1 b) also the RAS spectrum of the surface after the complete desorption of the deposited Bi from the growth surface. The obtained blue spectrum completely correlates to the signal of the c(4 × 4)β surface reconstruction. This shows that the Bi can be removed by heating to higher temperatures, which will be detailed discussed in Section 3.2.

To get more insight into the formation of the Bi induced surface reconstruction the time to reach the Bi induced surface reconstruction in dependence on the ambient conditions at a temperature of 400 °C was studied by RAS transient measurements at 1.52 eV. The times determined to reach the Bi induced surface with a fixed TMBi partial pressure of 1.6 × 10^{-3} mbar and varying TBAs supply is shown in Fig. 2a). Within the error of the evaluation the time to reach the Bi induced surface reconstruction remains constant. Therefore, changes in TBAs supply have little to no impact on the formation of the Bi induced surface reconstruction. This also means, that there is no change in the competition for lattice sites on the surface between Bi and As for a change in TBAs supply. For all used partial pressures the Bi induced surface reconstruction has been additionally recorded by a complete RAS spectrum which are all in very good agreement to each other. Only for a ratio of As/Bi < 1 some small deviations occur in the spectrum between 1.52 eV and 3 eV (S3). This could be caused by an even more Bi rich surface due to a possible change in the group V competition for very low TBAs supply.

On the other hand, an increase of the TMBi partial pressure shows a linear decrease in the formation time of the Bi induced surface. This is shown in Fig. 2 b). The Bi induced surface is reached in a shorter time, if the TMBi supply is increased. With regard to the growth of Ga(As,Bi) this implies that the time of the surface coverage has to be adopted with respect to the growth conditions used. Additionally, the integral amount of TMBi with respect to the supply time is plotted. This is expected to be constant, if the formation of the Bi induced surface is only dependent of the amount of Bi supplied to the surface. The evaluation shows that a linear increasing amount of Bi is necessary to form the Bi terminated surface. An explanation would be that a part of the Bi can already desorb from the surface, which is shown in some of our experiments even at 400 °C. However, the desorption process is slow compared to the supply time. Another idea is that the decomposition rate of the TMBi precursor can limit the formation of the surface reconstruction. This could include methyl groups which are still sticking to the growth surface at this low temperature, leading to blocking of adsorption sides on the surface. A further explanation would be that the additional Bi is adsorbed as an additional layer or film on top of the surface reconstruction, leading to a dependence of the formation on the diffusion of Bi on the surface. The latter idea is supported by our measurements shown in the next section.

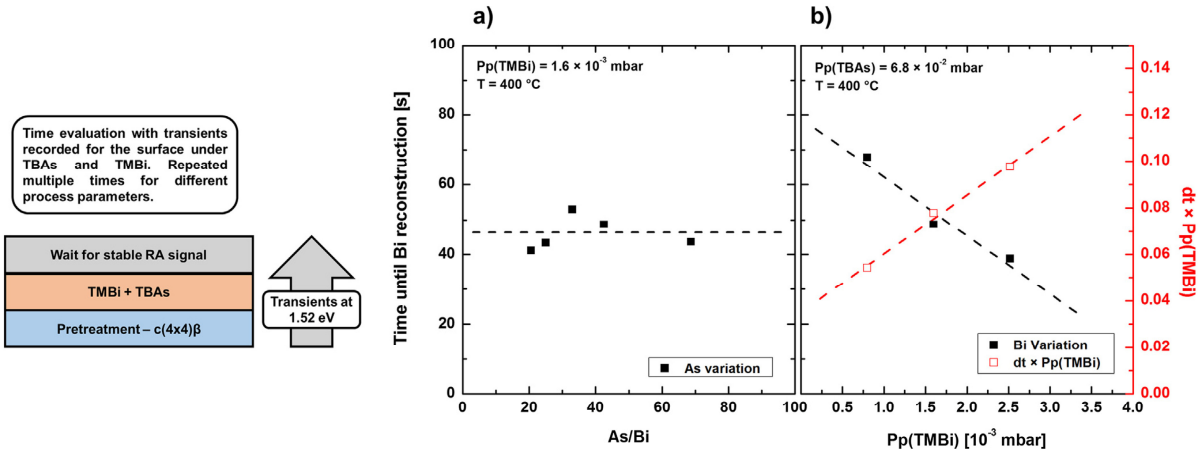

Fig. 2. Time to reach the Bi terminated surface evaluated from RAS transient measurements at 1.52 eV. a) In dependence of the As/Bi ratio by variation of the TBAs partial pressure. b) In dependence of the TMBi partial pressure at a constant TBAs supply. Additionally, the integral amount of supplied TMBi with respect to the supply time is plotted.

3.2. Thermal stability of the Bi induced surface reconstruction

In the next part, the thermal stability of the Bi induced surface reconstruction will be discussed with respect to desorption of Bi and change of the carrier gas within the reactor. As mentioned in the introductory part Bi was found to stick on the growth surface at low temperatures. Therefore, baking steps at higher temperatures are applied to remove the remaining Bi from the growth surface. Since we found that Bi alters the surface reconstruction, which was discussed in Section 3.1., we utilize the RAS signal to quantify the desorption of Bi from the surface and show how to stabilize the observed surface reconstruction at higher temperatures. This can be useful for an *in situ* control of Bi as a surfactant. [6,42,43,46]. Furthermore, the gained knowledge will give insight into the current lower temperature limit for Ga(As,Bi) growth.

Fig. 3 shows a RAS transient at 1.52 eV during a desorption experiment of Bi from the Bi induced surface.

The surface was prepared by continuous supply of TBAs and TMBi with a partial pressure of 3.3 × 10^{-2} mbar and 1.6 × 10^{-3} mbar, respectively, for 10 min. Starting from the Bi induced surface under TBAs stabilization with 2.02 × 10^{-2} mbar, the reactor temperature is ramped up to 625 °C to desorb Bi from the surface reconstruction. This step is also introduced into optimized growth of Ga(As,Bi) on GaAs to avoid the formation of Bi droplet and Bi incorporation into the layers grown on top of the Ga(As,Bi) layer [8,33,58]. A first sharp drop of the RAS signal occurs at around 450 °C, which is assumed to be due to a significant increase in Bi desorption rate from the surface. At 450 °C Bi can be desorbed from the GaAs (001) surface which was studied in additional experiments and can also be seen in MBE experiments [28,40–44]. However, the process still takes a long time at this temperature, depending on the amount of deposited Bi as already seen at a temperature of 400 °C (S2). After 400 s a temperature of 625 °C is reached in the reactor, which is indicted by the grey shaded area. At this temperature the RAS intensity seems to be stable, but has still not

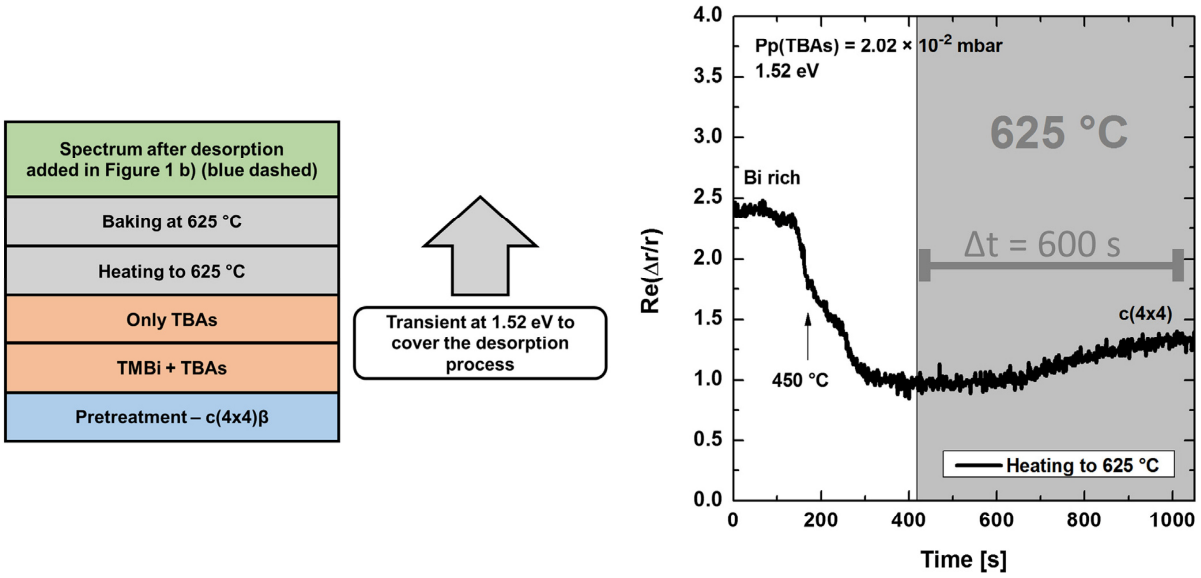

Fig. 3. RAS transient at 1.52 eV during the desorption of Bi from the Bi terminated surface by heating of the reactor to 625 °C. The desorption time at 625 °C used for the evaluation is marked within the figure.

Table 1
Evaluation of the desorption time (t_{desorb}) of Bi from the Bi terminated surface reconstruction. The surface had been prepared by addition of TBAs and TMBi for 10 min. The supply time of 10 min for TMBi is labeled as Δt. The product of the supply time Δt of TMBi with the partial pressure P_P(TMBi) of TMBi is given by Δt × P_P(TMBi). Δt × P_P(TMBi) gives a quantity for the total amount of TMBi to the reactor. The expression (t_{desorb})/(Δt × P_P(TMBi) relates the desorption time with the total amount of TMBi in the reactor. If this value is expected to be constant if the total amount of deposited Bi on the surface is responsible for the increase in the desorption time.

Pp(TMBi) in [mbar]	Pp(TBAs) in [mbar]	Δt × Pp(TMBi) in [s × mbar]	t_{desorb} at 625 °Cin [s]	t_{desorb} /Δt × Pp(TMBi) in [1/mbar]
8.0×10^{-4}	6.8×10^{-2}	4.8×10^{-1}	450 ± 50	$(9 \pm 1) \times 10^{2}$
1.6×10^{-3}	3.3×10^{-2}	9.6×10^{-1}	600 ± 50	$(6 \pm 1) \times 10^{2}$
2.5×10^{-3}	6.8×10^{-2}	1.5	1200 ± 50	$(8 \pm 1) \times 10^{2}$

reached the signal of the c(4 × 4)β surface reconstruction. It then takes additional 600 s to fully desorb the Bi from the surface. This is proven by remeasuring the full RAS spectrum after cooling the surface to 400 °C. This measurement is included as blue dashed spectrum into Fig. 1b). The RAS spectrum perfectly agrees to the As rich surface without any Bi deposited on top. Furthermore, no evidence of droplet formation or surface roughening was shown in the AFM measurement (S4). The same experiment was carried out for preparation of the Bi surface with different TMBi partial pressures for the same duration. The results are shown in Table 1.

As proven above, the variation of the TBAs partial pressure should have little to no impact. Due to the different TMBi partial pressures used, the amount of deposited Bi is increased. The total amount of supplied Bi into the reactor can be expressed by the supply time of TMBi (Δt) multiplied with the partial pressure of TMBi (P_P(TMBi)). This results in the expression Δt × P_P(TMBi), which is correlated to the total amount of supplied Bi. From the RAS transients the desorption time is estimated with the time, that is necessary to reach the signal of the c (4 × 4)β surface reconstruction. The desorption time ($t_{desorp.}$) increases with increasing TMBi partial pressure. Since we believe that additional Bi can stick to the surface, more Bi should accumulate on the surface with increasing TMBi partial pressure. To support this assumption, the used amount of TMBi is evaluated with respect to the desorption time at 625 °C. This is done in Table 1 by calculating the ratio of the desorption time and the amount of supplied Bi (t_{desorb})/(Δt × P_P(TMBi). This value must be constant, if the desorption time is directly related to the amount of Bi deposited on the surface. The determined values of 9×10^{2} 1/mbar, 6×10^{2} 1/mbar and 8×10^{2} 1/mbar for the three different TMBi partial pressures are constant within the error of the measurement and are given in Table 1. The error is dominated by the evaluation technique of the RAS transient, since it is quite subjective at which point the RAS signal of the c(4 × 4)β surface reconstruction is recovered. The mentioned constant ratio is an indication that Bi is accumulated on the surface after formation of the Bi induced surface reconstruction. This additional Bi layer or layers should be isotropic and therefore not be seen in the RAS signal due to symmetry.

In the next step, the prepared Bi induced surface is analyzed during cooling to room temperature. Until 350 °C the surface is stabilized with 3.3×10^{-2} mbar of TBAs. Afterwards the surface is kept under H_2 ambient until room temperature is reached. At this point the carrier gas is changed to N_2. The corresponding RAS spectra are shown in Fig. 4. The RAS signal only changes as expected due to the cooling of the sample. All peaks increase in intensity due to the overall decrease of the reflectivity, which is in the denominator of the RAS signal. Additionally, the intensity increases due to less thermal energy, which leads to a more distinct anisotropy of the surface. Furthermore, the peaks of the spectrum shift to higher energy according to the increase in the transition energies of the GaAs critical points [59,65]. The surface reconstruction should therefore be nearly unchanged by cooling to room temperature and also the change to N_2 seems to not affect the Bi induced surface. The changes in the RAS spectrum under N_2 can be attributed to the strain of the window, which is necessary to pass the light into the reactor and only contributes to the spectrum, if the spectrum is obtained without sample rotation. These findings could be used to transfer the sample into an UHV chamber for characterization of the surface reconstruction by e.g. STM or LEED. However, a successful transfer has yet to be realized with our current approach. A realization of this transfer will be the topic in prospective work.

The influence of heating on the Bi induced surface under continuous supply of 1.26×10^{-3} mbar of TMBi and 4.2×10^{-2} mbar of TBAs is shown in Fig. 5 a). At the starting temperature of 250 °C the prepared c (4 × 4)β surface reconstruction remains unchanged, even though TBAs and TMBi are supplied. At this temperature, both precursors are not decomposed [57,66,67]. Therefore, no additional As or Bi is supplied to the surface. Due to the low temperature the As rich surface reconstruction remains stable, since the thermal energy is too low in order to desorb As from the surface. At 300 °C the peak at 2.6 eV in the RAS spectrum starts to decrease. This would not be the case if only TBAs is supplied to the surface, since additional As would only stabilize the c(4 × 4)β surface reconstruction as shown for the surface at 400 °C under TBAs stabilization as black spectrum in Fig. 1 (a). This means that the TMBi precursor is at least partly decomposed and Bi adsorbs on the surface leading to a change in the RAS response. At 350 °C the spectrum changed completely to the signal obtained for the Bi terminated surface, which fits to the grey spectrum from Fig. 1a). This shows that Bi is adsorbed on the surface, but no As is available, otherwise the signal for TBAs and TMBi supply would be expected, which is shown as red spectrum in Fig. 1b). Therefore, a surface temperature of 350 °C is not enough to decompose the TBAs molecules within the gas phase. At 375 °C, the RAS signal changes further, especially between 2 eV and 3.5 eV. This shows that the TBAs is starting to decompose, leading to As supply to the surface. The As supply changes the surface reconstruction and therefore the measured RAS spectrum to the one seen under TBAs and TMBi supply. Above 400 °C the spectrum completely agrees with the previous experiment, shown as red spectrum in Fig. 1b). Still some deviations in the RAS signal are seen when increasing the temperature towards 625 °C. This could be attributed to increasing desorption of Bi and As atoms from the surface. Both should be possible as shown previously for the Bi surface and due to the incongruent evaporation known for As. Overall, this gives an indirect measurement of the decomposition temperatures of TMBi and TBAs.

Furthermore, the experiment shows that the Bi terminated surface can be obtained over a large temperature range between 375 °C and 625 °C. This can be very relevant for the growth of Ga(As,Bi) and other III/V material systems. For the Ga(As,Bi) material system, it is shown that the Bi incorporation severely drops at higher temperatures and above 500 °C almost no Bi is incorporated into the layers [33,58]. This Bi terminated surface can therefore be used as a surfactant effect at higher temperatures. The surfactant can for example lead to less carbon incorporation into the layers grown, improve the interface quality in heterostructures or alter the incorporation behavior since the surface reconstruction is changed [6,42,45,46].

The decomposition of the precursors was additionally measured by mass spectrometry with the ion trap attached to the same reactor. The measured intensities, normalized to the highest intensity, are shown in Fig. 5 b) versus the temperature. For TMBi the same partial pressure of 1.26×10^{-3} mbar was used and for TBAs a slightly higher partial pressure of 7.5×10^{-2} mbar was used, which should not affect the

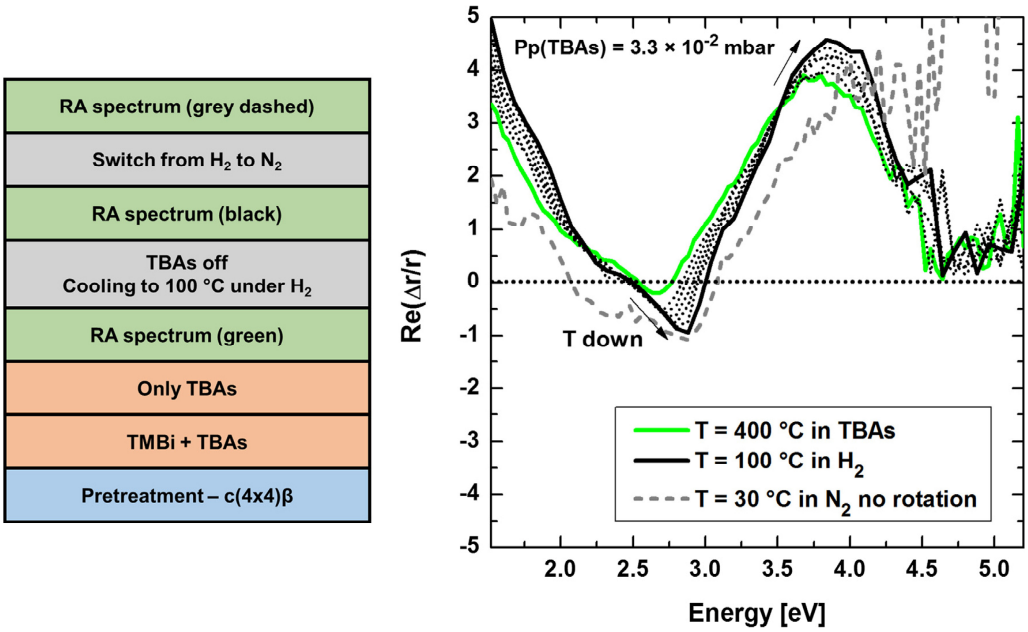

Fig. 4. Evolution of the RAS signal of the Bi terminated surface during cooling of the reactor under TBAs supply with 3.3 × 10^{-2} mbar down to 350 °C, followed by cooling under H_2 to room temperature and change of the carrier gas to N_2.

decomposition temperature [66]. For both precursors quite sensitive ionization conditions are used, which have been found in the past for this setup [56,57]. This leads to only small fragmentation of the parent molecule due to the electron bombardment. Therefore, the TBAs molecule can be tracked directly and the $Bi(CH_3)_2$ (DMBi) signal is used to track the TMBi decomposition. The DMBi is chosen due to the higher intensity in the mass spectrum compared to the TMBi signal. From these decomposition curves, the decomposition temperature of TMBi is determined with 290 ± 10 °C and for TBAs with 330 ± 10 °C from the temperature at which the signal drops to half of the measured intensity. The decomposition temperature of TBAs fits within the error of the measurement to the one known from literature [66]. The gas phase temperature at the collection point of the bypass in this measurement is determined by correlation to decomposition data of TBAs [56,57]. The relative shift in the decomposition temperature between TBAs and TMBi fits very well to the observation of the change in the surface reconstruction monitored with the RAS as discussed before. However, both temperatures are determined lower than expected from the RAS measurement. This can either be due to an under estimation of the gas phase temperature in the setup. On the other hand, the As and Bi supply in the low temperature regime of the decomposition could be too low to have a significant impact on the surface reconstruction since the precursors are only partly decomposed. However, a slow conversion towards the surface reconstruction would then be expected. This seems not to be confirmed by our measurements (S5). The lower decomposition temperature of TMBi compared to TBAs indicates that for Ga(As,Bi) with the currently used metal organic precursors, the realization of lower growth temperatures is rather limited by the decomposition of the TBAs precursor, compared to the decomposition of the TMBi precursor.

3.3. Investigations of the Ga(As,Bi) growth surface

In the last part the changes in the surface reconstruction during growth of Ga(As,Bi) layers within the known "growth window" for MOVPE is discussed, compared to the developed growth models and set in contrast to MBE results [33,58].

The RAS spectra for the growth of Ga(As,Bi) bulk layers at 400 °C are shown in Fig. 6 a). The TEGa and TMBi partial pressures were kept at 4.2 × 10^{-2} mbar and 1.6 × 10^{-3} mbar, respectively. The TBAs partial pressure was varied to cover the known "growth window" for Ga(As,Bi) between a TBAs/TEGa ratio of 0.75 to 3 [33,38,58]. The corresponding results from the XRD analysis is plotted in Fig. 6 b). Crossed data points indicates droplet formation on top of the surfaces. All other surfaces show very low roughness with a root mean square value below 0.5 nm (S6). The RAS spectra show a strong modulation within this parameter range. For the highest TBAs/TEGa ratio of 3.5 the RAS spectrum (blue spectrum) has a similar shape as the spectrum of the c(4 × 4)α surface reconstruction in the range for photon energies above 2.5 eV. The c(4 × 4)α surface reconstruction is commonly observed during GaAs growth [59]. However, the spectrum is modulated for the low energy range. The positive anisotropy peak at 1.7 eV is not discriminable and the negative peak at 2.65 eV is less pronounced compared to the spectrum of the c(4 × 4)α surface reconstruction (S7). For this sample no Bi incorporation was observed. It is therefore expected that the Bi only acts as a surfactant during this experiment and therefore alters the surface reconstruction, leading to the change in the RAS spectrum for low photon energies as mentioned above. For all other samples a Bi incorporation between 2.5 and 4.5 % and a decrease in growth rate towards low TBAs/TEGa ratios is observed which is in good agreement to former experiments done in the same reactor system [38]. The RAS signal changes quite a lot by adjusting the TBAs/TEGa ratio to lower values. However, there is also a very strong change in the RAS signal of GaAs growth under the same conditions, which is shown in the supporting information (S8). The GaAs growth only shows the expected signal for a c(4 × 4)α surface reconstruction at a TBAs/TEGa ratio of 1. This strong deviation of the RAS signal for low temperature GaAs growth is not fully understood so far and not shown for GaAs grown in MBE [59]. This change in the RAS spectra could on the one hand be affected by adsorbed alkyl groups from the used precursor molecules, which stick to the surface since the desorption rate of the molecules from the surface should be low at this temperature. On the other hand, the surface could also convert into an even more As rich surface due to the additional TBAs supply which leads to a higher V/V competition

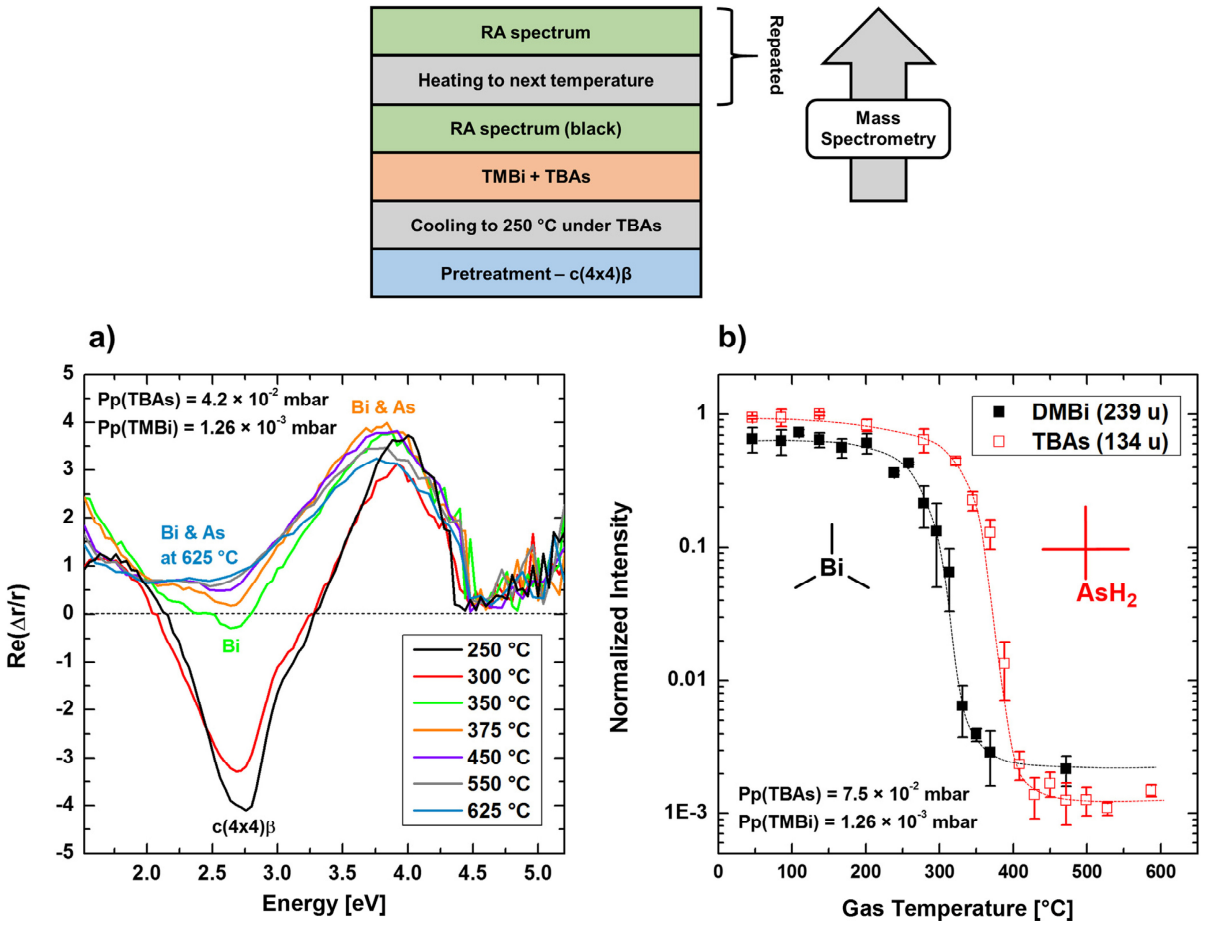

Fig. 5. a) RAS spectra of the Bi terminated surface during continuous supply of 4.2 × 10^{-2} mbar TBAs and 1.26 × 10^{-3} mbar TMBi at different reactor temperatures. b) Decomposition curves of TBAs (134 u) and TMBi (254 u) at comparable partial pressures measured by mass spectrometry. TMBi is was tracked by DMBi (239 u) due to fragmentation of the parent molecule by electron ionization.

when Bi is additionally supplied. The V/V competition could explain the prevention of Bi incorporation above a TBAs/TEGa ratio of 3.5. Furthermore, in the case of Ga(As,Bi) growth the modulation of the RAS spectrum is additionally overlapped by Fabry-Pérot oscillations. These were observed during the growth of Ga(As,Bi) on GaAs due to the change of the refractive index between the materials. An example is given in the supporting information (S9). These oscillations overlap the RAS spectra especially in the low photon energy range for this material system. This will modulate the RAS spectra in dependence of the used wavelength, thickness of the growing layer and connected to this the growth rate. The interference of the RAS signal is therefore changed throughout the measurement, since a full spectrum has a measurement time of around 1 min. This implies that one has to be very careful while interpreting the measurement data. Nevertheless, one sees that the surface reconstruction is severely changing in the available growth window for Ga(As,Bi) samples. The strongly modulated RAS spectra indicate that the surface structure is probably very complex during the growth of Ga(As,Bi) under these conditions, which leads to concentration gradients in the structures observed with HRXRD measurements [33]. Introduction of a surface coverage prior to the growth seemingly avoids this, which is investigated in terms of changes to the surface reconstruction in the next step.

For a TBAs/TEGa ratio of 0.75 the RAS spectrum shows a more pronounced negative anisotropy for low photon energies and a positive anisotropy for higher energies which is plotted in comparison to the RAS signal of the c(4 × 4)β surface reconstruction of GaAs and the RAS signal for the Bi terminated surface in Fig. 7. The RAS spectrum was obtained for a sample grown with preflux of TBAs and TMBi (surface coverage) prior to the growth (black spectrum) and without (red spectrum). Without surface coverage a composition gradient was observed in the XRD measurement, which was removed by using the surface coverage as described in [33,58]. The surface coverage also affects the measured RAS spectrum. The observed double peak at low photon energies is removed from the spectrum and the shape looks identical to the signal of a c(4 × 4)β surface reconstruction. However the spectrum is shifted to lower energies compared to the c(4 × 4)β spectrum for GaAs (red dotted spectrum).

Compared to the previous RAS spectra, the detected anisotropy shows that especially at 2.65 eV it becomes much higher and more distinct. This is an indication of a more well order surface structure, which is probably beneficial to gain a homogenous Bi incorporation. A similar energy shift of the RAS spectrum is for example seen for the RAS spectrum of the GaSb (0 0 1) c(4 × 4)β surface reconstruction in comparison to the RAS signal of the GaAs (0 0 1) c(4 × 4)β surface reconstruction [68]. If one uses the band gap reduction for Bi incorporation in GaAs by 80–90 meV/%, the band gap of the grown Ga(As,Bi) layer changes by 0.37 ± 0.05 eV. If the same is true for the corresponding transition, which is similar to the critical point energy

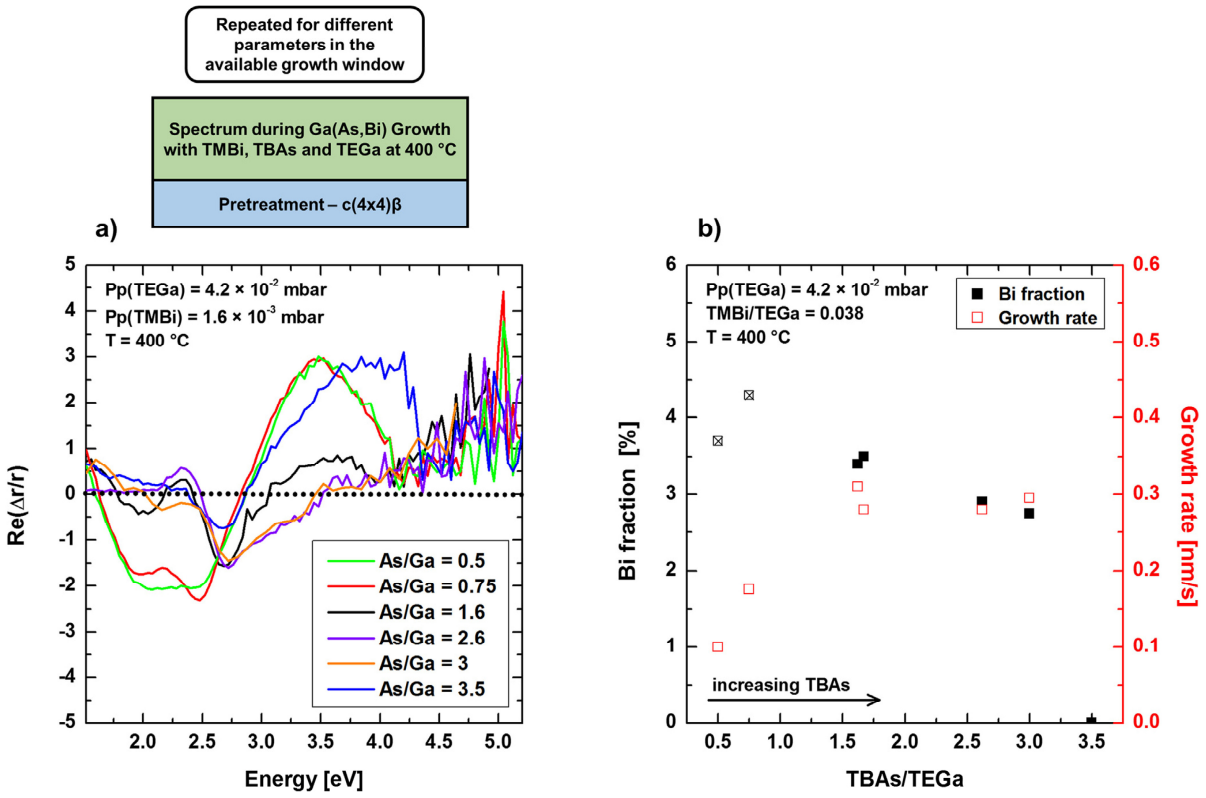

Fig. 6. a) RAS spectra during growth of Ga(As,Bi) layers on GaAs (001) surfaces with supplied partial pressures of 4.2×10^{-2} mbar TEGa, 1.6×10^{-3} mbar TMBi for varied TBAs partial pressures. b) Corresponding results for Bi incorporation and growth rate from XRD analysis. Crossed data points indicate droplet formation on the sample surface.

E_1, the related peak in the RAS spectra should be detected around 2.26 ± 0.05 eV. This shift of 0.3–0.4 eV fits very well to the observed RAS spectrum.

Like discussed for the Bi terminated surfaces, the RAS spectra of the growth surface also seems to be stable upon cooling to room temperature and changing the carrier gas to N_2 does not affect the surface reconstruction. However, the Fabry-Pérot oscillations overlap the RAS signal in dependence of the layer thickness grown. This makes it difficult to state if any change occurs between the surface reconstruction during growth to the one measured after the growth of the layer. The measured spectra after growth of the samples show that the double peak, mentioned above, could be caused by two individual features on the growth surface (S10).

Additionally, some more experiments have been done for Ga(As,Bi) grown at a higher temperature of 450 °C and for growth at 400 °C on a beforehand prepared (2 × 4) surface reconstruction. The samples grown at 450 °C also showed the RAS spectrum of the c(4 × 4)β surface reconstruction (S11). This shows that Ga(As,Bi) forms the same surface under the chosen conditions at higher temperatures. As expected the Bi incorporation decreased significantly from 4.3% for the sample grown at 400 °C to around 2.1% at 450 °C under the elsewise same growth parameters. To see if the surface reconstruction has an impact on the Bi incorporation one additional sample was grown on a (2 × 4) surface reconstruction. This surface is less As rich than the c(4 × 4)β and only barely reachable in MOVPE at this low temperature due to the As/Ga ratios used for growth. This leads to an As rich ambient within the reactor, that stabilizes the c(4 × 4) surfaces. Due to this the starting surface reconstruction was prepared by growing GaAs at 450 °C with an As/Ga ratio of 2.5 and cooling down to 400 °C during growth. While cooling the sample the RAS signal slightly changed, probably to a transition state between the c(4 × 4) and the (2 × 4) surface. After this, during growth of the Ga(As,Bi) layer on top with a As/Ga ratio of 2.5 the RAS signal showed the signal of a (2 × 4) surface reconstruction (S12).

This shows that the surface reconstruction of the starting surface, already determines the surface reconstruction during the growth of the material. The Bi concentration of this layer is determined with 2.6% and already showed formation of droplets on the surface (S13). The droplets are an indication that the growth is already in the regime of Bi saturation as observed in former studies [26,33,58]. The measured Bi incorporation is lower than the value determined for comparable layers grown on the c(4 × 4)β surface reconstruction, which are shown in Fig. 6. This shows that the surface reconstruction can influence the Bi incorporation and that the c(4 × 4)β surface reconstruction seems more beneficial for Bi incorporation than the (2 × 4) surface reconstruction under MOVPE conditions.

With the current understanding the Ga(As,Bi) material system seems to form a c(4 × 4)β surface reconstruction during growth of the material under the used growth conditions, but can also be grown on a (2 × 4) surface with the proper preparation. In comparison to the surface reconstructions observed in MBE environment our results agree quite well. During growth of the material various surface reconstruction with (1 × 3), (2 × 3), (2 × 4), (4 × 3) and (2 × 1) symmetry have been reported and predicted depending on the experimental conditions [31,47–50]. Starting from a (2 × 4) surface reconstruction the Ga(As,Bi) surface formed also a (2 × 4) symmetry during the growth of the actual layers in MBE. This is in good agreement with our findings for the sample grown on the prepared (2 × 4) surface reconstruction. For growth on the c(4 × 4) reconstruction, the formation of a (2 × 1) surface has been observed, which converts into a (4 × 3) surface via the

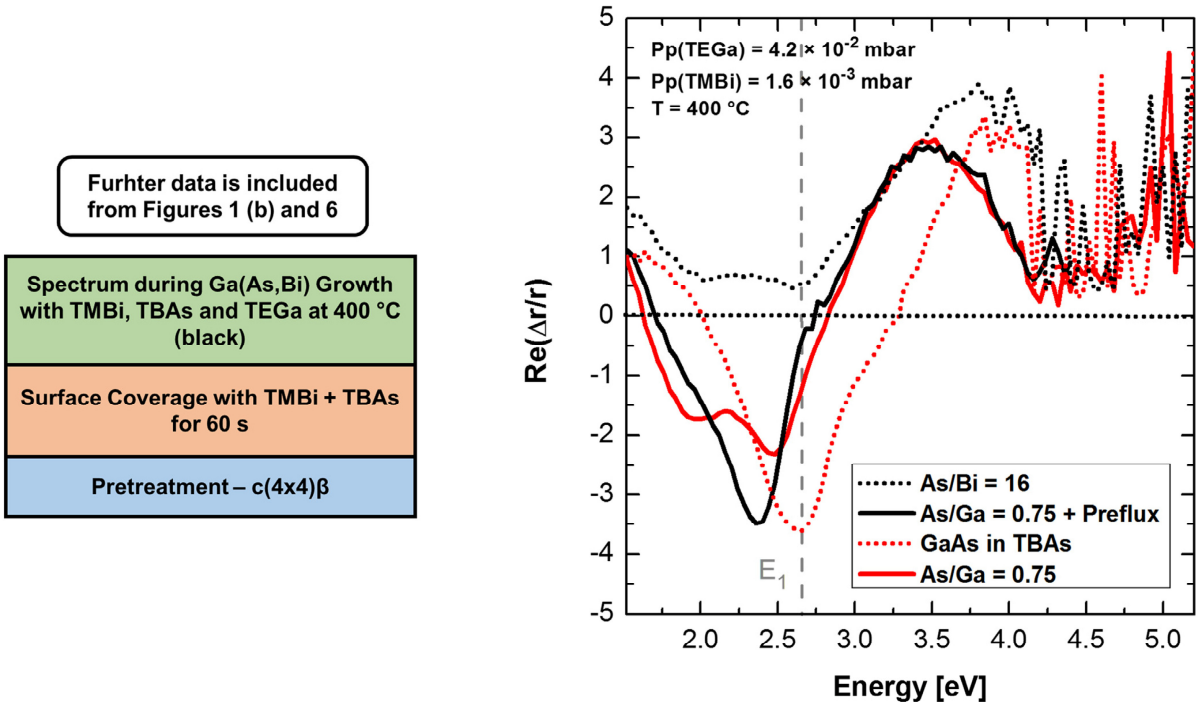

Fig. 7. RAS spectra during growth of Ga(As,Bi) layers on GaAs (001) surfaces with a As/Ga ratio of 0.75, with (black spectrum) and without (red spectrum) surface coverage prior to the growth. RAS spectra of the GaAs (001) surface under TBAs ambient (black dotted spectrum) and of the Bi terminated surface (red dotted spectrum) are added for comparison. (For interpretation of the references to colour in this figure legend, the reader is referred to the web version of this article.)

formation of a (1 × 3) surface reconstruction by loss of 1/3 ML of Bi [31]. Furthermore, calculations for MBE growth of Ga(As,Bi) on the c(4 × 4)α surface reconstruction show the formation of Bi-Bi dimer on this surface while keeping the overall symmetry of the surface reconstruction [47]. Both experiments could give an idea and "proof" for our findings, for the formation of a c(4 × 4)β reconstruction during Ga(As,Bi) growth, but additional experimental methods or calculations would be ideal to confirm our findings.

4. Summary and outlook

In this paper the influence of TMBi on the surface reconstruction of GaAs (001) surfaces has been investigated under MOVPE conditions by RAS. The first experiments were carried out on the c(4 × 4)β surface reconstruction. The supply of TMBi severely changes the surface reconstruction, which is most likely by adsorption of Bi. This is seen by a change in the RAS spectra at low photon energies, mainly influencing the negative anisotropy related to the As-As dimers of the surface. Therefore, the adsorbed Bi probably alters the As dimer configuration on the surface or forms dimers perpendicular to the As dimers. The surface reconstruction formed can also be created by continuous supply of TMBi together with TBAs, leading to a very similar RAS spectrum with slight deviations. This Bi terminated surface reconstruction is obtained under the same conditions that are used for the surface coverage prior to growth of Ga(As,Bi) to realize homogenous layers with high crystalline quality and can be used for process optimization and *in situ* control of the Bi surface coverage. Moreover, for reactors not equipped with a RAS measurement system, the process of a surface coverage can be monitored by measuring the reflection signal. The Bi terminated surface is further shown to be stable upon cooling and to a change of the carrier gas from H_2 to N_2. By heating of these surfaces the Bi could be completely desorbed again. Furthermore, under the continuous supply of TMBi and TBAs the Bi terminated surface can be stabilized up to a temperature of around 600 °C. This shows, how Bi can act on the surface reconstruction as a surfactant. By comparison to MBE a (1 × 3) or (4 × 3) surface reconstruction could be expected, however the RAS spectra for these reconstructions are unknown. This comparison should therefore be treated carefully.

In the second part the surface reconstructions during growth of Ga(As,Bi) layers are discussed. The RAS signal under optimized growth conditions, by using the Bi terminated surface as a surface coverage, can be identified with a c(4 × 4)β surface reconstruction. However, the RAS spectrum is shifted to lower energies compared to the RAS spectrum of the c(4 × 4)β surface reconstruction of GaAs, but correlates to the expected shift in relation to the band gap reduction of Bi in GaAs. Furthermore, Ga(As,Bi) has also been grown on a prepared (2 × 4) surface reconstruction. The grown layer showed under the same growth parameters the RAS signal of a (2 × 4) surface reconstruction, a Bi incorporation of 2.6% and formation of droplets compared to the sample grown on the c(4 × 4)β surface reconstruction with a Bi concentration of 3% without droplet formation. This leads to the assumption that the c(4 × 4)β surface reconstruction leads to higher Bi incorporation. The results fit very well to the current understanding of Ga(As,Bi) growth by MOVPE and the RAS measurements support and explain the developed growth model for this material system. Furthermore, the results fit well to the change and influence of Bi on the GaAs (001) surface reconstruction, which has been studied in MBE environment by electron based analysis, like STM, LEED, RHEED, etc.

CRediT authorship contribution statement

O. Maßmeyer: Conceptualization, Methodology, Validation, Formal analysis, Investigation, Writing - original draft, Visualization, Project administration, Supervision. **T. Hepp:** Conceptualization, Investigation, Writing - review & editing. **R. Günkel:** Writing - review & editing. **J. Glowatzki:** Writing - review & editing. **W. Stolz:** Resources,

Supervision. **K. Volz:** Conceptualization, Resources, Writing - review & editing, Supervision, Funding acquisition, Project administration.

Declaration of Competing Interest

The authors declare that they have no known competing financial interests or personal relationships that could have appeared to influence the work reported in this paper.

Acknowledgements

This work was supported by the German Research Foundation (GRK 1782: “Functionalization of Semiconductors” & SFB 1083 “Structure & Dynamics of Internal Interfaces”) and the support for the mass spectrometer (iTrap) was provided by the Carl Zeiss SMT GmbH.

Appendix A. Supplementary data

Supplementary data to this article can be found online at https://doi.org/10.1016/j.apsusc.2020.147401.

References

[1] P. Carrier, S.-H. Wei, Calculated spin-orbit splitting of all diamondlike and zinc-blende semiconductors: Effects of < math display = “inline” > < mrow > < msub > < mi > p < /mi > < mrow > < mn > 1 < /mn > < mo > / < /mo > < mn > 2 < /mn > < /mrow > < /msub > < /mrow > < /math > local orbitals and chemical trends, Phys. Rev. B. 70 (2004) 035212, , https://doi.org/10.1103/PhysRevB.70.035212.

[2] K. Oe, H. Okamoto, New semiconductor alloy GaAs 1-xBi x grown by metal organic vapor phase epitaxy, Japanese J. Appl. Phys., Part 2 Lett. 37 (1998) 1–4, https://doi.org/10.1143/jjap.37.l1283.

[3] N. Hossain, I.P. Marko, S.R. Jin, K. Hild, S.J. Sweeney, R.B. Lewis, D.A. Beaton, T. Tiedje, Recombination mechanisms and band alignment of GaAs 1-xBi x/GaAs light emitting diodes, Appl. Phys. Lett. 100 (2012) 2012–2015, https://doi.org/10.1063/1.3681139.

[4] R.N. Kini, L. Bhusal, A.J. Ptak, R. France, A. Mascarenhas, Electron hall mobility in GaAsBi, J. Appl. Phys. 106 (2009), https://doi.org/10.1063/1.3204670.

[5] D.A. Beaton, R.B. Lewis, M. Masnadi-Shirazi, T. Tiedje, Temperature dependence of hole mobility in GaAs1-xBix alloys, J. Appl. Phys. 108 (2010), https://doi.org/10.1063/1.3493734.

[6] M.R. Pillai, S.S. Kim, S.T. Ho, S.A. Barnett, Growth of InxGa1-xAs/GaAs heterostructures using Bi as a surfactant, J. Vac. Sci. Technol. B Microelectron. Nanom. Struct. 18 (2000) 1232–1236, https://doi.org/10.1116/1.591367.

[7] S.J. Sweeney, S.R. Jin, Bismide-nitride alloys: Promising for efficient light emitting devices in the near- and mid-infrared, J. Appl. Phys. 113 (2013), https://doi.org/10.1063/1.4789624.

[8] P. Ludewig, N. Knaub, N. Hossain, S. Reinhard, L. Nattermann, I.P. Marko, S.R. Jin, K. Hild, S. Chatterjee, W. Stolz, S.J. Sweeney, K. Volz, Electrical injection Ga(AsBi)/(AlGa)As single quantum well laser, Appl. Phys. Lett. 102 (2013) 20–23, https://doi.org/10.1063/1.4811736.

[9] J. Yoshida, T. Kita, O. Wada, K. Oe, Temperature dependence of GaAs1-xBix band gap studied by photoreflectance spectroscopy, Japanese J. Appl. Phys., Part 1 Regul. Pap. Short Notes Rev. Pap. 42 (2003) 371–374, https://doi.org/10.1143/jjap.42.371.

[10] L. Wang, L. Zhang, L. Yue, D. Liang, X. Chen, Y. Li, P. Lu, J. Shao, S. Wang, Novel dilute bismide, epitaxy, physical properties and device application, Crystals. 7 (2017), https://doi.org/10.3390/cryst7030063.

[11] S. Francoeur, M.J. Seong, A. Mascarenhas, S. Tixier, M. Adamcyk, T. Tiedje, Band gap of GaAs1-xBix, 0 < x < 3.6%, Appl. Phys. Lett. 82 (2003) 3874–3876, https://doi.org/10.1063/1.1581983.

[12] S. Tixier, M. Adamcyk, T. Tiedje, S. Francoeur, A. Mascarenhas, P. Wei, F. Schiettekatte, Molecular beam epitaxy growth of GaAs1-xBix, Appl. Phys. Lett. 82 (2003) 2245–2247, https://doi.org/10.1063/1.1565499.

[13] H. Li, Z.M. Wang, Bismuth-Containing Compounds vol. 186, Springer, New York, NY, 2013.

[14] K. Alberi, O.D. Dubon, W. Walukiewicz, K.M. Yu, K. Bertulis, A. Krotkus, Valence band anticrossing in GaBi xAs 1–x, Appl. Phys. Lett. 91 (2007) 1–4, https://doi.org/10.1063/1.2768312.

[15] B. Fluegel, S. Francoeur, A. Mascarenhas, S. Tixier, E.C. Young, T. Tiedje, Giant spin-orbit bowing in GaAs1-xBix, Phys. Rev. Lett. 97 (2006) 11–14, https://doi.org/10.1103/PhysRevLett.97.067205.

[16] Z. Batool, K. Hild, T.J.C. Hosea, X. Lu, T. Tiedje, S.J. Sweeney, The electronic band structure of GaBiAs/GaAs layers: influence of strain and band anti-crossing, J. Appl. Phys. 111 (2012), https://doi.org/10.1063/1.4728028.

[17] M. Usman, C.A. Broderick, A. Lindsay, E.P. O’Reilly, Tight-binding analysis of the electronic structure of dilute bismide alloys of GaP and GaAs, Phys. Rev. B - Condens. Matter Mater. Phys. 84 (2011) 1–13, https://doi.org/10.1103/PhysRevB.84.245202.

[18] C.A. Broderick, M. Usman, E.P. O’Reilly, Derivation of 12- and 14-band k · p Hamiltonians for dilute bismide and bismide-nitride semiconductors, Semicond. Sci. Technol. 28 (2013), https://doi.org/10.1088/0268-1242/28/12/125025.

[19] C.A. Broderick, M. Usman, S.J. Sweeney, E.P. O’Reilly, Band engineering in dilute nitride and bismide semiconductor lasers, Semicond. Sci. Technol. 27 (2012), https://doi.org/10.1088/0268-1242/27/9/094011.

[20] S.J. Sweeney, A.F. Phillips, A.R. Adams, E.P. O’Reilly, P.J.A. Thijs, The effect of temperature dependent processes on the performance of 1.5-μm compressively strained InGaAs(P) MQW semiconductor diode lasers, IEEE Photonics Technol. Lett. 10 (1998) 1076–1078, https://doi.org/10.1109/68.701507.

[21] T. Higashi, S.J. Sweeney, A.F. Phillips, A.R. Adams, E.P. O’Reilly, T. Uchida, T. Fujii, Experimental analysis of temperature dependence in 1.3-μm AlGaInAs-InP strained MQW lasers, IEEE J. Sel. Top. Quantum Electron. 5 (1999) 413–419, https://doi.org/10.1109/2944.788399.

[22] M. Silver, E.P. O’Reilly, A.R. Adams, Determination of the wavelength dependence of auger recombination in long-wavelength quantum-well semiconductor lasers using hydrostatic pressure, IEEE J. Quantum Electron. 33 (1997) 1557–1566, https://doi.org/10.1109/3.622637.

[23] H. Jacobsen, B. Puchala, T.F. Kuech, D. Morgan, Ab initio study of the strain dependent thermodynamics of Bi doping in GaAs, Phys. Rev. B - Condens. Matter Mater. Phys. 86 (2012) 1–10, https://doi.org/10.1103/PhysRevB.86.085207.

[24] H. Fitouri, I. Moussa, A. Rebey, A. Fouzri, B. El Jani, AP-MOVPE of thin GaAs1-xBix alloys, J. Cryst. Growth. 295 (2006) 114–118, https://doi.org/10.1016/j.jcrysgro.2006.06.052.

[25] A.G. Norman, R. France, A.J. Ptak, Atomic ordering and phase separation in MBE GaAs1−xBix, J. Vac. Sci. Technol. B, Nanotechnol. Microelectron. Mater. Process. Meas. Phenom. 29 (2011) 03C121, https://doi.org/10.1116/1.3562512.

[26] E. Sterzer, N. Knaub, P. Ludewig, R. Straubinger, A. Beyer, K. Volz, Investigation of the microstructure of metallic droplets on Ga(AsBi)/GaAs, J. Cryst. Growth 408 (2014) 71–77, https://doi.org/10.1016/j.jcrysgro.2014.09.006.

[27] R.M. Feenstra, J.M. Woodall, G.D. Pettit, Observation of bulk defects by scanning tunneling microscopy and spectroscopy: arsenic antisite defects in GaAs, Phys. Rev. Lett. 71 (1993) 1176–1179, https://doi.org/10.1103/PhysRevLett.71.1176.

[28] M. Yoshimoto, S. Murata, A. Chayahara, Y. Horino, J. Saraie, K. Oe, Metastable GaAsBi Alloy Grown by Molecular Beam Epitaxy, Japanese J. Appl. Physics, Part 2 Lett. 42 (2003), https://doi.org/10.1143/jjap.42.l1235.

[29] X. Lu, D.A. Beaton, R.B. Lewis, T. Tiedje, M.B. Whitwick, Effect of molecular beam epitaxy growth conditions on the Bi content of GaAs1-x Bix, Appl. Phys. Lett. 92 (2008) 1–4, https://doi.org/10.1063/1.2918844.

[30] Y. Tominaga, Y. Kinoshita, K. Oe, M. Yoshimoto, Structural investigation of GaAs1-xBix/GaAs multiquantum wells, Appl. Phys. Lett. 93 (2008) 3–6, https://doi.org/10.1063/1.2993343.

[31] F. Bastiman, A.G. Cullis, J.P.R. David, S.J. Sweeney, Bi incorporation in GaAs(100)-2×1 and 4×3 reconstructions investigated by RHEED and STM, J. Cryst. Growth. 341 (2012) 19–23, https://doi.org/10.1016/j.jcrysgro.2011.12.058.

[32] A.J. Ptak, R. France, D.A. Beaton, K. Alberi, J. Simon, A. Mascarenhas, C.S. Jiang, Kinetically limited growth of GaAsBi by molecular-beam epitaxy, J. Cryst. Growth. 338 (2012) 107–110, https://doi.org/10.1016/j.jcrysgro.2011.10.040.

[33] P. Ludewig, L. Nattermann, W. Stolz, K. Volz, MOVPE growth mechanisms of dilute bismide III/V alloys, Semicond. Sci. Technol. 30 (2015) 94017, https://doi.org/10.1088/0268-1242/30/9/094017.

[34] K. Oe, Characteristics of semiconductor alloy GaAs1-xBix, Japanese J. Appl. Phys., Part 1 Regul. Pap. Short Notes Rev. Pap. 41 (2002) 2801–2806, https://doi.org/10.1143/jjap.41.2801.

[35] K. Oe, Metalorganic vapor phase epitaxial growth of metastable GaAs1-xBix alloy, J. Cryst. Growth. 237–239 (2002) 1481–1485, https://doi.org/10.1016/S0022-0248(01)02301-6.

[36] I. Moussa, H. Fitouri, A. Rebey, B. El Jani, Atmospheric-pressure metalorganic vapour phase epitaxy optimization of GaAsBi alloy, Thin Solid Films 516 (2008) 8372–8376, https://doi.org/10.1016/j.tsf.2008.04.062.

[37] K. Forghani, A. Anand, L.J. Mawst, T.F. Kuech, Low temperature growth of GaAs1-yBiy epitaxial layers, J. Cryst. Growth 380 (2013) 23–27, https://doi.org/10.1016/j.jcrysgro.2013.05.033.

[38] P. Ludewig, Z.L. Bushell, L. Nattermann, N. Knaub, W. Stolz, K. Volz, Growth of Ga(AsBi) on GaAs by continuous flow MOVPE, J. Cryst. Growth 396 (2014) 95–99, https://doi.org/10.1016/j.jcrysgro.2014.03.041.

[39] P. Ludewig, N. Knaub, W. Stolz, K. Volz, MOVPE growth of Ga(AsBi)/GaAs multi quantum well structures, J. Cryst. Growth 370 (2013) 186–190, https://doi.org/10.1016/j.jcrysgro.2012.07.002.

[40] W.Y. Jiang, J.Q. Liu, M.G. So, K. Myrtle, K.L. Kavanagh, S.P. Watkins, Surface modifications induced by bismuth on (0 0 1) GaAs surfaces, J. Cryst. Growth 277 (2005) 85–90, https://doi.org/10.1016/j.jcrysgro.2005.01.060.

[41] M. Ahola-Tuomi, P. Laukkanen, M.P.J. Punkkinen, R.E. Perälä, I.J. Väyrynen, M. Kuzmin, K. Schulte, M. Pessa, Formation of an ordered pattern of Bi nanolines on InAs(100) by self-assembly, Appl. Phys. Lett. 92 (2008) 2–5, https://doi.org/10.1063/1.2831691.

[42] P. Laukkanen, M. Ahola-Tuomi, M. Kuzmin, R.E. Perälä, I.J. Väyrynen, A. Tukiainen, J. Pakarinen, M. Saarinen, M. Pessa, Structural properties of Bi-stabilized reconstructions of GaInAs(100) surface, Appl. Phys. Lett. 90 (2007), https://doi.org/10.1063/1.2560954.

[43] P. Laukkanen, J. Pakarinen, M. Ahola-Tuomi, M. Kuzmin, R.E. Perälä, I.J. Väyrynen, A. Tukiainen, J. Konttinen, P. Tuomisto, M. Pessa, Structural and electronic properties of Bi-adsorbate-stabilized reconstructions on the InP(100) and Ga Asx N1–x (100) surfaces, Phys. Rev. B - Condens. Matter Mater. Phys. 74 (2006) 1–6, https://doi.org/10.1103/PhysRevB.74.155302.

[44] P. Laukkanen, M.P.J. Punkkinen, H.P. Komsa, M. Ahola-Tuomi, K. Kokko, M. Kuzmin, J. Adell, J. Sadowski, R.E. Perälä, M. Ropo, T.T. Rantala, I.J. Väyrynen, M. Pessa, L. Vitos, J. Kollár, S. Mirbt, B. Johansson, Anomalous bismuth-stabilized (2×1) reconstructions on GaAs(100) and InP(100) surfaces, Phys. Rev. Lett. 100 (2008) 1–4, https://doi.org/10.1103/PhysRevLett.100.086101.

[45] S. Tixier, M. Adamcyk, E.C. Young, J.H. Schmid, T. Tiedje, Surfactant enhanced growth of GaNAs and InGaNAs using bismuth, J. Cryst. Growth. 251 (2003) 449–454, https://doi.org/10.1016/S0022-0248(02)02217-0.

[46] E.C. Young, S. Tixier, T. Tiedje, Bismuth surfactant growth of the dilute nitride GaNxAs 1–x, J. Cryst. Growth. 279 (2005) 316–320, https://doi.org/10.1016/j.jcrysgro.2005.02.045.

[47] I. Murasen, T. Akiyama, K. Nakamura, T. Ito, Ab initio-based approach to initial incorporation of Bi on |GaAs(001)-c(4 × 4)α surface, J. Cryst. Growth 378 (2013) 21–24, https://doi.org/10.1016/j.jcrysgro.2012.12.047.

[48] M.P.J. Punkkinen, P. Laukkanen, H.P. Komsa, M. Ahola-Tuomi, N. Räsänen, K. Kokko, M. Kuzmin, J. Adell, J. Sadowski, R.E. Perälä, M. Ropo, T.T. Rantala, I.J. Väyrynen, M. Pessa, L. Vitos, J. Kollár, S. Mirbt, B. Johansson, Bismuth-stabilized (2×1) and (2×4) reconstructions on GaAs(100) surfaces: Combined first-principles, photoemission, and scanning tunneling microscopy study, Phys. Rev. B - Condens. Matter Mater. Phys. 78 (2008) 1–10, https://doi.org/10.1103/PhysRevB.78.195304.

[49] A. Duzik, J.C. Thomas, J.M. Millunchick, J. Lång, M.P.J. Punkkinen, P. Laukkanen, Surface structure of bismuth terminated GaAs surfaces grown with molecular beam epitaxy, Surf. Sci. 606 (2012) 1203–1207, https://doi.org/10.1016/j.susc.2012.03.021.

[50] A. Duzik, J.C. Thomas, A. Van Der Ven, J.M. Millunchick, Surface reconstruction stability and configurational disorder on Bi-terminated GaAs(001), Phys. Rev. B - Condens. Matter Mater. Phys. 87 (2013) 1–9, https://doi.org/10.1103/PhysRevB.87.035313.

[51] M. Masnadi-Shirazi, D.A. Beaton, R.B. Lewis, X. Lu, T. Tiedje, Surface reconstructions during growth of GaAs 1-xBi x alloys by molecular beam epitaxy, J. Cryst. Growth. 338 (2012) 80–84, https://doi.org/10.1016/j.jcrysgro.2011.09.055.

[52] M. Ahola-Tuomi, M.P.J. Punkkinen, P. Laukkanen, M. Kuzmin, J. Lång, K. Schulte, A. Pietzsch, R.E. Perälä, N. Räsänen, I.J. Väyrynen, Properties of self-assembled Bi nanolines on InAs(100) studied by core-level and valence-band photoemission, and first-principles calculations, Phys. Rev. B - Condens. Matter Mater. Phys. 83 (2011) 1–8, https://doi.org/10.1103/PhysRevB.83.245401.

[53] S. Horng, Epitaxial growth of Bi on GaAs(100) surfaces, J. Vac. Sci. Technol. B Microelectron. Nanom. Struct. 7 (1989) 931, https://doi.org/10.1116/1.584583.

[54] O. Maßmeyer, E. Sterzer, L. Nattermann, W. Stolz, K. Volz, Influence of UDMHy on GaAs (0 0 1) surface reconstruction before and during growth of Ga(NAs) by MOVPE, Appl. Surf. Sci. 458 (2018) 512–516, https://doi.org/10.1016/j.apsusc.2018.07.098.

[55] H.Y. Chung, M. Aliman, G. Fedosenko, A. Laue, R. Reuter, V. Derpmann, L. Gorkhover, M. Antoni, Very sensitive real-time inline process mass spectrometer based on FFT Ion Trap technique, in: 2016 27th Annu. SEMI Adv. Semicond. Manuf. Conf., IEEE, 2016: pp. 263–266. https://doi.org/10.1109/ASMC.2016.7491140.

[56] O. Maßmeyer, S. Inacker, T. Hepp, J. Glowatzki, L. Nattermann, E. Sterzer, C. Ritter, C. Von Hänisch, W. Stolz, K. Volz, Decomposition mechanisms of Di-tert-butylaminoarsane (DTBAA), Organometallics 38 (2019) 3181–3186, https://doi.org/10.1021/acs.organomet.9b00442.

[57] L. Nattermann, O. Maßmeyer, E. Sterzer, V. Derpmann, H.Y. Chung, W. Stolz, K. Volz, An experimental approach for real time mass spectrometric CVD gas phase investigations, Sci. Rep. 8 (2018) 319, https://doi.org/10.1038/s41598-017-18662-7.

[58] T. Hepp, L. Nattermann, K. Volz, MOVPE Growth and Device Applications of Ternary and Quaternary Dilute Bismide Alloys on GaAs Substrates., in: S. Wang, P. Lu (Eds.), Wang S., Lu P. Bismuth-Containing Alloy. Nanostructures, 1st ed., Springer, Singapore, 2019: pp. 37–58. https://doi.org/10.1007/978-981-13-8078-5_3.

[59] A. Ohtake, Surface reconstructions on GaAs(001), Surf. Sci. Rep. 63 (2008) 295–327, https://doi.org/10.1016/j.surfrep.2008.03.001.

[60] W. Richter, In-situ observation of MOVPE epitaxial growth, Appl. Phys. A Mater. Sci. Process. 75 (2002) 129–140, https://doi.org/10.1007/s003390101061.

[61] D.E. Aspnes, New developments in spectroellipsometry: the challenge of surfaces, Thin Solid Films 233 (1993) 1–8, https://doi.org/10.1016/0040-6090(93)90050-Y.

[62] O. Supplie, S. Brückner, O. Romanyuk, H. Döscher, C. Höhn, M.M. May, P. Kleinschmidt, F. Grosse, T. Hannappel, Atomic scale analysis of the GaP/Si(100) heterointerface by in situ reflection anisotropy spectroscopy and ab initio density functional theory, Phys. Rev. B - Condens. Matter Mater. Phys. 90 (2014) 1–7, https://doi.org/10.1103/PhysRevB.90.235301.

[63] D.E. Aspnes, S.M. Kelso, R.A. Logan, R. Bhat, Optical properties of AlxGa1 − x As, J. Appl. Phys. 60 (1986), https://doi.org/10.1063/1.337426.

[64] H.J. Hagemann, W. Gudat, C. Kunz, Optical constants from the far infrared to the X-RAY REGION: Mg, Al, Cu, Ag, Au, Bi, C, and Al2O3, J. Opt. Soc. Am. 65 (1975) 742–744, https://doi.org/10.1364/JOSA.65.000742.

[65] P. Lautenschlager, M. Garriga, S. Logothetidis, M. Cardona, Interband critical points of CsaAs and their temperature dependence, Phys. Rev. B. 35 (1987) 9174–9189 https://doi.org/10.1103/PhysRevB.35.9174.

[66] C.A. Larsen, N.I. Buchan, S.H. Li, G.B. Stringfellow, Decomposition mechanisms of tertiarybutylarsine, J. Cryst. Growth. 94 (1989) 663–672, https://doi.org/10.1016/0022-0248(89)90090-0.

[67] S.J.W. Price, A.F. Trotman-Dickenson, Metal-carbon bonds, Trans. Faraday Soc. 54 (1958) 1630–1637 https://doi.org/10.1039/TF9585401630.

[68] C. Hogan, R. Magri, R. Del Sole, Role of surface structural motifs on the stability and reflectance anisotropy spectra of Sb-rich GaSb(001) reconstructions, Phys. Rev. B - Condens. Matter Mater. Phys. 83 (2011) 1–15, https://doi.org/10.1103/PhysRevB.83.155421.

Supporting information

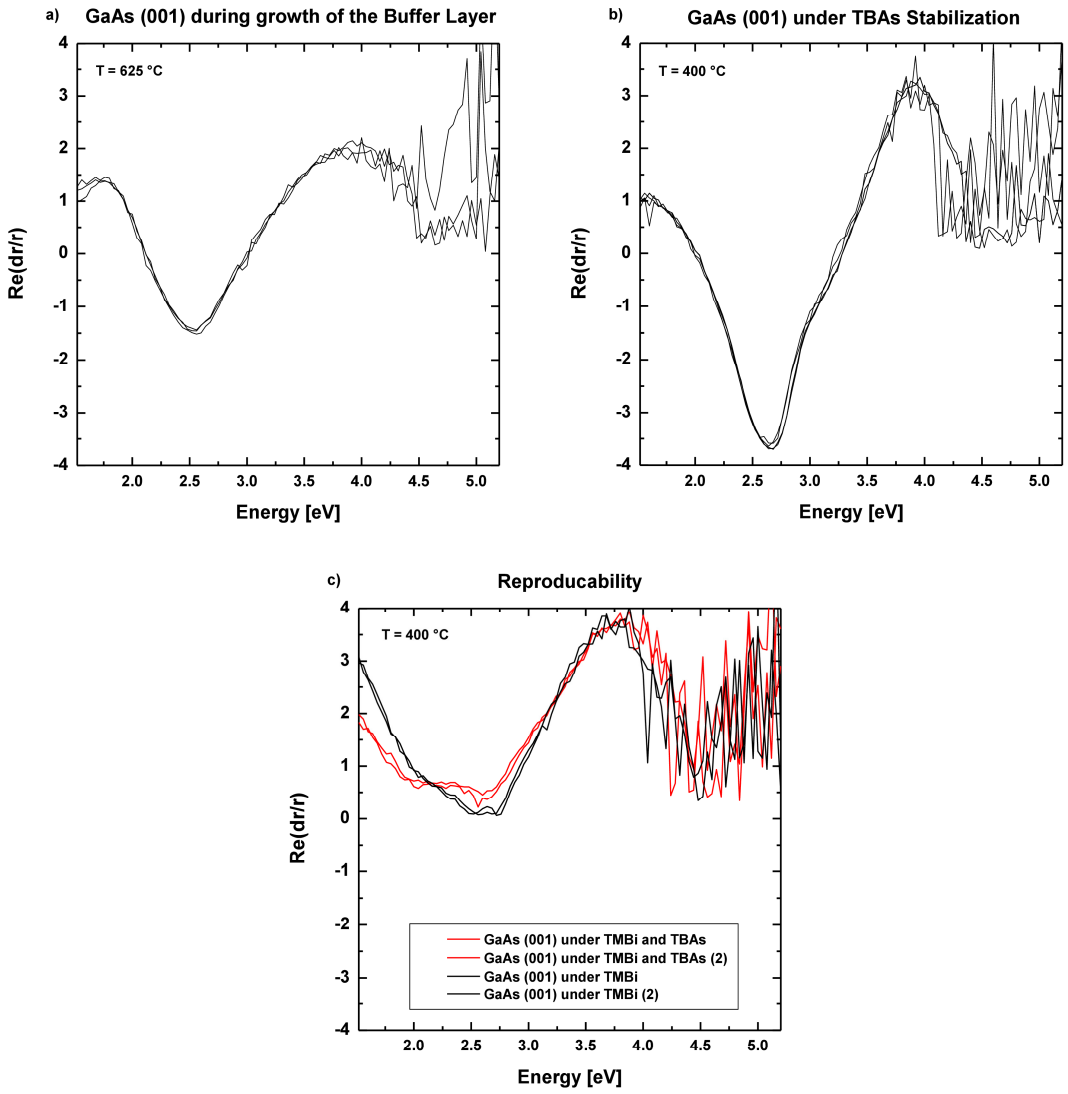

Supporting information 0: RA spectra obtained in different experimental sessions, showing the reproducibility to allow an estimation of the experimental error. Shown are spectra obtained during growth of the GaAs buffer at 625 °C (a), under TBAs stabilization at 400 °C (b) and for the GaAs (001) surface under TMBi and TBAs and under TMBi only (c).

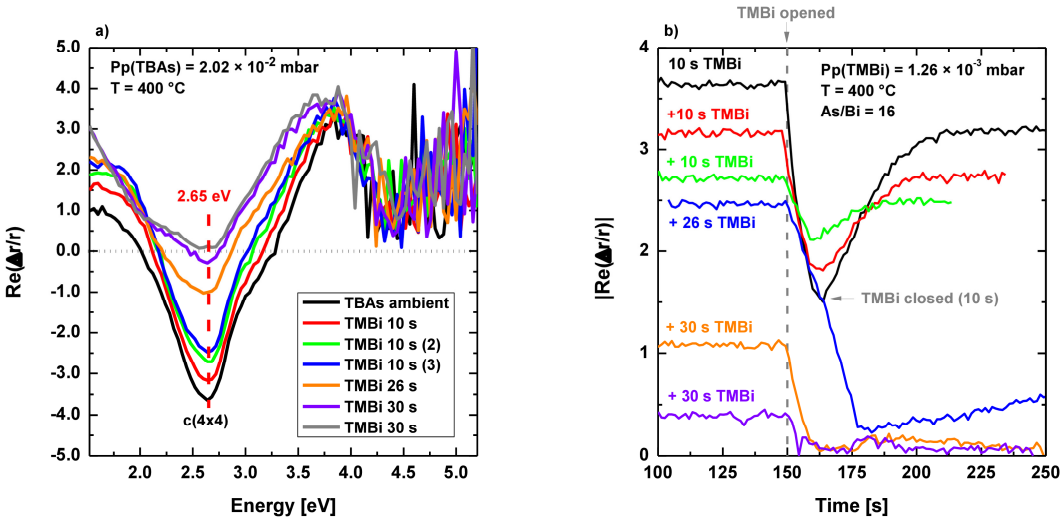

Supporting information 1: a) Plot of all RAS spectra from figure 1 in color coded fashion. b) Corresponding RAS transients during the pulse experiment at a photon energy of 2.65 eV. Duration of the individual TMBi pulses are given within the figure. For each pulse a change in the RAS signal is observed as soon as TMBi is supplied (drop in RAS intensity). After the pulse the RAS signal recovers, but does not reach the original value. At this stable RAS signal the RAS spectra were recorded. The color indicates the initial RAS signal after the complete RAS spectrum from a) was measured.

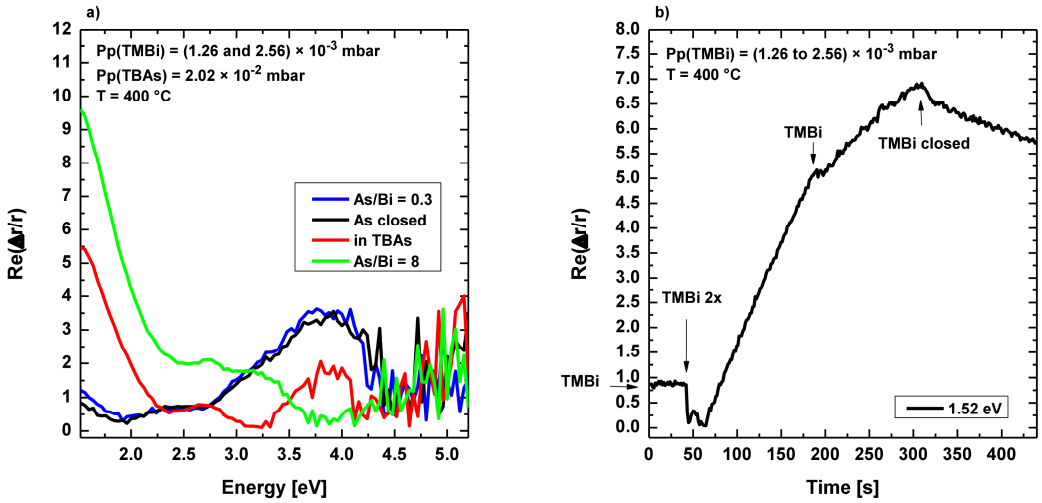

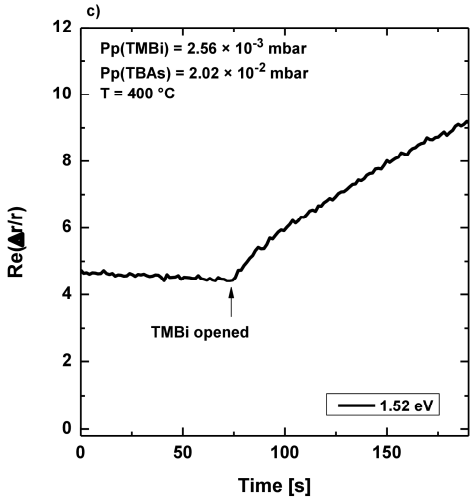

Supporting information 2: All partial pressures are given within the figures. a) RAS spectra during the supply of TMBi and TBAs for an estimated time of 30 min. Starting from the Bi terminated surface reconstruction (blue spectrum), the TBAs supply was switched off. Under the supply of only TMBi the RAS spectrum did not change significantly (black spectrum). Starting from this the evolution of the RAS signal can be seen in the transient measurement b) at 1.52 eV. Right as the TMBi supply is doubled, the RAS signal changes continuously. The change is attributed to additional Bi adsorbing onto the surface. This leads to droplet formation on the surface, which was visible under the light microscope. Additionally, the slope of the increasing RAS signal is halved, right as the TMBi supply is halved. The increase is stopped, right as the TMBi supply is stopped and following a decrease in the RAS signal is observed. In the RAS spectrum measured afterwards, the previous features in the signal are still visible, but the intensities are varied (red spectrum). c) Shows the further change of the RAS signal after the red spectrum was detected. The RAS signal rises again, if additional TMBi is supplied to the surface. The green spectrum was measured after the 2nd transient under TMBi and TBAs supply. A further modulation of the RAS signal is observed. All these findings indicate that Bi can accumulate on the GaAs (001) surface leading to droplet formation for extensive TMBi supply. Additionally, the RAS signal changes if no TMBi is supplied. This indicates that Bi can at least partly desorb from the surface at this comparably low temperature of 400 °C. However, the process is expected to be very slow compared to the growth rates used in MOVPE.

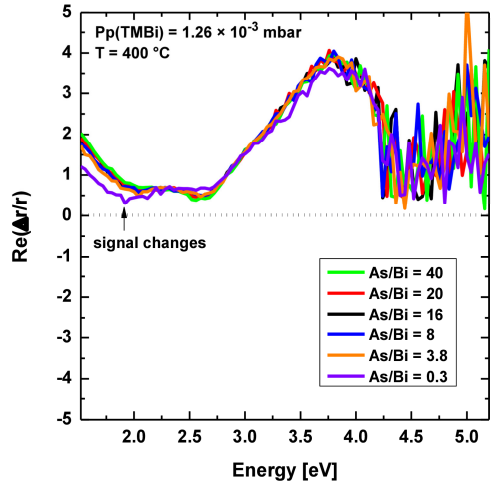

Supporting information 3: RAS spectra of the Bi terminated surface under a constant partial pressure of 1.26 × 10-3 mbar TMBi and varied TBAs supply at 400 °C. At a reduced As/Bi of 0.3 the RAS spectrum starts to change. This is attributed to the Bi accumulating on the surface over time. This can occur since the Bi desorption

rate at this temperature is expected to be low compared to the additional TMBi supply which is offered to the surface. As seen in (S2) the RAS signal changes rapidly if TMBi is supplied alone to the surface. In this case the ratio of As/Bi < 1 might lead to a similar effect, however the total supply time of TMBi is roughly 30 min for this experiment, which could cause the change in the RAS signal due to accumulation of Bi on the surface.

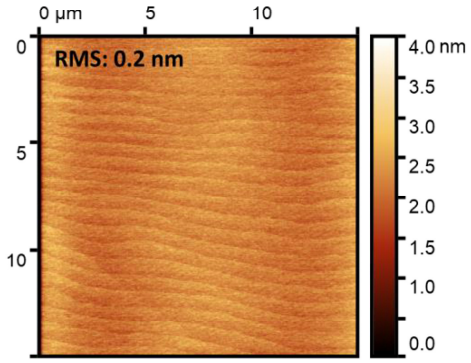

Supporting information 4: AFM image of the GaAs (001) surface after the TMBi desorption experiments. The image shows a very smooth surface with an RMS value of 0.2 nm and steps like expected for a well prepared GaAs surface. No evidence of droplet formation is seen.

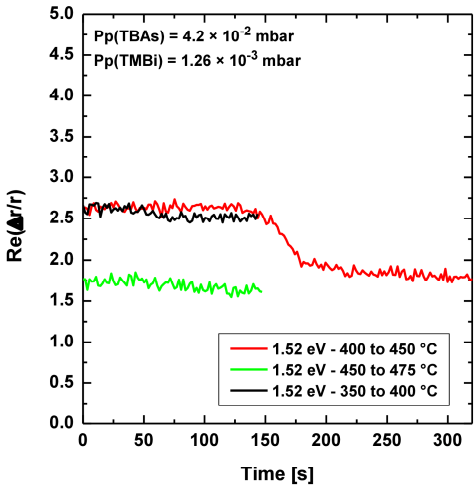

Supporting information 5: All partial pressures are given within the figure. Exemplary proof of the stability of the RAS signal throughout the temperature dependent measurement under TMBi and TBAs supply. The shown RAS transients at 1.52 eV are detected during heating between the shown spectra in the publication. As mentioned the RAS signal is constant after the last RAS spectrum was measured and before the next one is started. Due to the temperature increase the RAS signal changes in the middle of the RAS transients, respectively.

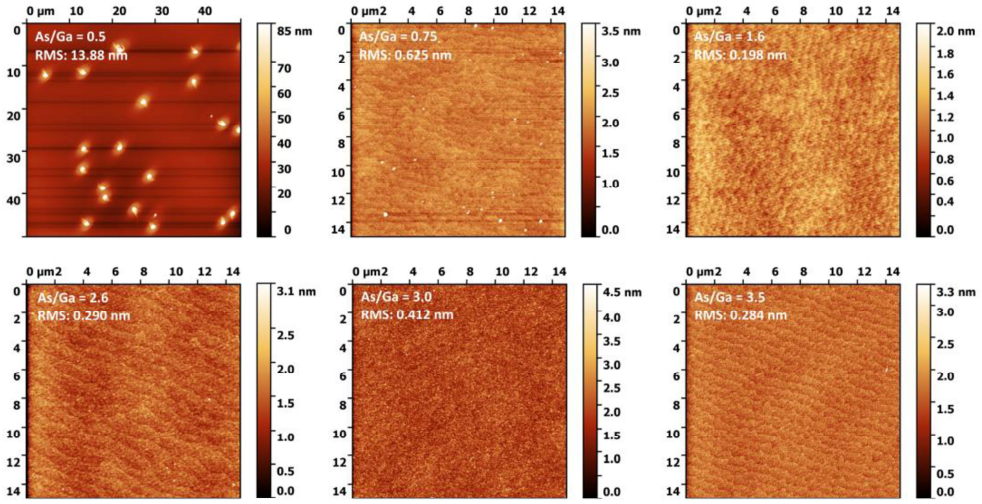

Supporting information 6: The corresponding growth parameters are given within the publication. AFM measurements of all Ga(As,Bi) bulk layers shown. For an As/Ga ratio of 0.5 formation of large droplets is seen. These "volcano like" structures have been also observed before [1]. By increasing the As/Ga ratio droplet formation can be avoided. Also the surface for the sample with an As/Ga ratio of 3.5 shows a smooth surface even though no Bi incorporation was observed. At an As/Ga ratio of 3 a higher RMS value is observed. The rougher surface is probably caused due to growth at the edge of the growth window. Even small fluctuations in the gas phase ratio can lead to a fluctuation in Bi incorporation, which can influence the step flow growth.

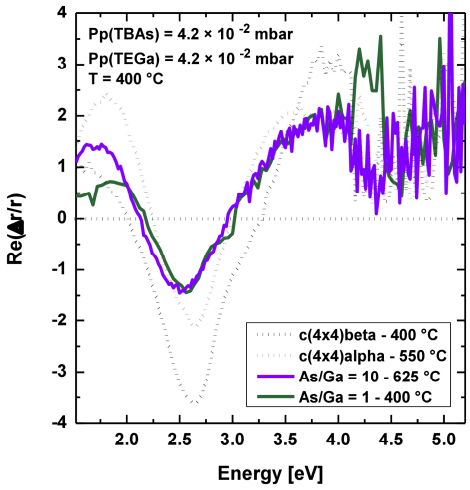

Supporting information 7: The partial pressures for the samples during growth at 400 °C and for an As/Ga of 1 are given within the figure. RAS spectra of the GaAs (001) surface at different temperatures during growth (continuous spectra) and after growth (dotted spectra) are shown. During growth the c(4×4)α surface reconstruction is observed for optimized growth conditions at 625 °C with an As/Ga ratio of 10. At 400 °C an As/Ga ratio of 1 is necessary to observe the c(4×4)α surface reconstruction. At 400 °C small deviations at low photon energies (1.52 to 2 eV) and a new feature at 4.3 eV is observed. As comparison the RAS signal of the c(4×4)α and c(4×4)β surface reconstruction are shown which can be reached at different temperatures, but also depending on the TBAs supply in the reactor.

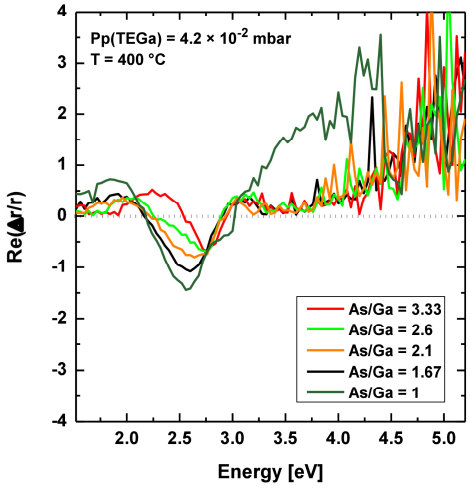

Supporting information 8: Further RAS spectra during growth of GaAs at 400 °C for different As/Ga ratios. As seen in S7 the GaAs (001) surface forms a c(4×4)α surface reconstruction at an As/Ga ratio of 1. For higher ratios a strong modulation of the RAS spectra is seen. The corresponding change in the surface reconstruction is so far unknown. An idea would be that the alkyl groups of the precursors used can stick to the surface at this low temperatures leading to a modulation of the RAS signal or that the surface converts to an even more As rich surface reconstruction, since excess As is supplied. The additionally supplied As should stick to the surface since the desorption of As at 400 °C is expected to be low.

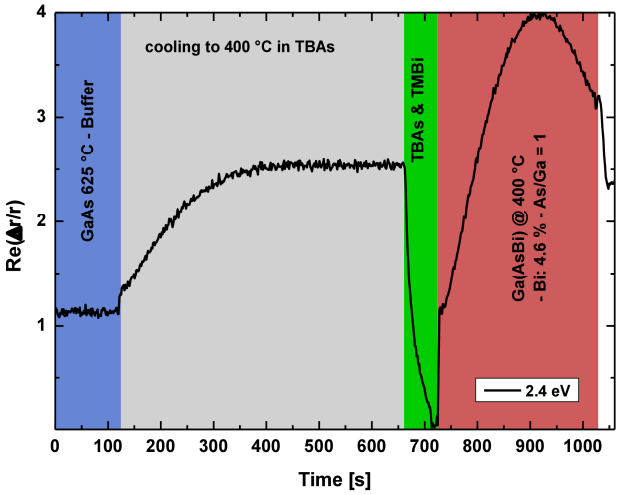

Supporting information 9: RAS transient measured at 2.4 eV during the growth procedure of an Ga(As,Bi) sample. At 625 °C the end of the buffer growth is depicted which can be correlated to the c(4×4)α surface reconstruction. After this the TEGa supply is stopped leading to a jump in the RAS signal. This is correlated to the conversion of the c(4×4)α to the c(4×4)β surface reconstruction. In the next step the RAS intensity rises due to the cooling to 400 °C under TBAs supply until a constant temperature is reached. In the next step the surface coverage with TMBi and TBAs is supplied for 60 s. This leads to the formation of the Bi terminated surface, as discussed in the paper. After this the growth of the Ga(As,Bi) layer is started by adding TEGa. A sudden increase of the RAS signal is observed, right as the growth starts. Afterwards, the RAS signal is additionally modulated by a Fabry-Pérot oscillation. This behavior was observed at various photon energies for different samples.

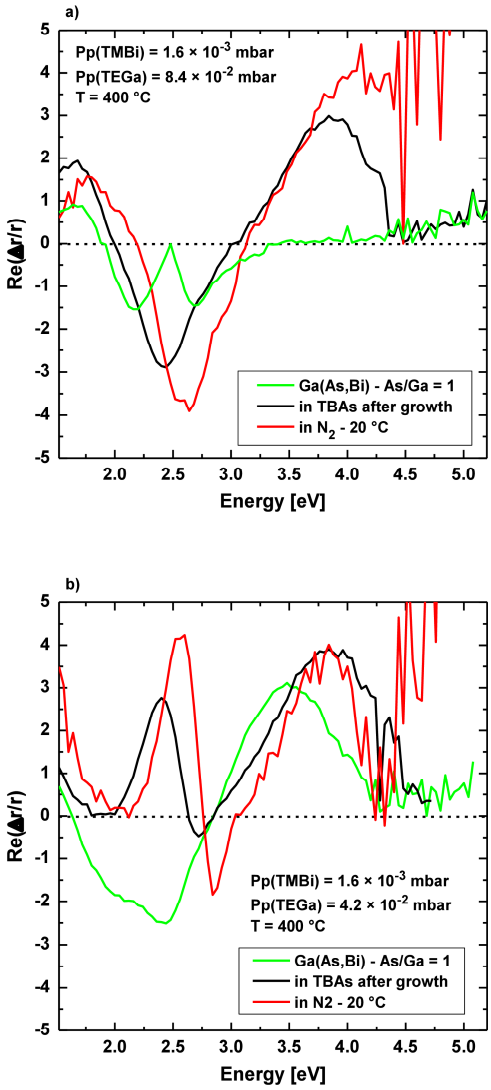

Supporting information 10: All partial pressures are given within the figure. RAS spectra during growth of Ga(As,Bi) layers, after growth in TBAs and after cooling to room temperature with an exchange of the carrier gas to N_2. A surface coverage with TBAs and TMBi of 60 s was applied prior to the Ga(As,Bi) growth. a) Sample with 2.9 % Bi incorporation as an example of a Ga(As,Bi) surface showing the double peak feature at an As/Ga ratio of 1 (green spectrum). After growth under TBAs stabilization the double peak feature is no longer observed (black spectrum). This remains the case upon cooling to room temperature, showing the stability of the surface reconstruction. Only the expected shift of the peaks corresponding to the shift in the band gap energy with respect to temperature is seen. b) Sample with 4.3 % Bi incorporation showing a more or less single feature in the spectrum during growth (green spectrum). After growth under TBAs stabilization two distinct peaks at 2.4 eV and 2.75 eV evolve in the RAS spectrum (black spectrum). These remain unchanged upon cooling to room temperature (red spectrum). As mentioned above the peaks only shift in energy as expected.

Overall these findings can support the idea of two separate features on the surface reconstruction, that are responsible for the formation of the two peaks in the RAS spectrum. However, this can still be caused by the difference in the phase of the Fabry-Perot oscillation, since the interference is wavelength (energy) dependent.

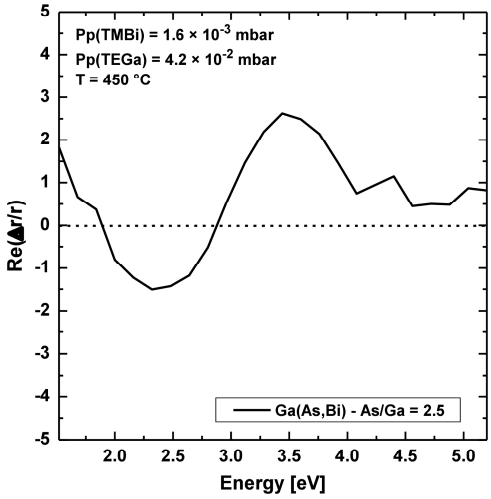

Supporting information 11: All partial pressures are given within the figure. RAS spectrum of a Ga(As,Bi) layer grown at 450 °C with an As/Ga ratio of 2.5. The XRD result showed a Bi incorporation of 2.1 %. The RAS spectrum corresponds to the signal of a c(4×4)α surface reconstruction but shifted in energy as discussed for the sample shown in figure 7 of the publication.

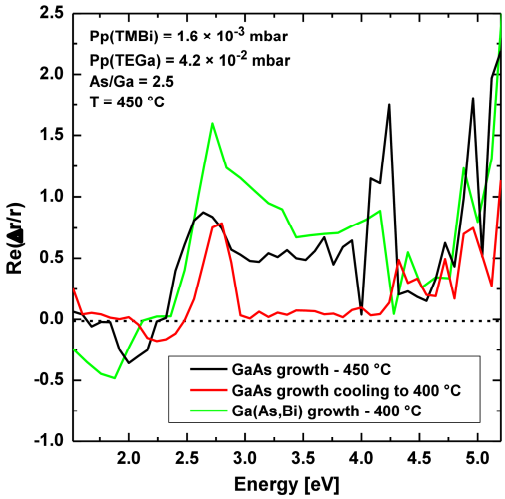

Supporting information 12: All partial pressures are given within the figure. During preparation the GaAs (001) surface forms a (2×4) surface reconstruction during growth at 450 °C with an As/Ga ratio of 2.5 (black spectrum). To prevent the surface to form a c(4×4)α surface reconstruction, the sample was cooled to 400 °C while continuously growing GaAs. During this step the RAS signal changes to the red spectrum. This change could be explained by the formation of a transition state between the c(4×4)α and the (2×4) surface reconstruction. During the followed growth of Ga(As,Bi) the RAS signal of the (2×4) surface reconstruction is observed (green spectrum). This shows that Ga(As,Bi) can also be grown on the (2×4) surface reconstruction. The corresponding Bi incorporation is determined with 2.6 %.

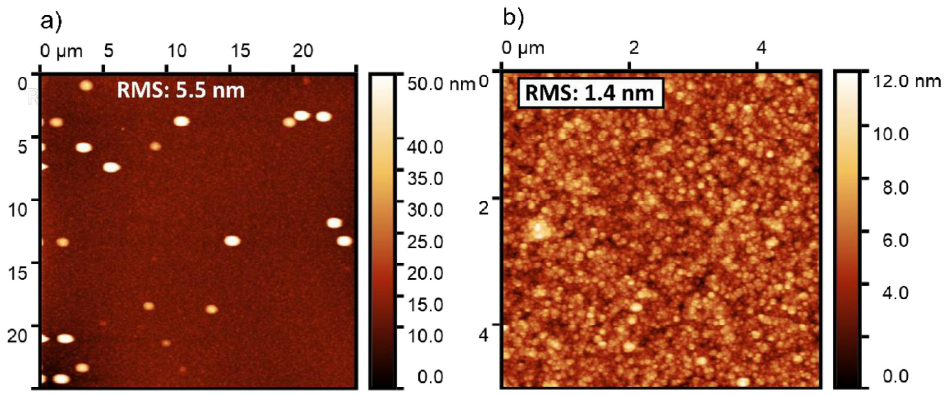

Supporting information 13: AFM images of the Ga(As,Bi) layer grown on the prepared (2×4) surface reconstruction at 400 °C. a) AFM image showing droplet formation on the growth surface on the larger lateral scale. b) Surface in between the droplets. A relatively smooth surface with an RMS value of 1.4 nm is observed. The surface shows formation of small islands compared to formation of larger terraces for an ideal surface.

References

[1] P. Ludewig, L. Nattermann, W. Stolz, K. Volz, MOVPE growth mechanisms of dilute bismide III/V alloys, Semicond. Sci. Technol. 30 (2015) 94017. doi:10.1088/0268-1242/30/9/094017.

7.2.3 Decomposition Mechanisms of Di-*tert*-butylaminoarsane (DTBAA)

Authors: Oliver Maßmeyer, Sebastian Inacker, Thilo Hepp, Johannes Glowatzki, Lukas Nattermann, Eduard Sterzer, Christian Ritter, Carsten von Hänisch, Wolfgang Stolz and Kerstin Volz

Publication: Organometallics, Volume 38, 15 August 2019, Pages 3181-3186

DOI: 10.1021/acs.organomet.9b00442

Abstract: III–V semiconductors containing small amounts of nitrogen ("dilute nitrides") are very promising material systems for optoelectronic applications. Devices based on 'dilute nitrides' currently suffer from problematic C incorporation. To overcome this problem, a novel nitrogen (N) and arsenic (As) precursor for metal–organic vapor phase epitaxy (MOVPE) of the 'dilute nitride' di-*tert*-butyl-amino-arsane (DTBAA) has been introduced. DTBAA in comparison to the commonly used 1,1-di-methyl-hydrazine (UDMHy) showed a significantly improved N incorporation efficiency. The molecule exhibits no strong carbon (C)–N bond, and the C is only present in large alkyl groups which form fewer C radicals since *β-H elimination* is the dominating decomposition process. This should significantly lower the problematic C incorporation in 'dilute nitrides' and lead to highly efficient devices. To understand the high N incorporation efficiency as well as the As incorporation, the gas phase decomposition of this novel precursor has been studied with a real time Fourier transform (FT) quadrupole ion trap mass spectrometer (iTrap) from Carl Zeiss SMT GmbH in a horizontal Aixtron Aix 200 GFR MOVPE reactor. Formation of isobutane and isobutene proves a *radical* cleavage and *β-H-elimination* as decomposition processes of the *tert*-butyl groups attached to the molecule. Furthermore, the appearance of ammonia (NH_3) has been detected. This indicates a direct cleavage of the As–N bond of the molecule, resulting in the formation of an aminyl radical (NH_2•). The formation of NH_2• explains the high N incorporation efficiency of DTBAA as well as its limitations due to desorption of NH_3 at higher temperatures.

Authors' Contributions: My contribution to this work was the planning, the execution and interpretation of the majority of all shown decomposition experiments. S. Inacker assisted with the measurement of the DTBAA decomposition by mass spectrometry and helped with the data interpretation in the framework of a project practical course. All co-authors helped with the interpretation of the data and with the review of the manuscript. C. Ritter and C. von Hänisch conducted the synthesis of the novel DTBAA precursor and especially helped with chemistry related questions. W. Stolz and K. Volz supervised the work and secured the funding to support this study.

ORGANOMETALLICS
Cite This: Organometallics 2019, 38, 3181−3186
Article
pubs.acs.org/Organometallics

Decomposition Mechanisms of Di-*tert*-butylaminoarsane (DTBAA)

Oliver Maßmeyer,*[,†] Sebastian Inacker,[‡] Thilo Hepp,[†] Johannes Glowatzki,[†] Lukas Nattermann,[†] Eduard Sterzer,[†] Christian Ritter,[‡] Carsten von Hänisch,[‡] Wolfgang Stolz,[†] and Kerstin Volz[†]

[†]Material Sciences Center and Department of Physics, Philipps-Universität Marburg, 35032 Marburg, Germany
[‡]Material Sciences Center and Department of Chemistry, Philipps-Universität Marburg, 35032 Marburg, Germany

ABSTRACT: III−V semiconductors containing small amounts of nitrogen ("dilute nitrides") are very promising material systems for optoelectronic applications. Devices based on dilute nitrides currently suffer from problematic C incorporation. To overcome this problem, a novel nitrogen (N) and arsenic (As) precursor for metal−organic vapor phase epitaxy (MOVPE) of the dilute nitride di-*tert*-butylaminoarsane (DTBAA) has been introduced. DTBAA in comparison to the commonly used 1,1-dimethylhydrazine (UDMHy) showed a significantly improved N incorporation efficiency. The molecule exhibits no strong carbon (C)−N bond, and the C is only present in large alkyl groups which form fewer C radicals since β-H elimination is the dominating decomposition process. This should significantly lower the problematic C incorporation in dilute nitrides and lead to highly efficient devices. To understand the high N incorporation efficiency as well as the As incorporation, the gas-phase decomposition of this novel precursor has been studied with a real time Fourier transform (FT) quadrupole ion trap mass spectrometer (iTrap) from Carl Zeiss SMT GmbH in a horizontal Aixtron Aix 200 GFR MOVPE reactor. Formation of isobutane and isobutene proves a radical cleavage and β-H-elimination as decomposition processes of the *tert*-butyl groups attached to the molecule. Furthermore, the appearance of ammonia (NH_3) has been detected. This indicates a direct cleavage of the As−N bond of the molecule, resulting in the formation of an aminyl radical ($NH_2^{\bullet}$). The formation of $NH_2^{\bullet}$ explains the high N incorporation efficiency of DTBAA as well as its limitations due to desorption of NH_3 at higher temperatures.

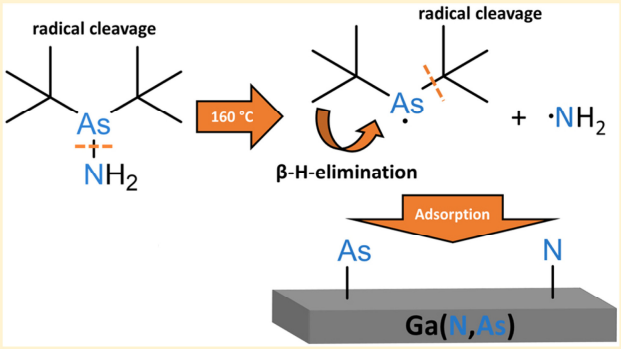

INTRODUCTION

Metal−organic vapor phase epitaxy (MOVPE) is a well-established commercial production technique for many kinds of electronic and photonic devices, such as LEDs, laser diodes, solar cells, high electron mobility transistors, integrated circuits, and many more.[1] MOVPE is suitable to grow basically all III/V and II/VI semiconductors, including metastable alloys such as nitrogen (N)-containing III/V species ("dilute nitrides"). Highly purified metal−organic precursors (MOs) and good process control is necessary to realize these devices, since even impurity levels in the parts per million range can lead to high defect densities in these devices.[2] Especially for dilute nitrides a main remaining challenge is the unintentional carbon (C) incorporation which arises, especially in MOVPE, from the alkyl groups of the MOs used. One source of C incorporation is the conventionally used N source 1,1-dimethylhydrazine (UDMHy). Due to strong C−N bonds in the precursor, the C is likely to incorporate into the devices which leads, for example, to an increase in the threshold current density in (Ga,In)(N,As) lasers.[3] This is additionally shown by mass spectrometric decomposition studies of UDMHy, showing the formation of CH_4 and larger stable fragments such as $(CH_3)_2NH$ and CH_3NCH_2, which presumably lead to C incorporation. In addition, the direct N−N bond within the molecule was found to be very stable and responsible for intermolecular coupling reactions which result in the formation of N_2.[4] Quantum chemical gas phase calculations also support the strength of the N−N bond.[5] This might explain the poor incorporation efficiency of the precursor.

In this work the thermal decomposition of the novel metal−organic precursor di-*tert*-butylaminoarsane (DTBAA) was investigated. The DTBAA molecule exhibits a direct As−N bond and can be used as an arsenic (As) as well as an N source in MOVPE. Therefore, no additional As source is necessary to grow e.g. Ga(N,As) with DTBAA and triethylgallium (TEGa). In comparison to UDMHy no direct C−N bond is present in DTBAA and the C is only present in large alkyl groups which are most probably sterically hindered from being incorporated into the growing layer.[6] In growth studies it has been shown that DTBAA is suitable for the low-temperature growth of dilute nitrides with up to 40 times higher incorporation efficiency in comparison to layers grown with UDMHy.[5,7] To understand the high N incorporation efficiency as well as the As incorporation, the decomposition pathways of DTBAA have been investigated with a novel real-time FT quadrupole ion trap mass spectrometer (iTrap) from Carl Zeiss SMT

Received: July 1, 2019
Published: August 15, 2019

DOI: 10.1021/acs.organomet.9b00442
Organometallics 2019, 38, 3181−3186

GmbH in a horizontal Aixtron Aix 200 GFR MOVPE reactor.[8,9]

In this paper first the thermal decomposition products and decomposition temperature of the introduced precursor molecule DTBAA are discussed. From the products that arise, the preferred reaction pathways during the decomposition of the DTBAA are examined. Afterward the decomposition will be compared to the decomposition of UDMHy to show the advantages of the novel N precursor. Furthermore, from the results the activation energy of the decomposition reaction is determined and compared to literature results from DFT calculations as well as correlated to the N incorporation behavior of DTBAA.

EXPERIMENTAL PROCEDURE

The investigated precursors were carried by palladium-purified hydrogen (purity 9.0) into an Aixtron Aix 200 horizontal GFR (gas foil rotation) reactor. The reactor is operated under a constant pressure of 50 mbar (37.5 Torr) and a total flux of 6800 sccm. The thermal cracking of the precursor molecules is initialized by a uniformly heated graphite susceptor using six infrared lamps within the reactor chamber. The susceptor was first baked out at a high temperature of 800 °C to desorb molecules that could eventually influence the experiments and was kept uncoated during the experiments. To stick to actual growth conditions within the reactor chamber the substrate was rotated at 50−70 rpm, which is applied to ensure homogeneous growth of the III/V species. The partial pressure of DTBAA was also kept in a range from 2.5×10^{-3} to 2.6×10^{-2} mbar, which is suitable to incorporate a sufficient amount of N into GaAs in a realistic growth experiment.

The thermal decomposition of DTBAA and UDMHy was monitored by an FT quadrupole ion trap mass spectrometer (FTQIT-iTrap) from Carl Zeiss SMT GmbH. The FTQIT showed high sensitivity by detection of a pptV of B_2H_6 in H_2 within a fast single-shot measurement (~3 s).[8] This new setup is very promising for in situ gas-phase and growth interaction analysis during MOVPE without disturbing the growth process itself and has been successfully applied for decomposition analysis of *tert*-butylarsine (TBAs), which has been described in detail in ref 9.

The FTQIT is connected with a bypass system to the MOVPE reactor. The bypass is operated under stable gas flow and pressure conditions, similar to the pressure in the reactor. The analyte is collected right above the middle of the susceptor with a quartz crystal nozzle and carried into the bypass system. For analysis a small gas volume of analyte is pulsed by an atomic layer deposition valve directly into the QIT of the mass spectrometer. Therefore, in comparison to setups used in the past, no expensive pressure reduction stages are needed.[10] The quadrupole of the trap consists of a top, a bottom, and a ring electrode. The analyte is first ionized by electron ionization (EI) at 70 eV, and the created ions are then captured by an oscillating electric field which is applied to the ring electrode in the mass spectrometer. The applied field is oscillating in the radio frequency (RF) range with a used RF voltage between 80 and 400 V, which is adjusted in according with the measured mass range. The resulting motions of the ions within the FTQIT induce a mirror image current in the top and bottom electrodes. After resonant excitation of the ions a full mass spectrum can be generated by fast Fourier transformation (FFT) of the detected damped image current. Due to the FFT technique the overall recording time for a single mass spectrum is below 2 s, which enables real time analysis, a high data point density, and good statistics.

The setup is furthermore suitable to remove a selected range of mass over charge ratios (m/z) from the trap by using stored waveform inverse Fourier transform (SWIFT) to enable ultrahigh-resolution measurements.[8,11]

During the decomposition analysis the susceptor temperature was varied from room temperature (20 °C) up to 800 °C. Due to the distance of the nozzle to the susceptor, the effective temperature of the collected gas phase was determined by correlation of the TBAs decomposition results[9] with data from ref 12.

RESULTS AND DISCUSSION

In this paper the thermal decomposition pathways of DTBAA (205 u) have been investigated by an extremely sensitive (pptV level) and very fast (<2 s) FT quadrupole ion trap mass spectrometer (iTrap) from Carl Zeiss SMT GmbH which was used inline in a metal−organic vapor phase epitaxy (MOVPE) system.

In Figure 1 the mass spectra of DTBAA measured at low temperature with a supplied partial pressure of 2.5×10^{-3} mbar DTBAA are shown. The applied radio frequency (RF) voltage was kept at an amplitude of 200 V. Due to electron ionization (EI) at 70 eV the analyte is cracked into many fragments, which can be seen in Figure 1a.

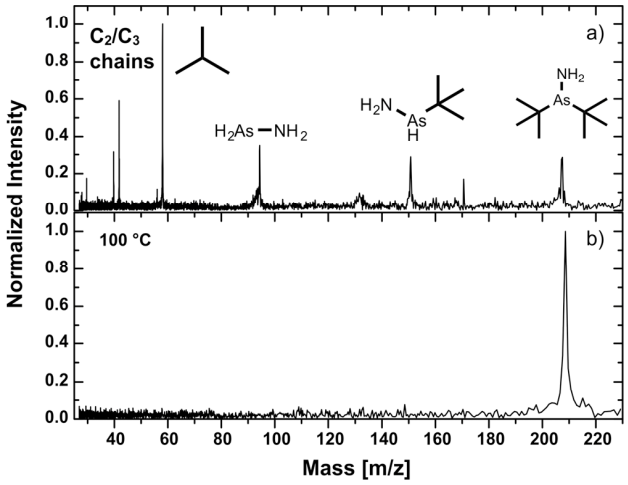

Figure 1. DTBAA (205 u) mass spectra collected at a reactor temperature of 100 °C with a supply of 2.5×10^{-3} mbar DTBAA and an applied radio frequency with an amplitude of 200 V. All intensities have been normalized to the detected intensity of the most frequent fragment. (a) Various fragmentation products by cracking of the DTBAA molecules during electron ionization (EI) at 70 eV. (b) Sensitive ionization conditions occurring by applying a comparably low filament current, ionization time, and waiting time between the gas inlet and ionization in the FTQIT.

Only a small portion of the DTBAA molecules has not been cracked, resulting in a small detected intensity at 205 u. All further peaks can be related to fragments of the DTBAA molecule itself. Figure 1b shows a mass spectrum detected using the same partial pressure, temperature, and reactor pressure but with changed conditions within the FTQIT. For this and the following measurements a reduced filament current in the electron gun, a reduced ionization time, and a reduced time between the gas inlet and ionization of the analyte have been used. Under these conditions, no fragmentation of the captured DTBAA molecules is observed and only one peak around 205 u arises.

These seemingly more sensitive ionization conditions are also very similar to those observed in the case of TBAs (134 u)[9] and seem to be valid for all investigated group V precursors. In contrast, it was not possible up to now to find similar conditions for group III precursors.

At a gas-phase temperature of 175 °C the DTBAA molecule is already partially decomposed due to the supplied thermal

DOI: 10.1021/acs.organomet.9b00442
Organometallics 2019, 38, 3181−3186

energy, which is shown in Figure 2. In the low-mass range NH_3 (17 u) was detected by the used FTQIT at 18 u due to the

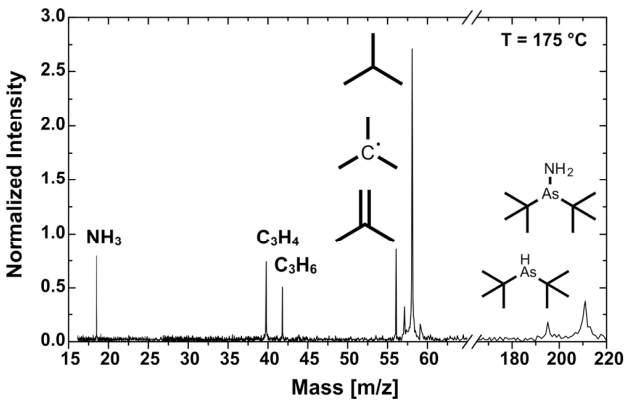

Figure 2. Mass spectrum of partly decomposed DTBAA (205 u) collected at a gas-phase temperature of 175 °C with a supply of 2.5×10^{-3} mbar DTBAA and an applied radio frequency with an amplitude of 200 V. All intensities have been normalized to the detected intensity of the parent molecule peak of DTBAA from Figure 1b.

formation of NH_4^+ (18 u) within the mass spectrometer. This protonation reaction was confirmed by the measurement of an ammonia test gas that was directly supplied to the mass spectrometer, which resulted in the detection of NH_4^+ under the chosen conditions. Under the EI conditions used in Figure 1a the NH_3 test gas showed an expected fragmentation of the molecule into NH_2 (16 u), NH (15 u), and N (14 u). NH_3 is the product of aminyl radicals ($NH_2^\bullet$) that are formed during the decomposition of the DTBAA molecule. Details on $NH_2^\bullet$ formation will be discussed later. Furthermore, formation of alkyl groups around 40 and 42 u which most likely can be attributed to formation of propyne (40 u) and propene (42 u) were detected. These fragments can be attributed to EI-induced fragmentation of isobutane (58 u) and isobutene (56 u). This was checked by investigations of the appropriate test gases. The isobutane test gas showed under the FTQIT settings used in Figure 1a an expected electron ionization spectrum which can be found in ref 13. Under the FTQIT settings of Figure 1b the isobutane fragmented partially into propyne and propene. In contrast, only propyne was detected as a fragment for the electron-induced cracking of the isobutene test gas. One can therefore attribute the detected propene intensity in Figures 1 and 2 to thermally induced formation of isobutane and the propyne intensity to the formation of isobutane as well as isobutene.

In contrast, detection of isobutane, *tert*-butyl radical (57 u) and isobutene can be attributed to the thermal decomposition of the *tert*-butyl groups attached to the molecule. Formation of isobutane and *tert*-butyl radical indicate a radical decomposition of the As−C bond. This radical decomposition leads to the formation of *tert*-butyl radicals, which can react with H radicals or H_2 present in the system to form isobutane, which is shown in Scheme 1. H radicals would only be present if they are formed during the decomposition of DTBAA or within the mass spectrometer due to EI.

Isobutane can also be the result of an intramolecular coupling reaction (Scheme 2). This reaction was predicted by DFT calculations for the DTBAA molecule and has also been shown for other metal−organic precursors such as TBAs.[12,14]

Scheme 1. Radical Decomposition of the As−C Bond

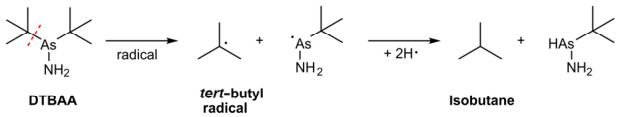

Scheme 2. Intramolecular Coupling

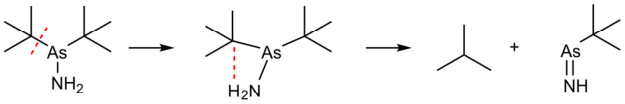

Formation of isobutene indicates a second available decomposition pathway occurring through β-H elimination of one or both *tert*-butyl groups. During β-H elimination one of the C_β−H bonds of one C atom in a β position is interacting with the As orbitals. This leads to the formation of a C=C double bond, which is shown in Scheme 3.

Scheme 3. β-H Elimination of the *tert*-Butyl Groups

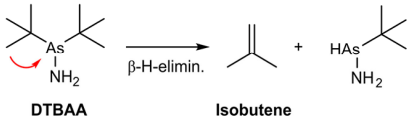

Additionally, a further broad peak around 195 u is detected within the mass spectrum. This can most likely be attributed to a di-*tert*-butylarsine molecule (DTBAs, 190 u), since for higher masses a mass offset is present at the given RF voltage of 200 V, which can be removed by adjusting the RF voltage to a higher value of 300−400 V within a second measurement. Due to the higher amplitude of the electric field, higher masses will be preferably trapped, which results in a better sensitivity of the FTQIT in this mass range. The DTBAs could be a result of a radical cleavage of the N−As bond of DTBAA. At the chosen temperature the parent molecule is still not completely decomposed and under the settings used is detected at around 210 u with the same mass offset as the DTBAs molecule.

Furthermore, a high intensity of ammonia (NH_3) is detected. It is assumed that ammonia is formed due to a radical decomposition reaction (Scheme 4) of the N−As bond

Scheme 4. Radical Decomposition of the N−As Bond

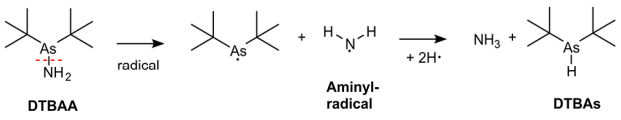

within the DTBAA molecule under the formation of an aminyl radical ($NH_2^\bullet$) and DTBAs$^\bullet$ (189 u). Due to the available H radicals both radicals are expected to be detected as ammonia and DTBAs in the FTQIT, respectively.

In contrast to the main proposed reaction pathways in ref 5, whose initial steps are depicted as Schemes 2 and 3, radical decomposition of the N−As bond was not treated in the gas-phase decomposition calculations. Our findings support that a direct cleavage of the N−As bond must be energetically accessible and highly probable under the applied conditions. This decomposition process is shown as Scheme 4.

DOI: 10.1021/acs.organomet.9b00442
Organometallics 2019, 38, 3181−3186

The formation of aminyl radicals ($NH_2^\bullet$) during the decomposition of DTBAA could explain the up to 40 times higher reported nitrogen incorporation efficiency using DTBAA at low temperatures in comparison to that using UDMHy (60 u).[5,15] The formed aminyl radicals ($NH_2^\bullet$) should be highly reactive if they are near a surface and are likely to be incorporated. At higher temperatures formation and desorption of NH_3 from the surface should become more probable. This explains the observed exponential decay of N incorporation with increasing growth temperature reported in ref 5.

Scheme 5 shows a proposed decomposition pathway including formation of isobutane and isobutene resulting in

Scheme 5. Proposed Reaction Pathway

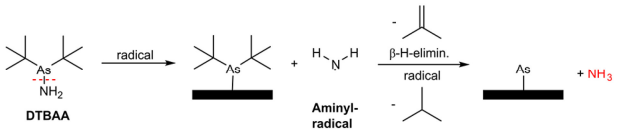

incorporation of As and desorption of NH_3, which can be detected by the FTQIT in the experiment. Therefore, this decomposition reaction would fully explain our measured reaction products.

In Figure 3a the detected intensities are plotted against the gas-phase temperature within the reactor chamber of the MOVPE system. The DTBAA starts to drop to half of the intensity around T_{decomp} = 160 ± 10 °C. The decomposition temperature T_{decomp} is comparably low in comparison to that of the conventionally used N source UDMHy that decomposes at T_{decomp} = 420 °C, which was determined by mass spectrometric investigations[4] and can be confirmed by our studies within the same reactor system (Figure 4). The low decomposition temperature makes DTBAA very suitable for growth of dilute nitrides, which are typically grown at comparably low temperatures, and has been proven for growth of Ga(N,As), (Ga,In)(N,As), and Ga(N,As,Sb) on GaAs.[5,7,15] It has also been shown that DTBAA is capable of growing Ga(N,As) with just the addition of triethylgallium (TEGa). This makes DTBAA very promising for future applications, especially at comparably low temperatures.

Furthermore, the reaction barriers for DTBAA decomposition reactions were determined by DFT calculations. The reaction barrier for β-H elimination at 400 °C into isobutene (Scheme 3) was determined with 266 kJ/mol in comparison to a reaction barrier of 257 kJ/mol for the formation of isobutane by radical decomposition (Scheme 2). Since both reaction barriers are quite similar, the kinetically most favorable reaction is β-H elimination, which exhibits a lower Gibbs reaction energy of −62.7 kJ/mol in comparison to −38.9 kJ/mol for Scheme 2.[5]

These findings can be compared to the detected intensities of isobutane (radical reaction pathway) and isobutene (β-H elimination) within our measurement. First, the activation energy of 266 ± 57 kJ/mol determined from our data fits within the error the proposed reaction barrier and will be shown and discussed at the end of the paper in Figure 4.

In our data the signal intensity of isobutane (radical reaction pathway) remains higher than that of isobutene (β-hydrogen elimination). This shows a higher probability for the radical decomposition pathway of the *tert*-butyl groups from the molecule in comparison to β-hydrogen elimination. This

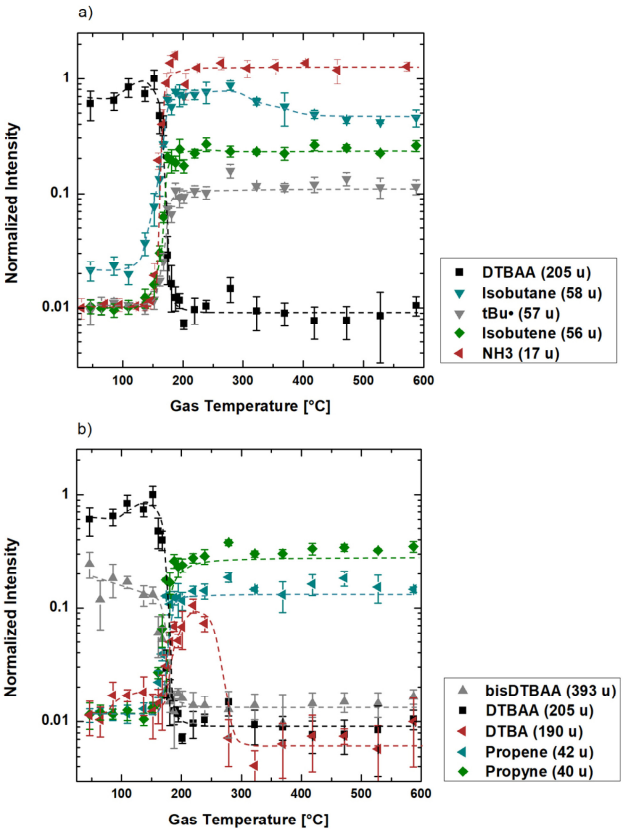

Figure 3. (a) Breakdown curves of DTBAA (205 u) and the main decomposition products isobutane (C_4H_{10}, 58 u), *tert*-butyl radical ($C_4H_9^\bullet$, 57 u), isobutene (C_4H_8, 56 u), and aminyl radical ($NH_2^\bullet$, 16 u) detected as ammonia (NH_3, 17 u). (b) Breakdown curves of DTBAA and bisDTBAA (393 u) with further decomposition products DTBAs ($(C_4H_9)_2AsH$, 190 u), propene (C_3H_6, 42 u), and propyne (C_3H_4, 40 u).

somehow contradicts the determined Gibbs reaction energies. However, we do observe a drop of the isobutane intensity to nearly half of its value around 300 °C in our measurement. An explanation could be that the radical decomposition of one of the two *tert*-butyl groups is hindered or is less favorable at higher temperatures.

In addition, there is hardly any difference in temperature at which decomposition into isobutane and isobutene sets in. The temperature determination of the gas phase in our experiment might not be sufficient to distinguish between the proposed minor difference of reaction barriers for the formation of isobutane and isobutene in ref 5.

A very similar behavior of a *tert*-butyl group attached to an As atom has also been observed for the TBAs molecule. Theoretical and experimental results of TBAs decomposition have shown a temperature difference between the onset of radical decomposition and β-hydrogen elimination, which becomes the main decomposition pathway at higher temperatures.[9,12,16,17] This supports the idea of the less favorable radical decomposition of one of the *tert*-butyl groups attached to the DTBAA molecule and supports the relevance of the β-hydrogen elimination.

Figure 3b shows the detected intensities of further decomposition products. As mentioned above, propyne and propene can be attributed to the fragmentation of DTBAA due

DOI: 10.1021/acs.organomet.9b00442
Organometallics 2019, 38, 3181−3186

to electron ionization. At very high masses bisDTBAA (393 u) has been detected. In this synthesis DTBAA is distilled for purification. During this process bisDTBAA can form due to a condensation reaction under abstraction of ammonia (NH_3). This possibility has been shown for the antimony analogue.[18] bisDTBAA dissolves within the DTBAA precursor and was detected within the FTQIT. The bisDTBAA intensity starts to drop even before DTBAA is decomposed, while the intensities of DTBAA and DTBAs slightly increase. Therefore, bisDTBAA seems to decompose into radicals of DTBAA as well as DTBAs that can react with the present $H^{\bullet}$ radicals to form DTBAA and DTBAs, respectively. In addition, the bisDTBAA is fully decomposed around the same temperature as in the case for DTBAA. Since the decomposition of the condensation product results in the formation of DTBAA, no negative effect on the N incorporation of the precursor is expected. The corresponding growth experiments on Ga(N,As) exhibit no influence of the bisDTBAA on the incorporation mechanism.[5] The DTBAs intensity increases further and remains present up to a temperature of 250 °C. At this temperature the DTBAs seemingly becomes unstable and decomposes. As shown in Scheme 5, it is likely to form isobutane and isobutene by radical cleavage and β-H elimination of the As−C bonds, respectively.

No further decomposition products including As have been observed within the FTQIT. The remaining As might form As_2 or As_4 and could adsorb on available surfaces within the reactor, which is visible as a black coating of the liner as well as in the line in the mass spectrum. Therefore, they are not likely to be detected within our FTQIT setup if they are formed during decomposition of the DTBAA.

The decomposition temperature of DTBAA on the bare graphite susceptor is compared to the decomposition temperatures of TBAs, UDMHy, and DTBAA on an introduced 2 in. GaAs (001) surface in Figure 4. For all precursors the decomposition temperature was determined by tracking the intensity of the mother molecule peak, which fits to findings from the literature for TBAs (T_{decomp} = 350 ± 10 °C) and UDMHy (T_{decomp} = 440 ± 10 °C).[4,5,16] Seemingly, the conventionally used As and N precursors decompose at higher temperatures in comparison to the novel As and N source DTBAA. By introduction of a 2 in. GaAs (001) surface into the reactor system a slight decrease of T_{decomp} from 160 ± 10 to 150 ± 10 °C was observed. This shows to some extent a catalytic effect of an actual growth surface on the DTBAA decomposition. Nevertheless, the accuracy of the temperature and the influence of the measurement setup has to be kept in mind for stating a significant surface effect. The comparably low decomposition temperature of DTBAA shows further the advantage of DTBAA over the currently used precursors, in looking for high N incorporation and enabling growth of devices at low temperatures by MOVPE. Especially metastable alloys that are able to be grown in molecular beam epitaxy (MBE) at lower temperatures might become accessible in MOVPE. The currently used precursors for MOVPE are decomposition-limited in the temperature range used for these devices.

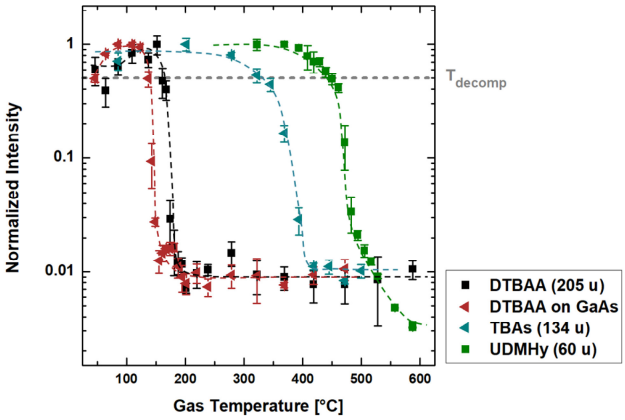

Figure 4. Breakdown curves of DTBAA (205 u) on the bare graphite susceptor, of DTBAA on a 2 in. GaAs (001) surface (81 cm^2), and of TBAs (134 u) and UDMHy (60 u) within the same reactor system on the bare graphite susceptor. The intersection points with the gray line indicate the decomposition temperature T_{decomp}, which is defined where the intensity drops to 50%.

Figure 5 shows an Arrhenius plot created out of the breakdown curve of DTBAA from Figure 4. Evaluation of the slope allows the determination of the pre-exponential attempt frequency factor A as well as the activation energy of the decomposition reaction. The activation energy of the DTBAA decomposition is determined to be 2.75 ± 0.6 eV which corresponds to 266 ± 57 kJ/mol.

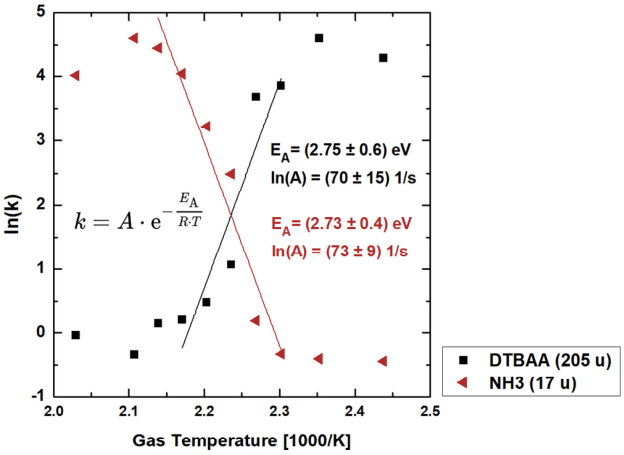

Figure 5. Arrhenius plot for the detected intensities of DTBAA (205 u) and ammonia (NH_3, 17 u). Linear regression of the slopes allows the determination of the activation energy of the reactions as well as the pre-exponential attempt frequency factor A.

This fits to the proposed reaction barriers from DFT calculations in the literature and the determined activation energy ($E_A \approx 2.5$ eV) of the temperature-dependent N incorporation data.[5] From the reversed slope of the NH_3 signal in the Arrhenius plot of our data an identical activation energy of 2.72 ± 0.4 eV is determined. This supports the assumption that the aminyl radical ($NH_2^{\bullet}$) measured as NH_3 signal is directly related to the N incorporation into dilute nitrides such as Ga(N,As) during growth with DTBAA and explains the incorporation efficiency at low temperatures.

■ SUMMARY AND OUTLOOK

The thermal decomposition of DTBAA has been investigated by an extremely sensitive and very fast FT quadrupole ion trap (FTQIT) mass spectrometer from Carl Zeiss SMT GmbH, which was used inline in a metal−organic vapor phase epitaxy

DOI: 10.1021/acs.organomet.9b00442
Organometallics 2019, 38, 3181−3186

(MOVPE) system. Due to fine adjustment of the ionization conditions within the FTQIT, the typically observed fracturing by electron ionization at 70 eV was avoided, leading to a straightforward interpretation of the measurement data. The temperature-dependent breakdown curve of the investigated nitrogen and arsenic source DTBAA has shown different decomposition pathways. The production of isobutane indicates radical decomposition of the As−C bonds within the molecule. Furthermore, formation of isobutene showed β-hydrogen elimination of the *tert*-butyl groups attached to the molecule. Both decomposition reactions seem to be relevant over the whole investigated temperature range from the start of the decomposition up to 600 °C. The temperature at which the DTBAA intensity drops to 50% was determined with T_{decomp} = 160 ± 10 °C. The decomposition temperature of DTBAA was found to be slightly reduced by introducing a 2 in. GaAs (001) wafer into the reactor, which acts as a catalyst for the decomposition. Activation energies of the observed reactions were found to be in good agreement with the activation energies proposed in ref 5. In addition to the proposed decomposition pathways, radical cracking of the N−As bond within the molecule seems to be a possible reaction pathway, resulting in a high intensity observed for ammonia. The ammonia signal is interpreted to be a reaction product of formed aminyl radicals ($NH_2^{\bullet}$) which react on the way to the FTQIT with the present H radicals in the system. This is further supported by the determined activation energy of 2.7 eV, which fits well to the activation energies for N incorporation into Ga(N,As).[5] Overall the comparably low decomposition temperature of DTBAA should make the precursor suitable for growth of dilute nitrides at low temperatures, leading to high nitrogen incorporation efficiencies. In addition, only large alkyl groups have been detected during the decomposition. Therefore, and due to the absence of a direct C−N bond within the molecule, DTBAA should be suitable to reduce C incorporation into devices based on dilute nitrides.

AUTHOR INFORMATION

Corresponding Author

*E-mail for O.M.: Oliver.Massmeyer@physik.uni-marburg.de.

ORCID

Oliver Maßmeyer: 0000-0001-6101-5706

Notes

The authors declare no competing financial interest.

ACKNOWLEDGMENTS

This work was supported by the German Research Foundation (GRK 1782: "Functionalization of Semiconductors"), and the support for the mass spectrometer (iTrap) was provided by Carl Zeiss SMT GmbH.

REFERENCES

(1) Stringfellow, G. B. Development and Current Status of Organometallic Vapor Phase Epitaxy. *J. Cryst. Growth* **2004**, *264* (4), 620−630.

(2) Brauers, A. Alternative Precursors for III/V MOVPE. *Prog. Cryst. Growth Charact. Mater.* **1991**, *22*, 1−18.

(3) Volz, K.; Torunski, T.; Kunert, B.; Rubel, O.; Nau, S.; Reinhard, S.; Stolz, W. Specific Structural and Compositional Properties of (GaIn)(NAs) and Their Influence on Optoelectronic Device Performance. *J. Cryst. Growth* **2004**, *272* (1−4), 739−747.

(4) Lee, R. T.; Stringfellow, G. B. Pyrolysis of 1,1 Dimethylhydrazine for OMVPE Growth. *J. Electron. Mater.* **1999**, *28* (8), 963−969.

(5) Sterzer, E.; Beyer, A.; Duschek, L.; Nattermann, L.; Ringler, B.; Leube, B.; Stegmüller, A.; Tonner, R.; von Hänisch, C.; Stolz, W.; et al. Efficient Nitrogen Incorporation in GaAs Using Novel Metal Organic As−N Precursor Di-Tertiary-Butyl-Arsano-Amine (DTBAA). *J. Cryst. Growth* **2016**, *439*, 19−27.

(6) Porchia, M.; Zanella, P.; Rossetto, G.; Williams, J. O.; Brianese, N.; Ossola, F. Organometallic Precursors in the Growth of Epitaxial Thin Films of III-V Semiconductors by Metal-Organic Chemical Vapor Deposition (MOCVD). *Chem. Mater.* **1991**, *3* (2), 225−242.

(7) Sterzer, E.; Maßmeyer, O.; Nattermann, L.; Jandieri, K.; Gupta, S.; Beyer, A.; Ringler, B.; Von Hänisch, C.; Stolz, W.; Volz, K. 1 EV Ga(NAsSb) Grown by MOVPE Using Di- Tertiary -Butyl-Arsano-Amine (DTBAA). *AIP Adv.* **2018**, *8* (5), 055329.

(8) Chung, H. Y.; Aliman, M.; Fedosenko, G.; Laue, A.; Reuter, R.; Derpmann, V.; Gorkhover, L.; Antoni, M. Very Sensitive Real-Time Inline Process Mass Spectrometer Based on FFT Ion Trap Technique. *2016 27th Annu. SEMI Adv. Semicond. Manuf. Conf. ASMC* **2016**, 263−266.

(9) Nattermann, L.; Maßmeyer, O.; Sterzer, E.; Derpmann, V.; Chung, H. Y.; Stolz, W.; Volz, K. An Experimental Approach for Real Time Mass Spectrometric CVD Gas Phase Investigations. *Sci. Rep.* **2018**, *8*, 1.

(10) Yoshida, M.; Watanabe, H.; Uesugi, F. Mass Spectrometric Study of Ga(CH3)3 and Ga(C2H5) 3 Decomposition Reaction in H2 And. *J. Electrochem. Soc.* **1985**, *132* (3), 677−679.

(11) Guan, S.; Marshall, A. G. Stored Waveform Inverse Fourier Transform (SWIFT) Ion Excitation in Trapped-Ion Mass Spectometry: Theory and Applications. *Int. J. Mass Spectrom. Ion Processes* **1996**, *157*−*158*, 5−37.

(12) Larsen, C. A.; Buchan, N. I.; Li, S. H.; Stringfellow, G. B. Decomposition Mechanisms of Tertiarybutylarsine. *J. Cryst. Growth* **1989**, *94* (3), 663−672.

(13) Stevenson, D. P.; Hipple, J. A. Ionization and Dissociation by Electron Impact: Normal Butane, Isobutane, and Ethane. *J. Am. Chem. Soc.* **1942**, *64* (7), 1588−1594.

(14) Stringfellow, G. B. *Organometallic Vapour Phase Epitaxy: Theory and Practice*, 2nd ed.; Academic Press: 1989.

(15) Sterzer, E.; Ringler, B.; Nattermann, L.; Beyer, A.; von Hänisch, C.; Stolz, W.; Volz, K. (GaIn)(NAs) Growth Using Di-Tertiary-Butyl-Arsano-Amine (DTBAA). *J. Cryst. Growth* **2017**, *467*, 132−136.

(16) Larsen, C. A.; Li, S. H.; Buchan, N. J.; Stringfellow, G. B. MECHANISMS OF GaAs GROWTH USING TERTIARYBUTYLARSINE AND TRIMETHYLGALLIUM C.A. LARSEN, S.H. LI, N.J. BUCHAN and G.B. STRINGFELLOW. *J. Cryst. Growth* **1989**, *94*, 673.

(17) Foster, D. F.; Glidewell, C.; Cole-Hamilton, D. J. Probing the Mechanisms of Growth of Gallium Arsenide by Metalorganic Vapor Phase Epitaxy Using Experimental and Theoretical Studies of Designed Precursors. *J. Electron. Mater.* **1994**, *23* (2), 69−74.

(18) Ringler, B.; Von Hänisch, C. Novel Stibano Amines: Synthesis and Reactivity towards Group 13 Element Organics. *Z. Anorg. Allg. Chem.* **2016**, *642* (4), 294−298.

DOI: 10.1021/acs.organomet.9b00442
Organometallics 2019, 38, 3181−3186

7.2.4 Ga(N,P) Growth on Si and Decomposition Studies of the N−P Precursor Di-*tert*-butylaminophosphane (DTBAP)

Authors: Johannes Glowatzki, Oliver Maßmeyer, Marcel Köster, Thilo Hepp, Ebunoluwa Odofin, Carsten von Hänisch, Wolfgang Stolz, and Kerstin Volz

Publication: Organometallics, Volume 39, 30 April 2020, Pages 1772-1781

DOI: 10.1021/acs.organomet.0c00078

Abstract: III/V semiconductors containing small amounts of nitrogen (‘dilute nitrides’) are promising for applications such as lasers and solar cells. Metal–organic vapor-phase epitaxy (MOVPE) is a widely used technique for growing III/V semiconductors on an industrial scale, and the growth of ‘dilute nitrides’ with this method is promising for later successful market entry. The main issues of ‘dilute nitrides’ are carbon incorporation and low nitrogen incorporation efficiency of the conventional N precursors. Due to the high N incorporation efficiency and the low decomposition temperature of the As and N precursor di-*tert*-butyl-amino-arsane (DTBAA), a similar P- and N-containing precursor, di-*tert*-butyl-amino-phosphane (DTBAP), was synthesized and purified on a laboratory scale. Growth studies using this precursor were carried out in this work realizing Ga(N,P)/GaP multi quantum wells on Si and GaP substrates. The structures show evidence of N incorporation, and good layer structures were confirmed by high-resolution X-ray diffraction. Following the influence of different growth parameters on the N incorporation, the growth rate and surface morphology were characterized to set a foundation for possible growth applications in the future. DTBAP shows many advantages over the conventional N source 1,1-di-methyl-hydrazine (UDMHy) such as a much lower decomposition temperature of 310 °C and the realization of Ga(N,P) layers grown at temperatures as low as 475 °C with a high N incorporation of over 10 %. Furthermore, the gas-phase decomposition of DTBAP has been studied with a real-time fast Fourier transform quadrupole ion trap mass spectrometer attached inline to the MOVPE reactor. The decomposition of DTBAP behaves very similarly to the As analogue DTBAA. On the one hand, the *tert*-butyl groups attached to DTBAP decompose radically, leading to the formation of isobutane, and decompose, on the other hand, by *β-H elimination*, leading to the formation of isobutene. Furthermore, the decomposition products indicate a direct cleavage of the P–N bond of the molecule, resulting in the formation of aminyl radicals ($NH_2^{\bullet}$). The formation of $NH_2^{\bullet}$ explains the high N incorporation efficiency of DTBAP at low temperatures as well as its limitations due to loss of NH_3 at higher temperatures.

Authors’ Contributions: My contribution to this work was the planning, the execution and interpretation of all shown decomposition experiments of DTBAP. J. Glowatzki contributed equally to this publication. He planned, executed and interpreted the growth of Ga(N,P) structures on GaP and GaP/Si with the novel DTBAP precursor. This includes the structural analysis of the grown samples by HR-XRD and AFM. M. Köster and C. von Hänisch conducted the synthesis of the novel DTBAP precursor and helped with chemistry related questions. E. Odofin assisted with the lab work and the mass spectrometry investigations in the framework of a project practical course. All co-authors helped with the interpretation of the data and with the review of the manuscript. W. Stolz and K. Volz supervised the work and secured the funding to support this study.

ORGANOMETALLICS

pubs.acs.org/Organometallics Article

Ga(N,P) Growth on Si and Decomposition Studies of the N−P Precursor Di-*tert*-butylaminophosphane (DTBAP)

Johannes Glowatzki,*,§ Oliver Maßmeyer,*,§ Marcel Köster, Thilo Hepp, Ebunoluwa Odofin, Carsten von Hänisch, Wolfgang Stolz, and Kerstin Volz

Cite This: https://dx.doi.org/10.1021/acs.organomet.0c00078 Read Online

ACCESS | Metrics & More | Article Recommendations

ABSTRACT: III/V semiconductors containing small amounts of nitrogen (dilute nitrides) are promising for applications such as lasers and solar cells. Metal−organic vapor-phase epitaxy (MOVPE) is a widely used technique for growing III/V semiconductors on an industrial scale, and the growth of dilute nitrides with this method is promising for later successful market entry. The main issues of dilute nitrides are carbon incorporation and low nitrogen incorporation efficiency of the conventional N precursors. Due to the high N incorporation efficiency and the low decomposition temperature of the As and N precursor di-*tert*-butylaminoarsane (DTBAA), a similar P- and N-containing precursor, di-*tert*-butylaminophosphane (DTBAP), was synthesized and purified on a laboratory scale. Growth studies using this precursor were carried out in this work realizing Ga(N,P)/GaP multi quantum wells on Si and GaP substrates. The structures show evidence of N incorporation, and good layer structures were confirmed by high-resolution X-ray diffraction. Following the influence of different growth parameters on the N incorporation, the growth rate and surface morphology were characterized to set a foundation for possible growth applications in the future. DTBAP shows many advantages over the conventional N source 1,1-dimethylhydrazine (UDMHy) such as a much lower decomposition temperature of 310 °C and the realization of Ga(N,P) layers grown at temperatures as low as 475 °C with a high N incorporation of over 10%. Furthermore, the gas-phase decomposition of DTBAP has been studied with a real-time fast Fourier transform quadrupole ion trap mass spectrometer attached inline to the MOVPE reactor. The decomposition of DTBAP behaves very similarly to the As analogue DTBAA. On the one hand, the *tert*-butyl groups attached to DTBAP decompose radically, leading to the formation of isobutane, and decompose, on the other hand, by *β*-H elimination, leading to the formation of isobutene. Furthermore, the decomposition products indicate a direct cleavage of the P−N bond of the molecule, resulting in the formation of aminyl radicals ($NH_2^•$). The formation of $NH_2^•$ explains the high N incorporation efficiency of DTBAP at low temperatures as well as its limitations due to loss of NH_3 at higher temperatures.

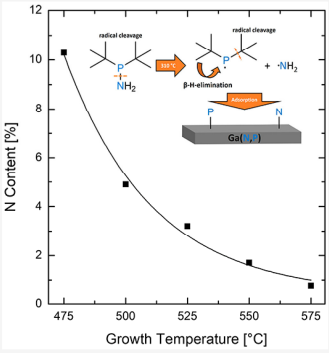

1. INTRODUCTION

GaP-based III/V semiconductors containing small amounts of nitrogen ("dilute nitrides") have been investigated because of their promising optoelectronic properties. The interaction of the nitrogen (N) level with the conduction band (band anticrossing model) leads to a strong reduction of the band gap energy.[1,2] The material system Ga(N,As,P) can be grown on silicon (Si) without relaxation and also shows direct band gap behavior.[3−5] It is a candidate for a monolithically integrated laser on Si. First optically and electrically pumped lasers were demonstrated on GaP and Si substrates, respectively.[6−8] This material class with different compositions is also a candidate for the top junction of a two-junction solar cell on Si.[9] Si as a substrate offers huge advantages in comparison to common III/V substrates. It is abundant, nontoxic, and well established in industry. In addition, solar cells, nanowires, and water-splitting solar cells were demonstrated with Ga(N,P).[10−13]

The GaP-based material systems have been grown with molecular beam epitaxy (MBE) and metal−organic vapor-phase epitaxy (MOVPE). For later realization of devices in mass production, MOVPE is a preferable method. Devices such as lasers and LEDs are produced these days with this method because of good scalability and high production output.[14] The disadvantages of MOVPE and the metal−organic precursors are the unintentional incorporation of impurities of alkyl groups and the restriction of growth temperatures because of the necessary thermal decomposition of the precursor. Large alkyl groups such as propyl and butyl groups are preferable because carbon (C) incorporation is probably more unlikely due to steric hindrance and the higher stability of the forming radicals in comparison to methyl

Received: February 5, 2020

https://dx.doi.org/10.1021/acs.organomet.0c00078
Organometallics XXXX, XXX, XXX−XXX

groups. However they also reduce the vapor pressure of the precursor. For the growth of dilute nitrides the nitrogen incorporation with the conventional precursor 1,1-dimethylhydrazine (UDMHy) is low and precursors with higher N incorporation efficiency are desirable.[15]

A novel arsenic (As)- and N-containing precursor (di-*tert*-butylaminoarsane, DTBAA) for the growth of GaAs-based dilute nitrides was investigated in the last few years and showed a high N incorporation in Ga(N,As), (Ga,In)(N,As), and Ga(N,As,Sb) and a low decomposition temperature.[16−19] On the basis of the experience with this precursor a similar N- and phosphorus (P)-containing precursor (di-*tert*-butylaminophosphane, DTBAP) was synthesized and tested in the function of a precursor for MOVPE.

To get further insight into the N incorporation of the novel precursor its thermal decomposition has been studied. Like the As analogue DTBAA DTBAP exhibits a N−group V bond instead of a direct C−N bond and the C is only present in large alkyl groups. Due to prevention of the strong C−N bond and steric restriction of the large alkyl groups it is expected that C incorporation will be reduced in the growing layers using these novel precursors.[20] In this regard the precursors should have an advantage in comparison to the commonly used N precursor 1,1-dimethylhydrazine (UDMHy). UDMHy exhibits strong N−N and C−N bonds as well as small alkyl groups. As shown in former decomposition studies, this leads to formation of CH_4, N_2, and larger stable fragments such as $(CH_3)_2NH$ and CH_3NCH_2 upon decomposition.[21] These fragments probably lead to comparably high C incorporation and low N incorporation efficiencies due to the high bond strength, especially for use at low growth temperatures.

In the following the synthesis, growth, and mass spectrometer results of the novel precursor DTBAP are presented. In the beginning N incorporation in GaP on Si substrates will be demonstrated and systematic investigations of the dependence on growth temperature and triethylgallium (TEGa), *tert*-butylphosphane (TBP), and DTBAP partial pressures will be shown. Subsequently the growth on GaP will be demonstrated and compared to the growth on Si. Finally, thermal decomposition studies of DTBAP via mass spectrometry will be shown.

2. SYNTHESIS OF tBu$_2$PNH$_2$ (DTBAP)

An early synthesis of tBu$_2$PNH$_2$ was performed by Scherer and Schieder in 1968.[22] In a first reaction of the Grignard reagent tBuMgCl with PCl_3 the compound tBu$_2$PCl was prepared. This reactant was aminated with gaseous ammonia to give the desired product tBu$_2$PNH$_2$.[22] The synthesis is sketched in Scheme 1.

2.1. General Considerations. All working procedures were conducted under rigorous exclusion of oxygen and moisture using a Schlenk line and nitrogen/argon atmosphere. Solvents were dried and freshly distilled before use. The starting materials tBuCl and PCl_3 were purchased from Acros Organics, and magnesium was obtained from Sigma-Aldrich. NMR (nuclear magnetic resonance) spectra were recorded on a Bruker AvanceHD 300 instrument with the following multiplicities: s = singlet, d = doublet.

2.2. tBu$_2$PCl. A solution of tBuCl (55.1 mL, 0.50 mol, 2.5 equiv) and 150 mL of diethyl ether was added dropwise to a suspension of magnesium (12.2 g, 0.50 mol, 2.5 equiv) and 200 mL of diethyl ether at room temperature. This Grignard solution was then added dropwise to a solution of PCl_3 (17.5 mL, 0.20 mol, 1.0 equiv) in 400 mL of diethyl ether at −40 °C. After the mixture was warmed to rt, the formed precipitate was filtered and washed twice with 40 mL portions of *n*-pentane. Removal of the solvent *in vacuo* provided the raw product as a colorless liquid which was purified via fractional distillation at 10 mmHg at 63 °C (18.0 g, 0.10 mol, 50% yield). ^{1}H NMR (300.13 MHz, C_6D_6): δ/ppm 1.09 [d, $^3J_{HP}$ = 12.1 Hz, 18H, CH_3]. ^{13}C{^{1}H}-NMR (75.47 MHz, C_6D_6): δ/ppm 27.9 [d, $^2J_{CP}$ = 17.1 Hz, CH_3], 35.9 [d, $^1J_{CP}$ = 41.3 Hz, C_{quart}]. ^{31}P{^{1}H}-NMR (121.54 MHz, C_6D_6): δ/ppm 148.1 [s, *P*Cl].

2.3. tBu$_2$PNH$_2$. Gaseous ammonia was passed through a solution of tBu$_2$PCl (10 g, 0.55 mol, 1.0 equiv) and 10 mL of diethyl ether for 1 h at −50 °C. The resulting precipitate was filtered after it was warmed to rt and washed twice with 10 mL portions of *n*-pentane. Removal of the solvent *in vacuo* provided the raw product as a colorless liquid which was purified via fractional distillation at 5 mmHg and 55 °C (8.06 g, 0.50 mol, 90% yield). ^{1}H NMR (300.13 MHz, C_6D_6): δ/ppm 0.92 [s, 2H, N*H*], 1.03 [d, $^3J_{H,P}$ = 11.2 Hz, 18H, CH_3]. ^{13}C{^{1}H}-NMR (75.47 MHz, C_6D_6): δ/ppm 28.1 [d, $^2J_{C,P}$ = 15.4 Hz, CH_3], 33.0 [d, $^1J_{C,P}$ = 21.5 Hz, C_{quart}]. ^{31}P{^{1}H}-NMR (121.54 MHz, C_6D_6): δ/ppm 63.0 [s, *P*NH_2].

Scheme 1. Synthesis of tBu$_2$PNH$_2$ (DTBAP)

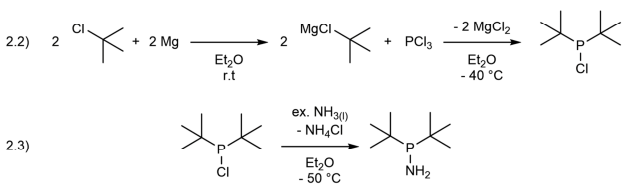

3. GROWTH AND CHARACTERIZATION OF Ga(N,P)-CONTAINING SAMPLES

All samples were grown using MOVPE. An AIXTRON AIX 200 reactor system with gas foil rotation was used. The reactor pressure was held at 50 mbar under a total gas flow of 6800 sccm for all experiments. Palladium cell purified hydrogen (purity: 9.0) was used as the carrier gas. *tert*-Butylphosphane (TBP), triethylgallium (TEGa), and DTBAP were used as precursors. The vapor pressure of the novel precursor DTBAP was unknown at the beginning of the experiments and was estimated via consumption calculations afterward to be around 1 mbar at 20 °C. The samples were grown either on exact semiinsulating Si (001) substrates with a 28 nm GaP nucleation on top or on exact semiinsulating GaP (001) substrates. For a high-quality surface both substrates were processed with a pretreatment. The GaP/Si substrate was heated (unstabilized and TBP stabilized) and a thin 12 nm GaP buffer was grown under optimized conditions at 675 °C. A thicker buffer was not possible because of relaxation at large GaP thickness. The GaP substrate was processed with different etching steps before pretreatment in the reactor. The samples were heated and afterward overgrown with a 250 nm thick GaP buffer. Test structures were grown to determine the N incorporation as three times multi quantum wells (MQWs) at temperatures between 475 and 575 °C. Cooling after buffer growth was done under TBP stabilization to prevent P desorption. Between 7 and 21 nm thick Ga(N,P) QWs and thin 7−11 nm GaP barriers were grown. Thicker barriers were avoided to prevent the samples from relaxation. The structure

https://dx.doi.org/10.1021/acs.organomet.0c00078
Organometallics XXXX, XXX, XXX−XXX

was always finished with a QW and cooled to 350 °C under TBP stabilization to determine the surface morphology realistically. The TEGa, DTBAP, and TBP partial pressures and also the growth temperature were varied systematically and the influence on the N incorporation, growth rate, and surface morphology were investigated.

The surface morphology of the samples was investigated using a Nanoscope IIIa atomic force microscopy (AFM) setup from Digital Instruments. The AFM images shown have a size of 5 × 5 μm.

The structure of the samples was investigated using a Panalytical X'Pert Pro high-resolution X-ray diffraction (HRXRD) system with a Cu anode monochromated to the Cu K_α line (wavelength of 0.15405 nm). By measurements around the substrate (Si or GaP) (004) reflection and dynamic simulations of the diffractograms with the X'Pert Epitaxy smooth and fit software the N content and growth rate of the Ga(N,P) layers could be determined. At different times during the experiments, samples with nominally the same growth conditions were prepared to ensure reproducibility and obtain the error for different growth runs. The growth conditions were as follows: T_{gr} = 525 °C, P_p(TBP) = 0 mbar, P_p(TEGa) = 7.1 × 10^{-3} mbar, and P_p(DTBAP) = 1.8 × 10^{-2} mbar. The average N content of these samples is 2.12% with a standard deviation of 0.13%. As this value is larger than the estimated error from the simulations, this value is taken as the error for the compositions. For the growth rate the estimated error of the simulations leads to an error of 0.01 nm/s for the growth rate, if not noted differently.

4. MASS SPECTROMETER MEASUREMENTS OF DTBAP

To study the thermal decomposition of DTBAP, a quadrupole ion trap mass spectrometer from Carl Zeiss GmbH (iTrap) was used in line with the MOVPE system. The setup is designed to achieve measurement conditions as close to realistic growth conditions as possible and has been successfully used for gas-phase investigations of *tert*-butylarsane (TBAs) and DTBAA before.[16,23] The ion trap uses standard electron impact ionization with 70 eV for ion generation. The ions were then captured by an oscillating electric field applied to the ring electrode of the ion trap. The frequency of the oscillation used is within the radio frequency (RF) range. The mass range of interest can be selected by the adjustment of the applied RF voltage, which changes the strength of the electric field. Due to the oscillations of the ions within the trap an induced mirror image current within the top and bottom electrodes of the trap can be measured. This current signal was then analyzed by fast Fourier transformation, which enabled recording times for a single mass spectrum below 2 s. Therefore, the setup is suitable for real time analysis during the MOVPE process and the fast measurement times allow high data point densities and good statistics. Generally, quadrupole ion traps offer high sensitivity leading to detection of impurities in the parts per trillion concentration level with this setup.[24]

Due to the setup, the precise measurement of the gas-phase temperature at the point of gas collection was not possible and only the surface temperature of the susceptor was measured. By correlation of TBAs decomposition curves from ref 23 with data taken from ref 25 the gas-phase temperature was determined.

5. RESULTS AND DISCUSSION

The following part is organized as follows. In the beginning the first evidence of nitrogen incorporation in GaP on the Si substrate will be shown and experiments with varying growth conditions will follow. Furthermore, Ga(N,P) growth on GaP substrates will be shown and compared to growth on Si substrates. Finally mass spectrometer measurements and decomposition curves of the DTBAP will be shown.

5.1. MOVPE Growth Experiments on Si. The first evidence of Ga(N,P) growth including sufficient nitrogen incorporation using DTBAP was obtained with HRXRD for all investigated samples.

As an example, the HRXRD diffractogram and dynamic simulation of one sample grown with a partial pressure of DTBAP of 1.8 × 10^{-2} mbar and a TEGa partial pressure of 7.1 × 10^{-3} mbar without TBP at a growth temperature of 525 °C are shown in Figure 1.

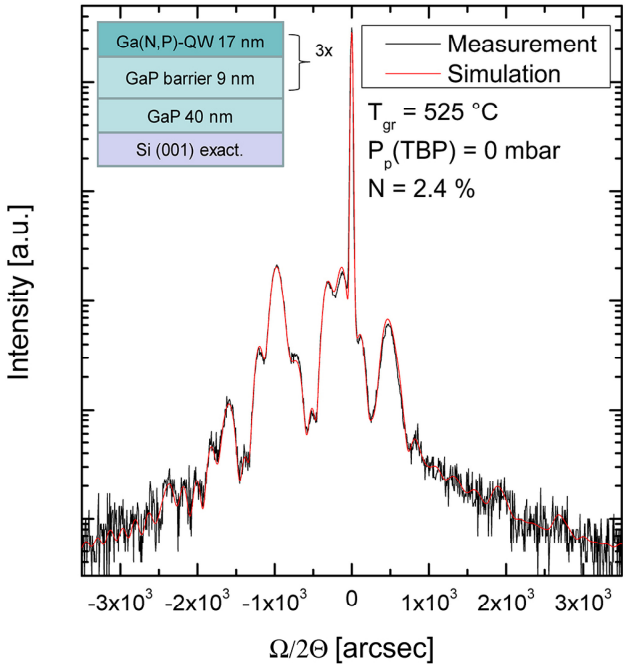

Figure 1. Example of an HRXRD diffractogram of a Ga(N,P)/GaP multiquantum well on Si with dynamic simulation.

Simulation and measurement are in good agreement, and all fringes are resolved well, which indicates high-quality layers. If not noted otherwise, all samples show good HRXRD measurements. Thus, in the following only the N content and growth rate are plotted.

In Figure 2 the N incorporation and the growth rate are plotted versus the TBP partial pressure for two different DTBAP partial pressures. For all samples the TEGa partial pressure as well as the growth temperature were kept constant (7.1 × 10^{-3} mbar and 525 °C, respectively). An additional supply of TBP during growth reduces the N incorporation. The highest N incorporation was obtained using no TBP and a higher DTBAP partial pressure, while the N incorporation was reduced for lower DTBAP partial pressure and no TBP. This also means that no additional P source is needed and DTBAP delivers both elements N and P simultaneously. This behavior was also seen for the As analogue DTBAA. In this case

https://dx.doi.org/10.1021/acs.organomet.0c00078
Organometallics XXXX, XXX, XXX−XXX

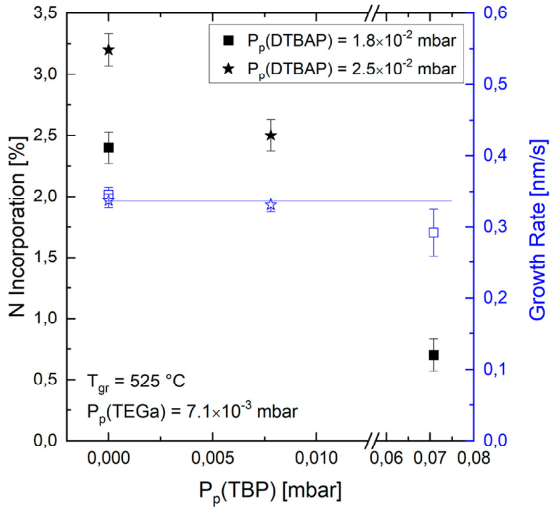

Figure 2. N incorporation and growth rate in dependence of the TBP partial pressure. DTBAP and TEGa partial pressures and growth temperature were kept constant.

Ga(N,As) layers on GaAs were realized without an additional As source.[19]

The N incorporation is low compared to the P incorporation, which means that P is much more efficiently incorporated. This can be related to the metastability of Ga(N,P) grown on GaP. Under equilibrium conditions the solubility of N in GaP is in the parts per million level. Only due to the growth far from equilibrium can N incorporation in GaP be realized, as is done in MOVPE.[26,27] Also additional P from the TBP is competing for the group V lattice sites and further reduces the N incorporation. The N/P ratio seems to be crucial for the N incorporation, as is also seen for growth studies of Ga(N,P) with UDMHy and for the growth of Ga(N,As) with the As analogue DTBAA.[15,19] The TBP partial pressure has no influence on the growth rate, since the group III supply should be growth-limiting under these conditions. This means also that the effective V/III ratio is larger than 1.

Since there is no need to add TBP and the highest N incorporation was reached without TBP, further experiments were carried out without TBP. The DTBAP partial pressure was varied systematically at a growth temperature of 525 °C while TEGa partial pressure was kept constant (7.1×10^{-3} mbar). The results of this experiment are shown in Figure 3a.

Increasing the DTBAP partial pressure increases the N incorporation linearly. There are many reasons this dependence could happen. As was mentioned before, the N/P ratio seems to be crucial for N incorporation but the N/P ratio is fixed to unity in the molecule itself. However, gas-phase reactions in combination with surface and catalytic reactions could lead to varying N/P ratios dependent on the DTBAP partial pressure and the (N + P)/Ga ratio. One can also consider the influence of the surface reconstruction, which may change depending on the (N + P)/Ga ratio. A change of the surface reconstruction on the V/III ratio has been widely studied for GaAs (001) surfaces and is also seen for GaP (001) surfaces.[28−31] Even an increase in the N incorporation on more Ga rich surfaces has been seen for Ga(N,As) grown in GaAs as well as has been predicted for Ga(N,P).[32,33] The complete mechanism behind this incorporation behavior remains unclear and has to be investigated in the future in more detail.

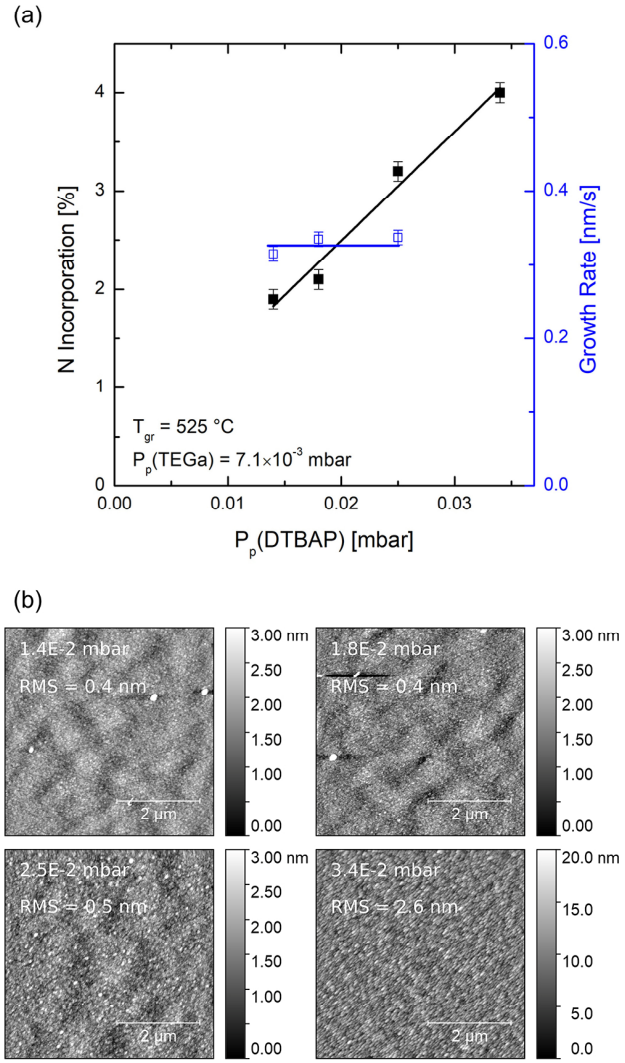

Figure 3. (a) N incorporation and growth rate dependence on the DTBAP partial pressure. The TEGa partial pressure and growth temperature were kept constant, and no TBP was added. (b) AFM images (size 5 × 5 μm) of some samples from (a). DTBAP partial pressures and RMS values are given as insets.

Furthermore, the growth rate does not seem to change, which is expected because of the same reasons mentioned before in the discussion of Figure 2. AFM images from the surfaces of the samples grown with different DTBAP partial pressures are shown in Figure 3b. At lower amounts of DTBAP the surfaces are flat and show a small roughness but there are some larger three-dimensional (3D) structures on it. Most likely these are Ga droplets occurring because of a low effective (N + P)/Ga ratio. The sample grown with P_p(DTBAP) = 2.5×10^{-2} mbar is smooth without 3D features but is rougher than the surfaces mentioned before. A higher P_p(DTBAP) leads to a very rough surface with 3D islandlike structures. In addition, the HRXRD measurement of this sample showed a single Ga(N,P) layer instead of a three times multi quantum well structure. Probably due to high strain the growth mode changed and only highly defective layers were deposited after a specific thickness.

Further the TEGa partial pressure was varied systematically at a growth temperature of 525 °C and a fixed DTBAP partial pressure of 1.8×10^{-2} mbar. The N incorporation and growth

https://dx.doi.org/10.1021/acs.organomet.0c00078
Organometallics XXXX, XXX, XXX−XXX

rate are plotted in Figure 4. With increasing TEGa partial pressure the N incorporation decreased and the last data point

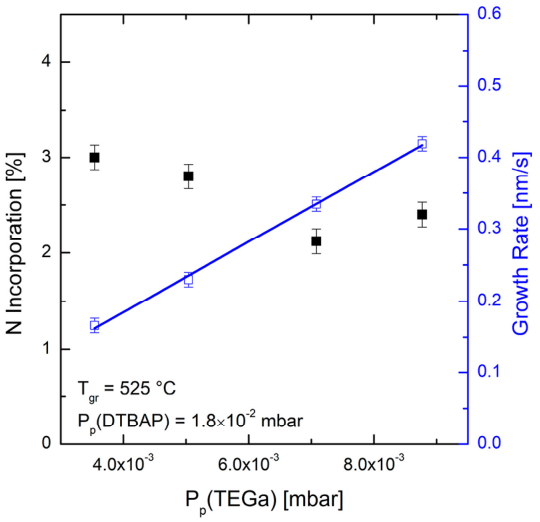

Figure 4. N incorporation and growth rate dependent on the TEGa partial pressure. The DTBAP partial pressure and growth temperature were kept constant, and no TBP was added.

remained constant within the error or even increased again. Possible explanations for the decreasing N content could be most likely the lowering of the (N + P)/Ga ratio that resulted in a lower N incorporation as seen in Figure 3a. In addition a constant sticking coefficient at a certain temperature of the active N species could explain this behavior, since by increasing the growth rate less N can be incorporated due to the shorter period of time per monolayer growth.

The increased N incorporation at higher TEGa partial pressures perhaps originates from a change in the surface reconstruction at low V/III ratios. At low V/III ratios the surface can change to a more Ga rich surface reconstruction.[30,31] For these more Ga rich surfaces an enhanced N incorporation has been predicted in the literature and some evidence for this has been seen for growth of Ga(N,As) on GaAs (001) surfaces.[32,33] The growth rate is increasing proportionally to the TEGa partial pressure due to the growth-limiting character of the group III supply in the group V rich growth regime.

While the gas phase composition was kept constant, the growth temperature was changed systematically. The DTBAP and the TEGa partial pressures were kept constant at 2.5 × 10^{-2} mbar and 7.1 × 10^{-3} mbar, respectively. In Figure 5a the N content and the growth rate are plotted versus the growth temperature. The N incorporation is increasing exponentially (exponential behavior is discussed later in section 5.3) with a decrease in the growth temperature, and a N content of about 10% was reached at a growth temperature of 475 °C. Growth with this amount of N at this low temperature has not been reported for MOVPE growth with the conventional N precursor UDMHy.[15] By further optimization of the growth conditions even higher N contents should be realizable, which could compete with N fractions of up to 16% realized in Ga(N,P) layers grown by MBE.[34] This exponential behavior of the N incorporation implies a thermally activated loss process with an activation energy, which will be shown in section 5.3. One can think of loss processes such as desorption of the active

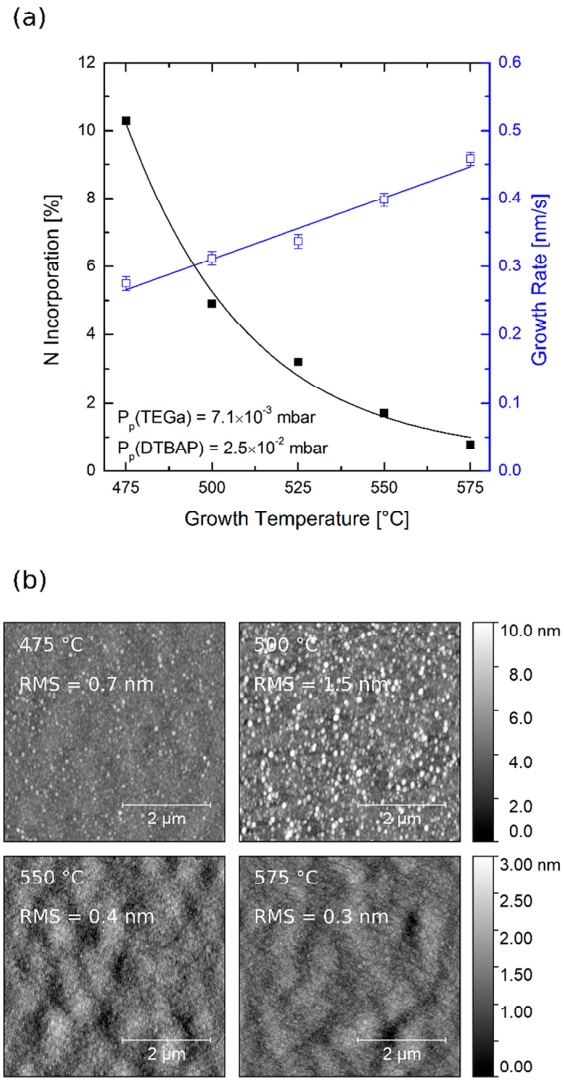

Figure 5. (a) N incorporation and growth rate dependent on the growth temperature. TEGa and DTBAP partial pressures were kept constant, and no TBP was added. (b) AFM images (size 5 × 5) of some samples from (a). Temperature and RMS values are given as insets.

nitrogen species from the surface or a loss due to gas-phase reactions of the active species to more stable products, which are not incorporated efficiently. This idea is supported by formation of aminyl radicals ($NH_2^•$) that form upon decomposition. $NH_2^•$ is likely to form NH_3, which could prevent N incorporation at higher temperatures and will be discussed in section 5.3. The growth rate is increasing linearly with the growth temperature. Possibly there is a larger supply of the growth-limiting group III species due to a higher diffusion rate from the boundary layer to the surface. Higher decomposition of the Ga precursor should not be the reason, since the decomposition temperature in our reactor is measured as 250 °C, which is in agreement with the literature data for TEGa.[35,36] The desorption of surface-blocking alkyl groups could also explain the increase in growth rate. The site blocking seems to be the most likely explanation, since it has been studied in different growth experiments with MOVPE.[37−39] In Figure 5b 5 × 5 μm AFM images of the

https://dx.doi.org/10.1021/acs.organomet.0c00078
Organometallics XXXX, XXX, XXX−XXX

surfaces from samples grown at different temperatures are shown. For higher temperatures the surfaces do not show steps or an otherwise distinct morphology but they are smooth with wavylike modulation in the micrometer lateral range. The wavylike modulation can be directly related to nucleation of the GaP on the Si substrate, as it is not seen on GaP substrates. This will be shown in section 5.2. For lower growth temperatures, the surfaces are rougher and show 3D features on top and the underlying surfaces are looking similarly smooth as the samples grown at higher temperatures. Roughening of the surface and 3D island formation could be related to the higher N content and the lower diffusion rate on the surface with decreased temperature. In addition samples of the TEGa and DTBAP partial pressure series, which are discussed in Figure 3a, showed rougher surfaces and similar (but smaller) 3D features for higher N contents. It is remarkable that the surface got smoother and showed fewer 3D features for the lowest growth temperature with the highest amount of N. Probably the formation of these 3D features is related to the strain induced by the high N content and the high miscibility gap in this metastable material system. Additionally, an activation energy should be necessary for the change in growth mode from 2D to 3D growth which occurs at higher temperatures. Thus, the formation seems to be both temperature as well as strain induced.

5.2. MOVPE Growth Experiments on GaP. In addition to the growth experiments on GaP/Si, a few samples were grown under similar growth conditions on GaP substrates for comparison. AFM images (size 5 x 5 μm) of samples grown under same conditions on GaP/Si and GaP substrates are shown in Figure 6.

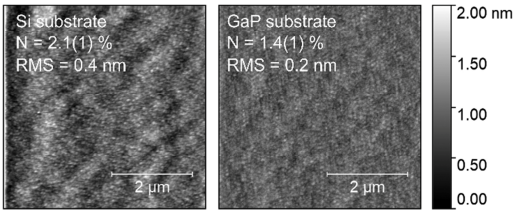

Figure 6. AFM images (size 5 x 5 μm) of samples grown under the same growth conditions but on different substrates (Si vs GaP). The growth conditions are P_p(TEGa) = 7.1 × 10^{-3} mbar, P_p(DTBAP) = 2.5 × 10^{-2} mbar, and T_g = 525 °C. In the AFM images the N incorporation and the RMS values are shown.

The surfaces look very similar, but the sample grown on GaP/Si shows a wavylike modulation in the micrometer lateral range as mentioned above and the sample grown on GaP does not show these modulations. This implies that these modulations occur due to the growth on Si. The N incorporation of 2.1 ± 0.1% in layers grown on GaP/Si is significantly higher than that on GaP (1.4 ± 0.1%). In general, the effects of lattice pulling and lattice latching have been described in the literature and can describe the observed incorporation effect. The epitaxial growth of thin layers with a lattice constant different from that of the substrate introduces a strain energy due to lattice deformation, which increases the total free energy of the system. One way to reduce the total free energy is a change in the alloy composition and, therefore, a change in lattice constant and mismatch.[39] For the material system (Ga,In)P the effect of lattice mismatch on the composition of the solid was investigated in 1972 for the liquid-phase epitaxy method.[40] Lattice pulling effects were also seen in the MOVPE growth of (Ga,In)N on GaN and also for the dilute nitride material system (Ga,In)(N,As) on (Ga,In)-As.[41,42] An effect of lattice mismatch on solid composition was also seen for MOVPE grown Ga(N,As) on GaP. In contrast to the growth on GaAs the N incorporation was improved drastically by a factor of about 10. This was explained by the compressive strain of Ga(N,As) on GaP up to a fraction of 17.8% N which results in strain compensation. In contrast N incorporation results in tensile strain over the whole composition window for Ga(N,As)/GaAs.[43] In this study the compressive strain of Ga(N,P) on Si up to a N content of around 2% also leads to the lattice pulling effect and allows a higher incorporation due to the strain-compensating effect of N at these compositions. This is in contrast to the growth on GaP, where N incorporation introduces tensile strain for every composition.

5.3. Decomposition Studies via Mass Spectrometry. To provide a deeper insight into the N incorporation behavior into Ga(N,P), the thermal decomposition of DTBAP (161 u) has been investigated with an ion trap connected to the MOVPE system. The detected mass spectrum at a temperature of 50 °C for a supplied partial pressure of 3 × 10^{-3} mbar is shown in Figure 7a. For comparison the detected intensities

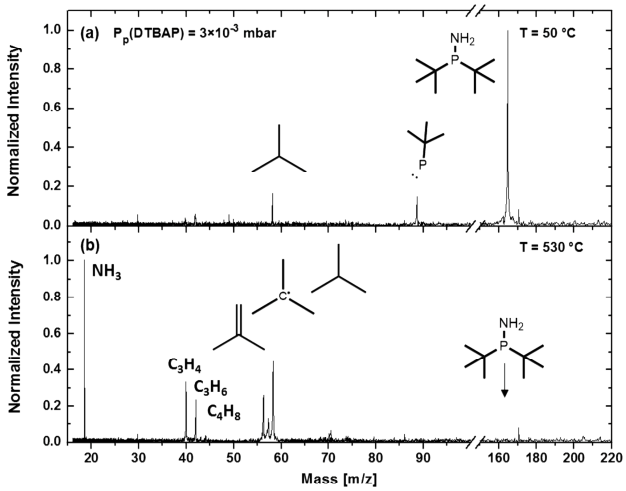

Figure 7. Detected mass spectra of DTBAP (161 u) at different temperatures for a partial pressure of 3 × 10^{-3} mbar. (a) Electron-induced fragmentation of DTBAP at 50 °C. Due to a comparably low filament current of 1.3 A and a short time between the gas inlet and the ionization with 70 eV, only a few fragments with low intensity are detected. (b) Decomposition spectrum of DTBAP at 530 °C. Mainly isobutane (58 u), *tert*-butyl radicals (57 u), isobutene (56 u), and NH_3 (17 u) are detected. The detected carbon chains at 40, 42, and 44 u can be attributed to electron-induced fragmentation of isobutane and isobutene.

are normalized to the signal of DTBAP at 161 u. At this temperature no decomposition occurs and all fragmentation products within this figure are induced by electron impact ionization. Using optimized parameters within the ion trap, the electron-induced fragmentation is reduced to a minimum. Therefore, most DTBAP molecules are not fragmented by the electrons and only a few fragments such as isobutane (58 u) and probably $C_4H_9P^{\bullet\bullet}$ (88 u) are visible. This simplifies the interpretation of the DTBAP decomposition.

https://dx.doi.org/10.1021/acs.organomet.0c00078
Organometallics XXXX, XXX, XXX−XXX

The thermally induced decomposition of DTBAP at a temperature of 530 °C can be seen in Figure 1b. The intensity of DTBAP completely vanishes at this temperature, indicating complete decomposition of the DTBAP. As fragments mainly isobutane (58 u), *tert*-butyl radicals (57 u), isobutene (56 u), and NH_3 (17 u) are detected. These can all be attributed to thermal decomposition. Isobutane and *tert*-butyl radicals are the products of radical decomposition of the C−P bond within the molecule. This radical cleavage leads to the formation of *tert*-butyl radicals that can react with available H radicals or H_2 to form isobutane. Furthermore, there is the possibility of an intramolecular coupling reaction of the *tert*-butyl group with an H atom of the aminyl group, resulting in formation of isobutane. These reaction pathways have been predicted by density functional theory calculations for the As analogue DTBAA and are on the one hand shown in decomposition studies of this precursor. On the other hand these pathways are also known for other metal−organic precursors with *tert*-butyl groups such as TBAs.[16,25,44] Another expected reaction pathway of the *tert*-butyl groups is decomposition through *β*-H elimination. In this case a H atom at one of the C atoms in a *β* position within the *tert*-butyl group interacts with the p orbitals of the phosphorus atom of the same molecule. This leads to the formation of a C=C double bond (formation of isobutene) and a PH group. The corresponding reaction scheme can be found in ref 16 for the DTBAA molecule. *β*-H elimination seems to be a relevant decomposition pathway of at least one of the *tert*-butyl groups of the DTBAP, since isobutene was detected within the same magnitude as that for the *tert*-butyl radicals and the isobutane.

In the decomposition spectrum also lighter alkyl groups are visible. From former investigations of appropriate test gases, the intensities of the smaller alkyl chains around 42 and 40 u can be attributed to electron-induced fragmentation of isobutane and isobutene. The test gases have been investigated under the same ion trap settings and showed formation of propene (42 u) and propyne (40 u) in the case of isobutane and formation of propyne (40 u) for isobutene.

Additionally, NH_3 was detected with the same intensity as that for DTBAP. The detected NH_3 is attributed to the formation of aminyl radicals ($NH_2^\bullet$ 16 u) during the decomposition of DTBAP and was also observed as a decomposition product of DTBAA.[16] This indicates a radical decomposition of the N−P bond of the molecule, which leads to the formation of $NH_2^\bullet$ and DTBP$^\bullet$ (145 u). No evidence for DTBP$^\bullet$ has been found within this measurement, but the As analogue DTBA$^\bullet$ has been detected in the case of DTBAA. Therefore, it is expected that the DTBP$^\bullet$ fragments are either less stable or more reactive in comparison to DTBA$^\bullet$ in the decomposition of DTBAA. Either this is caused by dissociation into isobutane, *tert*-butyl radicals, isobutene and P or the DTBP$^\bullet$ adsorbs first to an available surface before dissociation and is therefore not detectable within the ion trap. No further fragments containing P have been measured. Any elemental P arising from the reaction would react to give P_2 or P_4, which is seen as a coating of the liner in the reactor. The $NH_2^\bullet$ radicals formed explain to some extent the N incorporation behavior seen in Figure 5a. At high temperatures $NH_2^\bullet$ is very likely to form NH_3 in the presence of H_2 or H$^\bullet$ and can therefore easily desorb from the growth surface or be generated in the gas phase. For low temperatures $NH_2^\bullet$ radicals are more likely to stick to the surface, leading to the efficient incorporation of N. These considerations lead to the predicted decomposition pathway for P incorporation shown in Scheme 2. The aminyl radicals are expected to be incorporated at low temperatures.

Scheme 2. Proposed Reaction Pathway

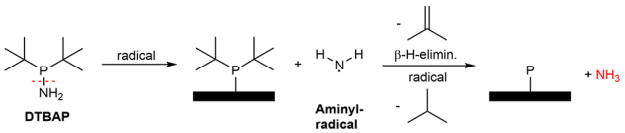

The temperature-dependent decomposition of DTBAP is shown in Figure 8. All major decomposition products

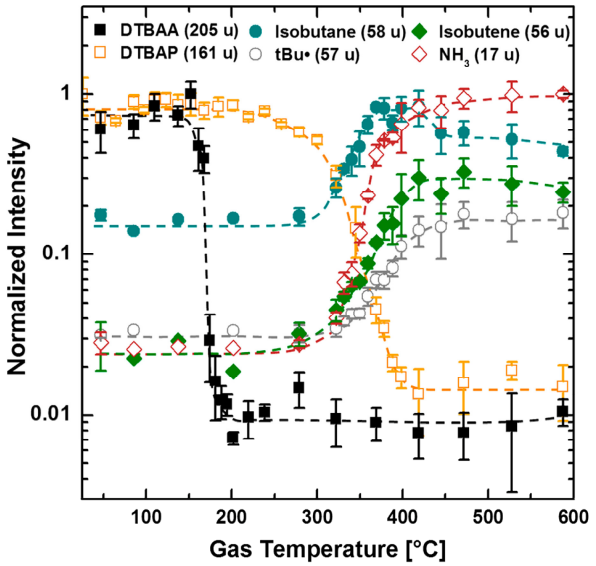

Figure 8. Decomposition curves of DTBAP (161 u) and DTBAA (205 u) for partial pressures of 3×10^{-3} mbar and 2.5×10^{-3} mbar, respectively. The most relevant decomposition fragments isobutane (58 u), *tert*-butyl radicals (57 u), isobutene (56 u), and NH_3 (17 u) of the DTBAP decomposition are included. Data of DTBAA from ref 16 measured within the same reactor are included as a comparison.

discussed above are included. As a comparison the decomposition curve of the As analogue DTBAA is included from ref 16. In comparison to DTBAA (T_{decomp} = 160 ± 10 °C) the DTBAP decomposes at a higher temperature of T_{decomp} = 310 ± 10 °C, which is defined as the point where the DTBAP signal drops to half of its intensity. This change in decomposition temperature is known, for example, for precursors such as TBAs (T_{decomp}* = 350 ± 10 °C) in comparison to TBP (T_{decomp}* = 400 ± 10 °C). (Values marked by * measured within the same reactor system. These determined temperatures are 30−50 °C lower in comparison to values from refs 25 and 45. This might be caused by the different experimental setups, different surface areas within the experiment, or different temperature measurement.) Immediately as the DTBAP decomposes, the intensities of isobutane, *tert*-butyl radicals, isobutene and NH_3 are increasing. Regarding the decomposition of the *tert*-butyl groups the radical or intramolecular coupling reaction seems to be the most relevant pathway over the whole temperature range, since isobutane summed together with the *tert*-butyl radicals shows the highest intensities. Nevertheless, the isobutane signal drops again for higher temperatures of around 450 °C. This shows

https://dx.doi.org/10.1021/acs.organomet.0c00078
Organometallics XXXX, XXX, XXX−XXX

similarly to the DTBAA decomposition that one of the radical pathways might be hindered and the β-H elimination reaction becomes more relevant above this temperature. This is shown by the isobutene intensity, which is still increasing, while the isobutane intensity is already constant and remains stable within the same magnitude at higher temperatures.

An Arrhenius plot of the DTBAP decomposition data from Figure 8 and the nitrogen incorporation data from Figure 5a is shown in Figure 9. From the linear regression one can extract

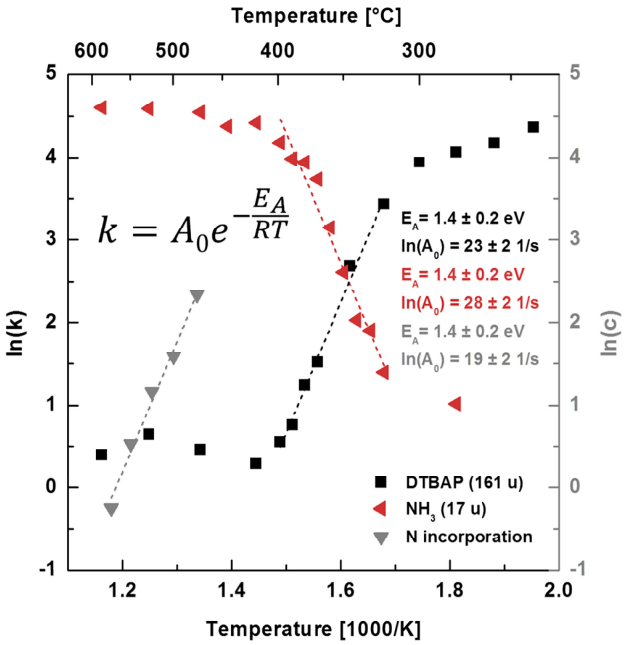

Figure 9. Arrhenius plot of the detected intensities of DTBAP and NH_3 together with the N concentration from Figure 5a. Activation energies and attempt frequency factors A_0 for the decomposition and N incorporation can be determined from the slope according to the Arrhenius equation shown in the inset.

the activation energies as well as the pre-exponential attempt frequency factors A_0. The activation energies of the DTBAP decomposition and the NH_3 production as well as the N incorporation are all determined with 1.4 ± 0.2 eV. The attempt frequency factors are 23 ± 2 1/s for DTBAP, 28 ± 2 1/s for NH_3, and 19 ± 2 1/s for the N incorporation, which are all within a similar frequency. Notably the agreement in activation energies supports the assumption, on the one hand, that the N−P bond breaks within the first step of the DTBAP decomposition, leading to the formation of the aminyl radicals ($NH_2^\bullet$) and, on the other hand, that the formation of the aminyl radicals ($NH_2^\bullet$) is directly related to the N incorporation. As mentioned above, at low temperatures $NH_2^\bullet$ is likely to stick to the growth surface, leading to N incorporation. At higher temperatures $NH_2^\bullet$ can react with available H_2 or $H^\bullet$ radicals to form NH_3, which is stable under these conditions. This could enhance the desorption rate of N from the surface or prevent the adsorption to the surface by formation within the gas phase. These findings could fully explain the exponential dependence of N incorporation in Ga(N,P) on the growth temperature discussed in Figure 5a.

6. SUMMARY

In this work the novel N and P precursor di-*tert*-butylaminophosphane (DTBAP) was introduced and the very first MOVPE growth experiments and gas-phase decomposition measurements were carried out. The first evidence of significant N incorporation in GaP on Si and GaP substrates, resulting in good structural quality samples, was shown. The growth parameters were varied systematically, and the influence on N incorporation, growth rate, and surface morphology were determined to create a foundation for further growth studies aiming toward device applications.

Offering the additional P precursor TBP leads to a lowering of N incorporation due to competition for group V lattice sites and a decreasing N/P ratio. Increasing the amount of TEGa leads to a linear increase in growth rate and for higher V/III ratios to a decrease in N incorporation.

As for the precursor DTBAA, an increasing partial pressure of DTBAP leads to a linear increase in N incorporation. Since the N/P ratio is fixed to unity within the molecule, this is unexpected on first sight. Some mechanisms were discussed, but this behavior has to be checked in future experiments to give a reliable answer.

Increasing the growth temperature leads to an exponential decrease of N incorporation in the grown Ga(N,P) samples. As possible reasons thermally activated loss processes of the active nitrogen species due to desorption or gas-phase reactions were discussed. These correlate to the formation of aminyl radicals found in the decomposition study of DTBAP. The observed linear increase in growth rate is most likely related to a partial surface blocking by adsorbed alkyl groups at low temperatures. Additionally, a N content of over 10% was confirmed with HRXRD for a growth temperature of 475 °C, which has not been realized for Ga(N,P) samples grown by MOVPE before. Nitrogen incorporation on the Si substrate was significantly higher than that on GaP, which is related to lattice-pulling effects caused by the strain compensation for growth on Si.

The decomposition temperature of DTBAP was determined with T_{decomp} = 310 °C from the decomposition curve, which makes it suitable for low-temperature growth in MOVPE. The decomposition studies suggest for DTBAP the same reaction pathway as for DTBAA.[16] The *tert*-butyl groups either undergo radical and intramolecular coupling reactions leading to formation of isobutane and *tert*-butyl radicals or dissociate from the molecule by β-H elimination, which is detected by the appearance of isobutene. These larger alkyl groups, especially the stable isobutene, should lead to lower C incorporation into the growing layer in comparison to structures grown with UDMHy. Furthermore, the N−P bond of DTBAP decomposes radically under the formation of aminyl radicals ($NH_2^\bullet$). The $NH_2^\bullet$ radicals seem to be directly related to the N incorporation. This is shown by the activation energy of 1.35 eV for N incorporation from the growth studies, which is in agreement to the one obtained from $NH_2^\bullet$ formation during thermal decomposition. Therefore, $NH_2^\bullet$ should explain the high N incorporation at low temperatures due to adsorption of $NH_2^\bullet$. On the other hand, formation of NH_3 in the gas phase or at the surface leads to prevention of N incorporation at higher temperatures.

https://dx.doi.org/10.1021/acs.organomet.0c00078
Organometallics XXXX, XXX, XXX−XXX

Organometallics pubs.acs.org/Organometallics Article

AUTHOR INFORMATION

Corresponding Authors

Johannes Glowatzki − *Material Sciences Center and Department of Physics, Philipps-Universität Marburg, 35032 Marburg, Germany;* orcid.org/0000-0002-8440-2271; Email: Johannes.Glowatzki@physik.uni-marburg.de

Oliver Maßmeyer − *Material Sciences Center and Department of Physics, Philipps-Universität Marburg, 35032 Marburg, Germany;* orcid.org/0000-0001-6101-5706; Email: Oliver.Maßmeyer@physik.uni-marburg.de

Authors

Marcel Köster − *Material Sciences Center and Department of Chemistry, Philipps-Universität Marburg, 35032 Marburg, Germany*

Thilo Hepp − *Material Sciences Center and Department of Physics, Philipps-Universität Marburg, 35032 Marburg, Germany*

Ebunoluwa Odofin − *Material Sciences Center and Department of Physics, Philipps-Universität Marburg, 35032 Marburg, Germany*

Carsten von Hänisch − *Material Sciences Center and Department of Chemistry, Philipps-Universität Marburg, 35032 Marburg, Germany*

Wolfgang Stolz − *Material Sciences Center and Department of Physics, Philipps-Universität Marburg, 35032 Marburg, Germany*

Kerstin Volz − *Material Sciences Center and Department of Physics, Philipps-Universität Marburg, 35032 Marburg, Germany*

Complete contact information is available at: https://pubs.acs.org/10.1021/acs.organomet.0c00078

Author Contributions

[§]J.G. and O.M. contributed equally.

Notes

The authors declare no competing financial interest.

ACKNOWLEDGMENTS

This work was supported by the German Research Foundation (GRK 1782: "Functionalization of Semiconductors"), and the support for the mass spectrometer (iTrap) was provided by Carl Zeiss SMT GmbH.

ABBREVIATIONS

AFM, atomic force microscopy; dilute nitrides, III/V semiconductors containing small amounts of nitrogen; DTBA$^{\bullet}$, di-*tert*-butylarsane radical; DTBAA, di-*tert*-butylaminoarsane; DTBAP, di-*tert*-butylaminophosphane; DTBP$^{\bullet}$, di-*tert*-butylphosphane radical; HRXRD, high-resolution X-ray diffraction; LEDs, light-emitting diodes; MBE, molecular beam epitaxy; MOVPE, metal−organic vapor-phase epitaxy; MQWs, multi quantum wells; NH$^{\bullet}$, aminyl radical; NMR, nuclear magnetic resonance; QW, quantum well; RMS, root mean square; TBAs, *tert*-butylarsane; TBP, *tert*-butylphosphane; TEGa, triethylgallium; UDMHy, 1,1-dimethylhydrazine

REFERENCES

(1) Wu, J.; Shan, W.; Walukiewicz, W. Band Anticrossing in Highly Mismatched III−V Semiconductor Alloys. *Semicond. Sci. Technol.* **2002**, *17*, 860−869.

(2) Shan, W.; Yu, K. M.; Walukiewicz, W.; Wu, J.; Ager, J. W.; Haller, E. E. Band Anticrossing in Dilute Nitrides. *J. Phys.: Condens. Matter* **2004**, *16* (31), S3355−S3372.

(3) Kunert, B.; Zinnkann, S.; Volz, K.; Stolz, W. Monolithic Integration of Ga(NAsP)/(BGa)P Multi-Quantum Well Structures on (0 0 1) Silicon Substrate by MOVPE. *J. Cryst. Growth* **2008**, *310* (23), 4776−4779.

(4) Kunert, B.; Volz, K.; Koch, J.; Stolz, W. Direct Band Gap Ga(NAsP)-Material System Pseudomorphically Grown on GaP Substrate. *Appl. Phys. Lett.* **2006**, *88* (18), 182108.

(5) Kunert, B.; Volz, K.; Nemeth, I.; Stolz, W. Luminescence Investigations of the GaP-Based Dilute Nitride Ga(NAsP) Material System. *J. Lumin.* **2006**, *121* (2), 361−364.

(6) Borck, S.; Chatterjee, S.; Kunert, B.; Volz, K.; Stolz, W.; Heber, J.; Rühle, W. W.; Gerhardt, N. C.; Hofmann, M. R. Lasing in Optically Pumped Ga(NAsP)/GaP Heterostructures. *Appl. Phys. Lett.* **2006**, *89* (3), 031102−3.

(7) Kunert, B.; Reinhard, S.; Koch, J.; Lampalzer, M.; Volz, K.; Stolz, W. First Demonstration of Electrical Injection Lasing in the Novel Dilute Nitride Ga(NAsP)/GaP-Material System. *Phys. Status Solidi C* **2006**, *3* (3), 614−618.

(8) Liebich, S.; Zimprich, M.; Beyer, A.; Lange, C.; Franzbach, D. J.; Chatterjee, S.; Hossain, N.; Sweeney, S. J.; Volz, K.; Kunert, B.; Stolz, W. Laser Operation of Ga(NAsP) Lattice-Matched to (001) Silicon Substrate. *Appl. Phys. Lett.* **2011**, *99* (7), 071109.

(9) Geisz, J. F.; Olson, J. M.; Friedman, D. J.; Jones, K. M.; Reedy, R. C.; Romero, M. J. Lattice-Matched GaNPAs-on-Silicon Tandem Solar Cells. *Conf. Rec. Thirty-first IEEE Photovolt. Spec. Conf.* **2005**, 695−698.

(10) Sukrittanon, S.; Liu, R.; Breeden, M. C.; Pan, J. L.; Jungjohann, K. L.; Tu, C. W.; Dayeh, S. A. Radial Direct Bandgap P-i-n GaNP Microwire Solar Cells with Enhanced Short Circuit Current. *J. Appl. Phys.* **2016**, *120* (5), 055702.

(11) Sukrittanon, S.; Kuang, Y. J.; Dobrovolsky, A.; Kang, W. M.; Jang, J. S.; Kim, B. J.; Chen, W. M.; Buyanova, I. A.; Tu, C. W. Growth and Characterization of Dilute Nitride GaNxP1−x Nanowires and GaNxP1−x/GaNyP1−y Core/Shell Nanowires on Si (111) by Gas Source Molecular Beam Epitaxy. *Appl. Phys. Lett.* **2014**, *105* (7), 072107.

(12) Sukrittanon, S.; Liu, R.; Ro, Y. G.; Pan, J. L.; Jungjohann, K. L.; Tu, C. W.; Dayeh, S. A. Enhanced Conversion Efficiency in Wide-Bandgap GaNP Solar Cells. *Appl. Phys. Lett.* **2015**, *107* (15), 153901.

(13) Kargar, A.; Sukrittanon, S.; Zhou, C.; Ro, Y. G.; Pan, X.; Dayeh, S. A.; Tu, C. W.; Jin, S. GaP/GaNP Heterojunctions for Efficient Solar-Driven Water Oxidation. *Small* **2017**, *13* (21), 1603574.

(14) Jürgensen, H. Large-Scale MOVPE Production Systems. *Microelectron. Eng.* **1992**, *18* (1−2), 119−148.

(15) Kunert, B.; Koch, J.; Torunski, T.; Volz, K.; Stolz, W. MOVPE Growth Experiments of the Novel (GaIn)(NP)/GaP Material System. *J. Cryst. Growth* **2004**, *272* (1−4), 753−759.

(16) Maßmeyer, O.; Inacker, S.; Hepp, T.; Glowatzki, J.; Nattermann, L.; Sterzer, E.; Ritter, C.; Von Hänisch, C.; Stolz, W.; Volz, K. Decomposition Mechanisms of Di-Tert-Butylaminoarsane (DTBAA). *Organometallics* **2019**, *38* (16), 3181−3186.

(17) Sterzer, E.; Ringler, B.; Nattermann, L.; Beyer, A.; von Hänisch, C.; Stolz, W.; Volz, K. (GaIn)(NAs) Growth Using Di-Tertiary-Butyl-Arsano-Amine (DTBAA). *J. Cryst. Growth* **2017**, *467*, 132−136.

(18) Sterzer, E.; Maßmeyer, O.; Nattermann, L.; Jandieri, K.; Gupta, S.; Beyer, A.; Ringler, B.; Von Hänisch, C.; Stolz, W.; Volz, K. 1 EV Ga(NAsSb) Grown by MOVPE Using Di- Tertiary -Butyl-Arsano-Amine (DTBAA). *AIP Adv.* **2018**, *8* (5), 055329.

(19) Sterzer, E.; Beyer, A.; Duschek, L.; Nattermann, L.; Ringler, B.; Leube, B.; Stegmüller, A.; Tonner, R.; Von Hänisch, C.; Stolz, W.; Volz, K. Efficient Nitrogen Incorporation in GaAs Using Novel Metal Organic As-N Precursor Di-Tertiary-Butyl-Arsano-Amine (DTBAA). *J. Cryst. Growth* **2016**, *439*, 19−27.

(20) Zanella, P.; Porchia, M.; Rossetto, G.; Brianese, N.; Ossola, F.; Williams, J. O. Organometallic Precursors in the Growth of Epitaxial

https://dx.doi.org/10.1021/acs.organomet.0c00078
Organometallics XXXX, XXX, XXX−XXX

Thin Films of III-V Semiconductors by Metal-Organic Chemical Vapor Deposition (MOCVD). *Chem. Mater.* **1991**, *3* (2), 225−242.
(21) Lee, R. T.; Stringfellow, G. B. Pyrolysis of 1,1 Dimethylhydrazine for OMVPE Growth. *J. Electron. Mater.* **1999**, *28* (8), 963−969.
(22) Scherer, O. J.; Schieder, G. Metallorganische Aminophosphine Und Phosphinimine. *Chem. Ber.* **1968**, *101* (12), 4184−4198.
(23) Nattermann, L.; Maßmeyer, O.; Sterzer, E.; Derpmann, V.; Chung, H. Y.; Stolz, W.; Volz, K. An Experimental Approach for Real Time Mass Spectrometric CVD Gas Phase Investigations. *Sci. Rep.* **2018**, *8* (319), 1−7.
(24) Chung, H. Y.; Aliman, M.; Fedosenko, G.; Laue, A.; Reuter, R.; Derpmann, V.; Gorkhover, L.; Antoni, M. Very Sensitive Real-Time Inline Process Mass Spectrometer Based on FFT Ion Trap Technique. *Annu. SEMI Adv. Semicond. Manuf. Conf. ASMC 2016 27th* **2016**, 263−266.
(25) Larsen, C. A.; Buchan, N. I.; Li, S. H.; Stringfellow, G. B. Decomposition Mechanisms of Tertiarybutylarsine. *J. Cryst. Growth* **1989**, *94* (3), 663−672.
(26) Stringfellow, G. B. Calculation of the Solubility and Solid-Gas Distribution Coefficient of N in GaP. *J. Electrochem. Soc.* **1972**, *119* (12), 1780−1782.
(27) Kaprinski, J.; Jun, J.; Grzegory, I.; Bugajski, M. Crystal Growth of GaP Doped with Nitrogen under High Nitrogen Pressure. *J. Cryst. Growth* **1985**, *72* (3), 711−716.
(28) Ohtake, A. Surface Reconstructions on GaAs(001). *Surf. Sci. Rep.* **2008**, *63* (7), 295−327.
(29) Richter, W. In-Situ Observation of MOVPE Epitaxial Growth. *Appl. Phys. A: Mater. Sci. Process.* **2002**, *75* (1), 129−140.
(30) Döscher, H.; Hannappel, T. In Situ Reflection Anisotropy Spectroscopy Analysis of Heteroepitaxial GaP Films Grown on Si(100). *J. Appl. Phys.* **2010**, *107* (12), 123523.
(31) Law, D. C.; Sun, Y.; Hicks, R. F. Reflectance Difference Spectroscopy of Gallium Phosphide(001) Surfaces. *J. Appl. Phys.* **2003**, *94* (9), 6175−6180.
(32) Maßmeyer, O.; Sterzer, E.; Nattermann, L.; Stolz, W.; Volz, K. Influence of UDMHy on GaAs (0 0 1) Surface Reconstruction before and during Growth of Ga(NAs) by MOVPE. *Appl. Surf. Sci.* **2018**, *458* (15), 512−516.
(33) Zhang, S. B.; Zunger, A. Surface-Reconstruction-Enhanced Solubility of N, P, As, and Sb in III-V Semiconductors. *Appl. Phys. Lett.* **1997**, *71* (5), 677−679.
(34) Bi, W. G.; Tu, C. W. N Incorporation in GaP and Band Gap Bowing of GaNxP1−x. *Appl. Phys. Lett.* **1996**, *69* (24), 3710−3712.
(35) Lee, P. W.; Omstead, T. R.; McKenna, D. R.; Jensen, K. F. In Situ Mass Spectroscopy and Thermogravimetric Studies of GaAs MOCVD Gas Phase and Surface Reactions. *J. Cryst. Growth* **1987**, *85* (1−2), 165−174.
(36) Yoshida, M.; Watanabe, H.; Uesugi, F. Mass Spectrometric Study of Ga(CH3)3 and Ga(C2H5)3 Decomposition Reaction in H2 and N2. *J. Electrochem. Soc.* **1985**, *132* (3), 677−679.
(37) French, C. L.; Foord, J. S. Reaction Kinetics for the CBE Growth of GaAs from Triethylgallium; Computer Modelling Studies Incorporating Recent Surface Spectroscopic Data. *J. Cryst. Growth* **1992**, *120* (1−4), 63−70.
(38) Murrell, A. J.; Wee, A. T. S.; Fairbrother, D. H.; Singh, N. K.; Foord, J. S.; Davies, G. J.; Andrews, D. A. Surface Chemical Processes in Metal Organic Molecularbeam Epitaxy; Ga Deposition from Triethylgallium on GaAs(100). *J. Appl. Phys.* **1990**, *68* (8), 4053−4063.
(39) Stringfellow, G. B. *Organometallic Vapour Phase Epitaxy: Theory and Practice*, 2nd ed.; Academic Press: 1999.
(40) Stringfellow, G. B. The Importance of Lattice Mismatch in the Growth of GaxIn 1-XP Epitaxial Crystals. *J. Appl. Phys.* **1972**, *43* (8), 3455−3460.
(41) Stringfellow, G. B. Microstructures Produced during the Epitaxial Growth of InGaN Alloys. *J. Cryst. Growth* **2010**, *312* (6), 735−749.
(42) Sanorpim, S.; Katayama, R.; Onabe, K.; Usami, N.; Nakajima, K. Lattice-Latching Effect in Metalorganic Vapor Phase Epitaxy Growth of InGaAsN Film Lattice-Matched to Bulk InGaAs Substrate. *Jpn. J. Appl. Phys.* **2010**, *49* (4), 040202.
(43) Kunert, B.; Volz, K.; Koch, J.; Stolz, W. MOVPE Growth Conditions of the Novel Direct Band Gap, Diluted Nitride Ga(NAsP) Material System Pseudomorphically Strained on GaP-Substrate. *J. Cryst. Growth* **2007**, *298*, 121−125.
(44) Stringfellow, G. B. Development and Current Status of Organometallic Vapor Phase Epitaxy. *J. Cryst. Growth* **2004**, *264* (4), 620−630.
(45) Li, S. H.; Larsen, C. A.; Buchan, N. I.; Stringfellow, G. B. Pyrolysis of Tertiarybutylphosphine. *J. Electron. Mater.* **1989**, *18* (3), 457−464.

https://dx.doi.org/10.1021/acs.organomet.0c00078
Organometallics XXXX, XXX, XXX−XXX

7.2.5 Evaluation of the N incorporation behavior in Ga(N,As) on GaAs

Authors: Oliver Maßmeyer, Johannes Glowatzki, Manuel Kapitein, Johannes Haust, Thilo Hepp, Wolfgang Stolz and Kerstin Volz

Publication: to be submitted

Abstract: Dilute nitrogen containing III/V semiconductors have received high interest in recent decades because of their optoelectronic and structural properties leading to possible applications such as lasers and solar cells. The metalorganic vapor phase epitaxy is a widely used production technique for III/V semiconductors and very promising for the growth of 'dilute nitrides'. Disadvantages such as a high decomposition temperature and low N incorporation efficiency are attributed to the decomposition reactions of the standard precursor unsymmetrical-di-methyl-hydrazine (UDMHy). In the recent years a N-As precursor di-*tert*-butyl-amino-arsane (DTBAA) was developed as a precursor for 'dilute nitrides' that showed more efficient N incorporation as well as lower decomposition temperature, which is beneficial for N incorporation. For getting further insight into the N incorporation mechanisms of DTBAA and UDMHy and hopefully improved precursor properties the decomposition and the growth with the novel N-As precursor di-*tert*-butyl-arsenyl-di-methyl-hydrazine (DTBADMHy) was investigated systematically. The decomposition studies show bond *homolysis* of the As-N bond as first reaction step at a temperature of 170 °C. The formed decomposition products DTBAs• and UDMHy• further decompose at 270 °C and 250 °C. The proposed decomposition reactions agree overall to the decomposition reactions found for DTBAA and UDMHy, which show the formation of NH_2• and NH that are believed to be responsible for N incorporation. The growth studies show that the activation energy for N incorporation is equal for DTBAA and DTBADMHy, but the N incorporation behavior due to V/III ratio variation is different between these precursors and similar to UDMHy. N incorporation of over 6 % was reached at temperatures as low as 425 °C. The optical and structural characteristics, the composition and the surface morphology of Ga(N,As) grown on GaAs of were investigated using photoluminescence spectroscopy, high resolution X-ray diffraction and atomic force microscopy.

Authors' Contributions: My contribution to this work was the planning, the execution and interpretation of all shown decomposition experiments of DTBADMHy. J. Glowatzki contributed equally to this publication. He planned, executed and interpreted the growth of Ga(N,As) structures on GaAs with the novel DTBADMHy precursor. This includes the structural analysis of the grown samples by HR-XRD and AFM as well as the analysis of the optical properties by photoluminescence spectroscopy (PL). M. Kapitein conducted the synthesis of the novel DTBADMHy precursor. All co-authors helped with the interpretation of the data and with the review of the manuscript. W. Stolz and K. Volz supervised the work and secured the funding to support this study.

Evaluation of the N incorporation behavior in Ga(N,As) on GaAs

Oliver Maßmeyer[1], Johannes Glowatzki[1], Manuel Kapitein[2], Johannes Haust[1], Thilo Hepp[1], Wolfgang Stolz[1] and Kerstin Volz[1]

[1]Material Sciences Center and Department of Physics, Philipps-Universität Marburg, Germany

[2]Dockweiler Chemicals GmbH, 35041 Marburg, Germany

Abstract:

Dilute nitrogen containing III/V semiconductors have received high interest in recent decades because of their optoelectronic and structural properties leading to possible applications like lasers and solar cells. The metalorganic vapor phase epitaxy is a widely used production technique for III/V semiconductors and very promising for the growth of dilute nitrides. Disadvantages like a high decomposition temperature and low N incorporation efficiency are attributed to the decomposition reactions of the standard precursor unsymmetrical-dimethylhydrazine (UDMHy). In the recent years a N-As precursor ditertiarybutylaminoarsane (DTBAA) was developed as a precursor for dilute nitrides that showed more efficient N incorporation as well as lower decomposition temperature, which is beneficial for N incorporation. For getting further insight into the N incorporation mechanisms of DTBAA and UDMHy and hopefully improved precursor properties the decomposition and the growth with the novel N-As precursor ditertiarybutylarsenyl-unsymmetrical-dimethylhydrazine (DTBADMHy) was investigated systematically. The decomposition studies show bond homolysis of the As-N bond as first reaction step at a temperature of 170 °C. The formed decomposition products DTBAs• and UDMHy• further decompose at 270 °C and 250 °C. The proposed decomposition reactions agree overall to the decomposition reactions found for DTBAA and UDMHy, which show the formation of NH_2• and NH that are believed to be responsible for N incorporation. The growth studies show that the activation energy for N incorporation is equal for DTBAA and DTBADMHy, but the N incorporation behavior due to V/III ratio variation is different between these precursors and similar to UDMHy. N incorporation of over 6 % was reached at temperatures as low as 425 °C. The optical and structural characteristics, the composition and the surface morphology of Ga(N,As) grown on GaAs of were investigated using photoluminescence spectroscopy, high resolution X-ray diffraction and atomic force microscopy.

1. Introduction

In the recent years, III/V semiconductors containing small amounts of nitrogen (dilute nitrides) have received large interest because of their promising properties. Introducing a small amount of N strongly reduces the band gap (up to 180 meV/%N), which is explained by the band anti crossing model.[1–3] Also, the lattice constant is reduced strongly because of the small covalent radius of the N atoms. These characteristics are used in materials like Ga(N,As,Sb) and (Ga,In)(N,As) for realizing lattice matched or at least dislocation free growth on GaAs substrates. Simultaneously, low band gaps in the infrared regime can be reached for realization of materials with emission wavelengths around 1.31 and 1.55 µm, which are the transmission windows of traditional glass fibers in optical communication. These are promising properties for the growth of laser structures on GaAs.[4–8] Also the growth of Ga(N,As,P) laser structures on Si were realized and the results

are promising for the integration of photonics to Si based integrated circuits.[9–11] Further, materials lattice matched on Ge with a bandgap of around 1 eV were grown in the past for multijunction solar cells. Notably, world record cells were achieved using these materials.[12–14] While devices with world record efficiencies were grown with molecular beam epitaxy (MBE) the same efficiencies were not reached by using metalorganic vapor phase epitaxy (MOVPE).[15] But for higher cost efficiency and upscaling in industrial scale it would be desirable to build these devices using MOVPE.[16] Unfortunately, there are disadvantages using MOVPE, which are attributed to the utilized metalorganic precursors and in particular to the related carbon incorporation of the standard N precursor unsymmetrical-dimethylhydrazine (UDMHy).[17,18] Further, this precursor shows a low N incorporation, which is not fully understood until now. In the past a novel As-N precursor ditertiarybutylaminoarsane (DTBAA) was developed and the growth of various materials like Ga(N,As), (Ga,In)(N,As), Ga(N,As,Sb) and Ga(N,As,P) were investigated.[19–21] DTBAA showed in all these materials improved N incorporation efficiencies and a lower decomposition temperature compared to UDMHy and the arsenic precursor tertiarybutylarsane (TBAs).[22–25] For potentially better incorporation characteristics and a better fundamental understanding of the difference in N incorporation between the As-N precursor DTBAA and N only precursor UDMHy a precursor with similarities to both precursors was designed. This precursor is ditertiarybutylarsenyl-unsymmetrical-dimethylhydrazine (DTBADMHy).

In this work the thermal decomposition of DTBADMHy is investigated by mass spectrometry to determine the decomposition behavior of the As-N bond of the precursor, as well as to show the influence of the larger di-methylhydrazine group in the case of DTBADMHy compared to the aminyl group in the case of DTBAA on the decomposition. The thermal decomposition is studied in a novel quadrupole ion trap mass spectrometer connected inline to the MOVPE system. Possible decomposition reactions for DTBADMHy are proposed and the decomposition products are compared to the decomposition of UDMHy and DTBAA.[21,23,26] Furthermore, the MOVPE growth under variation of various growth parameters like temperature, growth rate, V/III ratio and additional supply of TBAs were investigated and compared to the decomposition study of DTBADMHy as well as to the growth characteristics of UDMHy and DTBAA. For investigations of the properties of the samples high resolution X-ray diffraction (HRXRD), atomic force microscopy (AFM) and photoluminescence (PL) spectroscopy were used.

2. Experimental Procedure

The thermal decomposition of DTBADMHy is studied in a horizontal AIXTRON AIX 200 GFR (gas foil rotation) MOVPE system. For all shown decomposition and growth studies the reactor is operated with highly purified H_2 carrier gas (purity: 9.0) under a total flux of 6800 sccm and at a reactor pressure of 50 mbar. The decomposition products are investigated in a temperature range between room temperature and 800 °C, which is realized by infrared heating lamps below the susceptor. The measurement of the temperature on the susceptor surface is calibrated using the phase transition of Al coated Si wafers occurring at 577 °C. The measured susceptor temperature is converted into the gas phase temperature at the collection point of the analyte in the reactor chamber, which is done by a correlation of the decomposition temperature of tertiarybutylarsane (TBAs) measured in this reactor system from ref. [25] with data from ref. [24]. The graphite susceptor is baked in between the measurements at 800 °C to allow desorption in order to prevent memory effects of the system.

The mass spectrometer used for the decomposition analysis is a fast Fourier transform based quadrupole ion trap from Carl Zeiss SMT GmbH (iTrap®). The ion trap is connected by a bypass system inline to the MOVPE reactor and is operated under stable flow and pressure conditions to

reduce fluctuation in the gas phase. The setup is designed to be as close to growth conditions used for device fabrication and is described in more detail in ref. [25–27]. The principle of the ion trap is based on the principle of a Paul trap and is designed to realize high sensitivity measurements, which was shown by detection of impurities down to the parts per trillion level.[28] Due to the fast Fourier transform based concept, measurement times below 2 s are realized for a single mass spectrum. This enables real time analysis of the process gas during the growth by MOVPE.
The incorporation behavior of DTBADMHy is systematically studied by growth of Ga(N,As)/GaAs heterostructures in the same MOVPE reactor. During growth the sample is rotated by gas foil rotation with a speed of 50-70 rpm. The Growth took place on semi insulating exact GaAs substrates, which were treated by etching with a H_2O:H_2O_2:NH_3 solution before inserting into the reactor. In order to have a defined high quality reproducible surface for all growth experiments the substrates were heated to 350 °C for evaporation of water and further heated under TBAs stabilization and annealed at 750 °C. A 250 nm thick GaAs buffer was grown at 625 °C under optimized growth conditions. Around 4-8 nm thick Ga(N,As) quantum wells followed by 25-50 nm GaAs barriers were grown as three time multiquantum well ending with the Ga(N,As) QW for realistic feedback of the growth surface. The vapor pressure of the novel precursor DTBADMHy is unknown for the used temperature (20 °C), therefore no partial pressure could be calculated and instead the source flow (Q_S) through the bubbler is used as metric for the amount of DTBADMHy in the reactor. The bubbler pressure was set to 150 mbar for all experiments.
For determining the composition and growth rate HRXRD measurements were carried out with a Panalytical X'Pert Pro diffractometer, which uses the Cu K-α line (0.15406 nm). Rocking curves around the (004) reflection of the GaAs substrates were recorded. Simulations of the diffractograms were done using the *X'Pert Epitaxy Smooth and Fit* software to determine the strain and thickness of the QWs and barrier thicknesses, which give the N composition and growth rate.

Further, PL spectroscopy was used to determine the optical quality and characteristics like the band gap energy of the material. For excitation a frequency doubled Nd:YAG laser operating at a wavelength of 532 nm was used with a power of 100 mW, which results in a power density of 1.53 kW/cm^2. The wavelength information was achieved by using a 1 m grating monochromator to disperse the different photon energies of the light. The light was detected using a lq. N_2 cooled Ge detector. For improving the signal to noise ratio standard lock in technique was applied with a chopper in the laser path. All samples were measured as grown at room temperature at the same day for better comparability.
For investigation of the surface morphology an AFM of the company Digital Instruments was used (Nanoscope IIIa). All shown images have a size of 5×5 µm and were recorded using tapping mode.

3. Results and Discussion

In the first part the decomposition of DTBADMHy will be discussed and compared to the decomposition studies of DTBAA and UDMHy reported in the literature. The measured decomposition products will be interpreted in terms of possible decomposition reactions and are related to the As and N incorporation of the precursor. In the second part the As and N incorporation is systematically studied by analysis of Ga(N,As) layers grown on GaAs.

3.1. Unimolecular decomposition of DTBADMHy

For analyzation of the thermal decomposition of DTBADMHy (248 u) the detected decomposition products are measured in dependence of the temperature. Due to the sensitive ionization conditions found for our setup, the number of electron ionization induced fragments is largely reduced, allowing a straightforward interpretation of the mass spectrometry data.[25–27] From the

detected mass spectra, decomposition curves of the parent molecule DTBADMHy and the arising decomposition products are created and shown in figure 1 a).

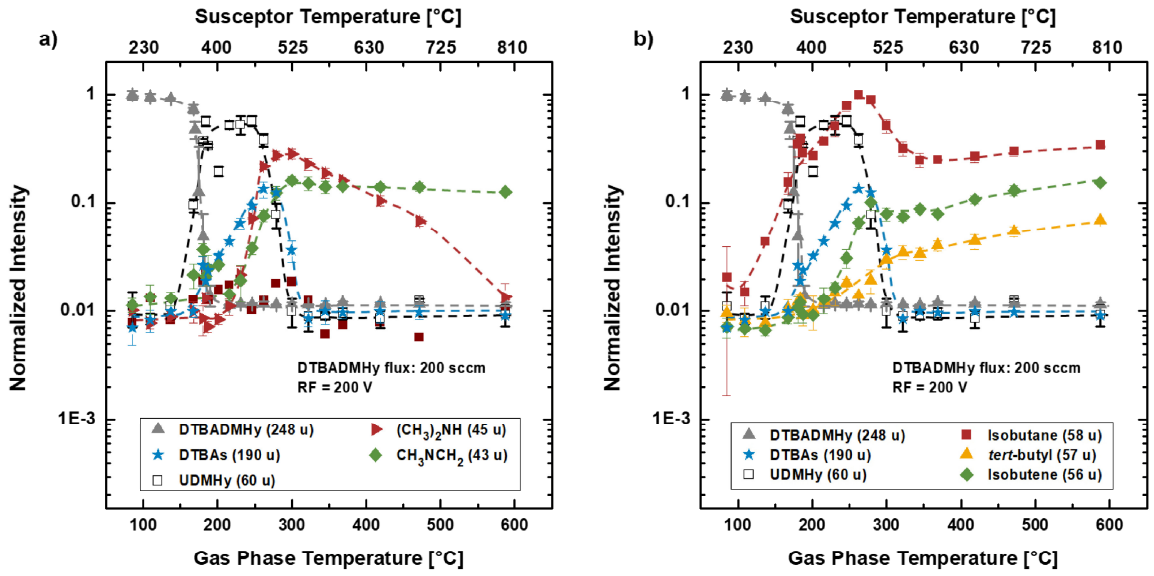

Figure 1: Temperature dependent decomposition curves of DTBADMHy (248 u) and of the occurring products detected upon decomposition. a) Decomposition products related to the As-N bond homolysis and the dissociation of the formed UDMHy• radicals. b) Decomposition products related to the dissociation of the *tert*-butyl groups from the molecule.

From the decomposition curve of DTBADMHy the decomposition temperature is determined with a value of 170 ± 10 °C from the point where the intensity of DTBADMHy drops to half of its value. At this temperature the As-N bond of DTBADMHy dissociates by homolytic fission as first decomposition step (reaction 1). This results in the formation of $(C_4H_9)_2As•$ and $(CH_3)_2NNH•$ (UDMHy•), which will react with H_2 before detection as $(C_4H_9)_2AsH$ (DTBAs - 190 u) and $(CH_3)_2NNH_2$ (UDMHy - 60 u). The breaking of the As-N bond in the first step of the decomposition reaction correlates well to the findings of DTBAA. Like the DTBADMHy the DTBAA exhibits an As-N bond, which was found to decompose under formation of DTBAs• and $NH_2•$.[26] Impressively the decomposition temperature of the As-N bond for DTBADMHy agrees well with the decomposition temperature of 160 ± 10 °C determined for the unimolecular decomposition reaction of DTBAA measured in the same setup.[26] According to reaction 1 an increase of the DTBAs intensity is detected proofing the formation of DTBAs• in the decomposition. The DTBAs intensity further increases with increasing temperature and starts to drop around 270 °C. From this curve, the decomposition temperature of DTBAs• is determined with 290 ± 10 °C, which is again consistent with the decomposition temperature of DTBAs• formed in the analogue DTBAA experiment.[26] Further the decomposition temperature of DTBAs• is about 60 °C lower than the decomposition temperature of 350 °C reported for the unimolecular decomposition of DTBAs in the literature.[29] This shows a lower thermal stability of the formed radical. The formed DTBAs• is likely connected to the As incorporation of this precursors, since it is the only detected As containing decomposition product.

Reaction 1: *Homolytic fission reaction of the As-N bond in DTBADMHy.*

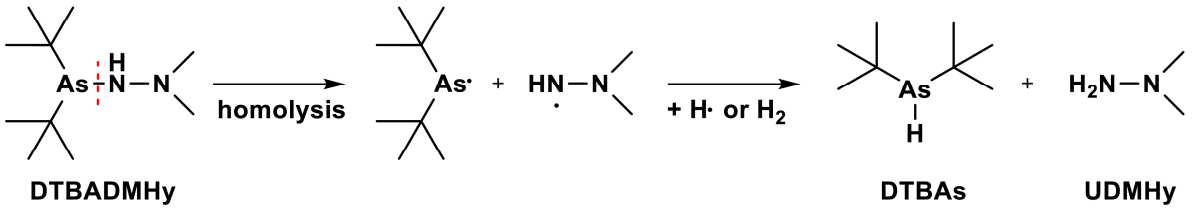

The decomposition curves show further an intensity increase of UDMHy, supporting the formation of UDMHy• in the decomposition reaction. The UDMHy rises right as the DTBADMHy intensity decreases and stays stable up to a temperature of 250 °C, indicating the decomposition of UDMHy•. The related decomposition temperature is determined with 270 ± 10 °C. This value is significantly lower than the decomposition temperature of 420 ± 10 °C for the unimolecular decomposition of UDMHy determined in the literature, which is supported by measurements of the unimolecular UDMHy decomposition in our reactor system.[23,26] Above 250 °C the UDMHy• radical is decomposing before it can collide and react with the H_2 carrier gas to form the more stable UDMHy molecule. Upon decomposition of UDMHy• first the intensity of $(CH_3)_2NH$ (45 u) starts to increase, followed by an increase of CH_3NCH_2 (43 u), which is added in figure 1 a). Analogue to the unimolecular UDMHy decomposition $(CH_3)_2NH$ is likely be formed by bond homolysis of the N-N bond, shown in decomposition reaction 2. In this homolytic fission first $(CH_3)_2N$• is formed, which then can react with H_2 to form the more stable $(CH_3)_2NH$ before detection. Additionally, NH is formed in the decomposition of the N-N bond of UDMHy•. The formed NH is expected to be very reactive and will either stick to the surface, leading to N incorporation or forms NH_3 (17 u) in a reaction with the carrier gas H_2. This N-N bond homolysis is analogous described for the unimolecular decomposition of UDMHy. Due to the lower stability of the formed UDMHy• the formation of $(CH_3)_2N$• occurs at lower temperatures.

Reaction 2: *Homolytic fission reaction of the N-N bond in the formed UDMHy•.*

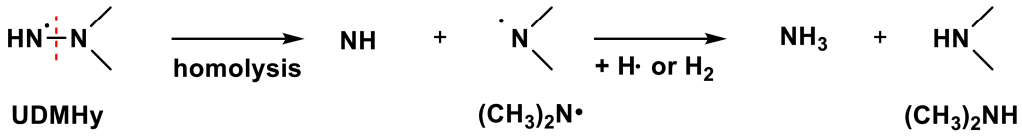

Reaction 3: *Intramolecular coupling reaction of the formed UDMHy•.*

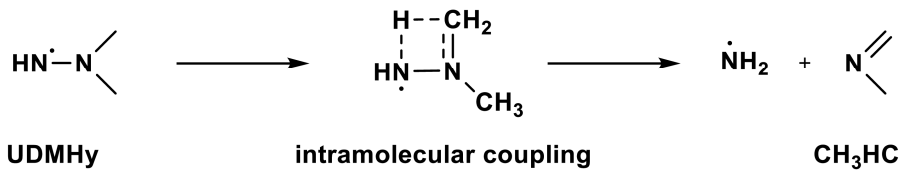

The second reaction product CH_3NCH_2 may be produced in the same reaction by abstraction of H• from $(CH_3)_2N$•. However, the decomposition of UDMHy• seemingly behaves similar to the unimolecular decomposition of UDMHy. Therefore, the CH_3NCH_2 is more likely produced in an intramolecular coupling reaction 3. Since UDMHy• is formed as a radical, the intramolecular coupling reaction produces NH_2• instead of the stable NH_3. This can possibly lead to a higher N incorporation compared to growth with UDMHy.

Above 350 °C the signal of $(CH_3)_2NH$ drops off over a large temperature range, indicating the decomposition of the formed $(CH_3)_2N$•. CH_3NCH_2 on the other hand shows a constant signal up

to 600 °C and is therefore not expected to be incorporated. The arising smaller decomposition fragments will be discussed below.
The temperature dependence of the decomposition products related to the dissociation of the *tert*-butyl group from DTBADMHy is shown in figure 1 b). As soon as the DTBADMHy decomposes, the intensity of isobutane (58 u) and of *tert*-butyl radicals (57 u) is rising. This indicates a homolytic fission of the As-C bonds of the molecule, which results in the formation of *tert*-butyl radicals, which partly react with H_2 before detection. Alternatively, the isobutane can be formed in an intramolecular coupling reaction.[24,26,27] The isobutane intensity hits its peak around 280 °C and drops to half off its value for higher temperatures. On the one hand, this could mean that one of the *tert*-butyl groups is dissociating by a different reaction at higher temperatures. The same reduction of the isobutane intensity to half of its value was seen in the decomposition studies of DTBAA and was referred to a reduced probability for homolysis of the *tert*-butyl group from the molecule.[26] Around 200 °C the intensity of isobutene (56 u) starts to increase and shows an increase over the investigated temperature range. Isobutene is formed in a β-H elimination reaction of the *tert*-butyl groups. In the β-H elimination reaction a C_β-H bond of one C atom in β position is interacting with the As p-orbitals, resulting in the formation of a C=C double bond.[30] The slightly higher appearance temperature of isobutene is attributed to a higher activation energy of the β-H elimination reaction. Consequently, this reaction becomes more probable at higher temperatures. No further larger reaction products like e.g. tertiarybutylarsenyl-unsymmetrical-dimethylhydrazine (TBADMHy) are seen in the mass spectra. These products are either unstable and decompose or adsorb at available surface before detection in the mass spectrometer or do not form at all. The latter argument agrees to the dissociation of the As-N bond as first reaction step.

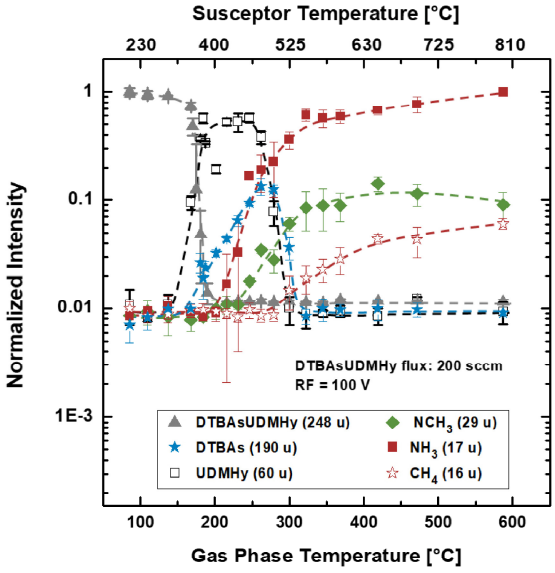

Figure 2: Temperature dependent decomposition curves of the products formed in the dissociation of UDMHy• of the molecule detected in the mass range below 40 u. The data of DTBADMHy and UDMHy• is added as a guideline.

The temperature dependence of smaller fragments related to the decomposition of the UDMHy• is shown in figure 2. As mentioned above the signal of $(CH_3)_2NH$ drops off at higher temperatures. As reported in the unimolecular decomposition of UDMHy, the formed $(CH_3)_2N$• radicals can decompose at higher temperatures under formation of NCH_3 (29 u) and CH_3• by bond homolysis shown in reaction 4.

Reaction 4: *Homolytic fission of the methyl group from $(CH_3)_2N$•.*

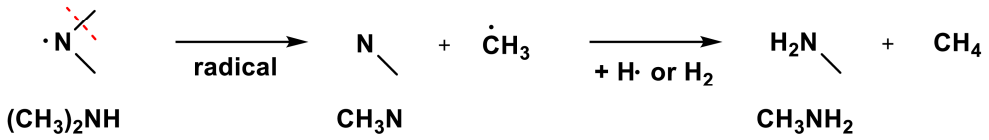

The intensity of NCH_3 is starting to increase around 250 °C and increases over the measured temperature range. This temperature also agrees to the formation of $(CH_3)_2N$•. This is attributed to formation of NCH_3 in the ionization process of $(CH_3)_2NH$. However, the intensity of NCH_3 does not decrease for higher temperature indicating that NCH_3 is formed as decomposition product. Furthermore, the intensity of CH_4 (16 u) increases around 300 °C. This indicates the formation of CH_3• in the decomposition and supports the occurrence of reaction 4. This C-N bond homolysis was analogous reported for the unimolecular decomposition of UDMHy. The related decomposition products $(CH_3)_2N$• and NCH_3 might be connected to the C incorporation for structures grown with this precursor [5,31].

According to the increase of $(CH_3)_2NH$ and CH_3NCH_2 the detected NH_3 signal is increasing and is further increasing over the measured temperature range. This is attributed to the formation of NH and NH_2• as discussed for reactions 2 and 3. Both species are very reactive and are likely to lead to N incorporation at low temperatures by sticking on the growth surface. At higher temperatures formation of NH_3 will limit the incorporation as it is thermally stable up to 900 °C.[32] Formation of NH_2• was also related to N incorporation for the unimolecular decomposition of UDMHy and DTBAA.[23,26] UDMHy furthermore showed formation of N_2, which together with the shown stable C-N decomposition products might be responsible for the lower N incorporation efficiency of UDMHy compared to DTBAA.[21,26] Formation of N_2 was not detected in our studies done for DTBADMHy. However, it cannot completely be excluded that N_2 is formed in the decomposition of DTBADMHy, since N_2 was not detected in the decomposition of unimolecular UDMHy in our setup, as well. This is due to the fact, that the ionization of N_2 is not easily realized and is so far only seen for very high N_2 concentrations in our setup.

3.2. Growth studies of Ga(N,As) on GaAs with DTBADMHy

The first proof of nitrogen incorporation in GaAs was given by HRXRD measurements and dynamical simulations for all samples. Figure 3 shows an example HRXRD diffractogram and dynamical simulation of a sample grown at 450 °C with a TEGa partial pressure of 7.1×10^{-3} mbar and a DTBADMHy source flow of 500 sccm. The simulation and measurement show good agreement, which indicates good layer quality and sharp interfaces. This sample also proves that growth of Ga(N,As) is possible with DTBADMHy as single group V source. Therefore, DTBADMHy is supplying both group V elements As and N like shown for DTBAA.[21] As seen in the mass spectrometry data, the As incorporation arises from the formed DTBAs• and the N incorporation is attributed to the formation of NH and NH_2• upon decomposition.

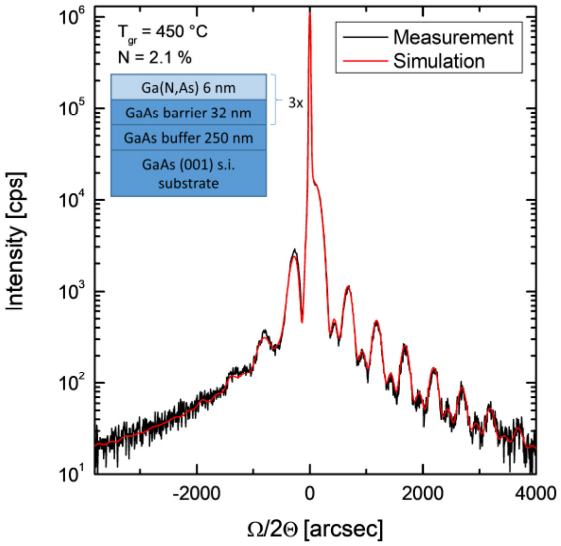

Figure 3: HRXRD diffractogram (black) and dynamical simulation (red).

Figure 4(a) shows the N incorporation and growth rate in dependence of the DTBADMHy source flow. A constant growth rate is seen for all samples. This behavior is expected because group III supply should be growth rate limiting under group V rich growth conditions. Further, the N incorporation does not seem to be dependent on the DTBADMHy partial pressure at higher V/III ratios as seen for the growth with UDMHy. For UDMHy the N incorporation is controlled by the N/As ratio, which in contrast is fixed in the DTBADMHy molecule itself.[33] In contrast to the composition determined via HRXRD measurements in figure 4(a) the PL spectra show a lower peak energy for the sample grown at Q_S(DTBADMHy) of 500 sccm. Due to the low strain at those low N contents the HRXRD measurements and simulations seem to be imprecise and the PL spectra indicate a higher N incorporation. This higher N incorporation is believed to occur due to a low V/III ratio close to one. The low V/III ratio causes a change of the surface reconstruction to a group III rich reconstruction, which enhances the N incorporation as seen in the literature.[34–36] At lowest DTBADMHy partial pressure the N incorporation decreased compared to higher V/III ratios. The low nitrogen content resulted in a significantly lowered strain making valid thickness determination impossible and hence, no growth rate could be calculated. This change is probably due to a low V/III ratio and due to a group III rich growth, which is further indicated by AFM measurements in figure 4(b-c). The surface of the sample grown at the lowest V/III ratio is very rough and shows a high RMS value. This is related to the high 3D features on the surface, which should be related to Ga droplets. They occur because of incomplete Ga incorporation due to low group V supply and insufficient desorption of the metallic species. The image at higher V/III ratio shows a flat stepped surface, which probably occurs due to a two dimensional (2D) step flow growth and represents also the surfaces of all samples grown at higher V/III ratios. At the transition point between the step flow growth and Ga droplet formation the effective V/III ratio has to be around one. Therefore, the vapor pressure of DTBADMHy can be roughly estimated to be around 0.4 ± 0.2 mbar.

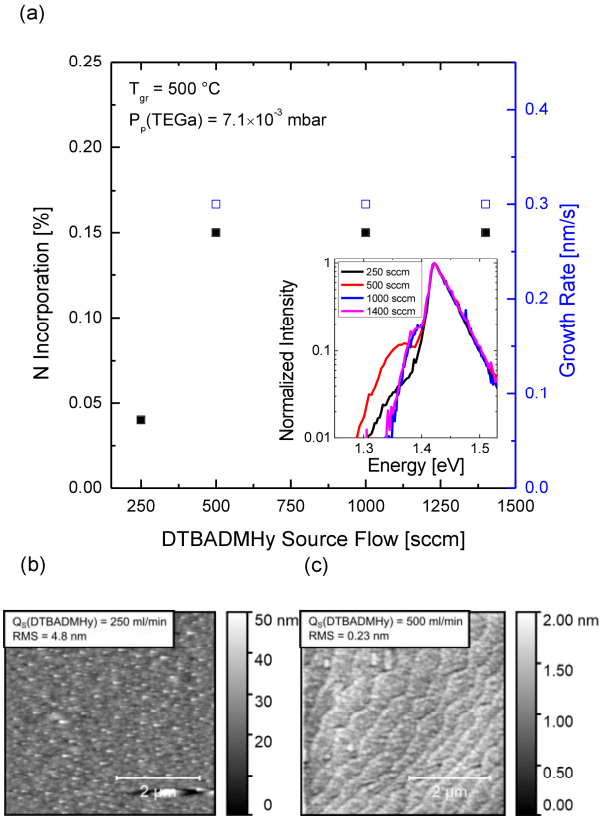

Figure 4: (a) N incorporation (black) and growth rate (blue) in dependence of the DTBADMHy partial pressure. The growth rate of the lowest partial pressure could not be obtained because of uncertainty in the thickness measurement due to low strain. (b) AFM image of Q_S(DTBADMHy) = 250 sccm out of (a). (c) AFM image of Q_S(DTBADMHy) = 500 sccm out of (a).

A second set of samples was grown with varying growth temperature. Figure 5 shows the N incorporation and growth rate in dependence of different growth temperatures. The N incorporation decreases exponential with increasing temperature as seen for the precursors DTBAA and UDMHy.[5,21,33] Explanations could be found in a temperature activated loss process like the desorption of the active N species or the loss of these species due to gas phase reactions. The mass spectrometry investigations suggest that this is related to the measured NH_3 species. At low temperature the reactive NH_2• and NH are likely to stick to the surface and incorporate. At higher temperature it seems to be more likely that this radical will react with the H_2 carrier gas or H radicals from precursor decompositions to form the stable NH_3. NH_3 was also detected for the precursors DTBAA, DTBAP and UDMHy, which show similar temperature dependent N incorporation behavior.[22,23,27] The growth rate increases with temperature, which could be explained by higher diffusion rates from the active Ga species from the boundary layer to the growth surface or by partially surface blocking of the growth surface by alkyl groups at lower temperatures as seen in the literature for various material systems grown via MOVPE.[29,37,38]

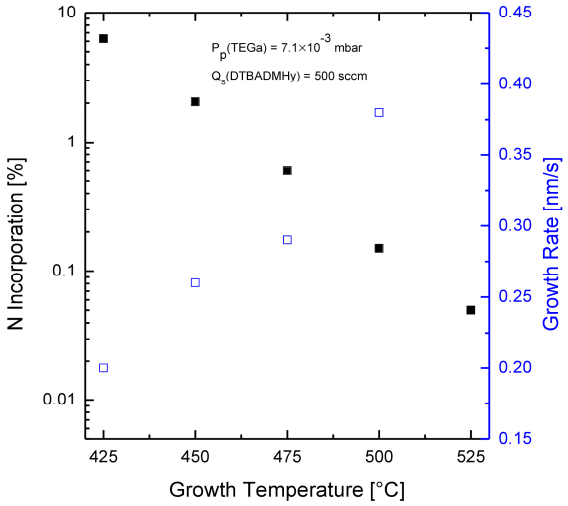

Figure 5: (a) Plot of the N incorporation (black) and growth rate (blue) in dependence of the growth temperature. The growth rate of the highest temperature could not be obtained because of uncertainty in thickness measurement due to low strain.

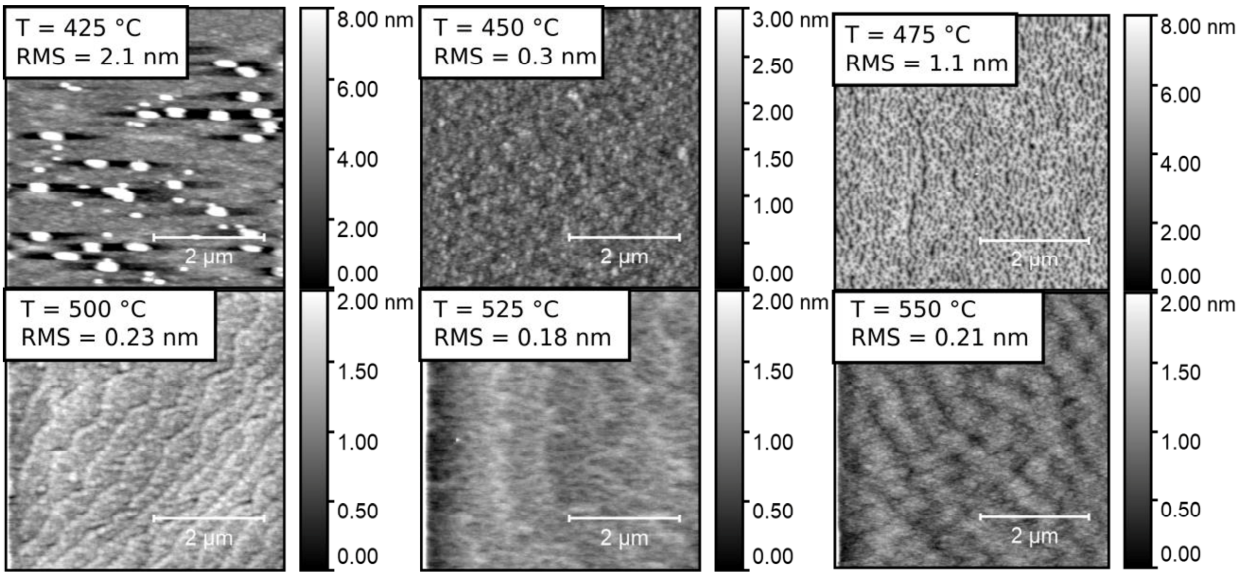

Figure 6: 5x5 µm AFM images of samples shown in figure 5.

The AFM images for different growth temperatures are shown in figure 6. For the higher temperatures (T_{gr} ≥ 500 °C) the surfaces are smooth with low RMS values (around 0.2 nm) and show steps indicating a 2D step flow growth. At lower temperatures (T_{gr} ≤ 450 °C) there are smooth surfaces without steps. Maybe due to the low growth temperatures and therefore low mobility of the adatoms a two dimensional island growth took place where the islands coalesced. At 425 °C additional 3D features are on top of the surface. Maybe they are related to the high N content and some clusters or other defects built during growth like also seen for the low temperature growth of highly strained Ga(N,P) on Si with DTBAP.[27] At 475 °C the surface morphology differs from that at high and low growth temperatures and even shows a higher RMS

value compared to a lower temperature (450 °C). Maybe the growth took place in an intermediate growth regime changing from two dimensional island growth to step flow growth.
Arrhenius plots of the N incorporation for the different precursors DTBADMHy, DTBAA and UDMHy are shown in figure 7. The DTBAA and DTBADMHy show a similar behavior and also the same activation energy within the uncertainty of the measurement (2.45 ± 0.09 eV and 2.36 ± 0.08 eV, respectively). In contrast the UDMHy has a much lower activation energy (0.96 ± 0.04 eV) and does not show an exponential behavior at low temperatures, which should be related to the incomplete decomposition.[23] The direct As-N bond in DTBAA and DTBADMHy maybe lead to the same activation energy and a much lower decomposition temperature as shown in the literature for DTBAA and in this study of DTBADMHy.[22] The low decomposition temperature and high N incorporation at very low temperatures (over 6 % at 425 °C) are a clear advantage of DTBADMHy compared to UDMHy. Hence, DTBADMHy is suitable for growth of highly strained alloys at low temperatures with small band gap energies. However, the N incorporation efficiency is lower in comparison to DTBAA as seen in figure 7.

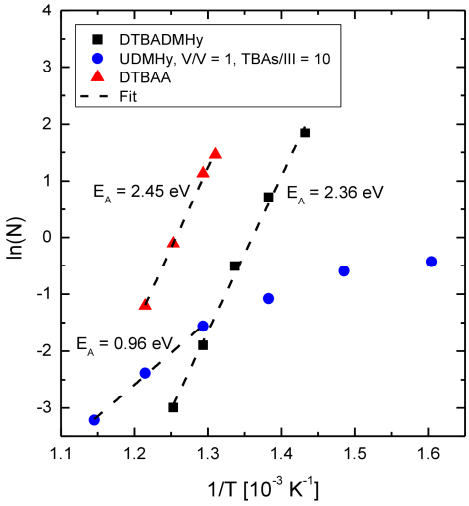

Figure 7: Arrhenius plots of N incorporation for different precursors DTBADMHy, DTBAA and UDMHy. Data of UDMHy and DTBAA taken from ref. [5,21]. E_A is the activation energy given by the slope of the linear fits.

At a growth temperature of 475 °C the influence of the TBAs partial pressure on the N incorporation and PL peak energy was investigated and the results are shown in figure 8 (a). The N incorporation seems to decrease with TBAs supply and stays constant at higher TBAs partial pressures. This information is from the HRXRD measurements, which showed undistinguishable diffractograms for all TBAs partial pressures deviating from 0. For this case the PL peak energy gives other information: The PL peak energy is slightly but monotonically increasing with increasing TBAs supply, which may appear due to lower N incorporations. In figure 8 (b) the normalized PL spectra are plotted for all samples grown at different TBAs partial pressures and one can see that the peak position is shifting to the GaAs substrate peak and remains only as shoulder at higher TBAs partial pressures. The decrease in N incorporation with higher TBAs partial pressure is probably due to the competition for group V lattice sites and therefore As is preventing N from incorporation. This effect is also well known for the precursors DTBAA and UDMHy.[5,21,33] For UDMHy the N incorporation is adjusted using the N/As ratio. The possibility of adjusting the N incorporation with TBAs/DTBADMHy ratio is very useful to grow Ga(N,As)

structures with defined N content. To incorporate a defined higher N content, the temperature combined with the TBAs supply can be adjusted to reach the desired composition.

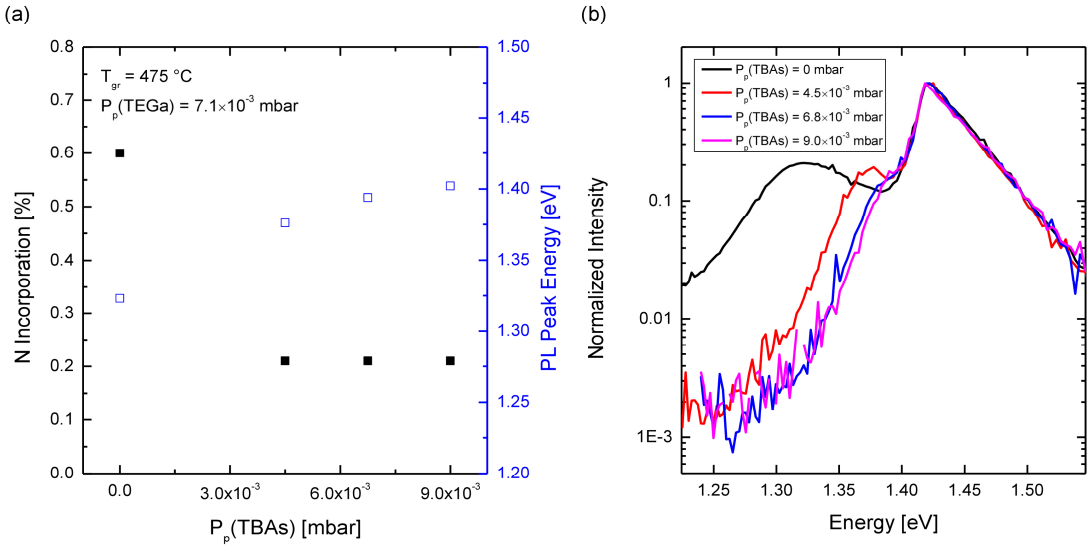

Figure 8: (a) Plot of the N incorporation (black) and growth rate (blue) in dependence of the TBAs partial pressure. (b) Normalized PL spectra of samples shown in (a).

In figure 9 the N incorporation of DTBADMHy and UDMHy is plotted vs. the growth rate. This means that the gas phase ratios of different precursors and the growth temperature were kept constant but the total precursor flow into the reactor was changed. For both precursors the behavior is the same: No influence of the growth rate on the N incorporation is observed. This behavior is proven for DTBADMHy by PL and HRXRD measurements, which are similar for all samples. An explanation for this behavior could be that the incorporation of the different group V species only depends on the competition for group V lattice sites and they are independent from the kinetics. For comparison of the difference in N incorporation between UDMHy and DTBADMHy the difference in N/As ratio (1 vs. 3.6) and different growth temperatures (525 °C vs. 500 °C) should be mentioned. The higher N/As ratio leads to a higher N incorporation of the UDMHy while the higher growth temperature leads to a decrease.

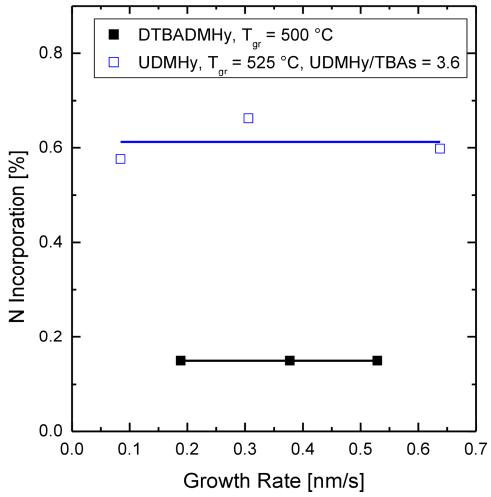

Figure 9: N incorporation vs. growth rate for growth with DTBADMHy and UDMHy. Data of UDMHy are taken from ref.[5].

For comparison of N content in samples grown with different N precursors the PL peak energy is plotted vs. the N content in figure 10. A line through the data is shown for comparison of the different samples as a guide for the eye. One can see that the black squares (DTBADMHy samples) fit to the reference data except of the 6 % sample, which is probably due to the low thickness (4.6 nm) resulting in a high quantization energy. This proves that N composition obtained from strain in HRXRD measurements fit to the band gaps obtained by PL measurements and that the precursor DTBADMHy is mainly incorporating N and As.

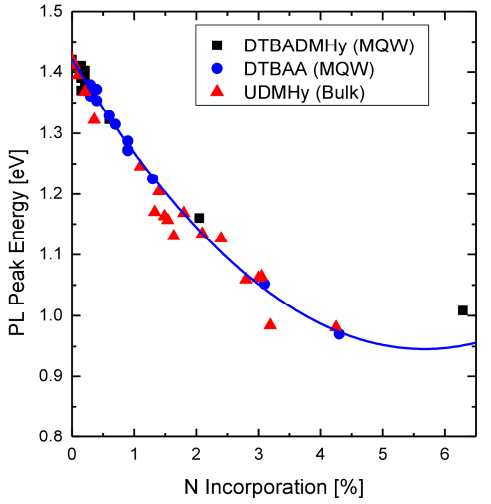

Figure 10: Plot of the PL peak energy in dependence of the N incorporation for samples grown with different precursors. Data for DTBAA and UDMHy are taken from [21]. The blue line shows a guide for the eye through the data.

4. Summary and Outlook

The thermal decomposition of a newly designed As-N precursor DTBADMHy was studied under MOVPE conditions in a horizontal AIXTRON AIX 200 system. The decomposition products were studied in an ion trap mass spectrometer connected inline to this system. The As-N bond of the DTBADMHy is shown to decompose by homolytic fission at 170 ± 10 °C and agrees to the decomposition temperature of DTBAA, which also exhibits an As-N bond and has been measured in the same reactor system in the past. The main decomposition products are DTBAs• and UDMHy•, which themselves are first stable and decompose at 290 ± 10 °C and 270 ± 10 °C, respectively. Both decomposition temperatures are determined lower compared to the decomposition temperatures of 350 °C for DTBAs and 420 °C for UDMHy, showing a lower thermal stability of formed radicals. The DTBAs• that is related to the As incorporation decomposes by dissociation of the *tert*-butyl groups from the molecule, which either occurs by homolysis of the As-C bond or by β-H elimination. The β-H elimination was seen to become relevant at higher temperatures. The UDMHy• decomposes similar to the decomposition reactions published for UDMHy. The main detected molecular species are $(CH_3)_2NH$ and CH_3NCH_2. The $(CH_3)_2NH$ is correlated to the formation of $(CH_3)_2N$• by homolytic fission of the N-N bond under formation of NH. The CH_3NCH_2 is formed in an intramolecular coupling of UDMHy• including the formation of NH_2•. The formed NH_2• and NH are found to be connected to the N incorporation behavior of the precursor.
The growth studies with the novel N-As precursor DTBADMHy show N as well as As incorporation. The activation energy of the N incorporation was determined with 2.36 ± 0.08 eV similar to the value of 2.45 ± 0.09 eV determined for the precursor DTBAA. In contrast, the activation energy of UDMHy is determined with 0.96 ± 0.04 eV showing that the dissociation of the As-N bond is responsible for the incorporation behavior and the low decomposition temperatures of DTBAA and DTBADMHy. The behavior of different V/III ratios varies from that of DTBAA and shows no increase with V/III ratio and therefore is comparable to that of UDMHy were the N incorporation is adjusted by varying the N/As ratio only. Lowering the N/As ratio by supplying additional TBAs lowers the N incorporation due to group V competition in good agreement to the growth with UDMHy or DTBAA. Further, no growth rate dependence of the N incorporation was observed as seen for UDMHy growth. High N incorporation of 6 % and growth temperatures as low as 425 °C were observed, which are promising for future applications with high N compositions.

Acknowledgements

This work was supported by the German Research Foundation (GRK 1782: “Functionalization of Semiconductors” & SFB 1083 “Structure & Dynamics of Internal Interfaces”) and the support for the mass spectrometer (iTrap) was provided by the Carl Zeiss SMT GmbH.

Declarations of Interest: none

Corresponding authors:

Johannes Glowatzki

E-mail address: Johannes.Glowatzki@physik.uni-marburg.de

Oliver Maßmeyer
E-mail address: Oliver.Massmeyer@physik.uni-marburg.de

References

(1) Shan, W.; Yu, K. M.; Walukiewicz, W.; Wu, J.; Ager, J. W.; Haller, E. E. Band Anticrossing in Dilute Nitrides. *J. Phys. Condens. Matter* **2004**, *16* (31), 3355–3372. https://doi.org/10.1088/0953-8984/16/31/024.

(2) J. Wu, W. S. and W. W. Band Anticrossing in Highly Mismatched III–V Semiconductor Alloys. *Semicond. Sci. Technol.* **2002**, *17*, 860–869. https://doi.org/10.1088/0268-1242/17/8/315.

(3) Shan, W.; Walukiewicz, W.; Ager, J. W.; Haller, E. E.; Geisz, J. F.; Friedman, D. J.; Olson, J. M.; Kurtz, S. R. Band Anticrossing in Gainnas Alloys. *Phys. Rev. Lett.* **1999**, *82* (6), 1221–1224. https://doi.org/10.1103/PhysRevLett.82.1221.

(4) Kondow, M.; Kitatani, T.; Larson, M. C.; Nakahara, K.; Uomi, K.; Inoue, H. Gas-Source MBE of GaInNAs for Long-Wavelength Laser Diodes. *J. Cryst. Growth* **1998**, *188* (1–4), 255–259. https://doi.org/10.1016/S0022-0248(98)00060-8.

(5) Volz, K.; Koch, J.; Höhnsdorf, F.; Kunert, B.; Stolz, W. MOVPE Growth of Dilute Nitride III/V Semiconductors Using All Liquid Metalorganic Precursors. *J. Cryst. Growth* **2009**, *311* (8), 2418–2426. https://doi.org/10.1016/j.jcrysgro.2008.09.210.

(6) Kondow, M.; Kitatani, T. Molecular Beam Epitaxy of GaNaS and GaInNAs. *Semicond. Sci. Technol.* **2002**, *17* (8), 746–754. https://doi.org/10.1088/0268-1242/17/8/302.

(7) Yuen, H. B.; Bank, S. R.; Wistey, M. A.; Harris, J. S.; Moto, A. Comparison of GaNAsSb and GaNAs as Quantum-Well Barriers for GaInNAsSb Optoelectronic Devices Operating at 1.3-1.55 Mm. *J. Appl. Phys.* **2004**, *96* (11), 6375–6381. https://doi.org/10.1063/1.1807028.

(8) F. Hohnsdorf, J. Koch, S. Leu, W. Stolz, B. B. and M. D. Reduced Threshold Current Densities of (GaIn)(NAs)/GaAs Single Quantum Well Lasers for Emission Wavelengths in the Range 1.28-1.38 Mm,. *Electron. Lett.* **1999**, *35* (7), 571–572.

(9) Kunert, B.; Reinhard, S.; Koch, J.; Lampalzer, M.; Volz, K.; Stolz, W. First Demonstration of Electrical Injection Lasing in the Novel Dilute Nitride Ga(NAsP)/GaP-Material System. *Phys. Status Solidi C Conf.* **2006**, *3* (3), 614–618. https://doi.org/10.1002/pssc.200564124.

(10) Kunert, B.; Zinnkann, S.; Volz, K.; Stolz, W. Monolithic Integration of Ga(NAsP)/(BGa)P Multi-Quantum Well Structures on (0 0 1) Silicon Substrate by MOVPE. *J. Cryst. Growth* **2008**, *310* (23), 4776–4779. https://doi.org/10.1016/j.jcrysgro.2008.07.097.

(11) Liebich, S.; Zimprich, M.; Beyer, A.; Lange, C.; Franzbach, D. J.; Chatterjee, S.; Hossain, N.; Sweeney, S. J.; Volz, K.; Kunert, B.; et al. Laser Operation of Ga(NAsP) Lattice-Matched to (001) Silicon Substrate. *Appl. Phys. Lett.* **2011**, *99* (7), 071109 1-3. https://doi.org/10.1063/1.3624927.

(12) Jackrel, D. B.; Bank, S. R.; Yuen, H. B.; Wistey, M. A.; Harris, J. S.; Ptak, A. J.; Johnston, S. W.; Friedman, D. J.; Kurtz, S. R. Dilute Nitride GaInNAs and GaInNAsSb Solar Cells by Molecular Beam Epitaxy. *J. Appl. Phys.* **2007**, *101* (11). https://doi.org/10.1063/1.2744490.

(13) Tan, K. H.; Wicaksono, S.; Loke, W. K.; Li, D.; Yoon, S. F.; Fitzgerald, E. A.; Ringel, S. A.; Harris, J. S. Molecular Beam Epitaxy Grown GaNAsSb 1 EV Photovoltaic Cell. *J. Cryst. Growth* **2011**, *335* (1), 66–69. https://doi.org/10.1016/j.jcrysgro.2011.09.023.

(14) Kurtz, S. R.; Allerman, A. A.; Jones, E. D.; Gee, J. M.; Banas, J. J.; Hammons, B. E. InGaAsN Solar Cells with 1.0 EV Band Gap, Lattice Matched to GaAs. *Appl. Phys. Lett.* **1999**, *74* (5), 729–731. https://doi.org/10.1063/1.123105.

(15) Jones-Albertus, R.; Becker, E.; Bilir, T.; Derkacs, D.; Fidaner, O.; Jory, D.; Liu, T.; Lucow, E.; Misra, P.; Pickett, E.; et al. Using Dilute Nitrides to Achieve Record Solar Cell Efficiencies. *MRS Proc.* **2013**, *1538*, 161–166. https://doi.org/10.1557/opl.2013.656.

(16) Jürgensen, H. Large-Scale MOVPE Production Systems. *Microelectron. Eng.* **1992**, *18* (1–2), 119–148. https://doi.org/10.1016/0167-9317(92)90125-B.

(17) Volz, K.; Torunski, T.; Kunert, B.; Rubel, O.; Nau, S.; Reinhard, S.; Stolz, W. Specific Structural and Compositional Properties of (GaIn)(NAs) and Their Influence on Optoelectronic Device Performance. *J. Cryst. Growth* **2004**, *272* (1–4), 739–747. https://doi.org/10.1016/j.jcrysgro.2004.09.012.

(18) Ptak, A. J.; Kurtz, S.; Curtis, C.; Reedy, R.; Olson, J. M. Incorporation Effects in MOCVD-Grown (In)GaAsN Using Different Nitrogen Precursors. *J. Cryst. Growth* **2002**, *243* (2), 231–237. https://doi.org/10.1016/S0022-0248(02)01412-4.

(19) Sterzer, E.; Ringler, B.; Nattermann, L.; Beyer, A.; von Hänisch, C.; Stolz, W.; Volz, K. (GaIn)(NAs) Growth Using Di-Tertiary-Butyl-Arsano-Amine (DTBAA). *J. Cryst. Growth* **2017**, *467*, 132–136. https://doi.org/10.1016/j.jcrysgro.2017.01.014.

(20) Sterzer, E.; Maßmeyer, O.; Nattermann, L.; Jandieri, K.; Gupta, S.; Beyer, A.; Ringler, B.; Von Hänisch, C.; Stolz, W.; Volz, K. 1 EV Ga(NAsSb) Grown by MOVPE Using Di-Tertiary -Butyl-Arsano-Amine (DTBAA). *AIP Adv.* **2018**, *8* (5), 055329 1-9. https://doi.org/10.1063/1.5034083.

(21) Sterzer, E.; Beyer, A.; Duschek, L.; Nattermann, L.; Ringler, B.; Leube, B.; Stegmüller, A.; Tonner, R.; Von Hänisch, C.; Stolz, W.; et al. Efficient Nitrogen Incorporation in GaAs Using Novel Metal Organic As-N Precursor Di-Tertiary-Butyl-Arsano-Amine (DTBAA). *J. Cryst. Growth* **2016**, *439*, 19–27. https://doi.org/10.1016/j.jcrysgro.2015.12.032.

(22) Maßmeyer, O.; Inacker, S.; Hepp, T.; Glowatzki, J.; Nattermann, L.; Sterzer, E.; Ritter, C.; von Hänisch, C.; Stolz, W.; Volz, K. Decomposition Mechanisms of Di- Tert - Butylaminoarsane (DTBAA). *Organometallics* **2019**, *38* (16), 3181–3186. https://doi.org/10.1021/acs.organomet.9b00442.

(23) Lee, R. T.; Stringfellow, G. B. Pyrolysis of 1,1 Dimethylhydrazine for OMVPE Growth. *J. Electron. Mater.* **1999**, *28* (8), 963–969. https://doi.org/10.1007/s11664-999-0205-9.

(24) Larsen, C. A.; Buchan, N. I.; Li, S. H.; Stringfellow, G. B. Decomposition Mechanisms of Tertiarybutylarsine. *J. Cryst. Growth* **1989**, *94* (3), 663–672. https://doi.org/10.1016/0022-0248(89)90090-0.

(25) Nattermann, L.; Maßmeyer, O.; Sterzer, E.; Derpmann, V.; Chung, H. Y.; Stolz, W.; Volz, K. An Experimental Approach for Real Time Mass Spectrometric CVD Gas Phase Investigations. *Sci. Rep.* **2018**, *8* (1), 319. https://doi.org/10.1038/s41598-017-18662-7.

(26) Maßmeyer, O.; Inacker, S.; Hepp, T.; Glowatzki, J.; Nattermann, L.; Sterzer, E.; Ritter, C.; Hänisch, C. Von; Stolz, W.; Volz, K. Decomposition Mechanisms of Di-Tert-Butylaminoarsane (DTBAA). *Organometallics* **2019**, *38* (16), 3181–3186. https://doi.org/10.1021/acs.organomet.9b00442.

(27) Glowatzki, J.; Maßmeyer, O.; Köster, M.; Hepp, T.; Odofin, E.; Hänisch, C. von; Stolz, W.; Volz, K. Ga(N,P) Growth on Si and Decomposition Studies of the N–P Precursor Di- Tert -

Butylaminophosphane (DTBAP). *Organometallics* **2020**, *39* (10), 1772–1781. https://doi.org/10.1021/acs.organomet.0c00078.

(28) Chung, H. Y.; Aliman, M.; Fedosenko, G.; Laue, A.; Reuter, R.; Derpmann, V.; Gorkhover, L.; Antoni, M. Very Sensitive Real-Time Inline Process Mass Spectrometer Based on FFT Ion Trap Technique. In *2016 27th Annual SEMI Advanced Semiconductor Manufacturing Conference (ASMC)*; IEEE, 2016; pp 263–266. https://doi.org/10.1109/ASMC.2016.7491140.

(29) Stringfellow, G. B. *Organometallic Vapour Phase Epitaxy: Theory and Practice*, 2nd ed.; Academic Press, 1999.

(30) Stegmüller, A.; Tonner, R. β-Hydrogen Elimination Mechanism in the Absence of Low-Lying Acceptor Orbitals in EH 2 (t -C 4 H 9) (E = N–Bi) . *Inorg. Chem.* **2015**, *54* (13), 6363–6372. https://doi.org/10.1021/acs.inorgchem.5b00687.

(31) Okumura, H.; Yoshida, S.; Okahisa, T. Optical Properties near the Band Gap on Hexagonal and Cubic GaN. *Appl. Phys. Lett.* **1994**, *64* (22), 2997–2999. https://doi.org/10.1063/1.111383.

(32) Liu, S. S. Growth Kinetics and Catalytic Effects in the Vapor Phase Epitaxy of Gallium Nitride. *J. Electrochem. Soc.* **1978**, *125* (7), 1161. https://doi.org/10.1149/1.2131641.

(33) Moto, A.; Tanaka, S.; Ikoma, N.; Tanabe, T.; Takagishi, S.; Takahashi, M.; Katsuyama, T. Metalorganic Vapor Phase Epitaxial Growth of GaNAs Using Tertiarybutylarsine (TBA) and Dimethylhydrazine (DMHy). *Japanese J. Appl. Physics, Part 1 Regul. Pap. Short Notes Rev. Pap.* **1999**, *38* (2 B), 1015–1018. https://doi.org/10.1143/jjap.38.1015.

(34) Ohtake, A. Surface Reconstructions on GaAs(001). *Surf. Sci. Rep.* **2008**, *63* (7), 295–327. https://doi.org/10.1016/j.surfrep.2008.03.001.

(35) Maßmeyer, O.; Sterzer, E.; Nattermann, L.; Stolz, W.; Volz, K. Influence of UDMHy on GaAs (0 0 1) Surface Reconstruction before and during Growth of Ga(NAs) by MOVPE. *Appl. Surf. Sci.* **2018**, *458* (15), 512–516. https://doi.org/10.1016/j.apsusc.2018.07.098.

(36) Richter, W. In-Situ Observation of MOVPE Epitaxial Growth. *Appl. Phys. A Mater. Sci. Process.* **2002**, *75* (1), 129–140. https://doi.org/10.1007/s003390101061.

(37) French, C. L.; Foord, J. S. Reaction Kinetics for the CBE Growth of GaAs from Triethylgallium; Computer Modelling Studies Incorporating Recent Surface Spectroscopic Data. *J. Cryst. Growth* **1992**, *120* (1–4), 63–70. https://doi.org/10.1016/0022-0248(92)90365-P.

(38) Murrell, A. J.; Wee, A. T. S.; Fairbrother, D. H.; Singh, N. K.; Foord, J. S.; Davies, G. J.; Andrews, D. A. Surface Chemical Processes in Metal Organic Molecularbeam Epitaxy; Ga Deposition from Triethylgallium on GaAs(100). *J. Appl. Phys.* **1990**, *68* (8), 4053–4063. https://doi.org/10.1063/1.346242.

(39) Krambrock, K.; Linde, M.; Spaeth, J. M.; Look, D. C.; Bliss, D.; Walukiewicz, W. Arsenic Antisite-Related Defects in Low-Temperature MBE Grown GaAs. *Semicond. Sci. Technol.* **1992**, *7* (8), 1037–1041. https://doi.org/10.1088/0268-1242/7/8/002.

7.2.6 Real-time Gas Phase Analysis during GaAs and GaP Growth by MOVPE

Authors: Oliver Maßmeyer, Johannes Haust, Thilo Hepp, Robin Günkel, Johannes Glowatzki, C. von Hänisch, Wolfgang Stolz and Kerstin Volz

Publication: to be submitted

Abstract: *Tert*-butyl-arsane (TBAs) and *Tert*-butyl-phosphane (TBP) are getting more and more established as group-V precursors for growth of V/III semiconductors by metal organic vapor phase epitaxy (MOVPE). Due to this development, the thermal decomposition of these precursors was studied during growth of GaAs and GaP utilizing the Ga precursors tri-methyl-gallium (TMGa), tri-ethly-gallium (TEGa) and tri-*tert*-butyl-gallium (TTBGa) in a horizontal AIXTRON AIX 200 GFR MOVPE system. The decomposition and reaction products were measured in line with a real time Fourier transform quadrupole ion trap mass spectrometer (iTrap) from Carl Zeiss SMT GmbH. The decomposition temperatures and the related activation energies are determined for all mentioned precursors under comparable reactor conditions. The decomposition curves suggest a catalytic effect of the GaAs surface on the decomposition of TBAs and TBP. The catalytic reaction reduces the decomposition temperature of TBAs and TBP by up to 200 °C. In addition, the decomposition products indicate *alkyl exchange* as a relevant process during decomposition. For the growth of GaAs with TBAs and TEGa a significant decrease of the decomposition temperature with an increasing V/III ratio is observed. This behavior is related to an effective V/III ratio that gives insight into low temperature GaAs growth.

Authors' Contributions: My contribution to this work was the planning, the execution and interpretation of the decomposition analysis by mass spectrometry. J. Haust assisted with the lab work and the mass spectrometry investigations in the framework of his research laboratory course. All co-authors helped with the interpretation of the data and with the review of the manuscript. W. Stolz and K. Volz supervised the work and secured the funding to support this study.

Real-time Gas Phase Analysis during GaAs and GaP Growth by MOVPE

O. Maßmeyer, J. Haust, T. Hepp, R. Günkel, J. Glowatzki, C. von Hänisch, W. Stolz and K. Volz

Material Sciences Center and Department of Physics, Philipps-Universität Marburg, Germany

E-Mail: Oliver.Massmeyer@physik.uni-marburg.de

Abstract

Tertiarybutylarsane (TBAs) and Tertiarybutylphosphane (TBP) are getting more and more established as group V precursors for growth of V/III semiconductors by metal organic vapor phase epitaxy (MOVPE). Due to this development, the thermal decomposition of these precursors was studied during growth of GaAs and GaP utilizing the Ga precursors trimethylgallium (TMGa), triethlygallium (TEGa) and tritertiarybutylgallium (TTBGa) in a horizontal AIXTRON AIX 200 GFR MOVPE system. The decomposition and reaction products were measured in line with a real time Fourier transform quadrupole ion trap mass spectrometer (iTrap) from Carl Zeiss SMT GmbH. The decomposition temperatures and the related activation energies are determined for all mentioned precursors under comparable reactor conditions. The decomposition curves suggest a catalytic effect of the GaAs surface on the decomposition of TBAs and TBP. The catalytic reaction reduces the decomposition temperature of TBAs and TBP by up to 200 °C. In addition, the decomposition products indicate alkyl exchange as a relevant process during decomposition. For the growth of GaAs with TBAs and TEGa a significant decrease of the decomposition temperature with an increasing V/III ratio is observed. This behavior is related to an effective V/III ratio that gives insight into low temperature GaAs growth.

Keywords: GaAs growth, GaP growth, mass spectrometry, TBAs, TBP, TMGa, TEGa, TTBGa, catalytic reaction, alkyl exchange

1. Introduction

Metal organic vapor phase epitaxy (MOVPE) is a well-established commercial production technique for many kinds of electronic and photonic devices based on semiconductor materials, such as LEDs, laser diodes, solar cells, high electron mobility transistors, integrated circuits and many more [1]. Large amounts of these applications are based on III/V semiconductor materials. To realize these devices by MOVPE the choice of the right metal organic precursor (MO) is essential to achieve the desired material compositions and purity. On the one hand, small changes in the gas phase mixture can have a significant impact on the growth characteristics, which influence the incorporation behavior. Consequently, the material composition is altered, which changes the device properties. On the other hand, the purity of the device is crucial since even impurities in the parts per million level can result in high defect densities within the crystal structure, which results in poor device performance [2]. To address those issues a thorough understanding of the gas phase reactions and an *in situ* gas phase analysis is desired to enhance the current understanding of the growth process during MOVPE and improve process control for fabrication of semiconductor devices. Different experimental setups using mass spectrometry have been invented in the past to enable decomposition analysis for III/V semiconductor materials. The need of decomposition studies started in the late 80's and early 90's with the development of novel precursors like tertiarybutylarsane (TBAs) and triethylgallium (TEGa) [3,4]. Unfortunately, the decomposition experiments in the early studies were done in various setups, which showed that changes of the experimental conditions like e.g. the choice of the carrier gas, the reactor pressure, the partial pressures of the metal organic precursors and the surface area have a severe impact on the decomposition [5–10]. Furthermore, due to the use of linear quadrupole mass spectrometers or time of flight mass spectrometers, additional pressure reduction stages were used

in these setups to allow the transition from the rough vacuum or ambient pressure in the reactor to high vacuum (< 10^{-5} mbar) conditions needed for mass spectrometry [11]. This pressure reduction can lead to changes in the gas phase, which makes *in situ* measurements very challenging. Nevertheless, the combination of all these studies has founded a basic knowledge for decomposition reactions of single precursors in the gas phase (unimolecular reactions) for many different metal organic precursors [5–8,12–18]. In addition, the decomposition of single precursors influenced by different surfaces (heterolytic reactions) were studied [5]. Also some approaches to study the simultaneous decomposition of different combinations of group V and group III precursors (bimolecular reactions) during the growth of GaAs, GaP and other III/V semiconductors are given [9,19,20]. However, especially the studies of bimolecular reactions do not cover all available precursor combinations and the mentioned use of different experimental setups make a satisfying comparison difficult.

Therefore, to enhance the current understanding of the bimolecular decomposition reactions and reaction products the growth of GaAs and GaP with the group V precursors tertiarybutylarsane and tertiarybutylphosphane (TBP) and the group III precursors trimethylgallium (TMGa), triethylgallium and tritertiarybutylgallium (TTBGa) is studied in this work. Especially, the combination of TTBGa with TBAs and TBP has not been studied so far and our results for the other precursor combinations show some deviation compared to the data from the literature. The decomposition and reaction products are investigated by mass spectrometry in a novel setup for *in situ* gas phase analysis, which is attached in line in a commercial AIXTRON AIX 200 MOVPE system. In contrast to the setups used in the past, the used mass spectrometer is based on a quadrupole ion trap that uses fast Fourier transformation for the generation of the mass spectrum [21]. Due to the resistance of the setup and the utilization of an atomic layer deposition valve, the process gas can be transferred into the mass spectrometer without the need of pressure reduction stages. This should reduce changes of the gas phase. Another huge advantage is the high sensitivity of the ion trap allowing the detection in the parts per trillion level, which gives new insights into the decomposition reactions. Furthermore, the fast Fourier transformation based concept allows the detection of a full mass spectrum in less than 2 s, which allows real time measurements during the MOVPE process.

In this study, this setup is used for *in situ* analysis during growth of GaAs and GaP. First, the unimolecular decomposition of the precursors TMGa, TEGa, TTBGa, TBAs and TBP is discussed to support the literature data, since these have not been measured in the same reactor system until now. Secondly, the influence of the Ga precursors on the decomposition of TBAs and TBP is shown, which results in a large reduction of the decomposition temperature under the chosen conditions. The detected decomposition products show that an alkyl exchange reaction is an important step in the bimolecular decomposition reaction and the reaction products are compared to findings in the literature. In the last part, the growth of GaAs with TEGa and TBAs shows a dependence of the decomposition temperature on the V/III ratio, which has so far not been systematically identified. From these results an effective V/III ratio is determined, which could especially help to understand the growth at comparably low temperatures (< 400 °C).

2. Experimental procedure

All decomposition studies are carried out in an AIXTRON AIX 200 horizontal GFR (gas foil rotation) reactor. In this system the precursors are carried by high purified hydrogen (purity 9.0) into to the reactor chamber. Notably, the precursors are carried through separated pipes for group V and group III precursors into the reactor and firstly meet around 10 cm before the growth area. This effectively prevents possible pre-reactions of the precursors. The total flow in the reactor is kept constant with 6800 sccm. The thermal energy necessary to initiate the decomposition of the precursors and therefore the crystal growth is generated by a graphite susceptor uniformly heated by halogen lamps located beneath the reactor. The temperature is controlled and measured by a thermocouple in the center of the susceptor and the surface temperature is calibrated by observing the phase transition of an Al-coated Si substrate. Prior to the

experiments the susceptor was baked out at 800 °C to desorb residual fragments, which could potentially be remaining from former experiments. For measurements of the unimolecular decomposition the susceptor was kept uncoated and no substrate was added into the reactor. No substrate was used for the investigation of the bimolecular reactions, as well. Since deposition occurs on all surfaces above a specific temperature, the reactor walls and components are being coated throughout the experiment. To avoid coating related effects, the exchangeable reactor components are cleaned in between the experiments. To stick to standard growth conditions, the growth area is rotated at 50 to 70 rpm, which is used to allow homogenous deposition in this reactor type. The reactor chamber includes a surface area of about 720 cm^2, including the surface area of the quartz liner and the graphite susceptor (100 cm^2) [21].
For all experiments TMGa, TEGa and TTBGa are used as group III precursors and TBAs and TBP are used as group V precursors. Throughout the experiments, the partial pressures of the precursors have been adjusted within a range, which is used in growth of semiconductor devices and the exact values are given within each experiment. This should ensure a good insight into the growth process. The thermal decomposition and reaction products are analyzed by a quadrupole ion trap mass spectrometer (iTrap) from Carl Zeiss SMT GmbH. The ion trap is connected with a bypass system to the MOVPE system. A quartz crystal nozzle located right above the middle of the growth area of the susceptor collects the process gas. This bypass is operated under stable gas flow and pressure conditions similar to the status in the reactor to minimize any disturbance of the system. Using an atomic layer deposition valve the collected process gas is then pulsed into the ion trap with a gas inlet time in the millisecond range. Therefore, in comparison to setups used in the past, no pressure reduction stages are needed [7]. The quadrupole of the ion trap is based on the principle of a Paul trap and consists of a top, a bottom and a ring electrode. The analyte is first ionized by electron ionization (EI) at 70 eV. The created ions are then captured by an oscillating electric field, which is applied to the ring electrode in the ion trap. The applied field is oscillating in the radio frequency range with a used voltage between 80 V and 400 V, which has to be adjusted in accordance with the desired mass range. The resulting motions of the ions within the ion trap induce a mirror image current in the top and bottom electrodes. After resonant excitation of the ions, a full mass spectrum can be generated by fast Fourier transformation (FFT) of the detected damped mirror image current. Furthermore, the setup is capable to remove a selected range of mass over charge ratios (m/z) from the trap by using stored waveform inverse Fourier transform (SWIFT) [22,23]. This concept was developed to enable very high sensitivity, which was demonstrated by the detection of a part per trillion volumes of diborane (B_2H_6) in H_2. Additionally, due to the FFT based concept the measurement time of a single mass spectrum can be lower than 2 s, which makes this setup very suitable for real time gas phase analysis and it should be capable for detection of impurities within the reactor system. This setup is additionally described in more detail in ref. [21] and has already been successfully used for gas phase analysis of TBAs, a novel N-As precursor ditertiarybutylaminoarsane (DTBAA) and the corresponding P analogue ditertiarybutylaminophosphane (DTBAP) [21,24].
As mentioned before, only the surface temperature of the susceptor is determined in this setup. Due to the distance of the gas collection point at the nozzle from the susceptor, the effective gas temperature is determined by correlation of the TBAs decomposition results of ref. [21] with data from ref. [5].

3. Results and discussion

In the first part the unimolecular decomposition of TMGa, TEGa, TTBGa, TBP and TBAs is discussed. For these experiments, the susceptor was kept uncoated. However, a small coating with Ga during the decomposition of the Ga precursors occurs, which can change the surface properties. During the decomposition of TBAs and TBP the reactor parts are being coated over time with arsenic or phosphorus, respectively. [25].

3.1. Unimolecular decomposition of TMGa, TEGa, TTBGa, TBP and TBAs

The decomposition curves of TMGa (114 u), TEGa (156 u), TTBGa (240 u), TBP (90 u) and TBAs (134 u) are shown in figure 1 a). The partial pressures (p_P) were chosen all in the same magnitude with p_P(TMGa) = 9.5 × 10^{-4} mbar, p_P(TEGa) = 7.5 × 10^{-3} mbar, p_P(TTBGa) = 3 × 10^{-3} mbar, p_P(TBP) = 8.2 × 10^{-3} mbar and Pp(TBAs) = 7.5 × 10^{-3} mbar, respectively. The small deviations are due to an optimization of the signal to noise ratio under the given reactor conditions. The decomposition temperatures for each precursor can be determined by the decomposition curves from the point, at which the intensity drops to half of its value (T_{50}). A grey dashed line in the respective figures marks this point. The decomposition temperatures (T_{decomp}) are determined with T_{decomp}^{TMGa} = 340 ± 10 °C, T_{decomp}^{TEGa} = 250 ± 10 °C, T_{decomp}^{TTBGa} = 140 ± 10 °C, T_{decomp}^{TBP} = 400 ± 10 °C and T_{decomp}^{TBAs} = 360 ± 10 °C. These and the values of the experiments shown in the next parts are listed in table 1 to give a general overview and comparison between the experiments done in this study. The decomposition temperatures determined from the data of TMGa, TEGa and TTBGa reduces strongly with increasing size of the alkyl groups in the molecule. This follows the behavior seen in detail for various As precursors [4] and fits to the trend in decomposition temperatures from data published in the literature with T_{decomp}^{TMGa} = 430 °C [15,18], T_{decomp}^{TEGa} = 290 °C [7,15] and $T_{decomp}^{TTBGa} < T_{decomp}^{TEGa}$ [12,17,26].

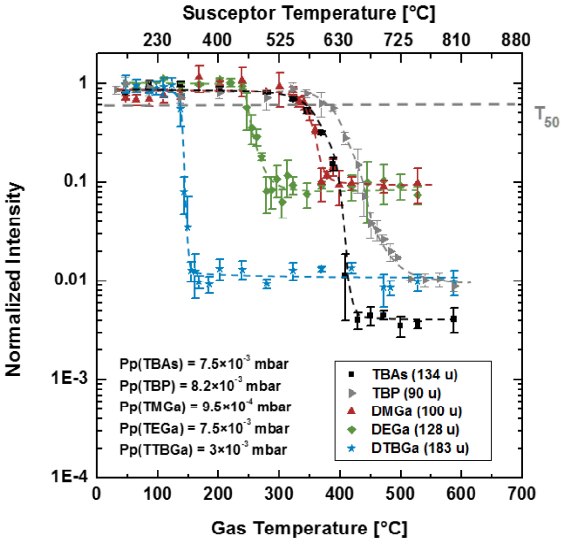

Figure 1: a) Temperature dependent decomposition curves of TBAs, TBP, TMGa, TEGa, and TTBGa on the bare graphite susceptor. Due to the electron impact ionization the Ga precursors are tracked by the largest detected fragment DMGa (100 u), DEGa (128 u) and DTBGa (183 u). The partial pressures are chosen with Pp(TBAs) = 7.5 × 10^{-3} mbar, Pp(TBP) = 8.2 × 10^{-3} mbar, Pp(TMGa) = 9.5 × 10^{-4} mbar, Pp(TEGa) = 7.5 × 10^{-3} mbar and Pp(TTBGa) = 3 × 10^{-3} mbar with values comparable to actual growth conditions. The temperature at which the intensity drops to half of its intensity (T_{50}) is marked by the grey dashed line and is defined as the decomposition temperature of the precursor.

The deviation of the decomposition temperatures compared to the values from the literature are expected due to the different experimental setups. The decomposition depends largely on the process parameters like reactor pressure, reactor flow, source partial pressure and surface area, as well as on the determination of the temperature of the analyzed process gas. Therefore, an extended study within our reactor system should give a specific insight into the available decomposition pathways in this reactor type and improve the general understanding of decomposition reactions during growth of III/V semiconductors.

Experiment	E_A in [eV]	E_A in [kcal/mol]	Log(A_0) in [1/s]	T_{decomp} in [°C]	Experiment	E_A in [eV]	E_A in [kcal/mol]	Log(A_0) in [1/s]	T_{decomp} in [°C]
TBAs[1]	2.3 ± 0.4	54 ± 10	16.9 ± 3.5	360 ± 10	V/III[3] = 10	3.9 ± 0.4	89 ± 10	32.2 ± 3.5	310 ± 10
TBP[1]	1.4 ± 0.1	32 ± 2	8.8 ± 1.0	400 ± 10	V/III[3] = 4	3.8 ± 0.4	88 ± 10	31.4 ± 3.5	310 ± 10
TMGa[1]	1.1 ± 0.2	26 ± 5	7.8 ± 1.5	340 ± 10	V/III[3] = 2	3.5 ± 0.4	81 ± 10	29.4 ± 4.0	290 ± 10
TEGa[1]	1.3 ± 0.1	30 ± 2	10.8 ± 1.0	250 ± 10	V/III[3] = 1	1.9 ± 0.1	44 ± 2	16.5 ± 1.0	250 ± 10
TTBGa[1,*]	3.1 ± 0.4	71 ± 10	36 ± 5.0	140 ± 10	V/III[3] = 0.75	1.5 ± 0.1	35 ± 2	13.4 ± 1.0	235 ± 10
TBAs + TMGa[2]	1.7 ± 0.5	39 ± 10	13.6 ± 4.5	310 ± 10	V/III[3,*] = 0.5	5.8 ± 2.0	135 ± 20	57.5 ± 10.0	220 ± 10
TBAs + TEGa[2]	1.9 ± 0.2	43 ± 5	18.2 ± 1.5	260 ± 10	TBAs - coated[3]	2.0 ± 0.2	47 ± 5	17.4 ± 1.5	250 ± 10
TBAs + TTBGa[2,*]	3.4 ± 1.0	80 ± 20	37.7 ± 12.0	170 ± 10					
TBP + TMGa[2]	2.1 ± 0.6	49 ± 15	15.9 ± 4.5	350 ± 10					
TBP + TEGa[2]	1.9 ± 0.2	43 ± 5	14.3 ± 2.0	315 ± 10					
TBP + TTBGa[2,*]	1.8 ± 0.8	42 ± 20	16.4 ± 7.0	250 ± 10					

Determined with Arrheinius plots of data from:
[1] Figure 1: unimolecular decomposition
[2] Figure 2: bimolecular decomposition
[3] Figure 6: V/III variation
** Only a few data points could be used due to the steep decomposition curve*

Table 1: Determined decomposition temperature (T_{decomp}), activation energies (E_A) and attempt frequency factors (A_0) from Arrhenius plots of the decomposition data of figure 1, figure 2 and figure 6. Depending on the data point density, due to the partially steep curves, the error of this evaluation can be significant.

The unimolecular decomposition of the TBAs and TBP can be directly tracked by the signal of the parent molecule in the detected mass spectra, as labeled in figure 1. This is made possible by the sensitive ionization settings found in ref. [21] for our setup. Even though electron impact ionization is used, only a small amount of the analyte is cracked in the ionization process, which facilitates the evaluation of the mass spectra. In the sensitive ionization settings a comparably low filament current of 1.3 A and a short waiting time between the gas inlet and the ionization of the molecules in the ion trap is used. The measured decomposition temperature of T_{decomp}^{TBAs} = 360 ± 10 °C for the unimolecular decomposition of TBAs fits to former measurements done in the literature [4,5,21]. The decomposition products show evidence for homolytic fission or intramolecular coupling reactions leading to formation of isobutane (58 u) and *tert*-butyl radicals (57 u) as well as β-H elimination which is supported by detection of Isobutene (56 u). This agrees to the well established decomposition pathways of TBAs. The corresponding decomposition data and reaction pathways are shown in S1. The decomposition temperature determined with our setup and the one of ref. [5] is in contrast to the decomposition temperature of 290 °C measured in a low pressure (~ 65 mbar) reactor setup [15]. This setup was designed for the measurement of the decomposition closely to the growth surface. This underlines that the used experimental setup as well as the temperature determination can have a large influence on the decomposition of the precursors.

The unimolecular decomposition of TBP shows like the TBAs decomposition the formation of isobutane (58 u) and *tert*-butyl radicals (57 u) underlining the importance of homolytic fission or intramolecular coupling reactions, as well as the formation of isobutene (56 u) indicating β-H elimination reactions upon decomposition. The possibility of a β-H elimination reaction for abstraction of the *tert*-butyl group was shown to become accessible under MOVPE conditions by calculations based on density functional theory [27]. Our data gives evidence, that the formation of isobutene (56 u) becomes more dominant at higher temperatures. The corresponding decomposition data and reaction schemes are shown in S2. Findings in the literature show a strong importance of bimolecular reactions, enhancing the TBP decomposition at higher input partial pressures under atmospheric pressure conditions [6]. A dependence on the TBP partial pressure has not been systematically studied in our setup so far. However, the probability of bimolecular reactions in the gas phase should be reduced in our setup due to the used rough vacuum of 50 mbar and low partial pressures in the 10^{-2} to 10^{-3} mbar range compared to the partial pressures used in ref [6]. For partial pressures of 1.7 mbar formation of isobutene (56 u) becomes dominant in their study. The isobutene (56 u) formation correlates to an increase in the formation of H_2 in their experiments, which gives rise to a unimolecular chain reaction. In this chain reaction first decomposition of TBP into *tert*-butyl radicals (57 u) and PH_2 occurs followed by H• abstraction from the *tert*-butyl radicals (57 u) to form isobutene (56 u). This chain reaction cannot be excluded by our findings. However, the H abstraction reaction seems to be very

unlikely from a chemical point of view due to the stability of the *tert*-butyl radicals due to hyperconjugation [28]. Therefore, the increase of isobutene (56 u) is referred to the β-H elimination reaction in our study, which matches the gas phase calculations mentioned above. The determined decomposition temperature of TBP in our setup is given with about 70 to 90 °C lower compared to values in the literature [6], which is expected due to the difference in the setups.

In the case of the group III precursors the decomposition is tracked by the largest available fragment of the precursors, since the parent molecule in this case is fractured by the ionization. The decomposition products for the Ga precursors compare well to the findings in the literature and are shown in S3 – S5. For the unimolecular decomposition of TMGa mainly methane (16 u) and methyl radicals (15 u) are detected indicating homolytic fission of the methyl groups from TMGa. This leads to methyl radicals which can attack the carrier gas (H_2) to form methane and $H^{\bullet}$. Studies in the literature show that the methyl radicals can then react with TMGa to enhance the decomposition [17]. In the literature further the formation of ethane (C_2H_6 – 30 u) is seen, which can be created in a chain termination step by reaction of two methyl radicals. Some ethane is detected within our measurement as well. However, this can be fully referred to the alkyl background in our setup. The lack of ethane in our experiment is explained by the lower reactor pressure of 50 mbar and partial pressures in the 10^{-3} mbar range. This makes the mentioned chain reaction quiet unlikely in our experiment. The collision of two reactive methyl radicals are very unlikely, since the methyl radicals more likely collide with H_2 first and react to methane.

The TEGa decomposition shows formation of ethane (30 u), ethyl radicals (29 u) and ethene (28 u), which agrees to the findings in the literature [7,15]. The corresponding decomposition data and reaction schemes are included in S4. Ethane and ethyl radicals indicate the homolytic fission of the alkyl group from the TEGa. The ethane is most likely formed by reaction of the ethyl radicals with the H_2 carrier gas and shows lower intensity compared to the detected ethyl and ethene signal. The ethane signal also drops for higher temperatures showing that the formation of ethane is more relevant at lower temperatures. The detected ethene is produced by β-H elimination of the alkyl groups. The signal of ethene shows the highest intensity over the whole temperature range. This supports the findings in the literature that β-H elimination is the dominant decomposition process for TEGa [7]. Surprisingly, the intensity of the ethyl radicals is detected with the same intensity. This shows that the homolytic fission reaction is relevant for the TEGa at higher temperatures under the used conditions.

TTBGa has received the least attention within the literature. The decomposition products measured for the decomposition of TTBGa and reaction pathways are shown in S5. Remarkably the decomposition temperature of TTBGa is determined by T_{decomp}^{TTBGa} = 140 ± 10 °C. Our determined value shows an about 100 °C lower decomposition temperature compared to T_{decomp}^{TEGa} and about 200 °C lower compared to T_{decomp}^{TMGa}, which agrees well to the finding of $T_{decomp}^{TTBGa} < T_{decomp}^{TEGa}$ and T_{decomp}^{TMGa} in ref. [12,17,26]. The measured decomposition curve of TTBGa shows a steeper decay compared to TEGa and TMGa, which results in a higher activation energy of 3.1 eV compared to 1.3 eV and 1.1 eV for TEGa and TMGa, respectively. Upon decomposition isobutane (58 u), *tert*-butyl radicals (57 u) and isobutene (56 u) are produced as major fragments. The isobutene (56 u) shows the highest intensity over the whole temperature range, showing that β-H elimination of the *tert*-butyl groups is the dominant decomposition reaction. Nevertheless, isobutane (58 u) and *tert*-butyl radicals (57 u) are detected with high intensities as well, indicating that the homolytic fission of the *tert*-butyl group is an important step in the decomposition. Presumably, one of the *tert*-butyl groups is abstracted by homolytic fission upon decomposition of TTBGa. The underlying reason could be a steric hindrance for the β-H elimination as a first reaction step, since the molecule has to rearrange in the transition state. Additionally, Ga (69/71 u) is detected upon decomposition. On the one hand, this could be attributed to desorption of deposited Ga on the reactor components. However, no Ga signal is detected for the decomposition of TMGa and TEGa. On the other hand, the Ga could also be detected due to formation of a larger Ga containing molecule. This could e.g. be the formation of

tertiarybutylgallium. This larger fragment can likely crack in the ionization process into *tert*-butyl radicals and Ga.

3.2. Influence of TMGa, TEGa and TTBGa on the decomposition of TBAs and TBP

In this section the influence of TMGa, TEGa and TTBGa on the decomposition of TBAs and TBP during growth of GaAs and GaP will be discussed, respectively.
The decomposition curves of TBAs during growth of GaAs with TMGa, TEGa and TTBGa is shown in figure 2 a). The partial pressures were chosen with 8.2 × 10^{-3} mbar for all precursors. This results in a V/III of one, which is crucial to detect the strong effect of the Ga precursor on the TBAs decomposition and will be discussed in section 3.4. The TBAs decomposition curves show that the decomposition temperature is almost reduced to the unimolecular decomposition temperature of the Ga precursors. The decomposition temperatures are reduced to $T_{decomp}^{TBAs+TMGa}$ = 310 ± 10 °C, $T_{decomp}^{TBAs+TEGa}$ = 260 ± 10 °C and $T_{decomp}^{TBAs+TTBGa}$ = 170 ± 10 °C compared to the unimolecular decomposition temperature of TBAs (T_{decomp}^{TBAs} = 360 ± 10 °C). This shows a significant reduction in the decomposition temperature of TBAs in all three cases. The decomposition temperature of the Ga precursors has been measured within the same experiment. These are determined with $T_{decomp}^{TMGa+TBAs}$ = 310 ± 10 °C, $T_{decomp}^{TEGa+TBAs}$ = 230 ± 10 °C and $T_{decomp}^{TTBGa+TBAs}$ = 150 ± 10 °C and show no deviation from the unimolecular decomposition, within the error of the measurement. The corresponding data is added into S6 for completeness. The larger deviation of the TBAs decomposition temperature from the TEGa decomposition temperature is referred to small deviations of the V/III ratio. Changes of the V/III ratio show a significant influence on the TBAs decomposition temperature, which will be discussed in section 3.4.

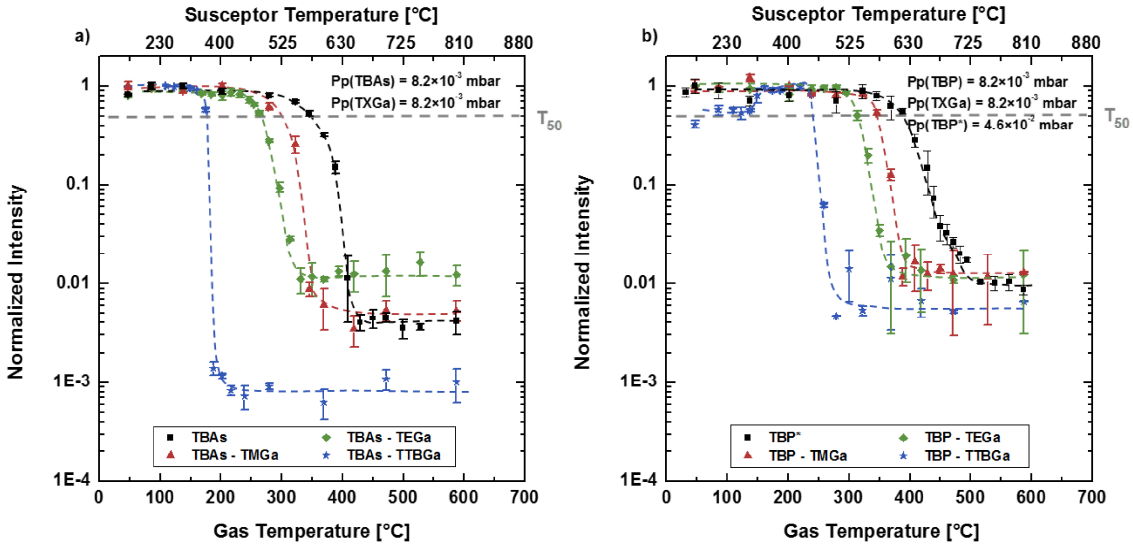

Figure 2: a) Temperature dependent decomposition curves of TBAs (134 u) during growth of GaAs by addition of the three different Ga sources TMGa, TEGa and TTBGa. The partial pressures are chosen with Pp(TBAs) = 8.2 × 10^{-3} mbar and Pp(TXGa) = 8.2 × 10^{-3} mbar. b) Analogous measurement for TBP (90 u) during growth of GaP by addition of the three different Ga sources TMGa, TEGa and TTBGa. The partial pressures are chosen with Pp(TBP) = 8.2 × 10^{-3} mbar and Pp(TXGa) = 8.2 × 10^{-3} mbar during growth and with Pp(TBP*) = 4.6 × 10^{-2} mbar for TBP alone. As before, the temperature at which the intensity drops to half of its intensity is marked by the grey dashed line and is defined as the decomposition temperature of the precursor.

These findings conflict in part to the literature data. In the case of TBAs and TMGa a strong reduction of the TMGa decomposition temperature by addition of TBAs is seen [20,29]. This effect cannot be seen in our data. This is mainly because the unimolecular decomposition of TBAs has been observed about 100 °C

lower compared to the TMGa decomposition temperature in their setup, which underlines that the different experimental conditions within the reactor can have a strong impact on the decomposition.
Additionally, no effect of TEGa on the TBAs decomposition temperature has been seen in the study presented in ref. [29]. Under their experimental conditions, both precursors decompose at the same temperature, which is also measured for unimolecular decomposition of the precursors. However, an effective lowering of the decomposition temperature by about 50 °C of trimethylarsane (TMAs) is seen in the presence of TEGa in the same setup, which was attributed to a possible adduct formation [29]. This is an example that the decomposition of a group V precursor is enhanced by addition of a group III precursor. A similar behavior has been seen for the bimolecular decomposition of TMGa and arsine (AsH_3) in different experimental setups [30–34]. The lowered decomposition temperature of AsH_3 is explained by a radical attack of methyl radicals from the TMGa decomposition. Furthermore, the formation of a surface adduct is used to explain the data. No decomposition data is presented for the growth with TTBGa with any other As compound in the literature.
Similar to the findings in the literature a adduct formation might explain the reduced decomposition temperature of TBAs. However, a formed adduct is expected to be detectable in our setup, which is supported by the observation of adducts between the nitrogen precursor unsymmetrical dimethylhydrazine and TMGa or TEGa in our setup. Furthermore, reactions including the attack of radicals created in the decomposition of the Ga precursors could also explain the reduced TBAs decomposition temperatures. However, due to the low partial pressures used in our setup the radical attack is improbable.
Therefore, the reduction of the TBAs decomposition temperature is more likely caused by a catalytic effect of the decomposed Ga precursors on the surfaces within the reactor. Since the Ga precursor decompose at lower temperature than the TBAs, they can provide Ga as well as radical species of the alkyl groups at the surface. This would be in accordance with the agreement in decomposition temperature of the Ga precursors. Furthermore, a very similar effect is seen for the bimolecular decomposition of TBP shown in figure 2 b). The decomposition temperatures are determined with $T_{decomp}^{TBP+TMGa}$ = 350 ± 10 °C, $T_{decomp}^{TBP+TEGa}$ = 315 ± 10 °C and $T_{decomp}^{TBP+TTBGa}$ = 250 ± 10 °C compared to the unimolecular decomposition temperature of TBP (T_{decomp}^{TBP} = 400 ± 10 °C) in this case.
The decomposition temperature of TBP lowers significantly by the addition of the Ga precursors in our study. The deviation in the decomposition temperatures correlates to some degree to the difference between the decomposition temperatures of the unimolecular decomposition of TBP and TBAs of 40 to 50 °C shown in figure 1 a). This suggests a higher stability of TBP compared to TBAs, which can be related to a higher bond strength of the C-P instead of the C-As bond [35]. Apparently, the absolute reduction in the case of TBP is comparable to the findings of TBAs, however the decomposition temperature is not reduced completely to the decomposition temperature of the respective Ga source. These findings cannot only be explained by a higher stability of TBP together with a simple catalytic effect of the Ga deposited on the reactor surfaces. If only the elemental Ga is involved, the TBP decomposition temperature should fit to that of the Ga precursor, at least at higher temperatures. This suggests that the Ga alkyl groups need to be involved in the decomposition reaction. Similarly, in the case of the bimolecular decomposition of TBP and TMGa formation of CH_4 and methlyphosphane (48 u) was detected in the literature, which is believed to occur by alkyl exchange on the surface [9]. The idea of an exchange of the alkyl groups of the Ga sources with the *tert*-butyl groups of TBP and TBAs on the surface could explain the change in the decomposition temperature. These reactions have to be dependent on the bond strength within both molecules, and therefore can account for the higher decomposition temperatures for TBP compared to the values determined in the case of TBAs. Due to the higher bond strength the alkyl exchange should occur at higher temperatures for TBP compared to TBAs, as supported by our data. The possibility for this alkyl exchange on the surface should be given, since many studies report a site blocking effect by alkyl groups sticking to the adsorbed Ga precursor at low temperatures [25,36,37].
Some more evidence for these reactions will be discussed in the next part of this paper.

3.3. Reaction products of the bimolecular decomposition of TBAs

In the next part, the decomposition products detected during the bimolecular decomposition of TBAs and the Ga precursors TMGa, TEGa and TTBGa will be discussed.
The temperature dependent evolution of the main fragments for the combination of TMGa and TBAs is shown in figure 3. For the bimolecular decomposition of TBAs and TMGa the decomposition products isobutane, *tert*-butyl radicals and isobutene as well as propyne arising from fragmentation of isobutane are detected. These fragments originate from the decomposition of the *tert*-butyl groups of TBAs, as discussed in section 3.1. Compared to the unimolecular decomposition of TBAs, the detected intensities of isobutane and of the *tert*-butyl radicals are increasing. This indicates that the homolytic fission of the *tert*-butyl group is enhanced. In contrast to the unimolecular decomposition of TBAs, no drop in the isobutane intensity for higher temperatures is seen, which shows that the homolytic fission dominates over the whole temperature range. In addition, a mass of 106 u is detected, whose intensity rises, as soon as the TBAs molecule starts to decompose. This fragment is identified with dimethylarsane (DMAs – 106 u). The occurrence of DMAs fits to the decomposition data in ref. [20,29]. In both studies the formation of an As compound with 1 or 2 attached methyl groups is reported. The formation of DMAs likely indicates that an alkyl exchange reaction occurs as reaction step in the catalyzed TBAs decomposition. The detected DMAs signal drops around a temperature of 360 °C. DMAs was found to be more stable compared to the TBAs and decomposes at 450 °C in an unimolecular decomposition [4]. The drop of the DMAs at 360 °C is expected, since the temperature fits to the unimolecular decomposition temperature of TBAs. Above this temperature the majority of the TBAs molecules are decomposed by unimolecular reactions before adsorbing on the surface. This severely reduces the possibility of an alkyl exchange, which could be the reason for the drop of the DMAs signal.
As further products mainly Ga (69/71 u) and a small increase of a mass around 84 u is seen. The produced Ga can either be attributed to Ga desorbing from the surface or it is the fragment of larger Ga containing fragments. These larger fragments are likely to be cracked in the ionization process. The detected fragment around 84 u is most likely methylgallium (MGa – 84 u). Further decomposition products and fragments are detected by utilizing the SWIFT method of the ion trap. The corresponding mass spectrum with and without SWIFT is shown S7. These further fragments are related to methylarsane (MAs – 92 u), ethylgallium (EGa – 98/100 u), isopropylgallium (112/114 u) and tertbutylgallium (TBGa – 126/128 u). All these fragments are probably related to the EI induced fragmentation of a larger Ga compound like TBGa, which is formed in the alkyl exchange reaction. However, the formation of a larger adduct cannot totally be excluded. Furthermore, one can think of a formation of the TBGa by reaction of formed *tert*-butyl radicals with Ga on the surface, followed by desorption.

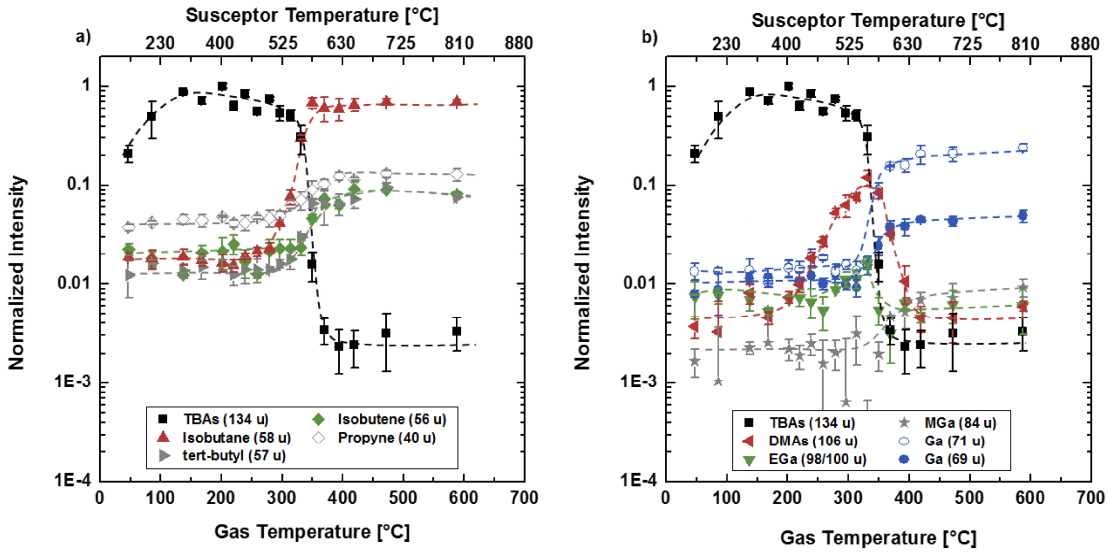

Figure 3: Decomposition curves of TBAs and TMGa druing growth of GaAs with partial pressures Pp(TBAs) = 8.2 × 10^{-3} mbar and Pp(TMGa) = 8.2 × 10^{-3} mbar. a) Decomposition products related to the decomposition of the *tert*-butyl group of TBAs. b) Further decomposition products related to a possible alkyl exchange reaction.

Similarly, the main fragments for the bimolecular decomposition of TEGa and TBAs are shown in figure 4. For the bimolecular decomposition of TBAs and TEGa the decomposition products isobutane, *tert*-butyl radicals and isobutene as well as propyne arising from fragmentation of isobutane are detected. The isobutane intensity is again detected with the highest intensity of the decomposition products and remains constant over the whole temperature range, like in the case of TMGa and TBAs. Furthermore, the isobutene signal, which is the result of the β-H elimination reaction, drops off and is detected with a lower intensity compared to the unimolecular decomposition of TBAs. This also indicates that the homolytic fission decomposition pathway is enhanced by surface catalytic reactions. As further fragments gallium (69/71 u), methylgallium (MGa – 84 u), a small amount of isopropylgallium (IPGa 112/114 u) and tertbutylgallium (TBGa 126/128 u), similar to the fragments seen for TMGa, are detected. These fragments show slightly higher intensities compared to the ones observed for TMGa. The produced Ga could be explained by desorption of Ga from the surface, but is more likely the fragment of a larger Ga containing compound. The MGa, IPGa and TBGa are possibly further fragments of the Ga containing compound. A view on further fragments is shown in the mass spectrum recorded with and without SWIFT in S8. The spectra show additional fragments, which are determined with galliumhydride (GaH – 72 u), methylarsane (MAs – 92 u), ethylgallium (EGa – 98/100 u) and ethylarsane (EAs – 106 u). Besides ethene, the GaH can be formed by H_2 abstraction from GaH_3, which is proposed to be formed by β-H elimination of the ethyl groups from TEGa [7,38]. The ethylarsane can be the result of an alkyl exchange reaction between the TEGa and the TBAs like mentioned for the formation of methylarsane in the case of TMGa. The methylarsane is probably created by fragmentation of ethylarsane during the ionization process. The methylgallium, ethylgallium and isopropylgallium signal is also attributed to the fragmentation of TBGa within the ion trap. The TBGa is formed within the alkyl exchange reaction between TEGa and TBAs, which additionally produces the ethylarsane.

These findings are in contrast to ref [29]. No influence between TBAs and TEGa is observed in the referred study.

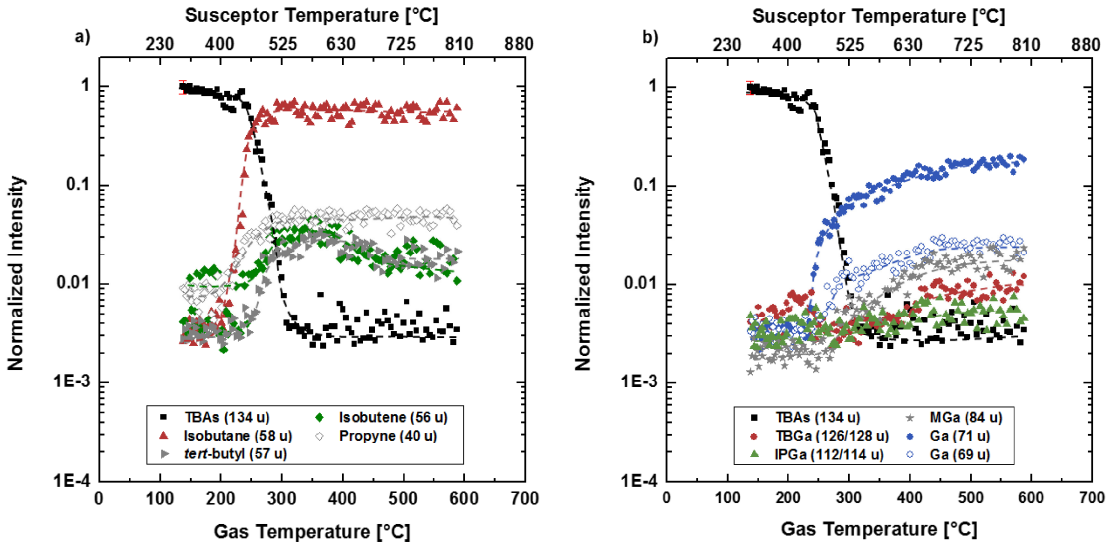

Figure 4: Decomposition curves of TBAs and TEGa druing growth of GaAs with partial pressures Pp(TBAs) = 8.2 × 10^{-3} mbar and Pp(TEGa) = 8.2 × 10^{-3} mbar. a) Decomposition products related to the decomposition of the *tert*-butyl group of TBAs. b) Further decomposition products related to possible alkyl exchange reaction.

The mentioned products are also seen in the bimolecular decomposition of TTBGa and TBAs shown in figure 5. For the bimolecular decomposition of TBAs and TTBGa mainly isobutane and propyne are detected as decomposition products. The measured propyne is arising from fragmentation of isobutane. The higher isobutane signal compared to the intensity in the unimolecular decomposition of TBAs can be attributed to the addition of TTBGa. The *tert*-butyl groups of TTBGa can decompose either radically or by β-H elimination leading to the detection of isobutane, *tert*-butyl radicals and isobutene, as seen in section 3.1. The lack of isobutene indicates an enhanced probability for the homolytic fission of the TBAs as well as for the TTBGa.

The additionally detected fragments are identified with Ga (69/71u), methylgallium (MGa – 84 u), ethylgallium (EGa – 98/100 u), isopropylgallium (IPGa - 112/114 u) and tertbutylgallium (TBGa – 126/128 u). The Ga signal can again either be attributed to Ga desorbing from the surface or to the fragmentation of a larger Ga containing compound. The formations of MGa, EGa, IPGa and TBGa are likely to be due to a cracking of a lager fragment like TBGa in the ionization process. The intensities of these fragments show higher values compared to the ones detected for TMGa and TEGa. Especially the intensity of TBGa is significantly enhanced. This is related to the *tert*-butyl groups, which are more likely to undergo alkyl exchange and adduct formations, which has been seen in experiments done in [39]. Another possibility is that the formed *tert*-butyl groups react with Ga on the surface to from the TBGa. Galliumhydride (GaH – 72 u), methylarsane (MAs – 92 u) ethylarsane (EAs – 106 u) are seen as further fragments in the sensitive SWIFT measurement in S9. The GaH can be produced by H_2 abstraction from GaH_3 formed in the β-H elimination of the *tert*-butyl groups from TTBGa. The MAs and EAs are believed to be fragments of TBAs.

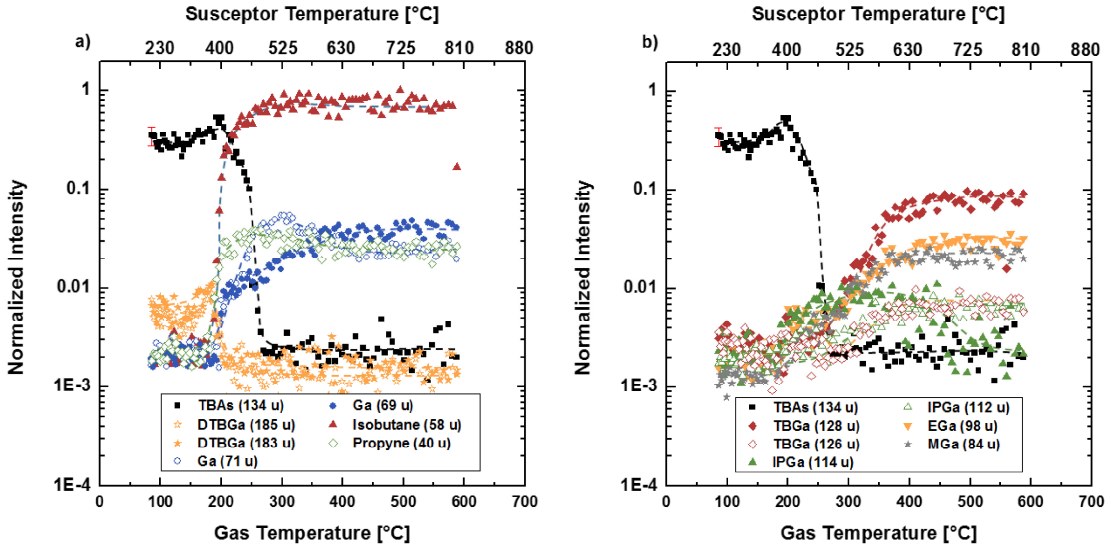

Figure 5: Decomposition curves of TBAs and TTBGa druing growth of GaAs with partial pressures Pp(TBAs) = 8.2 × 10^{-3} mbar and Pp(TTBGa) = 8.2 × 10^{-3} mbar. a) Decomposition products related to the decomposition of the *tert*-butyl group of TBAs. b) Further decomposition products related to possible alkyl exchange reaction. The Ga signal is added into a) to enhance the readability of b).

Conclusively, the bimolecular decomposition of TBAs and the Ga precursors indicates the possibility of an alkyl exchange reaction. This is mainly supported by the detection of a larger Ga fragment, which is likely to be TBGa. Further As compounds like MAs and EAs or DMAs can be a result of the same alkyl exchange reaction. The alkyl exchange might also explain the determined activation energies given in table 1. A simple catalytic effect of the Ga should result in a reduced activation energy. However, e.g. given for the TBP the activation energy increases with the addition of the Ga precursors, despite the observed reduction of the decomposition temperature. A more complex reaction, like an alkyl exchange, might be the underlying reason. Furthermore, No larger masses are detected, which could directly support an adduct formation. With the used settings of the mass spectrometer any formed adduct should be detectable, if it is formed in the gas phase. However, this does not exclude adduct formation on the surface.

3.4. Dependence of the bimolecular decomposition of TBAs and TEGa on the V/III ratio

As a next step, the influence of TEGa on the decomposition temperature of TBAs has been studied in dependence of the V/III ratio in the reactor. The corresponding decomposition curves of the bimolecular decomposition of TBAs and TEGa are shown in figure 6 a). With decreasing V/III ratio, a strong reduction of the decomposition temperature is seen in this case. The decomposition temperatures are determined with T_{decomp}^{TBAs} = 360 ± 10 °C, $T_{decomp}^{TBAs-coated}$ = 250 ± 10 °C, $T_{decomp}^{V/III=10}$ = 310 ± 10 °C, $T_{decomp}^{V/III=4}$ = 310 ± 10 °C, $T_{decomp}^{V/III=2}$ = 290 ± 10 °C, $T_{decomp}^{V/III=1}$ = 250 ± 10 °C, $T_{decomp}^{V/III=0.75}$ = 235 ± 10 °C, $T_{decomp}^{V/III=0.5}$ = 220 ± 10 °C. To determine the effect of the GaAs surface, which is created during the growth study on the reactor walls, the unimolecular decomposition of TBAs has been measured on the coated liner. A similar study reports that the change from the uncoated SiO_2 surface of 1200 cm² to the GaAs coated surface resulted in a decrease of the TBAs decomposition temperature by 70 °C [5]. In our setup with an effective surface area of 720 cm², an even larger effect is seen with a reduction of about 100 °C. This clearly underlines the catalytic effect of the GaAs surface on the TBAs decomposition, as described above.

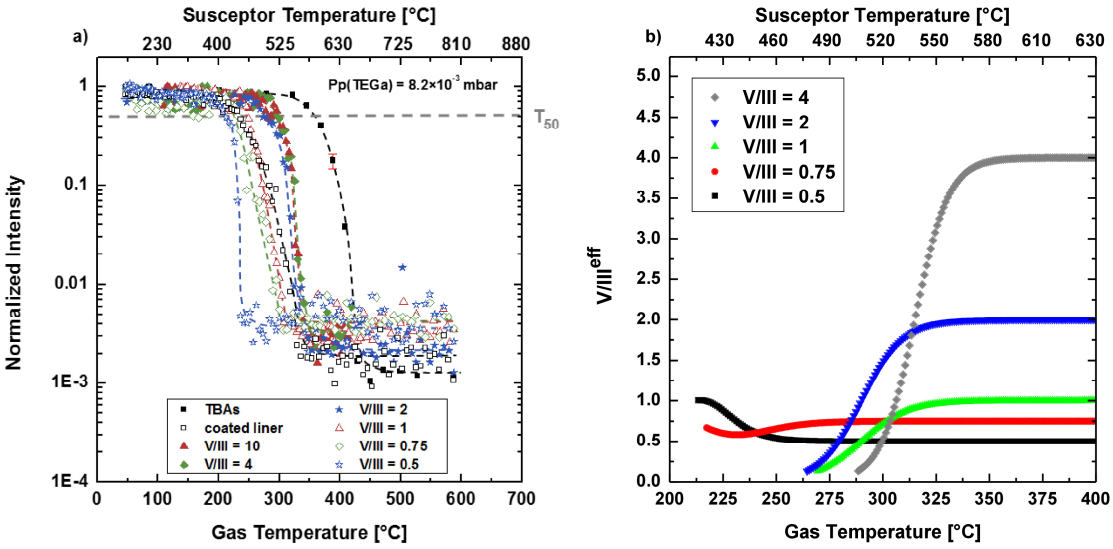

Figure 6: a) Temperature dependent decomposition curves of TBAs (134 u) during growth of GaAs with TEGa. For this experiment the TEGa partial pressure was fixed at Pp(TEGa) = 8.2 × 10^{-3} mbar and the TBAs partial pressure was varied systematically, which results in a change of the V/III ratio within the reactor chamber. For comparison, the decomposition curves of TBAs on the bare susceptor (black boxes) and a reference measured in the fully coated reactor (black open boxes) is added. To enhance the readability the error bars are only shown exemplary in red for the TBAs decomposition on the bare susceptor. As before, the temperature at which the intensity drops to half of its intensity is marked by the grey dashed line and is defined as the decomposition temperature of the precursor. b) Effective V/III^{eff} ratio within the reactor chamber calculated from the percentage decomposition of TBAs and TEGa. To stick to a reasonable y-scale, the curve for V/III = 10 is left out on purpose.

For the bimolecular decomposition, a dependence on the V/III ratio is seen. The V/III ratio was varied by keeping the TEGa partial pressure constant at 8.2 × 10^{-3} mbar and changing the TBAs partial pressure accordingly. This change in the decomposition temperature with increasing V/III ratio supports the idea of reactions occurring on the surface. Any simple stoichiometric reaction in the gas phase should not be affected by the additional TBAs that is supplied. In the stoichiometric case the TBAs is expected to only partly decompose earlier if the V/III ratio is larger than one. The excess TBAs present in the reactor most likely influences the catalytic reaction that is occurring. One effect of the increasing V/III ratio in the reactor is a change of the GaAs (001) surface reconstruction, which has been studied in the past [40,41]. With increasing V/III ratio, the surface reconstruction becomes more As rich. Therefore, it could reduce the possible reaction sites for TBAs on the surface and lead to a higher decomposition temperature of TBAs. Since the TBAs also decomposes at lower temperatures on the prepared GaAs surface, this cannot be the only reason. Another idea is an enhanced alkyl exchange on or near the surface. The excess TBAs in the presence of the TEGa should enhance the probability of these reactions. The TBAs and TEGa show that an alkyl exchange results in the formation of tertiarybutylgallium (TBGa - 126 u) and an As containing molecule like ethylarsane (EAs - 106 u) or diethylarsane (DEAs - 135 u). Furthermore, our data suggests that the formation of tertiarybutylgallium (126 u) is enhanced by increasing the V/III ratio in the reactor. The corresponding data is shown in S10. In the same exchange reaction also a higher amount of EAs or DEAs would be formed, which is probably sticking to the surface. Due to the higher stability, the EAs or DEAs might block the catalytic Ga sites on the surface [4]. With increasing the V/III ratio the probability that a TBAs molecule collides with a TEGa molecule at the surface is enhanced. This should enhance the probability of the alkyl exchange reactions and lead to a higher site blocking by the EAs or DEAs. This can effectively reduce the number of catalytic sites on the surface and therefore prevent the catalytic reactions of TBAs. This would explain the increase in the decomposition temperature as well of the activation energy by increasing the V/III ratio. Here a higher activation energy compared to the unimolecular decomposition of TBAs is seen for high V/III ratios and a lower activation energy for V/III ratios smaller than 1. The site

blocking also explains why the unimolecular decomposition of TBAs on the coated liner occurs at a lower temperature, than during growth of GaAs. In this case the alkyl groups of the Ga precursor should be desorbed and are no longer present at the surface. This would prohibit the alkyl exchange reaction and consequently no blocking of the catalytic TBAs decomposition occurs. The lower activation energy of 2 eV for the heterolytic decomposition compared to the 2.3 eV in the unimolecular case support a catalytic surface effect. At very low V/III ratios the number of adsorbed TEGa, DEGa, EGa or Ga increases, compared to the number of available TBAs molecules. This leads to an increase of the number of available catalytic reaction sites on the surface and explains why the TBAs molecule decomposes at even lower temperature. In this case, the intensity of TBGa drops below the detection limit, which is shown in S10.
These findings suggest that a precise adjustment of the V/III ratio is crucial to realize growth at low temperatures (T < 350 °C). From the presented decomposition data in figure 6 a) an effective V/III ratio is calculated. For this the partial pressures of the TBAs and the TEGa are weighted with the percentage of the decomposition of the precursor at a given temperature. The ratio of these values is taken as the effective V/III ratio on the growth surface. The used decomposition curves of the Ga precursors measured in the same experiment is exemplarily shown in S11. The decomposition temperature of the TEGa remains constant at $T_{decomp}^{TEGa+TBAs}$ = 230 ± 10 °C. This shows that the TBAs is not influencing the TEGa decomposition temperature. The resulting effective V/III ratio is plotted against the gas phase temperature in figure 6 b). At a used gas phase ratio of 0.5 (black curve), the start of the decomposition temperature of TEGa and TBAs agrees. Due to the Ga induced surface catalytic decomposition of TBAs, this results in an effective V/III ratio of 1. The effective V/III ratio then drops. This decrease is caused by the relatively higher amount of decomposed TEGa, due to the higher supply of TEGa with 8.2 × 10^{-3} mbar compared to the TBAs supply of 4.1 × 10^{-3} mbar. Therefore, more decomposed Ga is available at the surface. The drop continuous until a temperature of 260 °C, at which the value of the gas phase ratio is reached. At this point both precursors are fully decomposed. For a gas phase ratio of 0.75 a similar effect is seen (red curve). Since the TEGa starts to decompose earlier than the TBAs in this case, the effective V/III ratio starts at a value of V/III^{eff} = 0.75. The value then drops towards 0.5 and then rises again to the value of the gas phase ratio of 0.75 by further increasing the temperature. This is caused by the ealier decomposition of the TEGa compared to the decomposition compared to the TEGa decomposition. For all higher gas phase ratios, the TEGa is already fully decomposed, when the TBAs decomposition sets in. This results in a steady increase of the effective V/III ratio towards the gas phase ratio. The effective V/III ratio adapts to the chosen gas phase ratio above 350 °C in all cases. These findings suggest, that for growth at very low temperatures an effective V/III ratio of 1 can be reached, which could be used to realize low temperature growth. However, the results suggest, that many different reactions are occurring at this low temperatures, including site blocking at the surface or adduct formation, which hinders the growth. These most likely results in a strong reduction of the growth rate, as seen in [39]. Since also fragmentary products are detected at low temperatures, these can lead to unwanted incorporation of e.g. C from the alkyl groups of the precursors. Since our results suggest site blocking of the formed EAs or DEAs, this could furthermore lead to formation of As antisites as discussed in ref. [42].

4. Summary and Outlook

The influence of the Ga precursors trimethylgallium (TMGa), triethylgallium (TEGa), and tritertiarybutylgallium (TTBGa) on the decomposition of tertiarybutylarsane (TBAs) and tertiarybutylphosphane (TBP) has been studied in an AIXTRON AIX 200 GFR metal organic vapor phase epitaxy (MOVPE) system. In the first part the unimolecular decomposition of all mentioned precursors are studied on the bare graphite susceptor of the system. The products of the decomposition reactions are in good agreement to data published in the literature. However, some deviations occur due to the differences of the experimental setup compared to these studies. Especially the decomposition temperatures deviate to the determined temperatures published. The decomposition temperatures of the unimolecular

decomposition are determined with T_{decomp}^{TMGa} = 340 ± 10 °C, T_{decomp}^{TEGa} = 250 ± 10 °C, T_{decomp}^{TTBGa} = 140 ± 10 °C, T_{decomp}^{TBP} = 400 ± 10 °C and T_{decomp}^{TBAs} = 360 ± 10 °C. Our study allows a direct comparison between all mentioned precursors, since these are all investigated in the same reactor system. Following the bimolecular decomposition of TBAs and TBP with all used Ga precursors is measured. For the used ratio of V/III = 1 the decomposition temperatures are severely reduced towards the unimolecular decomposition temperature of the Ga precursors. For TBAs the decomposition temperature are determined with $T_{decomp}^{TBAs+TMGa}$ = 310 ± 10 °C, $T_{decomp}^{TBAs+TEGa}$ = 260 ± 10 °C and $T_{decomp}^{TBAs+TTBGa}$ = 170 ± 10 °C. The reduction of the decomposition temperature is explained with a catalytic effect of the Ga on the deposited GaAs surface on the reactor components. Gas phase reactions are believed to play a minor role due to the low reactor pressure of 50 mbar and the low partial pressures in the 10^{-2} to 10^{-3} mbar range. The TBP decomposition temperature reduces to $T_{decomp}^{TBP+TMGa}$ = 350 ± 10 °C, $T_{decomp}^{TBP+TEGa}$ = 315 ± 10 °C and $T_{decomp}^{TBP+TTBGa}$ = 250 ± 10 °C. Since the TBP decomposition is not reduced to a temperature as low as the ones of the Ga precursors, the effect is believed to be not a simple catalytic effect. The additional decomposition products detected in the bimolecular reactions of TBAs and the Ga precursors suggest alkyl exchange reactions or are possibly related to adduct formation occurring on the surface. Both depend on the bond strength of the group V precursor as well as on the bond strengths in the Ga precursors, which could explain the higher decomposition temperatures for the bimolecular decomposition of TBP with the Ga precursors compared to the findings for TBAs.

For the bimolecular decomposition of TBAs and TEGa the dependence of the decomposition temperature on the V/III ratio is additionally investigated. The decomposition temperatures are determined with T_{decomp}^{TBAs} = 360 ± 10 °C, $T_{decomp}^{TBAs-coated}$ = 250 ± 10 °C, $T_{decomp}^{V/III=10}$ = 310 ± 10 °C, $T_{decomp}^{V/III=4}$ = 310 ± 10 °C, $T_{decomp}^{V/III=2}$ = 290 ± 10 °C, $T_{decomp}^{V/III=1}$ = 250 ± 10 °C, $T_{decomp}^{V/III=0.75}$ = 235 ± 10 °C and $T_{decomp}^{V/III=0.5}$ = 220 ± 10 °C. The increase of the decomposition temperature with higher V/III ratio is referred to an enhanced probability of the alkyl exchange or adduct formation. The resulting As compounds could lead to site blocking of the catalytic reactions sites on the surface and therefore prevent the catalytic decomposition. The lowered decomposition temperature of TBAs on the coated reactor supports the catalytic effect of the surface and shows that the additional supply of Ga precursor changes the surface properties. The decomposition data from these experiments is used to calculate an effective V/III ratios for growth temperatures below 350 °C.

Acknowledgements

This work was supported by the German Research Foundation (GRK 1782: “Functionalization of Semiconductors”) and the support for the mass spectrometer (iTrap) was provided by the Carl Zeiss SMT GmbH.

Declarations of Interest: none

Graphical Abstract:

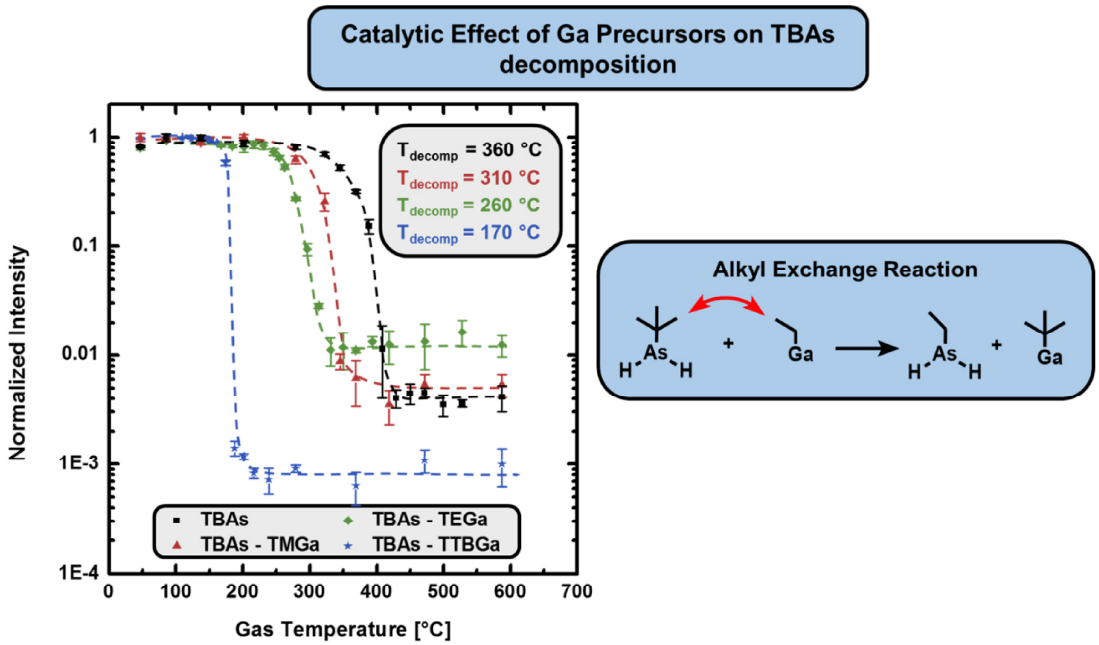

References

[1] G.B. Stringfellow, Development and current status of organometallic vapor phase epitaxy, J. Cryst. Growth. 264 (2004) 620–630. doi:10.1016/j.jcrysgro.2003.12.037.

[2] A. Brauers, Alternative precursors for III–V MOVPE — Promises and problems, Prog. Cryst. Growth Charact. Mater. 22 (1991) 1–18. doi:10.1016/0960-8974(91)90023-6.

[3] G.B. Stringfellow, Non-hydride group V sources for OMVPE, J. Electron. Mater. 17 (1988) 327–335. doi:10.1007/BF02652114.

[4] G.B. Stringfellow, Novel precursors for organometallic vapor phase epitaxy, J. Cryst. Growth. 128 (1993) 503–510. doi:10.1016/0022-0248(93)90376-8.

[5] C.A. Larsen, N.I. Buchan, S.H. Li, G.B. Stringfellow, Decomposition mechanisms of tertiarybutylarsine, J. Cryst. Growth. 94 (1989) 663–672. doi:10.1016/0022-0248(89)90090-0.

[6] S.H. Li, C.A. Larsen, N.I. Buchan, G.B. Stringfellow, Pyrolysis of tertiarybutylphosphine, J. Electron. Mater. 18 (1989) 457–464. doi:10.1007/BF02657995.

[7] M. Yoshida, H. Watanabe, F. Uesugi, Mass spectrometric study of Ga(CH3)3 and Ga(C2H5)3 decomposition reaction in H2 and N2, J. Electrochem. Soc. 132 (1985) 677–679. doi:10.1149/1.2113929.

[8] N.I. Buchan, C.A. Larsen, G.B. Stringfellow, Mass spectrometric studies of trimethylindium pyrolysis, J. Cryst. Growth. 92 (1988) 591–604. doi:10.1016/0022-0248(88)90044-9.

[9] S.H. Li, N.I. Buchan, C.A. Larsen, G.B. Stringfellow, OMVPE growth mechanism for GaP using tertiarybutylphosphine and trimethylgallium, J. Cryst. Growth. 96 (1989) 906–914. doi:10.1016/0022-0248(89)90651-9.

[10] N.I. Buchan, C.A. Larsen, G.B. Stringfellow, Elucidation of the organometallic vapor phase epitaxial growth mechanism for InP, Appl. Phys. Lett. 51 (1987) 1024–1026. doi:10.1063/1.99005.

[11] M. Mashita, S. Horiguchi, M. Shimazu, K. Kamon, M. Mihara, M. Ishii, The pyrolysis temperature of triethylgallium in the presence of arsine of trimethylaluminum, J. Cryst. Growth. 77 (1986) 194–199. doi:10.1016/0022-0248(86)90301-5.

[12] N. BAHLAWANE, F. REILMANN, L. SALAMEH, K. KOHSEHOINGHAUS, Mass-Spectrometric Monitoring of the Thermally Induced Decomposition of Trimethylgallium, Tris(tert-Butyl)Gallium, and Triethylantimony at Low Pressure Conditions, J. Am. Soc. Mass Spectrom. 19 (2008) 947–954. doi:10.1016/j.jasms.2008.04.015.

[13] D.F. Foster, C. Glidewell, D.J. Cole-Hamilton, Probing the mechanisms of growth of gallium arsenide by metalorganic vapor phase epitaxy using experimental and theoretical studies of designed precursors, J. Electron. Mater. 23 (1994) 69–74. doi:10.1007/BF02655248.

[14] R.T. Lee, G.B. Stringfellow, Pyrolysis of 1,1 dimethylhydrazine for OMVPE growth, J. Electron. Mater. 28 (1999) 963–969. doi:10.1007/s11664-999-0205-9.

[15] P.W. Lee, T.R. Omstead, D.R. McKenna, K.F. Jensen, In situ mass spectroscopy and thermogravimetric studies of GaAs MOCVD gas phase and surface reactions, J. Cryst. Growth. 85 (1987) 165–174. doi:10.1016/0022-0248(87)90218-1.

[16] C.A. Larsen, G.B. Stringfellow, Decomposition kinetics of OMVPE precursors, J. Cryst. Growth. 75 (1986) 247–254. doi:10.1016/0022-0248(86)90034-5.

[17] D.K. Russell, G.P. Mills, J.B. Raynor, A.D. Workman, Radical Processes in the Pyrolysis of Trialkyl Compounds of Group 13 CVD Precursors, Chem. Vap. Depos. 04 (1998) 61–67. doi:10.1002/(SICI)1521-3862(199803)04:02<61::AID-CVDE61>3.0.CO;2-R.

[18] C.A. Larsen, N.I. Buchan, S.H. Li, G.B. Stringfellow, Decomposition mechanisms of trimethylgallium, J. Cryst. Growth. 102 (1990) 103–116. doi:10.1016/0022-0248(90)90891-N.

[19] C.H. Chen, C.A. Larsen, G.B. Stringfellow, D.W. Brown, A.J. Robertson, MOVPE growth of InP using isobutylphosphine and tert-butylphosphine, J. Cryst. Growth. 77 (1986) 11–18. doi:10.1016/0022-0248(86)90274-5.

[20] C.A. Larsen, S.H. Li, N.I. Buchan, G.B. Stringfellow, Mechanisms of GaAs growth using tertiarybutylarsine and trimethylgallium, J. Cryst. Growth. 94 (1989) 673–682. doi:10.1016/0022-0248(89)90091-2.

[21] L. Nattermann, O. Maßmeyer, E. Sterzer, V. Derpmann, H.Y. Chung, W. Stolz, K. Volz, An experimental approach for real time mass spectrometric CVD gas phase investigations, Sci. Rep. 8 (2018) 319. doi:10.1038/s41598-017-18662-7.

[22] H.Y. Chung, M. Aliman, G. Fedosenko, A. Laue, R. Reuter, V. Derpmann, L. Gorkhover, M. Antoni, Very sensitive real-time inline process mass spectrometer based on FFT Ion Trap technique, in: 2016 27th Annu. SEMI Adv. Semicond. Manuf. Conf., IEEE, 2016: pp. 263–266. doi:10.1109/ASMC.2016.7491140.

[23] S. Guan, A.G. Marshall, Stored waveform inverse Fourier transform (SWIFT) ion excitation in trapped-ion mass spectometry: Theory and applications, Int. J. Mass Spectrom. Ion Process. 157–158 (1996) 5–37. doi:10.1016/S0168-1176(96)04461-8.

[24] O. Maßmeyer, S. Inacker, T. Hepp, J. Glowatzki, L. Nattermann, E. Sterzer, C. Ritter, C. Von Hänisch, W. Stolz, K. Volz, Decomposition Mechanisms of Di-tert-butylaminoarsane (DTBAA), Organometallics. 38 (2019) 3181–3186. doi:10.1021/acs.organomet.9b00442.

[25] G.B. Stringfellow, Organometallic vapour phase epitaxy: Theory and practice, 2nd ed., Academic Press, 1999.

[26] A.S. Grady, R.E. Linney, R.D. Markwell, G.P. Mills, D.K. Russell, P.J. Williams, A.C. Jones, Laser-powered homogeneous pyrolysis of triisobutylgallane and tri-tert-butylgallane, J. Mater. Chem. 2 (1992) 539. doi:10.1039/jm9920200539.

[27] A. Stegmüller, R. Tonner, β-Hydrogen Elimination Mechanism in the Absence of Low-Lying Acceptor Orbitals in EH 2 (t -C 4 H 9) (E = N–Bi), Inorg. Chem. 54 (2015) 6363–6372. doi:10.1021/acs.inorgchem.5b00687.

[28] I. V Alabugin, K.M. Gilmore, P.W. Peterson, Hyperconjugation, WIREs Comput. Mol. Sci. 1 (2011) 109–141. doi:10.1002/wcms.6.

[29] P.W. Lee, T.R. Omstead, D.R. McKenna, K.F. Jensen, In situ mass spectroscopy studies of the decomposition of organometallic arsenic compounds in the presence of Ga(CH3)3 and Ga(C2H5)3, J. Cryst. Growth. 93 (1988) 134–142. doi:10.1016/0022-0248(88)90518-0.

[30] D. J. Schlyer, M.A. Ring, An examination of the product-catalyzed reaction of trimethylgallium with arsine, J. Organomet. Chem. 114 (1976) 9–19. doi:10.1016/S0022-328X(00)87346-5.

[31] S.P. DenBaars, B.Y. Maa, P.D. Dapkus, A.D. Danner, H.C. Lee, Homogeneous and heterogeneous thermal decomposition rates of trimethylgallium and arsine and their relevance to the growth of GaAs by MOCVD, J. Cryst. Growth. 77 (1986) 188–193. doi:10.1016/0022-0248(86)90300-3.

[32] C.A. Larsen, S.H. Li, N.I. Buchan, G.B. Stringfellow, D.W. Brown, Kinetics of the reaction between trimethylgallium and arsine, J. Cryst. Growth. 102 (1990) 126–136. doi:10.1016/0022-0248(90)90893-P.

[33] J.E. Butler, N. Bottka, R.S. Sillmon, D.K. Gaskill, In situ, real-time diagnostics of OMVPE using IR-diode laser spectroscopy, J. Cryst. Growth. 77 (1986) 163–171. doi:10.1016/0022-0248(86)90297-6.

[34] J. Nishizawa, T. Kurabayashi, Mechanism of gallium arsenide MOCVD, Vacuum. 41 (1990) 958–962. doi:10.1016/0042-207X(90)93833-5.

[35] H.A. Skinner, The Strengths of Metal-to-Carbon Bonds, in: F.G.A. Stone, R. West (Eds.), Adv. Organomet. Chem. Acad. Press, Academic Press, 1965: pp. 49–114. doi:10.1016/S0065-3055(08)60077-5.

[36] C.L. French, J.S. Foord, Reaction kinetics for the CBE growth of GaAs from triethylgallium; computer modelling studies incorporating recent surface spectroscopic data, J. Cryst. Growth. 120 (1992) 63–70. doi:10.1016/0022-0248(92)90365-P.

[37] A.J. Murrell, A.T.S. Wee, D.H. Fairbrother, N.K. Singh, J.S. Foord, G.J. Davies, D.A. Andrews, Surface chemical processes in metal organic molecularbeam epitaxy; Ga deposition from triethylgallium on GaAs(100), J. Appl. Phys. 68 (1990) 4053–4063. doi:10.1063/1.346242.

[38] A. Stegmüller, P. Rosenow, R. Tonner, A quantum chemical study on gas phase decomposition pathways of triethylgallane (TEG, Ga(C2H5)3) and tert-butylphosphine (TBP, PH2(t-C4H9)) under MOVPE conditions, Phys. Chem. Chem. Phys. 16 (2014) 17018–17029. doi:10.1039/c4cp01584c.

[39] T.R. Omstead, P.M. Van Sickle, P.W. Lee, K.F. Jensen, Gas phase and surface reactions in the MOCVD of GaAs from triethylgallium, trimethylgallium, and tertiarybutylarsine, J. Cryst. Growth. 93 (1988) 20–28. doi:10.1016/0022-0248(88)90500-3.

[40] A. Ohtake, Surface reconstructions on GaAs(001), Surf. Sci. Rep. 63 (2008) 295–327. doi:10.1016/j.surfrep.2008.03.001.

[41] W. Richter, In-situ observation of MOVPE epitaxial growth, Appl. Phys. A Mater. Sci. Process. 75 (2002) 129–140. doi:10.1007/s003390101061.

[42] R.M. Feenstra, J.M. Woodall, G.D. Pettit, Observation of bulk defects by scanning

tunneling microscopy and spectroscopy: Arsenic antisite defects in GaAs, Phys. Rev. Lett. 71 (1993) 1176–1179. doi:10.1103/PhysRevLett.71.1176.

[43] C.A. Larsen, N.I. Buchan, G.B. Stringfellow, Reaction mechanisms in the organometallic vapor phase epitaxial growth of GaAs, Appl. Phys. Lett. 52 (1988) 480–482. doi:10.1063/1.99450.

[44] M.G. Jacko, S.J.W. Price, THE PYROLYSIS OF TRIMETHYL GALLIUM, Can. J. Chem. 41 (1963) 1560–1567. doi:10.1139/v63-213.

[45] M.C. Paputa, S.J.W. Price, Pyrolysis of triethylgallium by the toluene carrier technique, Can. J. Chem. 57 (1979) 3178–3181. doi:10.1139/v79-520.

Supporting Information

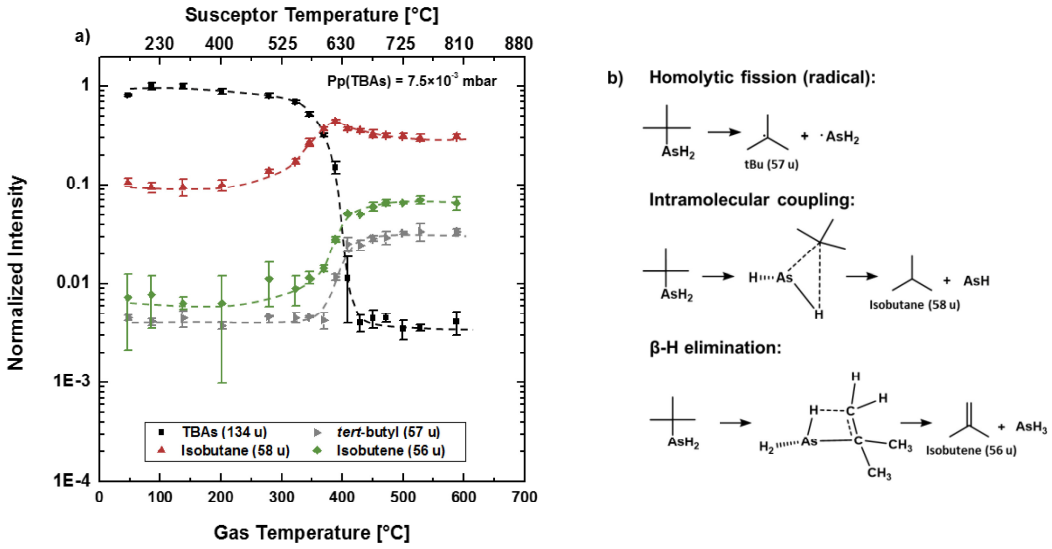

Figure S1: a) Decomposition curve showing the unimolecular decomposition of TBAs (134 u) measured on the bare graphite susceptor. A partial pressure of Pp(TBAs) = 7.5 × 10^{-3} mbar was used. The main decomposition products Isobutane (58 u), *tert*-butyl radicals (57 u) and Isobutene (56 u) are shown. Formation of isobutane (58 u) and *tert*-butyl radicals (57 u) indicates homolytic fission or intramolecular coupling reactions. Isobutene (56 u) is the product of a β-H elimination of the *tert*-butyl group of TBAs. b) Illustrated decomposition reactions. Importantly a common consideration after ref. [13] is abstraction of H or H_2 from the TBAs molecule as a first step in the reaction chain. This would result in formation of AsH or AsH_2 instead of AsH_3 in the β-H elimination reaction. The AsH or AsH_2 are likely to lead to As incorporation unlike the stable AsH_3. AsH_3 decomposes at comparably high temperatures (T_{decomp}~600 °C) compared to TBAs (T_{decomp} = 350 °C) [25,43].

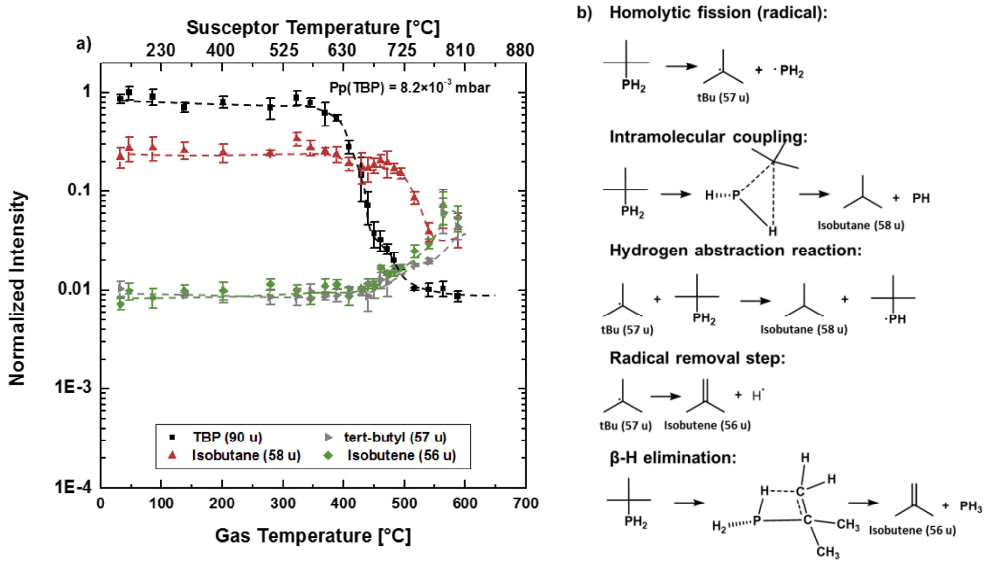

Figure S2: a) Unimolecular decomposition of TBP (90 u). A partial pressure of Pp(TBP) = 8.2 × 10^{-3} mbar was used. The main decomposition products isobutane (58 u), *tert*-butyl radicals (57 u) and isobutene (56 u) are shown. b) Possible reaction pathways for TBP. Homolytic fission and intermolecular coupling reactions, which results in the formation of isobutane and *tert*-butyl radicals seems to be the dominant reaction at temperatures between 350 to 550 °C. The *tert*-butyl can react with H_2 to form isobutane. Isobutane can also be formed in a hydrogen abstraction

reaction. However, this reaction is more unlikely in our setup due to the lower reactor and partial pressure used compared to ref. [6]. Isobutene can be the result of β-H elimination reaction or of a radical removal step involving the formed *tert*-butyl radicals. The later was correlated to an increase of the H_2 in the used D_2 ambient in ref. [6]. However, this reaction seems more unlikely compared to the β-H elimination reaction due to the stability of the *tert*-butyl radicals. The formation of isobutene becomes the domination reaction product above a temperature of 550 °C.

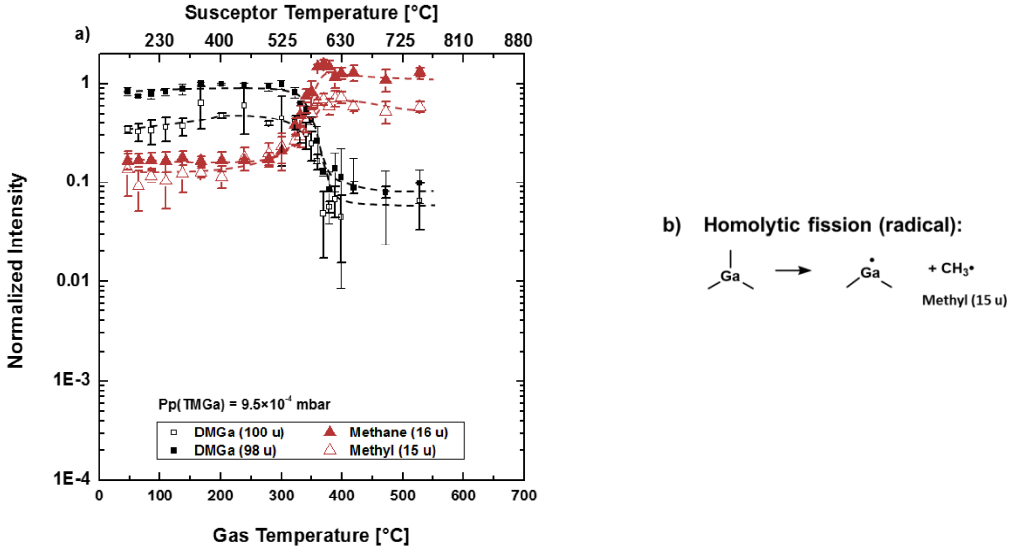

Figure S3: a) Unimolecular decomposition of TMGa (114/116 u). Due to the ionization DMGa (98/100 u) as the largest fragment is used to track the decomposition of TEGa. A partial pressure of Pp(TMGa) = 9.5 × 10^{-4} mbar was used. The main decomposition products are methyl radicals (15 u) and Methane (16 u). The methyl radicals are formed by homolytic fission of the C-Ga bonds. The resulting methyl radicals can react with the H_2 carrier gas to form methane (16 u). b) Schematic of the first step in the decomposition reaction of TMGa. The dimethylgallium fragment also decomposes by subsequent loss of the attached methyl groups. Furthermore, literature shows further reaction pathway like the possibility for an attack of the methyl radicals on the parent molecule [7,18,25,44].

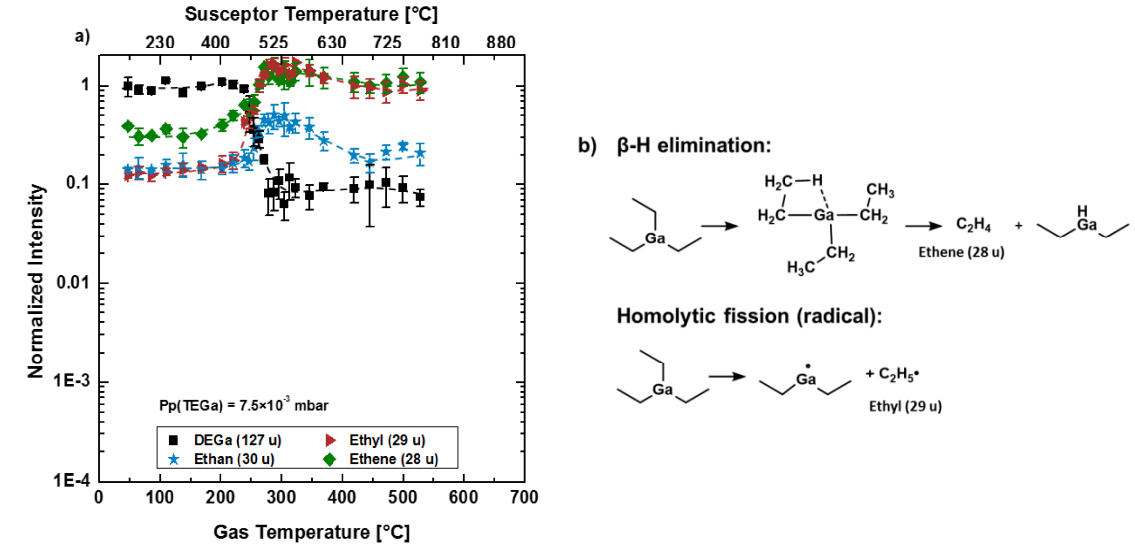

Figure S4: a) Unimolecular decomposition of TEGa (156/158 u). Due to the ionization DEGa (127/129 u) as the largest fragment is used to track the decomposition of TEGa. A partial pressure of Pp(TEGa) = 7.5 × 10^{-3} mbar was used. The decomposition products are mainly ethane (30 u), ethyl radicals (29 u) and ethene (28 u). Formation of

ethane and ethyl radicals indicate a homolytic fission of the ethyl groups attached to TEGa. The ethane is most likely formed by reaction of the ethyl radicals with the H_2 carrier gas. The ethene is produced by a β-H elimination reaction of the ethyl groups. Seemingly, the ethene formation is relevant over the whole temperature range showing the importance of the β-H elimination reaction in the TEGa decomposition. This has been studied in different experiments in the literature [7,15,25,45]. The homolytic fission reaction seems to be a relevant decomposition pathway, since the ethyl radical intensity follows the ethene signal, under the used experimental conditions. b) Schematic illustration of the decomposition reactions of TEGa.

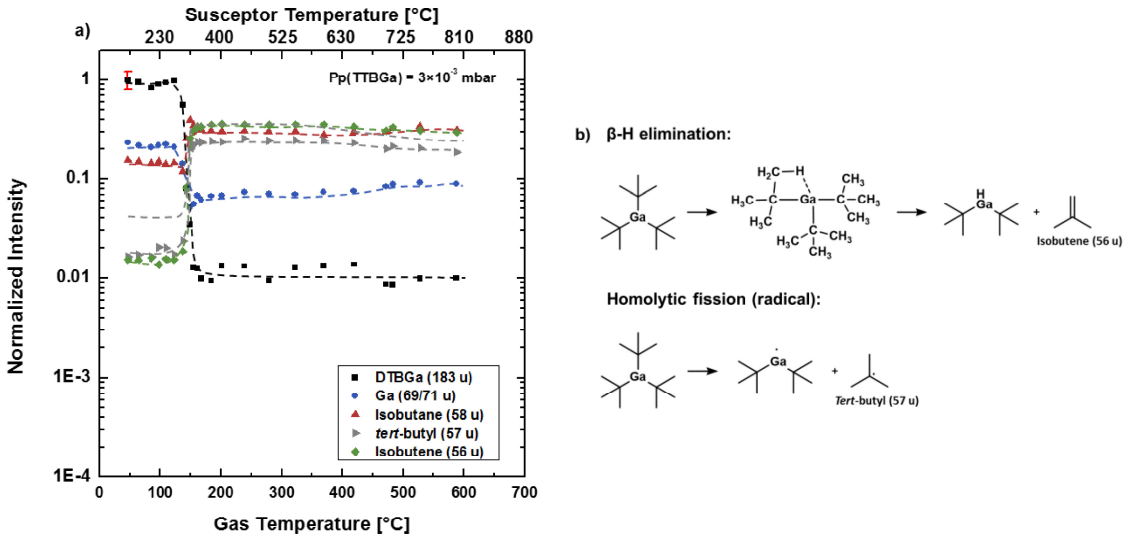

Figure S5: a) Unimolecular decomposition of TTBGa (240/242 u). Due to the ionization DTBGa (183/185 u) as the largest fragment is used to track the decomposition of TEGa. A partial pressure of Pp(TTBGa) = 3 × 10^{-3} mbar was used. The main fragments arising upon decomposition are isobutane (58 u), *tert*-butyl radicals (57 u) and isobutene (56 u). Formation of isobutane and *tert*-butyl radicals are produced by homolytic fission of the *tert*-butyl groups of the TTBGa molecule. The resulting *tert*-butyl radicals can reaction with the H_2 carrier gas to from isobutane. Isobutene is a product of β-H elimination reactions of the *tert*-butyl groups. The β-H elimination as decomposition pathway is also supported by data from the literature [12,26]. The error bars are intentionally left out to enhance the readability. The size of the error is shown exemplary in red. b) Schematic illustration of the decomposition reactions of TTBGa.

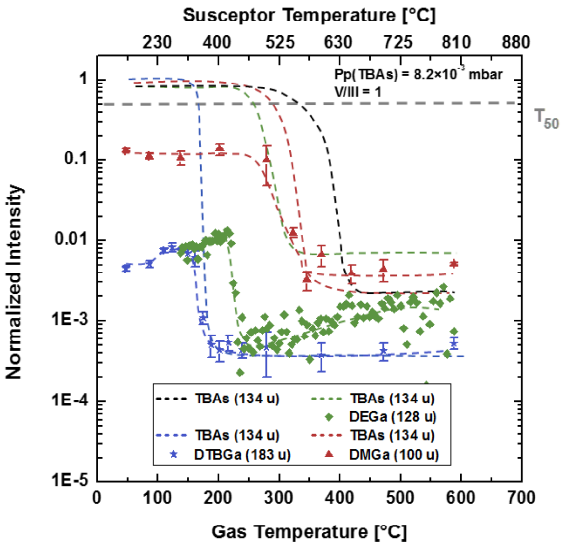

Figure S6: Decomposition curves of the Ga precursors TMGa, TEGa and TTBGa. The curves are measured during the bimolecular decomposition with TBAs. The corresponding TBAs decomposition curves from figure 2 are added and marked as dashed lines in the same color. The decomposition temperature fits well to the decomposition temperature of the TBAs. Only the determined decomposition temperature of TEGa shows a deviation of about 30 °C. This behavior is likely to be related to small deviations of the V/III ratio. The V/III is shown to have a large impact on the catalytic effect of the Ga precursor on the TBAs decomposition.

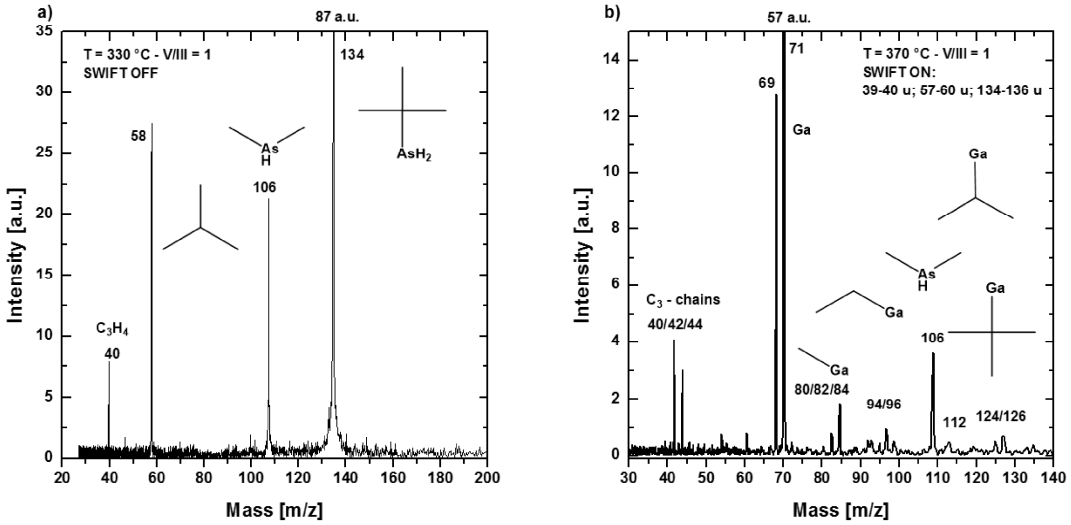

Figure S7: Mass spectra of the bimolecular decomposition of TMGa and TBAs. a) Mass spectrum detected at a temperature of 330 °C during the decomposition. The main additional feature is the formation of DMAs (106 u). The DMAs is believed to from by an alkyl exchange between the Ga and the As precursor. b) Mass spectrum utilizing the SWIFT method to remove the ions with high intensities out of the ion trap. Further decomposition products and ionization-induced fragments are seen. The fragments TBGa, IPGa, EGa, MGa indicate the formation of a larger Ga containing compound. This is likely to be TBGa formed in an alkyl exchange reaction. Furthermore, the fragments could also be due to an adduct formation on the surface. However, no larger fragments are observed.

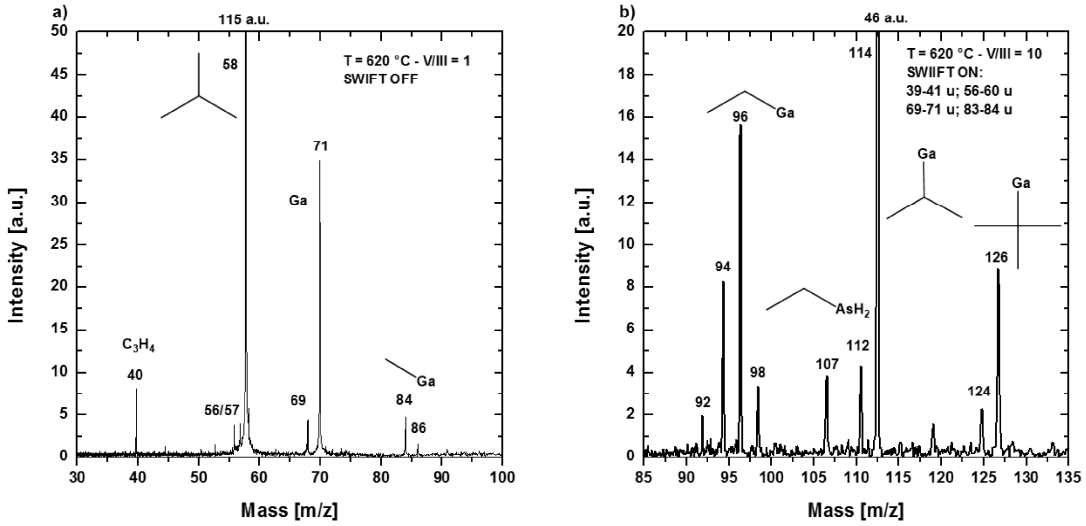

Figure S8: Mass spectra of the bimolecular decomposition of TEGa and TBAs. a) Mass spectrum detected at a temperature of 620 °C during the decomposition. The main additional feature is the formation MGa (84/86 u). The MGa is expected to form due to a fragmentation of a large Ga containing compound. b) Mass spectrum utilizing the SWIFT method to remove the ions with high intensities out of the ion trap. Further decomposition products and ionization-induced fragments are seen. The fragments TBGa, IPGa and EGa support the formation of a larger Ga

containing compound. This is likely to be TBGa formed in an alkyl exchange reaction between the Ga and the As precursor. Corresponding most likely EAs is detected, which is formed in the same alkyl exchange reaction. Furthermore, the fragments could also be due to an adduct formation on the surface. However, no larger fragments are observed.

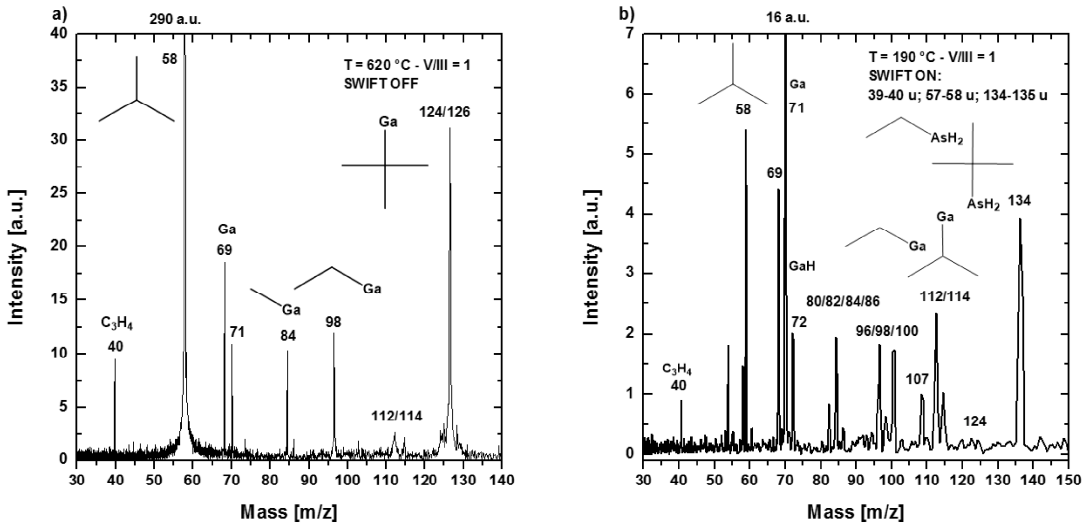

Figure S9: Mass spectra of the bimolecular decomposition of TTBGa and TBAs. a) Mass spectrum detected at a temperature of 620 °C during the decomposition. The main additional features are formation of TBGa, IPGa, EGa and MGa (84/86 u). These fragments are expected due to a fragmentation of a large Ga containing compound. b) Mass spectrum utilizing the SWIFT method to remove the ions with high intensities out of the ion trap. Further decomposition products and ionization-induced fragments are observed at 190 °C near the decomposition temperature of TTBGa. The low EAs intensity is likely to be due to fragmentation of TBAs. Alkyl exchange might occur, however both precursors contain the same alkyl group. The additional GaH is a result of β-H elimination or an additional fragment of the larger Ga containing compound.

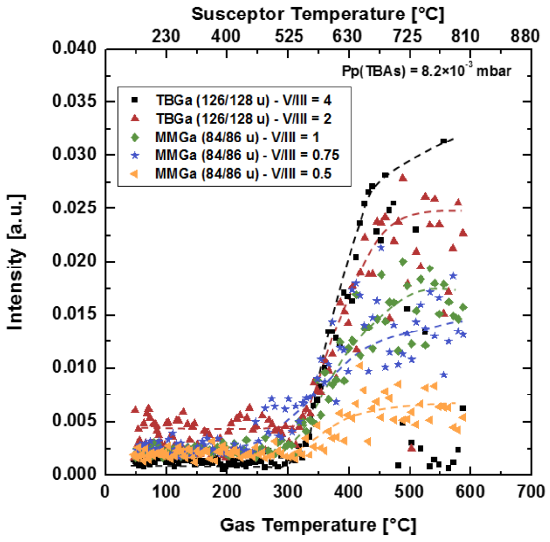

Figure S10: Evolution of the detected fragments related to the large Ga containing compound in the bimolecular decomposition of TBAs and TEGa. The formation seems to increase for higher V/III ratios. Especially TBGa is more

significantly detected at V/III ratios larger one. For V/III ratios smaller than 1 the main Ga containing fragment is MGa, which occurs with a lower intensity compared to the TBGa signal for higher V/III ratios.

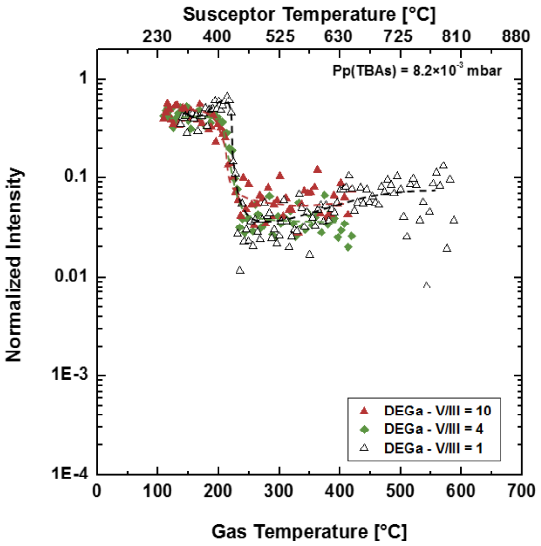

Figure S11: Exemplary decomposition curves of TEGa detected during the bimolecular decomposition of TBAs and TEGa for different V/III ratios. The TEGa decomposition temperature tracked by DEGa remains constant for a change of the V/III ratio.

7.3 Further Publications

Peer-Review Paper:

This subsection covers additional publications, which were issued during my PhD study. My contributions to these studies are assistance with the interpretation of the data and with the review of the written manuscript. It should be highlighted, that some of the PL measurements in publication 2 were executed by myself.

- L. Nattermann, O. Maßmeyer, E. Sterzer, V. Derpmann, H. Y. Chung, W. Stolz and K. Volz. An experimental approach for real time mass spectrometric CVD gas phase investigations. Scientific Reports volume 8, Article number: 319 (2018). https://doi.org/10.1038/s41598-017-18662-7

- E. Sterzer, O. Maßmeyer, L. Nattermann, K. Jandieri, S. Gupta, A. Beyer, B. Ringler, C. von Hänisch, W. Stolz, and K. Volz. 1 eV Ga(NAsSb) grown by MOVPE using di-tertiary-butyl-arsano-amine (DTBAA). AIP Advances 8, 055329 (2018). https://doi.org/10.1063/1.5034083

- T. Hepp, O. Maßmeyer, D. A. Duffy, S. J. Sweeney and K. Volz. Metalorganic vapor phase epitaxy growth and characterization of quaternary (Ga,In)(As,Bi) on GaAs substrates. Journal of Applied Physics 126, 085707 (2019). https://doi.org/10.1063/1.5097138

Conference Presentations:

- O. Maßmeyer, E. Sterzer, P. Ludewig, H. Döscher, L. Nattermann, W. Stolz and K. Volz.
  Influence of UDMHy on GaAs (001) Surface Reconstruction – RAS.
  DGKK Workshop on Epitaxy of III-V Compounds 2016. Duisburg, Germany

- O. Maßmeyer, E. Sterzer, L. Nattermann, P. Ludewig, W. Stolz and K. Volz.
  Influence of TMBi on the GaAs (001) Surface Reconstruction – RAS.
  8th International Workshop on Bismuth-Containing Semiconductors 2017. Marburg, Germany.

- O. Maßmeyer, L. Nattermann, E. Sterzer, C. von Hänisch, W. Stolz and K. Volz.
  Real time mass spectrometric MOVPE gas phase investigations.
  19th International Conference on Metal Organic Vapor Phase Epitaxy (ICMOVPE) 2018. Nara, Japan.

- O. Maßmeyer, J. Glowatzki, E. Odofin, M. Köster, C. von Hänisch, W. Stolz and K. Volz.
  Real Time Mass Spectrometric MOVPE Gas Phase Investigations of DTBPA.
  DGKK Workshop on Epitaxy of III-V Compounds 2018. Paderborn, Germany.

- O. Maßmeyer, J. Glowatzki, T. Hepp, C. von Hänisch, W. Stolz and K. Volz.
  Real time mass spectrometric gas phase investigations during MOVPE.
  18th European Workshop on Metal-Organic Vapour Phase Epitaxy (EW-MOVPE) 2019. Vilnius, Lithuania.

- O. Maßmeyer, J. Glowatzki, T. Hepp, W. Stolz and K. Volz.
  Decomposition Analysis of TBAs and TBP during GaAs and GaP Growth by MOVPE.
  DGKK Workshop on Epitaxy of III-V Compounds 2019. Dresden, Germany.

- O. Maßmeyer, J. Glowatzki, J. Haust, T. Hepp, W. Stolz and K. Volz. *Decomposition Analysis of TBAs and TBP during GaAs and GaP Growth by MOVPE.*
  Compound Semiconductor Week 2020. Stockholm, Sweden. Presentation cancelled due to Corona Pandemic.

- O. Maßmeyer, J. Haust, J. Glowatzki, T. Hepp, W. Stolz and K. Volz. *Decomposition Analysis of TBAs and TBP during GaAs and GaP Growth by MOVPE.*
  20th International Conference on Metalorganic Vapor Phase Epitaxy (ICMOVPE) 2020. Fellbach, Germany. Presentation cancelled due to Corona Pandemic.

List of Abbreviations

AFM ..... *atomic force microscopy*
ALD ..... *atomic layer deposition*
AsH_3 ..... *arsine*
CCD ..... *charge coupled device*
CG ..... *continous growth*
CHSH ..... *band transitions from the conduction band to the heavy hole band and from the spin-orbit split-off band to the heavy hole band*
DFT ..... *density functional theory*
dilute bismides ..... *III-V semiconductors containing small amounts of bismuth*
dilute nitrides ..... *III-V semiconductors containing small amounts of nitrogen*
DMAs ..... *di-methyl-arsane*
DTBAA ..... *di-tertiary-butyl-amino-arsan*
DTBADMHy ..... *di-tertiary-butyl-arsenyl-di-methyl-hydrazine*
DTBAP ..... *di-tert-butyl-amino-phosphane*
DTBAs• ..... *di-tertiary-butyl-arsane radical*
DTBP• ..... *di-tertiary-butyl-phosphane radical*
EAs ..... *ethyl-arsane*
EGa ..... *ethyl-gallium*
GaAs ..... *gallium arsenide*
Ga(As,Bi) ..... *gallium arsenide bismide*
Ga(As,Sb) ..... *gallium arsenide antimonide*
Ga(In,As) ..... *gallium indium arsenide*
(Ga,In)(As,P) ..... *gallium indium arsenide phosphide*
(Ga,In)(N,As) ..... *gallium indium nitride arsenide*
(Ga,In)N ..... *gallium indium nitride*
(Ga,In)P ..... *gallium indium phosphide*
Ga(N,As) ..... *gallium nitride arsenide*
Ga(N,As,Bi) ..... *gallium nitride arsenide bismide*
Ga(N,As,Sb) ..... *gallium nitride arsenide antimonide*
GaN ..... *gallium nitride*
GaP ..... *gallium phosphide*
GI ..... *growth interruptions*
HR-XRD ..... *high resolution X-ray diffraction*
InP ..... *indium phosphide*
IP ..... *isopropyl-gallium*
IVBA ..... *inter valence band absorption*
LDA ..... local density approximation
LEDs ..... *light emitting diodes*
LEED ..... *low energy electron diffraction*
MAs ..... *methyl-arsane*
MBE ..... *molecular beam epitaxy*

MGa ..... *methyl-gallium*
MMHy ..... tri-isopropyl-indium
MOs ..... *metal organic precursors*
MOVPE ..... *metal organic vapor phase epitaxy*
MS ..... *mass spectrometry*
NH_2• ..... *aminyl radical*
NH_3 ..... *ammonia*
PEM ..... *photo elastic modulator*
PG ..... *pulsed growth*
PH_3 ..... phosphine
RAS ..... *reflection anisotropy spectroscopy*
RDS ..... *reflectance difference spectroscopy*
RHEED ..... *reflection high energy electron diffraction*
SE ..... *surface exchange*
STM ..... *scanning tunneling microscopy*
SWIFT ..... *stored wave inverse Fourier transformation*
TBAs ..... *tertiary-butyl-arsane*
TBGa ..... *tertiary-butyl-gallium*
TBHy ..... tertiary-butyl-hydrazine
TBP ..... *tertiary-butyl-phosphane*
TEAs ..... *tri-ethyl-arsane*
TEGa ..... *tri-ethyl-gallium*
TEIn ..... *tri-ethyl-indium*
TEM ..... transmission electron microscopy
TESb ..... tri-ethyl-antimony
TIPIn ..... tri-isopropyl-indium
TIPSb ..... tri-isopropyl-antimony
TMAs ..... tri-methyl-arsane
TMBi ..... *tri-methyl-bismuth*
TMGa ..... *tri-methyl-gallium*
TMIn ..... *tri-methyl-indium*
TMSb ..... tri-methyl-antimony
TTBGa ..... *tri-tertiary-butyl-gallium*
UDMHy *1,1-di-methyl-hydrazine*
VCA ..... *virtual crystal approximation*
VCSEL ..... *vertical cavity surface emitting laser*

Bibliography

1. Hutt, R. What are the 10 biggest global challenges? *World Economic Forum* (2016). Available at: https://www.weforum.org/agenda/2016/01/what-are-the-10-biggest-global-challenges/.
2. Risikobewertung zu COVID-19. *Robert Koch Institut* (2020). Available at: https://www.rki.de/DE/Content/InfAZ/N/Neuartiges_Coronavirus/Risikobewertung.html.
3. Compound Semiconductor Market Size By Material Type, By Deposition Technology, By Product, By Geographic Scope and Forecast. *verified market research* 1–95 (2020).
4. An elemental change to laser design. *Compd. Semicond.* **19**, 53–57 (2013).
5. Jones, N. How to stop data centres from gobbling up the world's electricity. *Nature* **561**, 163–166 (2018).
6. Sweeney, S. J., Phillips, A. F., Adams, A. R., O'Reilly, E. P. and Thijs, P. J. A. The effect of temperature dependent processes on the performance of 1.5-μm compressively strained InGaAs(P) MQW semiconductor diode lasers. *IEEE Photonics Technol. Lett.* **10**, 1076–1078 (1998).
7. Chen, T. R. *et al.* Carrier leakage and temperature dependence of InGaAsP lasers. *Appl. Phys. Lett.* **43**, 217–218 (1983).
8. Adams, A. R., Asada, M., Suematsu, Y. and Arai, S. The Temperature Dependence of the Efficiency and Threshold Current of $In_{1-x}Ga_xAs_yP_{1-y}$Lasers Related to Intervalence Band Absorption. *Jpn. J. Appl. Phys.* **19**, L621–L624 (1980).
9. Sweeney, S. J. and Jin, S. R. Bismide-nitride alloys: Promising for efficient light emitting devices in the near- and mid-infrared. *J. Appl. Phys.* **113**, (2013).
10. Broderick, C. A., Usman, M., Sweeney, S. J. and O'Reilly, E. P. Band engineering in dilute nitride and bismide semiconductor lasers. *Semicond. Sci. Technol.* **27**, (2012).
11. Kunert, B., Volz, K., Koch, J. and Stolz, W. MOVPE growth conditions of the novel direct band gap, diluted nitride Ga(NAsP) material system pseudomorphically strained on GaP-substrate. *J. Cryst. Growth* **298**, 121–125 (2007).
12. Kondow, M. *et al.* GaInNAs: A Novel Material for Long-Wavelength-Range Laser Diodes with Excellent High-Temperature Performance. *Jpn. J. Appl. Phys.* **35**, 1273–1275 (1996).
13. Schmidt, J. *et al. Forschung und Entwicklung für die Photovoltaik zwischen Evolution und Revolution*. Conference: FVEE-Themenheft • At: Berlin • Volume: Forschung und Entwicklung für die Energiewende - Phasenübergänge aktiv gestalten (2014).
14. Friedman, D. J. Progress and challenges for next-generation high-efficiency multijunction solar cells. *Curr. Opin. Solid State Mater. Sci.* **14**, 131–138 (2010).
15. Yamaguchi, M. III–V compound multi-junction solar cells: present and future. *Sol. Energy Mater. Sol. Cells* **75**, 261–269 (2003).
16. Weltrekord-Solarzelle mit 44,7 Prozent Wirkungsgrad. *Fraunhofer ISE* (2013). Available at: https://www.ise.fraunhofer.de/de/presse-und-medien/presseinformationen/2013/weltrekord-solarzelle-mit-44-7-prozent-wirkungsgrad.html.
17. Oe, K. and Okamoto, H. New semiconductor alloy $GaAs_{1-x}Bi_x$ grown by metal organic vapor phase epitaxy. *Jpn. J. Appl. Physics, Part 2 Lett.* **37**, 1–4 (1998).
18. Ludewig, P., Nattermann, L., Stolz, W. and Volz, K. MOVPE growth mechanisms of dilute bismide III/V alloys. *Semicond. Sci. Technol.* **30**, 94017 (2015).
19. Forghani, K., Anand, A., Mawst, L. J. and Kuech, T. F. Low temperature growth of $GaAs_{1-y}Bi_y$ epitaxial layers. *J. Cryst. Growth* **380**, 23–27 (2013).
20. Jacobsen, H., Puchala, B., Kuech, T. F. and Morgan, D. Ab initio study of the strain dependent thermodynamics of Bi doping in GaAs. *Phys. Rev. B - Condens. Matter Mater. Phys.* **86**, 1–10 (2012).

21. Stringfellow, G. B. Calculation of the Solubility and Solid-Gas Distribution Coefficient of N in GaP. *J. Electrochem. Soc.* **119**, 1780 (1972).
22. Stringfellow, G. B. Calculation of ternary phase diagrams of III-V systems. *J. Phys. Chem. Solids* **33**, 665–677 (1972).
23. Goldschmidt, V. M. Crystal structure and chemical constitution. *Trans. Faraday Soc.* **25**, 253–283 (1929).
24. Phillips, J. C. Bonds and Bands in Semiconductors. *Science.* **169** (3950), 1035–1042 (1970).
25. Mullin, J. B., Straughan, B. W., Driscoll, C. M. H. and Willoughby, A. F. W. The lattice larameter of GaAs and InP with reference to interfaces. *C R C Crit. Rev. Solid State Sci.* **5**, 441–456 (1975).
26. Blakemore, J. S. Semiconducting and other major properties of gallium arsenide. *J. Appl. Phys.* **53**, (1982).
27. Stringfellow, G. B. Development and current status of organometallic vapor phase epitaxy. *J. Cryst. Growth* **264**, 620–630 (2004).
28. Vohl, P. *et al.* GaAs thin-film solar cells. *IEEE Trans. Electron Devices* **14**, 26–30 (1967).
29. Kittel, C. *Einführung in die Festkörperphysik*. (De Gruyter Oldenbourg, 2013).
30. Hunklinger, S. *Festkörperphysik*. (Walter de Gruyter, 2014).
31. Pohl, U. W. *Epitaxy of Semiconductors - Introduction to Physical Principles*. (Springer Science and Business Media, 2013).
32. Elliott, R. J. Spin-Orbit Coupling in Band Theory---Character Tables for Some 'Double' Space Groups. *Phys. Rev.* **96**, 280–287 (1954).
33. Van Vechten, J. A. and Bergstresser, T. K. Electronic Structures of Semiconductor Alloys. *Phys. Rev. B* **1**, 3351–3358 (1970).
34. Tixier, S. *et al.* Molecular beam epitaxy growth of $GaAs_{1-x}Bi_x$. *Appl. Phys. Lett.* **82**, 2245–2247 (2003).
35. Fluegel, B. *et al.* Giant spin-orbit bowing in $GaAs_{1-x}Bi_x$. *Phys. Rev. Lett.* **97**, 11–14 (2006).
36. Francoeur, S. *et al.* Band gap of $GaAs_{1-x}Bi_x$, 0<x< 3.6%. *Appl. Phys. Lett.* **82**, 3874–3876 (2003).
37. Huang, W., Yoshimoto, M., Takehara, Y., Saraie, J. and Oe, K. $GaN_yAs_{1-x-y}Bi_x$ Alloy Lattice Matched to GaAs with 1.3 μm Photoluminescence Emission. *Jpn. J. Appl. Phys.* **43**, L1350–L1352 (2004).
38. Li, H. and Wang, Z. M. *Bismuth-Containing Compounds*. (Springer, New York, NY, 2013).
39. Wei, S.-H. and Zunger, A. Giant and Composition-Dependent Optical Bowing Coefficient in GaAsN Alloys. *Phys. Rev. Lett.* **76**, 664–667 (1996).
40. Bi, W. G. and Tu, C. W. Bowing parameter of the band-gap energy of GaN_xAs_{1-x}. *Appl. Phys. Lett.* **70**, 1608–1610 (1997).
41. Shan, W. *et al.* Band anticrossing in GaInNAs alloys. *Phys. Rev. Lett.* **82**, 1221–1224 (1999).
42. Shan, W. *et al.* Band Anticrossing in III–N–V Alloys. *Phys. status solidi* **223**, 75–85 (2001).
43. Shan, W. *et al.* Band anticrossing in dilute nitrides. *J. Phys. Condens. Matter* **16**, 3355–3372 (2004).
44. J. Wu, W. S. and W. W. Band anticrossing in highly mismatched III–V semiconductor alloys. *Semicond. Sci. Technol.* **17**, 860–869 (2002).
45. Alberi, K. *et al.* Valence band anticrossing in $GaBi_xAs_{1-x}$. *Appl. Phys. Lett.* **91**, 1–4 (2007).
46. Alberi, K. *et al.* Valence-band anticrossing in mismatched III-V semiconductor alloys. *Phys. Rev. B* **75**, 45203 (2007).

47. Broderick, C. A., Usman, M. and O'Reilly, E. P. Derivation of 12- and 14-band k · p Hamiltonians for dilute bismide and bismide-nitride semiconductors. *Semicond. Sci. Technol.* **28**, (2013).

48. Seifikar, M., O'Reilly, E. P. and Fahy, S. Analysis of band-anticrossing model in GaNAs near localised states. *Phys. status solidi* **248**, 1176–1179 (2011).

49. Usman, M., Broderick, C. A., Lindsay, A. and O'Reilly, E. P. Tight-binding analysis of the electronic structure of dilute bismide alloys of GaP and GaAs. *Phys. Rev. B - Condens. Matter Mater. Phys.* **84**, 1–13 (2011).

50. Batool, Z. *et al.* The electronic band structure of GaBiAs/GaAs layers: Influence of strain and band anti-crossing. *J. Appl. Phys.* **111**, (2012).

51. Higashi, T. *et al.* Experimental analysis of temperature dependence in 1.3-μm AlGaInAs-InP strained MQW lasers. *IEEE J. Sel. Top. Quantum Electron.* **5**, 413–419 (1999).

52. Silver, M., O'Reilly, E. P. and Adams, A. R. Determination of the wavelength dependence of auger recombination in long-wavelength quantum-well semiconductor lasers using hydrostatic pressure. *IEEE J. Quantum Electron.* **33**, 1557–1566 (1997).

53. Volz, K. *et al.* Specific structural and compositional properties of (GaIn)(NAs) and their influence on optoelectronic device performance. *J. Cryst. Growth* **272**, 739–747 (2004).

54. Okumura, H., Yoshida, S. and Okahisa, T. Optical properties near the band gap on hexagonal and cubic GaN. *Appl. Phys. Lett.* **64**, 2997–2999 (1994).

55. Sterzer, E. *et al.* Efficient nitrogen incorporation in GaAs using novel metal organic As-N precursor di-tertiary-butyl-arsano-amine (DTBAA). *J. Cryst. Growth* **439**, 19–27 (2016).

56. Volz, K., Koch, J., Höhnsdorf, F., Kunert, B. and Stolz, W. MOVPE growth of dilute nitride III/V semiconductors using all liquid metalorganic precursors. *J. Cryst. Growth* **311**, 2418–2426 (2009).

57. Sterzer, E. *et al.* Investigation of the microstructure of metallic droplets on Ga(AsBi)/GaAs. *J. Cryst. Growth* **408**, 71–77 (2014).

58. Norman, A. G., France, R. and Ptak, A. J. Atomic ordering and phase separation in MBE $GaAs_{1-x}Bi_x$. *J. Vac. Sci. Technol. B, Nanotechnol. Microelectron. Mater. Process. Meas. Phenom.* **29**, 03C121 (2011).

59. Fitouri, H., Moussa, I., Rebey, A., Fouzri, A. and El Jani, B. AP-MOVPE of thin $GaAs_{1-x}Bi_x$ alloys. *J. Cryst. Growth* **295**, 114–118 (2006).

60. Ludewig, P., Knaub, N., Stolz, W. and Volz, K. MOVPE growth of Ga(AsBi)/GaAs multi quantum well structures. *J. Cryst. Growth* **370**, 186–190 (2013).

61. Ludewig, P. *et al.* Growth of Ga(AsBi) on GaAs by continuous flow MOVPE. *J. Cryst. Growth* **396**, 95–99 (2014).

62. Hepp, T., Nattermann, L. and Volz, K. MOVPE Growth and Device Applications of Ternary and Quaternary Dilute Bismide Alloys on GaAs Substrates. in *Wang S., Lu P. (eds) Bismuth-Containing Alloys and Nanostructures* (eds. Wang, S. and Lu, P.) 37–58 (Springer, Singapore, 2019).

63. Wang, S. *Bismuth-Containing Alloys and Nanostructures*. (Springer Series in Materials Science, 2019).

64. Henini, M.. *Dilute Nitride Semiconductors* (Elsevier, 2005).

65. Lüth, H. *Solid Surfaces, Interfaces and Thin Films*. (Springer Science and Business Media, 2010).

66. Harrison, W. A. Theory of polar semiconductor surfaces. *J. Vac. Sci. Technol.* **16**, 1492–1496 (1979).

67. Srivastava, G. P. The electron counting rule and passivation of compound semiconductor surfaces. *Appl. Surf. Sci.* **252**, 7600–7607 (2006).

68. Wood, E. A. Vocabulary of Surface Crystallography. *J. Appl. Phys.* **35**, 1306–1312 (1964).

69. Stringfellow, G. B. *Organometallic vapour phase epitaxy: Theory and practice*. (Academic Press, 1999).

70. Ohtake, A. Surface reconstructions on GaAs(001). *Surf. Sci. Rep.* **63**, 295–327 (2008).

71. Richter, W. In-situ observation of MOVPE epitaxial growth. *Appl. Phys. A Mater. Sci. Process.* **75**, 129–140 (2002).

72. Giling, L. J. and Van Enckevort, W. J. P. On the influence of surface reconstruction on crystal growth processes. *Surf. Sci.* **161**, 567–583 (1985).

73. Irvine, S. J. C. and Capper, P. Introduction to Metalorganic Vapor Phase Epitaxy. in *Metalorganic Vapor Phase Epitaxy (MOVPE)* 1–18 (John Wiley and Sons, Ltd, 2019).

74. Field, R. L. *et al.* Influence of surface reconstruction on dopant incorporation and transport properties of GaAs(Bi) alloys. *Appl. Phys. Lett.* **109**, 252105 (2016).

75. Shilov, A. Samsung's Aggressive EUV Plans: 6nm Production in H2, 5nm and 4nm On Track. (2019). Available at: https://www.anandtech.com/show/14695/samsungs-aggressive-euv-plans-6nm-production-in-h2-5nm-4nm-on-track.

76. Hasan, M. Z. and Kane, C. L. Colloquium: Topological insulators. *Rev. Mod. Phys.* **82**, 3045–3067 (2010).

77. Stringfellow, G. B. Novel precursors for organometallic vapor phase epitaxy. *J. Cryst. Growth* **128**, 503–510 (1993).

78. Irvine, S. and Capper, P. *Metalorganic Vapor Phase Epitaxy (MOVPE): Growth, Materials Properties, and Applications*. (Wiley, 2019).

79. Jones, A. C. and O'Brien, P. *CVD of Compound Semiconductors - Precursor Synthesis, Developmeny and Applications*. (John Wiley and Sons, 2008).

80. Shenai-Khatkhate, D. V *et al.* Organometallic molecules for semiconductor fabrication. *Philos. Trans. R. Soc. London. Ser. A, Math. Phys. Sci.* **330**, 173–182 (1990).

81. Alabugin, I. V, Gilmore, K. M. and Peterson, P. W. Hyperconjugation. *WIREs Comput. Mol. Sci.* **1**, 109–141 (2011).

82. Zimmermann, G. Einfluß neuartiger Ausgangsmaterialien in der Metallorganischen Gasphasenepitaxy (MOVPE) auf die physikalischen Eigenschaften von III/V-Halbleiterstructuren. (Dissertation, Philipps-Universität Marburg, 1994).

83. Grignard, V. Sur quelques nouvelles combinaisons organométalliques du magnésium et leur application à des synthèses d'alcools et d'hydrocarbures. *C.R. Hebd. Seances Acad. Sci.* **130**, 1322–1324 (1900).

84. Maruyama, K. and Katagiri, T. Mechanism of the Grignard reaction. *J. Phys. Org. Chem.* **2**, 205–213 (1989).

85. Tzschach, A. and Deylig, W. Organoarsenic compounds. V. Preparation of lithium derivatives of mono- and di-tert-butylarsine. *Zeitschrift fuer Anorg. und Allg. Chemie* **336**, 36–41 (1965).

86. Shenai-Khatkhate, Deodatta Vinayak; Amamchyan, Artashes; Power, Michael Brendan; Dicarlo, Ronald L.; Felton, J. E. Preparation of Alkyl group Va metal compounds useful as precursors for chemical vapor deposition. (Patent US6956127B2, 2005).

87. Scherer, O. J. and Schieder, G. Elementorganische amin/imin-verbindungen: IX. Metallorganische aminophosphinimine. *J. Organomet. Chem.* **19**, 315–326 (1969).

88. Ringler, B. and von Hänisch, C. Über Interpnictogenverbindungen und MOVPE-Präkursoren sowie deren Reaktionsverhalten gegenüber Trielen. (Dissertation, Philipps-Universität Marburg, 2018).

89. Scherer, O. J. and Schieder, G. Metallorganische Aminophosphine und Phosphinimine. *Chem. Ber.* **101**, 4184–4198 (1968).

90. Glowatzki, J. *et al.* Ga(N,P) Growth on Si and Decomposition Studies of the N–P Precursor Di-tert-butylaminophosphane (DTBAP). *Organometallics* **39**, 1772–1781 (2020).

91. Kovar, R. A., Loaris, G., Derr, H. and Callaway, J. O. Convenient preparation of base-free tributylgallium, dibutylgallium chloride, and butylgallium dichloride. Molecular association studies of butylgallium compounds in benzene. *Inorg. Chem.* **13**, 1476–1479 (1974).

92. Bradley, D. C. *et al.* Trimethylindium and Trimethylgallium. *Inorganic Syntheses* 67–74 (1996).

93. Fluck, E. *Ga Organogallium Compounds - Part 1*. (Springer Science and Business Media, 1987).

94. Okawara, R. Gallium and Indium annual survey covering the year 1975. *J. Organomet. Chem.* **130**, 345–363 (1977).

95. Elschenbroich, C. and Salzer, A. *Organometallics - A Concise Introduction*. (Wiley, 1992).

96. Wilkinson, G., Stone, F. G. A. and Abel, E. W. *Comprehensive Organometallic Chemistry - The Synthesis, Reactions, and Structures of Organometallic Compounds*. (Elsevier Science and Technology Books, 1982).

97. Glasstone, S., Laidler, K. J. and Eyring, H. *The theory of rate processes - the kinetics of chemical reactions, viscosity, diffusion and electrochemical phenomena*. (McGraw-Hill Book Company, inc., 1941).

98. Zellner, R. S.W. Benson: Thermochemical Kinetics, 2nd Ed. John Wiley and Sons, New York-London-Sydney-Toronto 1976. *Berichte der Bunsengesellschaft für Phys. Chemie* **81**, 877–878 (1977).

99. Kuech, T. F. III-V compound semiconductors: Growth and structures. *Prog. Cryst. Growth Charact. Mater.* **62**, 352–370 (2016).

100. Muller, P. Glossary of terms used in physical organic chemistry (IUPAC Recommendations 1994). *Pure Appl. Chem.* **66**, 1077–1184 (1994).

101. Larsen, C. A., Buchan, N. I., Li, S. H. and Stringfellow, G. B. Decomposition mechanisms of tertiarybutylarsine. *J. Cryst. Growth* **94**, 663–672 (1989).

102. Stegmüller, A. and Tonner, R. β-Hydrogen Elimination Mechanism in the Absence of Low-Lying Acceptor Orbitals in $EH_2(t\text{-}C_4H_9)$ (E = N–Bi) . *Inorg. Chem.* **54**, 6363–6372 (2015).

103. Foster, D. F., Glidewell, C. and Cole-Hamilton, D. J. Probing the mechanisms of growth of gallium arsenide by metalorganic vapor phase epitaxy using experimental and theoretical studies of designed precursors. *J. Electron. Mater.* **23**, 69–74 (1994).

104. Nattermann, L. K. MOVPE Growth Studies on Dilute Bismide Containing III / Vs and Development of an MOVPE in-situ Gas Phase Analysis Setup. (Dissertation, Philipps-Universität Marburg, 2017).

105. Russell, D. K. Gas-Phase Pyrolysis Mechanisms in Organometallic CVD. *Chem. Vap. Depos.* **2**, 223–233 (1996).

106. Kappers, M. J., Warddrip, M. L. and Hicks, R. F. Ligand exchange reactions in InGaAs metalorganic vapor-phase epitaxy. *J. Cryst. Growth* **191**, 332–340 (1998).

107. Lee, R. T. and Stringfellow, G. B. Pyrolysis of 1,1 dimethylhydrazine for OMVPE growth. *J. Electron. Mater.* **28**, 963–969 (1999).

108. Bourret-Courchesne, E. *et al.* Pyrolysis of dimethylhydrazine and its co-pyrolysis with triethylgallium. *J. Cryst. Growth* **217**, 47–54 (2000).

109. Amano, H., Kito, M., Hiramatsu, K. and Akasaki, I. P-type conduction in Mg-doped GaN treated with low-energy electron beam irradiation (LEEBI). *Jpn. J. Appl. Phys.* **28**, L2112–L2114 (1989).

110. Nakamura, S. GaN growth using GaN buffer layer. *Jpn. J. Appl. Phys.* **30**, L1705–L1707 (1991).

111. Nanishi, Y. Nobel Prize in Physics: The birth of the blue LED. *Nat. Photonics* **8**, 884–886 (2014).

112. Harris, J. S., O'Sullivan, T., Sarmiento, T., Lee, M. M. and Vo, S. Emerging applications for vertical cavity surface emitting lasers. *Semicond. Sci. Technol.* **26**, (2010).

113. Dimroth, F. *et al.* Wafer bonded four-junction GaInP/GaAs//GaInAsP/GaInAs concentrator solar cells with 44.7% efficiency. *Prog. Photovoltaics Res. Appl.* **22**, 277–282 (2014).

114. Ajayan, J. and Nirmal, D. A review of InP/InAlAs/InGaAs based transistors for high frequency applications. *Superlattices Microstruct.* **86**, 1–19 (2015).

115. Pohl, U. W. *Epitaxy of Semiconductors - Physics and Fabrication of Heterostructures*. (Springer International Publishing, 2020).

116. Weightman, P., Martin, D. S., Cole, R. J. and Farrell, T. Reflection anisotropy spectroscopy. *Reports Prog. Phys.* **68**, 1251–1341 (2005).

117. Aspnes, D. E. New developments in spectroellipsometry: the challenge of surfaces. *Thin Solid Films* **233**, 1–8 (1993).

118. McIntyre, J. D. E. and Aspnes, D. E. Differential reflection spectroscopy of very thin surface films. *Surf. Sci.* **24**, 417–434 (1971).

119. *EpiRAS TT - User's Manual*. (LayTec GmbH, 2007).

120. Selci, S., Ciccacci, F., Chiarotti, G., Chiaradia, P. and Cricenti, A. Surface differential reflectivity spectroscopy of semiconductor surfaces. *J. Vac. Sci. Technol. A* **5**, 327–332 (1987).

121. Martin, D. S., Maunder, A. and Weightman, P. Thermal behavior of the Cu(110) surface studied by reflection anisotropy spectroscopy and scanning tunneling microscopy. *Phys. Rev. B* **63**, 155403 (2001).

122. Cole, R. J. *et al.* Orientation of Molecular Adsorbates from Reflection Anisotropy Spectroscopy. *Phys. status solidi* **170**, 235–239 (1998).

123. Manghi, F., Del Sole, R., Selloni, A. and Molinari, E. Anisotropy of surface optical properties from first-principles calculations. *Phys. Rev. B* **41**, 9935–9946 (1990).

124. Sun, L. D., Hohage, M., Zeppenfeld, P., Balderas-Navarro, R. E. and Hingerl, K. Surface-induced d-band anisotropy on Cu(110). *Surf. Sci.* **527**, L184–L190 (2003).

125. Inglesfield, J. E. Surface electronic structure. *Reports Prog. Phys.* **45**, 223–284 (1982).

126. Aspnes, D. E. Above-bandgap optical anisotropies in cubic semiconductors: A visible–near ultraviolet probe of surfaces. *J. Vac. Sci. Technol. B Microelectron. Process. Phenom.* **3**, 1498–1506 (1985).

127. Armstrong, S. R. *et al.* A RHEED and reflectance anisotropy study of the MBE growth of GaAs, AlAs and InAs on GaAs(001). *Surf. Sci.* **274**, 263–269 (1992).

128. Pristovsek, M. *et al.* In-situ Determination of the Carrier Concentration of (001) GaAs by Reflectance Anisotropy Spectroscopy. *Phys. status solidi* **188**, 1423–1429 (2001).

129. LayTec AG. Available at: https://www.laytec.de/epiras/.

130. Fowles, G. R. *Introduction to Modern Optics*. (Courier Corporation, 2012).

131. Zorn, M. *et al.* MOVPE process development for 650nm VCSELS using optical in-situ techniques. *J. Cryst. Growth* **235**, 25–34 (2002).

132. Gross, J. H. *Mass spectrometry*. (Springer, Berlin, Heidelberg, 2011).

133. Hiraoka, K. *Fundamentals of Mass Spectrometry*. (Springer Science and Business Media, 2013).

134. Zanobetti, A., Franklin, M., Koutrakis, P. and Schwartz, J. Fine particulate air pollution and its components in association with cause-specific emergency admissions. *Environ. Heal.* **8**, 58 (2009).

135. Harris, W. A., Reilly, P. T. A. and Whitten, W. B. Detection of Chemical Warfare-Related Species on Complex Aerosol Particles Deposited on Surfaces Using an Ion Trap-Based Aerosol Mass Spectrometer. *Anal. Chem.* **79**, 2354–2358 (2007).

136. He, F., Hendrickson, C. L. and Marshall, A. G. Baseline Mass Resolution of Peptide Isobars: A Record for Molecular Mass Resolution. *Anal. Chem.* **73**, 647–650 (2001).

137. Fenselau, C. *et al.* Mass spectrometry in the exploration of Mars. *J. Mass Spectrom.* **38**, 1–10 (2003).

138. Goldstein, E. On the canal-ray group. *London, Edinburgh, Dublin Philos. Mag. J. Sci.* **15**, 372–385 (1908).

139. Rüchardt, E. Zur Entdeckung der Kanalstrahlen vor fünfzig Jahren. *Naturwissenschaften* **24**, 465–467 (1936).

140. Thomson, J. J. A. Rays of positive electricity. *London, Edinburgh, Dublin Philos. Mag. J. Sci.* **19**, 424–435 (1910).

141. Thomson, J. J. Bakerian Lecture: Rays of Positive Electricity. *Proc. R. Soc. London. Ser. A, Contain. Pap. a Math. Phys. Character* **89**, 1–20 (1913).

142. Dempster, A. J. A new Method of Positive Ray Analysis. *Phys. Rev.* **11**, 316–325 (1918).

143. Hu, Q. *et al.* The Orbitrap: a new mass spectrometer. *J. Mass Spectrom.* **40**, 430–443 (2005).

144. Field, F. H. and Franklin, J. L. *Electron Impact Phenomena and the Properties of Gaseous Ions*. (Academic Press, 2013).

145. Nier, A. O. Some reflections on the early days of mass spectrometry at the university of Minnesota. *Int. J. Mass Spectrom. Ion Process.* **100**, 1–13 (1990).

146. Tal'roze, V. L. and Ljubimova, A. K. Secondary processes in the ion source of a mass spectrometer (presented by academician N. N. Semenov 27 VIII 1952) : reprinted from Report of the Soviet Academy of Sciences, Volume LXXXVI, -N5 (1952). *J. Mass Spectrom.* **33**, 502–504 (1998).

147. Cole, R. B. *Electrospray Ionization Mass Spectrometry - Fundamentals, Instrumentation, and Applications*. (Wiley, 1997).

148. Inghram, M. G. and Gomer, R. Mass Spectrometric Analysis of Ions from the Field Microscope. *J. Chem. Phys.* **22**, 1279–1280 (1954).

149. Sampson, J. S., Hawkridge, A. M. and Muddiman, D. C. Generation and detection of multiply-charged peptides and proteins by matrix-assisted laser desorption electrospray ionization (MALDESI) fourier transform ion cyclotron resonance mass spectrometry. *J. Am. Soc. Mass Spectrom.* **17**, 1712–1716 (2006).

150. NIST Chemistry WebBook. Available at: https://doi.org/10.18434/T4D303.

151. Mark, T. D. Fundamental aspects of electron impact ionization. *Int. J. Mass Spectrom. Ion Phys.* **45**, 125–145 (1982).

152. Honig, R. E. Ionization Potentials of Some Hydrocarbon Series. *J. Chem. Phys.* **16**, 105–112 (1948).

153. Deutsch, H., Becker, K., Janev, R. K., Probst, M. and Märk, T. D. Isomer effect in the total electron impact ionization cross section of cyclopropane and propene (C_3H_6). *J. Phys. B At. Mol. Opt. Phys.* **33**, L865–L872 (2000).

154. Grill, V. *et al.* Absolute partial and total electron impact ionization cross sections for C_3H_8 from threshold up to 950 eV. *Zeitschrift für Phys. D Atoms, Mol. Clust.* **25**, 217–226 (1993).

155. Grill, V., Walder, G., Scheier, P., Kurdel, M. and Märk, T. D. Absolute partial and total electron impact ionization cross sections for C_2H_6 from threshold up to 950 eV. *Int. J. Mass Spectrom. Ion Process.* **129**, 31–42 (1993).

156. Jiao, C. Q., DeJoseph, C. A. and Garscadden, A. Electron impact ionization and ion reactions in n-butane. *J. Phys. D. Appl. Phys.* **40**, 409–414 (2007).

157. Rapp, D. and Englander-Golden, P. Total Cross Sections for Ionization and Attachment in Gases by Electron Impact. I. Positive Ionization. *J. Chem. Phys.* **43**, 1464–1479 (1965).

158. Von Engel, A. *Ionized Gases*. (Oxford University Press, 1965).

159. Thorman, R., R. Kumar T. P., Fairbrother, D. and Ingólfsson, O. The role of low-energy electrons in focused electron beam induced deposition: Four case studies of representative precursors. *Beilstein J. Nanotechnol.* **6**, 1904–1926 (2015).

160. Yoshida, M., Watanabe, H. and Uesugi, F. Mass spectrometric study of $Ga(CH_3)_3$ and $Ga(C_2H_5)_3$ decomposition reaction in H_2 and N_2. *J. Electrochem. Soc.* **132**, 677–679 (1985).

161. Nattermann, L. *et al.* An experimental approach for real time mass spectrometric CVD gas phase investigations. *Sci. Rep.* **8**, 319 (2018).

162. Paul, W. Electromagnetic Traps for Charged and Neutral Particles (Nobel Lecture). *Angew. Chemie Int. Ed. English* **29**, 739–748 (1990).

163. March, R. E. and Todd, J. F. J. *Practical Aspects of Trapped Ion Mass Spectrometry - Theory and Instrumentation*. (Taylor and Francis, 2010).

164. Paul-Falle Analogon. Available at: https://videoportal.uni-freiburg.de/video/Paul-Falle-Analogon/555142f46954fff834b7c075ea3be495.

165. Chung, H. Y. *et al.* Very sensitive real-time inline process mass spectrometer based on FFT Ion Trap technique. in *2016 27th Annual SEMI Advanced Semiconductor Manufacturing Conference (ASMC)* 263–266 (IEEE, 2016).

166. Guan, S. and Marshall, A. G. Stored waveform inverse Fourier transform (SWIFT) ion excitation in trapped-ion mass spectometry: Theory and applications. *Int. J. Mass Spectrom. Ion Process.* **157**–**158**, 5–37 (1996).

167. ZEISS Process Gas Analyzer. Available at: https://www.zeiss.com/semiconductor-manufacturing-technology/products-solutions/process-gas-analysis.html.

168. Röntgen, W. C. Über eine neue Art von Strahlen. *Sitzungsberichte der Würzburg. Phys. Gesellschaft Würzbg.* **137**, 132–141 (1895).

169. Friedrich, W., Knipping, P. and Laue, M. Interferenzerscheinungen bei Röntgenstrahlen. *Ann. Phys.* **346**, 971–988 (1913).

170. Bragg, W. H. and Bragg, W. L. The reflection of X-rays by crystals. *Proc. R. Soc. London. Ser. A, Contain. Pap. a Math. Phys. Character* **88**, 428–438 (1913).

171. Ewald, P. P. Zur Theorie der Interferenzen der Röntgenstrahlen in Kristallen. *Physikalische Zeitschrift* **14**, 465–472 (1913).

172. Miller, W. H. *A treatise on crystallography*. (Cambridge [England], 1839).

173. Pyykkö, P. and Atsumi, M. Molecular Single-Bond Covalent Radii for Elements 1–118. *Chem. A Eur. J.* **15**, 186–197 (2009).

174. Hagen, W. Tetragonal distortion in heteroepitaxial layers: Ge on GaAs. *J. Cryst. Growth* **43**, 739–744 (1978).

175. Vurgaftman, I., Meyer, J. R. and Ram-Mohan, L. R. Band parameters for III-V compound semiconductors and their alloys. *J. Appl. Phys.* **89**, 5815–5875 (2001).

176. Vegard, L. Die Konstitution der Mischkristalle und die Raumfüllung der Atome. *Zeitschrift für Phys.* **5**, 17–26 (1921).

177. Warren, B. E. *X-Ray Diffraction*. (Courier Corporation, 2012).

178. Binnig, G., Quate, C. F. and Gerber, C. Atomic Force Microscope. *Phys. Rev. Lett.* **56**, 930–933 (1986).

179. Ramsauer, C. *Grundversuche der Physik in Historischer Darstellung - Erster Band: Von den Fallgesetzen bis zu den elektrischen Wellen*. (Springer-Verlag, 2013).

180. Pauli, W. Über den Zusammenhang des Abschlusses der Elektronengruppen im Atom mit der Komplexstruktur der Spektren. *Zeitschrift für Phys.* **31**, 765–783 (1925).

181. Voigtländer, B. *Scanning Probe Microscopy - Atomic Force Microscopy and Scanning Tunneling Microscopy*. (Springer, 2015).

182. Maßmeyer, O. P. Untersuchung des Einflusses von UDMHy und TMBi auf die GaAs (001) Oberflächenrekonstruktion in der Metallorganischen Gasphasenepitaxie mittels Reflexionsanisotropiespektroskopie. (Master's thesis, Philipps-Universität Marburg, 2017).

183. Ohtake, A. Surface reconstructions on GaAs(001). *Surf. Sci. Rep.* **63**, 295–327 (2008).

184. Hoffmann, V. *et al.* Nitrogen–arsenic exchange processes and investigation of the nitrided GaAs surfaces in MOVPE. *J. Cryst. Growth* **272**, 30–36 (2004).

185. Fuchs, C., Beyer, A., Volz, K. and Stolz, W. MOVPE growth of (GaIn)As/Ga(AsSb)/(GaIn)As type-II heterostructures on GaAs substrate for near infrared laser applications. *J. Cryst. Growth* **464**, 201–205 (2017).

186. Fuchs, C. and Stolz., W. (Prof. D. . Epitaxial Growth and Characterization of GaAs-based Type-II (GaIn)As/Ga(AsSb)/(GaIn)As "W"-quantum Well Heterostructures and Lasers. (Dissertation, Philipps-Universität Marburg, 2017).

187. Tansu, N. and Mawst, L. J. Design analysis of 1550-nm GaAsSb-(In)GaAsN type-II quantum-well laser active regions. *IEEE J. Quantum Electron.* **39**, 1205–1210 (2003).

188. Odofin, E. M. GaNAs ML growth on GaAs with the use of MOVPE (Metal Organic Vapour Phase Epitaxy). (Master's thesis, Philipps-Universität Marburg, 2020).

189. Döscher, H. *et al.* GaP-interlayer formation on epitaxial GaAs(100) surfaces in MOVPE ambient. *J. Cryst. Growth* **464**, 2–7 (2017).

190. Müller-Caspary, K. *et al.* Materials characterisation by angle-resolved scanning transmission electron microscopy. *Sci. Rep.* **6**, 37146 (2016).

191. Beyer, A. *et al.* Influence of Plasmon Excitations on Atomic-Resolution Quantitative 4D Scanning Transmission Electron Microscopy. *Submitt. to Sci. reports* (2020).

192. Bastiman, F., Cullis, A. G., David, J. P. R. and Sweeney, S. J. Bi incorporation in GaAs(100)-2×1 and 4×3 reconstructions investigated by RHEED and STM. *J. Cryst. Growth* **341**, 19–23 (2012).

193. Young, E. C., Tixier, S. and Tiedje, T. Bismuth surfactant growth of the dilute nitride GaN_xAs_{1-x}. *J. Cryst. Growth* **279**, 316–320 (2005).

194. Laukkanen, P. *et al.* Structural properties of Bi-stabilized reconstructions of GaInAs(100) surface. *Appl. Phys. Lett.* **90**, (2007).

195. Stringfellow, G. B. Non-hydride group-V sources for OMVPE. *J. Electron. Mater.* **17**, 327–335 (1988).

196. Furr, A. K. *CRC Handbook of Laboratory Safety, 5th Edition*. (CRC Press, 2000).

197. Larsen, C. A. and Stringfellow, G. B. Decomposition kinetics of OMVPE precursors. *J. Cryst. Growth* **75**, 247–254 (1986).

198. Li, S. H., Larsen, C. A., Buchan, N. I. and Stringfellow, G. B. Pyrolysis of tertiarybutylphosphine. *J. Electron. Mater.* **18**, 457–464 (1989).

199. Larsen, C. A., Buchan, N. I. and Stringfellow, G. B. Mass spectrometric studies of phosphine pyrolysis and OMVPE growth of InP. *J. Cryst. Growth* **85**, 148–153 (1987).

200. Bahlawane, N., Reilmann, F., Salameh, I. and Kohsehoinghaus, K. Mass-Spectrometric Monitoring of the Thermally Induced Decomposition of Trimethylgallium, Tris(tert-Butyl)Gallium, and Triethylantimony at Low Pressure Conditions. *J. Am. Soc. Mass Spectrom.* **19**, 947–954 (2008).

201. Lee, P. W., Omstead, T. R., McKenna, D. R. and Jensen, K. F. In-situ mass spectroscopy and thermogravimetric studies of GaAs MOCVD gas phase and surface reactions. *J. Cryst. Growth* **85**, 165–174 (1987).

202. Larsen, C. A., Buchan, N. I., Li, S. H. and Stringfellow, G. B. Decomposition mechanisms of trimethylgallium. *J. Cryst. Growth* **102**, 103–116 (1990).

203. Li, S. H., Buchan, N. I., Larsen, C. A. and Stringfellow, G. B. OMVPE growth mechanism for GaP using tertiarybutylphosphine and trimethylgallium. *J. Cryst. Growth* **96**, 906–914 (1989).

204. Chen, C. H., Larsen, C. A., Stringfellow, G. B., Brown, D. W. and Robertson, A. J. MOVPE growth of InP using isobutylphosphine and tert-butylphosphine. *J. Cryst. Growth* **77**, 11–18 (1986).

205. Larsen, C. A., Li, S. H., Buchan, N. I. and Stringfellow, G. B. Mechanisms of GaAs growth using tertiarybutylarsine and trimethylgallium. *J. Cryst. Growth* **94**, 673–682 (1989).

206. FitzGerald, E. T., O'Hare, D., Jones, A. C. and Foord, J. S. Comparative studies of the thermal decomposition of tritertiarybutylgallium and tri-isobutylgallium on GaAs(100). *Surf. Sci.* **278**, 111–120 (1992).

207. Sterzer, E. *et al.* (GaIn)(NAs) growth using di-tertiary-butyl-arsano-amine (DTBAA). *J. Cryst. Growth* **467**, 132–136 (2017).

208. Sterzer, E. *et al.* 1 eV Ga(NAsSb) grown by MOVPE using di- tertiary -butyl-arsano-amine (DTBAA). *AIP Adv.* **8**, 055329 1–9 (2018).

209. Lide, D. R. *CRC Handbook of Chemistry and Physics, 87th Edition*. (Taylor and Francis, 2006).

210. Stegmüller, A. and Tonner, R. β-Hydrogen Elimination Mechanism in the Absence of Low-Lying Acceptor Orbitals in EH_2(t-C_4H_9) (E = N–Bi). *Inorg. Chem.* **54**, 6363–6372 (2015).

211. Hunter, E. P. L. and Lias, S. G. Evaluated Gas Phase Basicities and Proton Affinities of Molecules: An Update. *J. Phys. Chem. Ref. Data* **27**, 413–656 (1998).

212. Liu, S. S. Growth Kinetics and Catalytic Effects in the Vapor Phase Epitaxy of Gallium Nitride. *J. Electrochem. Soc.* **125**, 1161 (1978).

213. Donnelly, V. M. and McCaulley, J. A. Products of thermal decomposition of triethylgallium and trimethylgallium adsorbed on Ga-stabilized GaAs(100). *Surf. Sci.* **238**, 34–52 (1990).

214. Feenstra, R. M., Woodall, J. M. and Pettit, G. D. Observation of bulk defects by scanning tunneling microscopy and spectroscopy: Arsenic antisite defects in GaAs. *Phys. Rev. Lett.* **71**, 1176–1179 (1993).

215. Gaskill, D. K., Bottka, N. and Lin, M. C. Growth of GaN films using trimethylgallium and hydrazine. *Appl. Phys. Lett.* **48**, 1449–1451 (1986).

216. Thon, A. and Kuech, T. F. High temperature adduct formation of trimethylgallium and ammonia. *Appl. Phys. Lett.* **69**, 55–57 (1996).

217. Fetter, N. R. and Bartocha, B. The chemistry of aluminum-nitrogen compounds: i. reactions of trimethylaluminum and trimethylaluminum trimethylamine with several methylhydrazines. *Can. J. Chem.* **39**, 2001–2008 (1961).

218. Peters, D. W., Bourret, E. D., Power, M. P. and Arnold, J. Reactions of trialkylgalliums with substituted hydrazines leading to the formation of rings and cages: X-ray structures of ($iPr_2GaNHNMe_2$)$_2$ and (MeGaNHNtBu)$_4$. *J. Organomet. Chem.* **582**, 108–115 (1999).